Final Report

FHWA/IN/JTRP-99/8

PILE DESIGN BASED ON CONE PENETRATION TEST RESULTS

Rodrigo Salgado
Principal Investigator

Junhwan Lee
Research Assistant

and

School of Civil Engineering
Purdue University

Joint Transportation Research Program
Project Number: C-36-450
File Number: 6-18-14

Conducted in Cooperation with the
Indiana Department of Transportation
and the
Federal Highway Administration

Purdue University
West Lafayette, IN 47907
October 1999

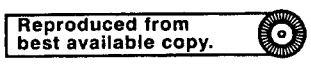

GENERAL DISCLAIMER

This document may have problems that one or more of the following disclaimer statements refer to:

- This document has been reproduced from the best copy furnished by the sponsoring agency. It is being released in the interest of making available as much information as possible.

- This document may contain data which exceeds the sheet parameters. It was furnished in this condition by the sponsoring agency and is the best copy available.

- This document may contain tone-on-tone or color graphs, charts and/or pictures which have been reproduced in black and white.

- The document is paginated as submitted by the original source.

- Portions of this document are not fully legible due to the historical nature of some of the material. However, it is the best reproduction available from the original submission.

TECHNICAL REPORT STANDARD TITLE PAGE

1. Report No.	2. Government Accession No.	3. Recipient's Catalog No.
FHWA/IN/JTRP-99/8		

4. Title and Subtitle	5. Report Date
Pile Designs Based on Cone Penetration Test Results	October 1999
	6. Performing Organization Code

7. Author(s)	8. Performing Organization Report No.
Rodrigo Salgado and Junhwan Lee	FHWA/IN/JTRP-99/8

9. Performing Organization Name and Address	10. Work Unit No.
Joint Transportation Research Program 1284 Civil Engineering Building Purdue University West Lafayette, Indiana 47907-1284	
	11. Contract or Grant No. SPR-2142

12. Sponsoring Agency Name and Address	13. Type of Report and Period Covered
Indiana Department of Transportation State Office Building 100 North Senate Avenue Indianapolis, IN 46204	Final Report
	14. Sponsoring Agency Code

15. Supplementary Notes

Prepared in cooperation with the Indiana Department of Transportation and Federal Highway Administration.

16. Abstract

The bearing capacity of piles consists of both base resistance and side resistance. The side resistance of piles is in most cases fully mobilized well before the maximum base resistance is reached. As the side resistance is mobilized early in the loading process, the determination of pile base resistance is a key element of pile design.

Static cone penetration is well related to the pile loading process, since it is performed quasi-statically and resembles a scaled-down pile load test. In order to take advantage of the CPT for pile design, load-settlement curves of axially loaded piles bearing in sand were developed in terms of normalized base resistance (q_b/q_c) versus relative settlement (s/B). Although the limit state design concept for pile design has been used mostly with respect to either s/B = 5% or s/B = 10%, the normalized load-settlement curves obtained in this study allow determination of pile base resistance at any relative settlement level within the 0 – 20% range. The normalized base resistance for both non-displacement and displacement piles were addressed.

In order to obtain the pile base load-settlement relationship, a 3-D non-linear elastic-plastic constitutive model was used in finite element analyses. The 3-D non-linear elastic-plastic constitutive model takes advantage of the intrinsic and state soil variables that can be uniquely determined for a given soil type and condition. A series of calibration chamber tests were modeled and analyzed using the finite element approach with the 3-D non-linear elastic-plastic stress-strain model. The predicted load-settlement curves showed good agreement with measured load-settlement curves. Calibration chamber size effects were also investigated for different relative densities and boundary conditions using the finite element analysis.

The value of the normalized base resistance q_b/q_c was not a constant, varying as a function of the relative density, the confining stress, and the coefficient of lateral earth pressure at rest. The effect of relative density on the normalized base resistance q_b/q_c was most significant, while that of the confining stress at the pile base level was small. At higher relative densities, the value of q_b/q_c was smaller (q_b/q_c = 0.12 -0.13 for D_R = 90%) than at lower relative densities (q_b/q_c = 0.19 - 0.2 for D_R = 30%). The values of the normalized base resistance q_b/q_c for displacement piles are higher than those for non-displacement piles, being typically in the 0.15 - 0.25 range for s/B = 5% and in the 0.22 - 0.35 range for s/B = 10%.

The values of the normalized base resistance q_b/q_c for silty sands are in the 0.12 – 0.17 range, depending on the relative density and the confining stress at the pile base level. The confining stress is another important factor that influences the value of q_b/q_c for silty sands. For lower relative density, the value of q_b/q_c decreases as the pile length increases while that for higher relative density increases.

For effective use of CPT-based pile design methods in practice, the method proposed in this study and some other existing methods reviewed in this study were coded in a FORTRAN DLL with a window-based interface. This program can be used in practice to estimate pile load capacity for a variety of pile and soil conditions with relatively easy input and output of desired data.

17. Key Words	18. Distribution Statement
piles, sands, cone penetration test, bearing capacity, constitutive model, finite element analysis, limit states design, calibration chamber test.	No restrictions. This document is available to the public through the National Technical Information Service, Springfield, VA 22161

19. Security Classif. (of this report)	20. Security Classif. (of this page)	21. No. of Pages	22. Price
Unclassified	Unclassified	249	

Form DOT F 1700.7 (8-69)

TABLE OF CONTENTS

	Page
TABLE OF CONTENTS	i
LIST OF TABLES	v
LIST OF FIGURES	vii
IMPLEMENTATION REPORT	x
CHAPTER 1 INTRODUCTION	1
1.1 Background	1
1.2 Statement of Problem	2
1.3 Objective and Scope	3
1.4 Report Outline	4
CHAPTER 2 PILE DESIGN BASED ON IN-SITU TEST RESULTS	7
2.1 Introduction	7
2.2 Estimation of Pile Load Capacity Based on SPT Results	9
2.2.1 Meyerhof's method	10
2.2.2 Aoki and Velloso's method	11
2.2.3 Reese and O'Neill's method	12
2.2.4 Briaud and Tucker's method	14
2.2.5 Neely's method	15
2.3 Estimation of Pile Load Capacity Based on CPT Results	17
2.3.1 The Dutch method	18
2.3.2 Schmertmann's method	20
2.3.3 Aoki and Velloso's method	22
2.3.4 LCPC method	22
2.4 Summary	27
CHAPTER 3 METHODS OF INTERPRETATION OF LOAD-SETTLEMENT CURVES	28
3.1 Introduction	28
3.2 Interpretation Methods	29

3.2.1 90% and 80% methods 29
3.2.2 Butler and Hoy's method 31
3.2.3 Chin's method 31
3.2.4 Davisson's method 33
3.2.5 De Beer's method 35
3.2.6 Permanent set method 35
3.3 Limit States Design 37
3.3.1 Limit states design in Eurocode 7 37
3.3.2 Limit states design for pile foundations 39
3.4 Tolerable Settlements for Buildings and Bridge Foundations 43
3.4.1 Buildings 43
3.4.2 Bridges 47
3.5 Summary 51

CHAPTER 4 MECHANICAL BEHAVIOR OF SAND 53

4.1 Introduction 53
4.2 Stress Tensor and Invariants 54
4.3 Elastic Stress-Strain Relationship 60
4.4 Elastic Behavior of Soil 67
4.4.1 Initial elastic modulus at small strain 67
4.4.2 Hyperbolic stress-strain relationship 71
4.4.3 Degradation of Elastic Modulus 75
4.5 Failure Criterion and Soil Plasticity 76
4.5.1 Failure criterion 76
4.5.2 Flow rule and stress hardening 79
4.5.3 Soil dilatancy and critical state of sand 82
4.6 Summary 85

CHPATER 5 3-D NON-LINEAR ELASTIC-PLASTIC STRESS-STRAIN MODEL 87

5.1 Introduction 87
5.2 Intrinsic and State Soil Variables 87
5.3 Modified Hyperbolic Model for Non-linear Elasticity 90
5.4 Non-Linear Elastic Model for Three Dimensions 95
5.4.1 Modified hyperbolic stress-strain relationship for three dimensions .. 95
5.4.2 Variation of bulk modulus and Poisson's ratio 99
5.4.3 Determination of the parameters f and g 101
5.5 Plastic Stress-Strain Relationship for Three Dimensions 118
5.5.1 Drucker-Prager failure criterion 118
5.5.2 Non-linear failure surface and flow rule 120
5.5.3 Incremental stress-strain relationship 121
5.6 Summary 126

CHAPTER 6 NUMERICAL ANALYSIS AND EXPERIMENTAL INVESTIGATION OF CALIBRATION CHAMBER TESTS 129

6.1 Introduction 129
6.2 Calibration Chamber Plate Load Tests 129
6.2.1 Description of test and experimental procedures 129
6.2.2 Test material and boundary conditions for calibration chamber plate load tests 131
6.3 Numerical Modeling of Plate Load Tests in Calibration Chambers 136
6.3.1 Program ABAQUS 136
6.3.2 Finite element modeling of plate load test 137
6.3.3 Predicted and measured plate resistance 139
6.4 Calibration Chamber Size Effects on Plate Load Test Results 155
6.4.1 Definition of size effect 155
6.4.2 Investigation of size effects for different boundary conditions 155
6.5 Summary 161

CHAPTER 7 DETERMINATION OF PILE BASE RESISTANCE 163

7.1 Introduction 163
7.2 Methods for Investigating Load-Settlement Response 164
7.3 Finite Element Modeling of Pile Load Test 165
7.4 Cone Penetration Resistance from Cavity Expansion Analysis 167
7.5 Determination of Base Resistance for Non-Displacement Piles 174
7.5.1 Load-settlement response for various soil conditions 174
7.5.2 Normalized base resistance for non-displacement piles 181
7.5.3 The effect of initial stress ratio K_0 187
7.6 Determination of Base Resistance for Displacement Piles 189
7.7 Normalized Base Resistance for Silty Sands 191
7.8 Summary 196

CHAPTER 8 ASSESSMENT OF PROPOSED NORMALIZED BASE RESISTANCE VALUES BASED ON CASE HISTORIES 198

8.1 Introduction 198
8.2 Non-Displacement Piles 200
8.2.1 Georgia Tech load test 200
8.2.2 São Paulo load test 200
8.2.3 Simonini's results 201
8.2.4 Calibration chamber plate load tests 201
8.3 Displacement Piles 202
8.3.1 Purdue university load test 202
8.3.2 NGI load tests 204
8.4 Summary 205

CHAPTER 9 PILE DESIGN USING CPT RESULTS 206

9.1 Introduction 206
9.2 Determination of Base and Shaft Resistance 206
9.2.1 Base resistance 206
9.2.2 Shaft resistance 209
9.2.3 Factor of safety 211
9.3 Use of SPT Blow Counts in CPT-based Method 214
9.4 Program CONEPILE 219
9.5 Summary 223

CHAPTER 10 SUMMARY, CONCLUSIONS AND RECOMMENDATIONS .. 224

10.1 Summary 224
10.2 Conclusions 226
10.3 Recommendations 228

LIST OF REFERENCES 229

APPENDIX 242

LIST OF TABLES

Table		Page
2.1	Values of K and α for different soil types	13
2.2	Values of F_1 and F_2 for different pile types	13
2.3	Values of correlation factor w for the Dutch method	18
2.4	Values of the factor c_{sf} by Schmertmann (1978)	20
2.5	Values of k_s for different soil and pile types	24
2.6	Values of k_c for different soil and pile types	25
3.1	Relationship between angular distortion and total settlement (after Skepmton and MacDonald 1956)	44
3.2	Tolerable movement for buildings (after Eurocode 1)	45
3.3	Settlement criteria for bridges expressed in terms of settlement magnitude	49
3.4	Tolerable angular distortion for bridge by Moulton et al. (1985)	50
3.5	Data used by Moulton et al. (1985) to establish criteria for angular distortion	50
4.1	Relationship between different elastic modulus	66
4.2	Values of C_g, e_g, and n_g for different sand type (after Salgado 1993, Salgado et al. 1999)	72
5.1	Basic properties of Ticino sand (after Ghionna et al. 1994)	102
5.2	Values of f and g from triaxial test results	117
5.3	Values of f and g for different relative densities	117
6.1	Soil and stress conditions in calibration chamber tests	133
6.2	Boundary conditions in calibration chamber tests	134
6.3	Size effect in calibration chamber test for BC1 condition	157
6.4	Size effect in calibration chamber test for BC2 condition	157
6.5	Size effect in calibration chamber test for BC3 condition	158
6.6	Size effect in calibration chamber test for BC4 condition	158
7.1	Basic soil properties used in finite element analysis	166
7.2	Pile geometry and soil conditions used in FEM analysis	175
7.3	Values of q_b/q_c according to several authors	184
7.4	Values of q_b/q_c at s/B = 5% and 10%	184
7.5	Base resistance ratio for displacement and non-displacement piles	190
7.6	Values of q_b/q_c for displacement piles	190
7.7	Values of soil intrinsic parameters with different silt contents (after Salgado	

	et al. 1999, Bandini 1999).	192
7.8	Values of friction angle ϕ_c at critical state and dilatancy parameters Q and R with different silt contents (after Salgado et al. 1999, Bandini 1999)	192
7.9	Values of f and g used in finite element analyses for silty sands	193
7.10	Values of q_b/q_c for silty sands with different relative densities and pile lengths	194
8.1	Values of q_b/q_c from load tests on non-displacement and displacement piles	199
9.1	Resistance modification factor f_p and factor of safety for different field tests (after Canadian Geotechnical Society 1992)	212
9.2	Partial factor of safety for the base resistance	214
9.3	Correlation between CPT and SPT	218
9.4	Correlation parameters for estimation of relative density	221

LIST OF FIGURES

Figure		Page
1.1	Research scope and process	5
2.1	Examples of methods for estimation of pile bearing capacity	8
2.2	Dutch method for determination of base resistance	19
2.3	Reduction factor in Schmertmann's method (1978)	21
2.4	Equivalent cone resistance q_{ca} for LCPC method	26
3.1	Definition of failure load in 90% criterion	30
3.2	Brinch Hansen's 80% criterion	30
3.3	Definition of failure load in Butler and Hoy's criterion	32
3.4	Chin's criterion for definition of failure load	32
3.5	Definition of failure load in Davisson's criterion	34
3.6	Definition of failure load in DeBeer's criterion	36
3.7	Definition of failure load in permanent set criterion	36
3.8	Load levels at ultimate and serviceability limit states	38
3.9	Differential settlements for (a) smaller-diameter and (b) larger-diameter piles	41
3.10	Load-settlement curves with load versus s_R (after Franke 1991)	42
3.11	Settlement criteria (after Wahls 1994)	46
3.12	Components of settlement and angular distortion in bridge for (a) uniform. settlement, (b) uniform tilt or rotation, (c) nonuniform regular settlement, and (d) nonuniform irregular settlement (after Duncan and Tan 1991)	48
4.1	Nine components of stress tensor in a soil element	55
4.2	Definition of mechanical behavior of a body (after Chen and Han 1988)	61
4.3	Non-linear stress-strain behavior of soil	68
4.4	Seismic cone penetration test	69
4.5	Hyperbolic model (a) stress-strain curve and (b) linear representation	73
4.6	Stress states for elastic-plastic material	78
4.7	Stress-strain behavior for hardening, perfectly plastic and softening material	81
4.8	Different behavior of dense and loose sand (after Lambe and Whitmann 1986)	83
5.1	Secant modulus for non-linear stress-strain behavior	89
5.2	Modulus degradation relationship for normally consolidated sand	

	(after Teachavorasinskun et al. 1991)	91
5.3	Modulus degradation curve for different values of f and g	93
5.4	Definition of τ_o, τ, and τ_{max} for (a) constant and (b) varying confinement	96
5.5	Modulus degradation curves for $D_R = 51.5\%$ and $\sigma_3 = 400$ kPa with f = 0.97 and g = 0.18	104
5.6	Modulus degradation curves for $D_R = 48.8\%$ and $\sigma_3 = 200$ kPa with f = 0.97 and g = 0.15	105
5.7	Modulus degradation curves for $D_R = 48.2\%$ and $\sigma_3 = 500$ kPa with f = 0.97 and g = 0.18	106
5.8	Modulus degradation curves for $D_R = 50.8\%$ and $\sigma_3 = 110$ kPa with f = 0.97 and g = 0.20	107
5.9	Modulus degradation curves for $D_R = 84.6\%$ and $\sigma_3 = 650$ kPa with f = 0.93 and g = 0.20	108
5.10	Modulus degradation curves for $D_R = 82.3\%$ and $\sigma_3 = 100$ kPa with f = 0.95 and g = 0.25	109
5.11	Modulus degradation curves for $D_R = 88.9\%$ and $\sigma_3 = 200$ kPa with f = 0.95 and g = 0.20	110
5.12	Modulus degradation curves for $D_R = 91.1\%$ and $\sigma_3 = 150$ kPa with f = 0.95 and g = 0.20	111
5.13	Modulus degradation curves for $D_R = 100\%$ and $\sigma_3 = 200$ kPa with f = 0.95 and g = 0.25	112
5.14	Modulus degradation curves for $D_R = 100\%$ and $\sigma_3 = 400$ kPa with f = 0.95 and g = 0.27	113
5.15	Modulus degradation curves for $D_R = 100\%$ and $\sigma_3 = 600$ kPa with f = 0.94 and g = 0.32	114
5.16	Modulus degradation curves for $D_R = 100\%$ and $\sigma_3 = 800$ kPa with f = 0.94 and g = 0.28	115
5.17	Modulus degradation curves for $D_R = 98.6\%$ and $\sigma_3 = 100$ kPa with f = 0.94 and g = 0.20	116
5.18	Drucker-Prager failure surface (a) in I_1-$\sqrt{J_2}$ plane and (b) in principal Stress plane	119
5.19	Plastic strain in Drucker-Prager failure criterion with associated flow rule	122
5.20	Non-linear failure surface with non-associated flow rule	122
6.1	Plate load test in calibration chamber	130
6.2	Types of boundary conditions in calibration chamber test	135
6.3	Finite element model for calibration chamber plate load test	138
6.4	Deformed finite element mesh of calibration chamber plate load test with $D_R = 55.2\%$, $\sigma'_v = 62.0$ kPa, and $\sigma'_h = 24.4$ kPa at s/B = 10%	141
6.5	Vertical stress distribution in calibration chamber plate load test with $D_R = 55.2\%$, $\sigma'_v = 62.0$ kPa, and $\sigma'_h = 24.4$ kPa at s/B = 10%	142
6.6	Vertical displacement distribution in calibration chamber plate load test with $D_R = 55.2\%$, $\sigma'_v = 62.0$ kPa, and $\sigma'_h = 24.4$ kPa at s/B = 10%	143
6.7	Horizontal displacement distribution in calibration chamber plate load test	

	with D_R = 55.2%, σ'_v = 62.0 kPa, and σ'_h = 24.4 kPa at s/B = 10%	144
6.8	Variation of shear modulus	145
6.9	Load-settlement curves for calibration chamber plate load tests (Test No. 300, 301, and 302)	146
6.10	Load-settlement curves for calibration chamber plate load tests (Test No. 303, 304, and 306)	147
6.11	Load-settlement curves for calibration chamber plate load tests (Test No. 307, 308, and 309)	148
6.12	Load-settlement curves for calibration chamber plate load tests (Test No. 310, 311, and 312)	149
6.13	Load-settlement curves for calibration chamber plate load tests (Test No. 313, 314, and 317)	150
6.14	Load-settlement curves for calibration chamber plate load tests (Test No. 321, 322, and 323)	151
6.15	Load-settlement curves for calibration chamber plate load tests (Test No. 324, 325, and 326)	152
6.16	Load-settlement curves for calibration chamber plate load tests (Test No. 327, 328, and 329)	153
6.17	Measured and predicted plate unit loads in calibration chamber tests	154
6.18	Comparison of pile base unit load with plate unit load in calibration chamber plate load tests	159
7.1	Load-settlement curves for pile load test at Georgia tech	168
7.2	Different failure mechanisms for deep penetration	170
7.3	Slip pattern under cone penetrometer (after Salgado 1993)	171
7.4	Stress rotation between different zones (after Salgado 1993)	173
7.5	Finite element model for 5-m pile	176
7.6	Finite element model for 10-m pile	177
7.7	Finite element model for 20-m pile	178
7.8	Base load-settlement curves for (a) 5-m, (b) 10-m, and (c) 20-m piles	179
7.9	Normalized load-settlement curves for (a) 5-m, (b) 10-m, and (c) 20-m piles in terms of q_b/q_c and s/B	182
7.10	Normalized base resistance q_b/q_c with (a) mean effective stress (σ'_m) at the pile base level and (b) relative d ensity (D_R)	186
7.11	Effect of K_0 on normalized base resistance q_b/q_c	188
7.12	Values of q_b/q_c for silty sand	195
8.1	Values of q_b/q_c in calibration chamber plate tests for (a) s/B = 5% and (b) s/B = 10%	203
9.1	Estimation of pile base resistance using different methods	208
9.2	Estimation of pile shaft resistance using different methods	210
9.3	CPT-SPT correlation with the mean grain size (after Robertson and Campanella 1983)	215
9.4	Cone resistance q_c and SPT blow count N with depth	217
9.5	Estimation of the base resistance for a given soil condition	222

IMPLEMENTATION REPORT

In the present study, in order to take advantage of the cone penetration test for pile design, load-settlement curves in terms of normalized base resistance (q_b/q_c) versus relative settlement (s/B) where q_c = cone resistance, s = pile base settlement, B = pile diameter were developed. Although the limit state design concept for pile design has been used mostly with respect to either s/B = 5% or s/B = 10%, the normalized load-settlement curves obtained in this study allow determination of pile base resistance for any relative settlement in the 0 – 20% range. This is important, as it permits consideration of specific project features, related to the superstructure or other components of the facility, by selecting a specific value of tolerable settlement for use in design.

The value of the normalized base resistance q_b/q_c is not a constant, varying as a function of the relative density, the confining stress, and the coefficient of lateral earth pressure at rest. The effect of relative density on the normalized base resistance is significant, while that of the confining stress at the pile base level is small. At higher relative densities, the value of q_b/q_c was smaller (q_b/q_c = 0.12 -0.13 for D_R = 90%) than at lower relative densities (q_b/q_c = 0.19 - 0.2 for D_R = 30%). It is usually very difficult to obtain undisturbed granular soil samples. It is, therefore, recommended that the estimation of the relative density be made through reasonable correlations based on in-situ test results such as the cone penetration test.

The normalized base resistance q_b/q_c proposed in this study can also be used for displacement piles. The values of q_b/q_c were typically in the 0.15 - 0.25 range for s/B = 5% and in the 0.22 - 0.35 range for s/B = 10%, depending on the value of relative density. CPT pile design methods can be used with the SPT blow count N for practical purposes, if a proper value of q_c/N is used for a given soil condition.

The evaluation of the relative settlement associated with the limit states design of piles should be done with consideration of the type, functionality, location, and

importance of the superstructure. The relative settlement s/B of piles leading to serviceability or ultimate limit states is usually in excess of 10%.

For implementation, use of the method in future INDOT piling projects is recommended. This may be done as part of an implementation project with extensive participation of INDOT design personnel. It is strongly recommended that a number of fully instrumented load tests on both driven piles and drilled shafts be performed along with the cone penetration test at representative sites in Indiana. The fully instrumented pile load test data would allow separate measurement of the base and the shaft resistance, and shaft resistance developed at the interface of the pile with different soil layers. This separation of load capacity in base and shaft capacities is essential for further validation of the design methods. It is also recommended that the selection of sites for pile load and cone penetration tests be such that sites with a variety of Indiana soil types be located. Results for such sites would be useful for further validation of the CPT-based pile design procedure for a wide range of soils.

CHAPTER 1 INTRODUCTION

1.1 Background

With the rapid growth of metropolitan areas, and fast industrialization resulting from the fast-paced economic globalization, there has been a need to build heavier and taller structures on marginal sites, where surface soils are weak and shallow foundations are usually not the best design solution. At the same time, advances in piling technology permit the installation of several types of piles, particularly non-displacement piles, at lower costs than was possible in the past. This in turn generates the motivation for further improvements in pile design capability. Additionally, there is a growing realization in the foundation engineering industry that certain types of deep foundation (such as large-diameter drilled shafts) are conservatively designed (Harrop-Williams 1989, Hirany and Kulhawy 1989, De Mello and Aoki 1993). In this context, advances in pile design methods can have significant economic impact and should be actively pursued.

Based on the method of installation, pile foundations are classified as either displacement or non-displacement piles. Driven piles are the most common type of displacement piles, and drilled shafts (bored piles) are the most common type of non-displacement piles. The load carrying capacity of both displacement and non-displacement piles consists of two components: base resistance and side resistance. The side resistance of piles is in most cases fully mobilized well before the maximum base resistance is reached (Franke 1993). After full mobilization of side resistance, any increment of axial load is transferred fully to the base. As the side resistance is

mobilized early in the loading process, the determination of base resistance is a key element in pile design.

1.2 Statement of Problem

Although friction piles are sometimes used, it is usually desirable to avoid relying solely on side resistance to develop the needed pile load capacity. This is done by placing the pile base on a bearing layer. Physically, what keeps a well designed pile from plunging when acted upon by an axial load is the base resistance developed in this layer, since the side resistance is fully mobilized early in the loading process. Plunging will take place only when the base unit load overcomes the limit base resistance q_{bL}, which is dependent not only on the density but also on the lateral confinement imposed by the surrounding soil immediately beneath the pile base.

A number of different methods have been proposed to assess deep bearing capacity based on the load-settlement curve obtained from pile load tests (Brinch Hansen 1963; De Beer 1967; Chin 1970; Davisson 1972). One modern pile design philosophy is based on the limit state concept. A limit state is evaluated with respect to either a loss of functionality or collapse of the superstructure and/or foundation (Franke 1990; Salgado 1995). According to Franke (1991), drilled shafts must typically undergo settlements greater than 10% of the base diameter before a limit state is reached. In some design situations, however, settlements less than 10% of the pile diameter may cause the foundations or the supported structure to reach a limit state. Irrespective of the specific value of settlement leading to a limit state, it is clearly necessary that a methodology be available to calculate the settlements caused by a given load and vice-versa in order to design piles within the limit-state framework. As shaft resistance is mobilized early in the loading process, the determination of the load-settlement relationship for the pile base is a key element in pile design and is the focus of this study.

Pile design in sands have been mostly based on results of the SPT test, which is today widely recognized to have numerous limitations (Seed et al.1985, Skempton1986). A serious limitation is that its main measurement, the number of blows required to drive a sampler one foot into the ground, is obtained based on a dynamic process, which is not well related to the quasi-static pile loading process. The SPT blow counts will also vary, sometimes significantly, with the operator and operating procedures. A much better alternative for pile design is to base it on data from a cone penetration test (CPT). In this test, a cylindrical penetrometer with a conical point is pushed into the ground quasi-statically, and a number of measurements are made.

The CPT was invented in northern Europe precisely for the purpose of pile foundation design (the test can be seen as a scaled-down load test on a pile), and has since been increasingly used in Europe, and to a lesser extent in the Americas and Asia, for pile design and other purposes. Although there have been several proposed methods of pile design based on cone penetration test results, an example of which is the LCPC method (Bustamante and Gianeselli 1982), only recently has a method based on establishing the relationship between cone tip resistance and the load-settlement relationship of a pile been proposed (Ghionna et al. 1993,1994; Salgado 1995). If such a relationship can be established reliably for a variety of soil conditions, significant economies in materials volume and pile installation charges will become possible with respect to current design methods.

1.3 Objective and Scope

The main objective of this research is to develop the methodology to determine pile load-carrying capacity based on the results of cone penetration test. The focus will be on the design of piles used to support typical transportation structures, with focus on the response of piles bearing on sandy soils to vertical loading.

In order to develop the load-settlement curves for a variety of soil conditions, 3-D finite element modeling is used. In general, the pile response to an external load is strongly non-linear and may involve large irreversible deformations. For more realistic modeling of soil behavior around axially loaded piles, a non-linear elastic-plastic stress-strain relationship will be used in the finite element analyses. The calculated load-settlement curves are normalized with the cone resistance q_c and the pile diameter B for the base resistance q_b and the settlement s, respectively. The fully developed load-settlement curves in terms of q_b/q_c versus s/B can be used to determine the normalized pile base resistance q_b/q_c for any settlement-based design criterion. The results of the analyses are compared with results from calibration chamber plate load tests and free field pile load tests. Figure 1.1 shows the general scope of this study.

1.4 Report Outline

This Report consists of ten chapters, including this introduction.

Chapter 2 reviews the pile design methods based on in-situ test results. The methods presented in Chapter 2 are based on the Standard Penetration Test (SPT) and Cone Penetration Test (CPT).

Chapter 3 describes the methodology for defining a "failure" load for a pile from its load-settlement curve. It also introduces the limit state design concept with main focus on ultimate and serviceability limit states that are important in geotechnical engineering. Tolerable settlements for different types of structures, including buildings and bridges are discussed as well.

Chapter 4 covers the conceptual framework for describing the mechanical behavior of soils, including stress tensors, invariants, linear and non-linear stress-strain relationships, and the concept of plasticity. Critical state, dilatancy and shear strength are all discussed.

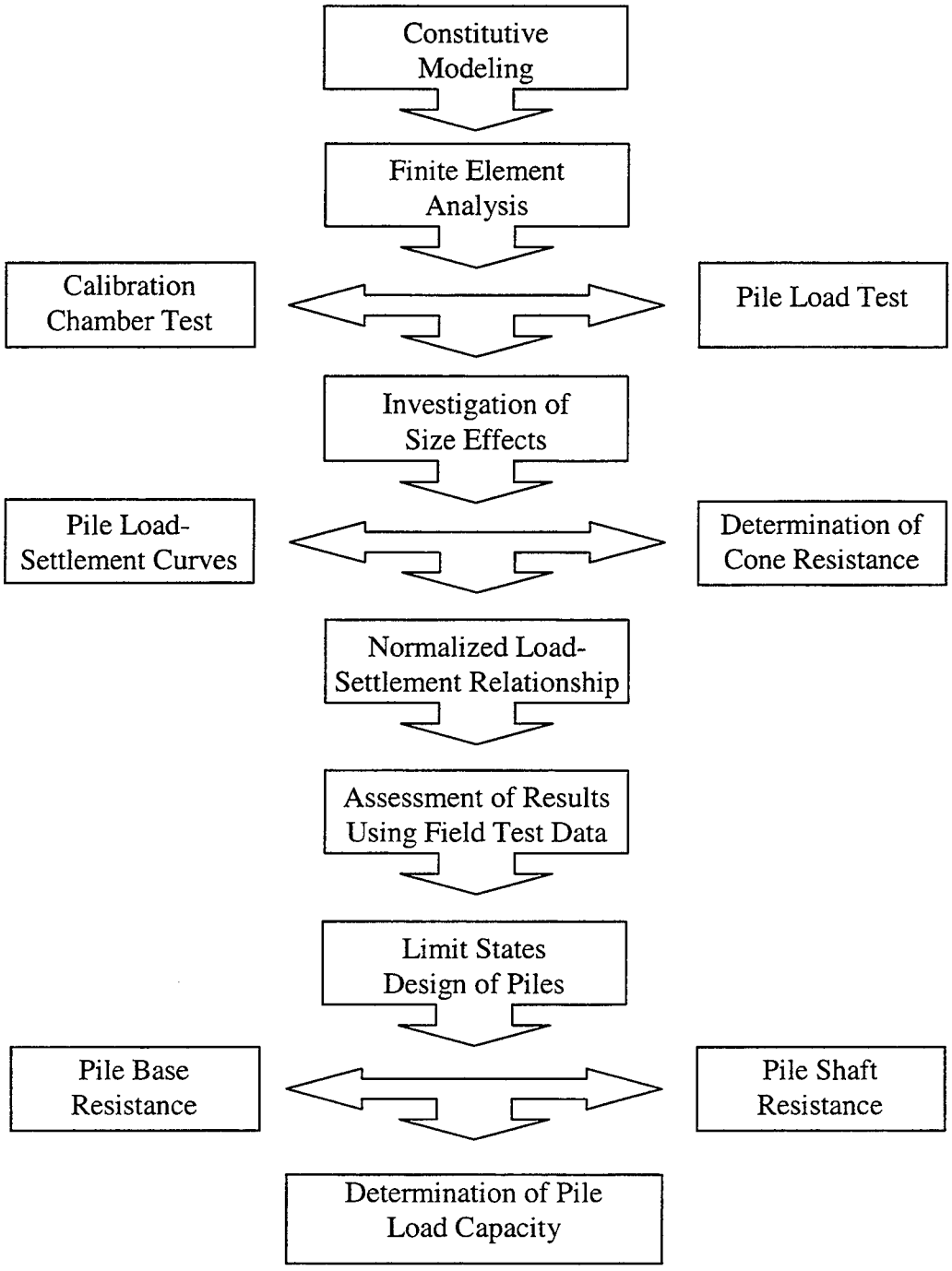

Figure 1.1 Research scope and process

Chapter 5 presents the non-linear elastic-plastic soil model used in this study. The concepts of intrinsic and state soil variables are explained. Values of the parameters required for the non-linear soil model are presented based on experimental test results. The Drucker-Prager plastic model for the definition of post-failure behavior of the soil is described with incremental stress-strain relationship.

Chapter 6 presents the finite element modeling and analysis of the calibration chamber plate load tests. The analytical results are compared with the measured values of plate resistance in calibration chamber plate load tests. This chapter aims to verify the accuracy of plate resistance predictions and assess the existence of chamber size effects on plate resistance values.

Chapter 7 presents the determination of pile base resistance based on the normalized load-settlement curves fully developed for axially loaded piles bearing in sand for a variety of soil and stress conditions. The effects of relative density and the coefficient of lateral earth pressure on the pile base resistance are explained.

Chapter 8 presents case histories for the validation of the results obtained in this study. The case histories include both non-displacement and displacement piles.

Chapter 9 discusses pile design using CPT results in the light of the results of Chapters 1 - 8. In order to present a more complete discussion on the subjects, correlations between SPT and CPT are also addressed. A computer program developed for estimating pile load capacity in practice is briefly also introduced.

Chapter 10 presents the conclusions drawn from this study.

CHAPTER 2 PILE DESIGN BASED ON IN-SITU TEST RESULTS

2.1 Introduction

In general the application of in-situ tests to pile design is done through:

(1) Indirect Methods

or

(2) Direct Methods

Indirect methods require the evaluation of the soil characteristic parameters, such as the internal friction angle ϕ and the undrained shear strength s_u, from in-situ test results. This requires consideration of complicated boundary-value problems (Campanella et al. 1989). On the other hand, with direct methods, one can make use of the results from in-situ test measurements for the analysis and the design of foundations without the evaluation of any soil characteristic parameter. The application of direct methods to the analysis and the design of foundations is, however, usually based on empirical or semi-empirical relationships. Figure 2.1 shows some examples of the methods available for indirect and direct approaches in different applications.

Indirect methods for pile design include Vesic (1977), Coyle and Castello (1981), and β method (Burland 1973) for cohesionless soil, and s_u method (Bowles 1988), α method (Tomlinson 1971), β method (Burland 1973), and λ method (Vijayvergiya and Focht 1972) for cohesive soil. Most indirect pile design methods define the correlation

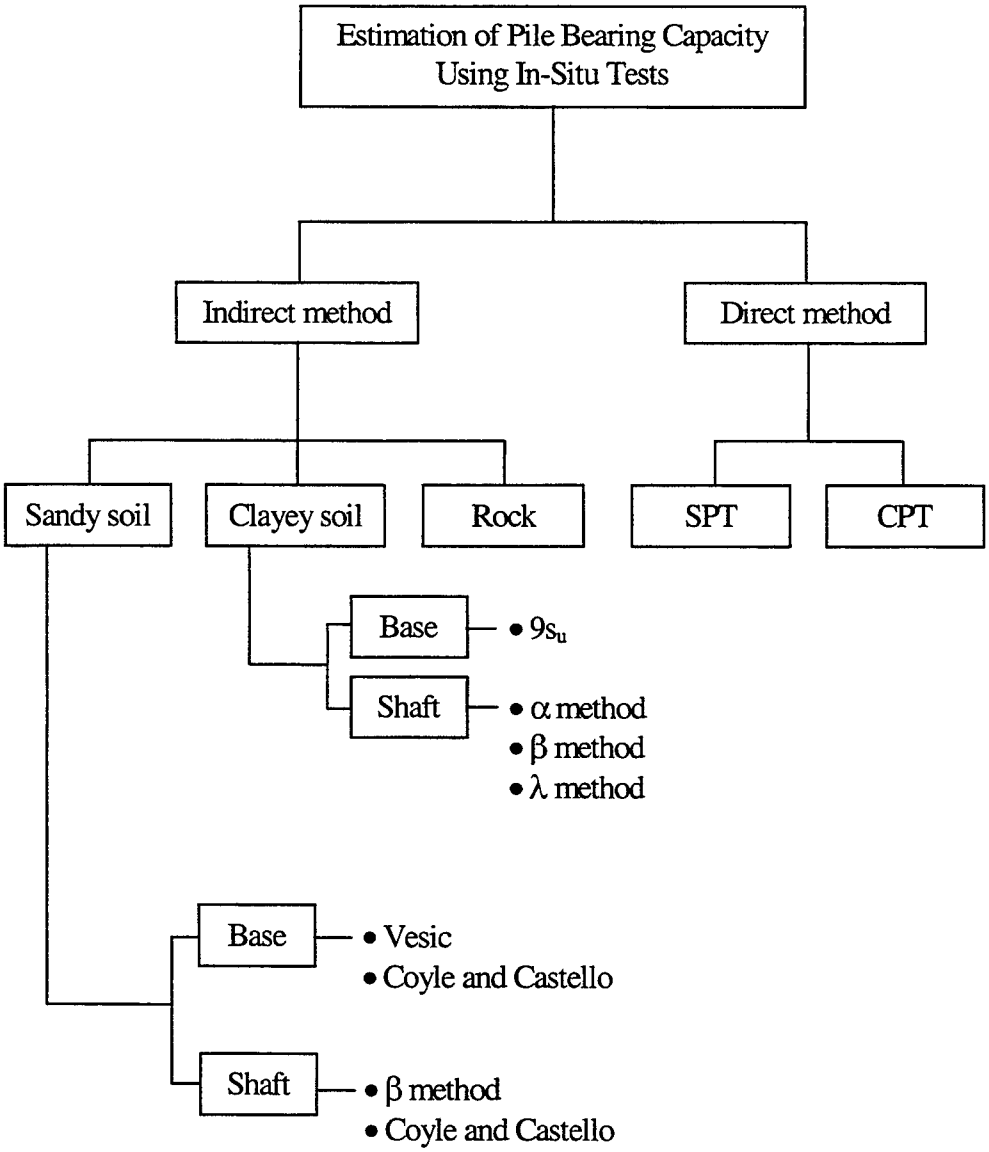

Figure 2.1 Examples of methods for estimation of pile bearing capacity.

factor between the stress state and base or shaft resistance based on the soil-strength parameters.

Direct methods used for pile design have been mainly based on the standard penetration test (SPT) and the cone penetration test (CPT). Although the SPT has been used more extensively, it is widely recognized that it has a number of limitations (Seed et al. 1985, Skempton 1986). A serious limitation is that its main measurement (the SPT blow count) is not well related to the pile loading process. The SPT blow count can also vary depending on operation procedures. The CPT is a superior test for pile design purposes. In this test, a cylindrical penetrometer with a conical tip is pushed into the ground as if it were a scaled pile load test. In addition to the similarity between the pile loading and cone penetration testing mechanisms, the possibility of simultaneous measurement of shear wave velocities makes it possible to estimate elastic properties of subsurface soils, which may improve the quality of the design with more accurate in-situ soil properties.

The main focus of this study is the estimation of pile bearing resistance based on direct methods, the cone penetration test in particular. In this chapter, the existing methods for pile design using the SPT and CPT, will be reviewed.

2.2 Estimation of Pile Load Capacity Based on SPT Results

In most SPT methods, the pile load capacities are defined in terms of the SPT blow count N and the correlation parameters. These relationships are typically of the form (Bandini and Salgado 1998):

$$q_b = n_b N_b \tag{2.1}$$

$$q_s = \sum n_{si} N_{si} \tag{2.2}$$

where q_b = base resistance

n_b = factor to convert SPT blow count to base resistance

N_b = representative N_{SPT} value at the pile base level

q_s = shaft resistance

n_{si} = factor to convert SPT blow count to shaft resistance

N_{si} = representative N_{SPT} value along the pile shaft in layer i.

For the computation of base resistance, it is recommended that the SPT N value should represent the condition near the pile base. Different ways to define the representative N value have been proposed. They will be discussed as the methods are presented.

2.2.1 Meyerhof's method

Meyerhof (1976, 1983) proposed the following expressions for the base resistance based on SPT results:

for sands and gravels

$$q_b = 0.4 N_{1,60} \frac{D}{B} P_a \leq 4.0 N_{1,60} P_a \qquad (2.3)$$

for nonplastic silts

$$q_b = 0.4 N_{1,60} \frac{D}{B} P_a \leq 3.0 N_{1,60} P_a \qquad (2.4)$$

where q_b = base resistance

$N_{1,60}$ = SPT N value corrected for field procedures and overburden stress

D = pile embedment depth

B = pile diameter

P_a = reference stress = 100 kPa = 0.1 MPa ≈ 1 tsf.

The upper limits of base resistance given in (2.3) and (2.4) are always applied in case of D/B ≥ 10 for sands and gravels, and D/B ≥ 7.5 for nonplastic silts. For pile

diameters within the range of $0.5 < B/B_R < 2$, where B_R = reference length = 1 m = 100 cm ≈ 40 in. ≈ 3.28 ft., q_b is reduced using the factor r_b as follows:

$$r_b = \left(\frac{B + 0.5B_R}{2B} \right)^n \leq 1 \tag{2.5}$$

where n = 1,2, or 3 for loose, medium, or dense sand, respectively. Meyerhof (1976, 1983) also proposed the expression of shaft resistance for small- and large-displacement piles:

for small-displacement piles in cohesionless soil

$$q_s = \frac{P_a}{100} N_{60} \tag{2.6}$$

for large-displacement pile in cohesionless soil

$$q_s = \frac{P_a}{50} N_{60} \tag{2.7}$$

where q_s = shaft resistance

N_{60} = SPT N value corrected for field procedures only.

2.2.2 Aoki and Velloso's method

Aoki and Velloso (1975) proposed the following formula for different soil and pile types:

$$q_b = \frac{K}{F_1} N_b P_a \tag{2.8}$$

$$q_{si} = \frac{\alpha K}{F_2} N_{si} P_a \tag{2.9}$$

where K = empirical factor in function of soil type

F_1 and F_2 = empirical factors in function of pile type

α = shaft resistance factor depending on soil type

N_b = average of the three N_{SPT} values close to the pile base

N_{si} = average of N_{SPT} values along the pile shaft in layer i, excluding those used to calculate N_b.

P_a = reference stress = 100 kPa = 0.1 MPa ≈ 1 tsf.

The values of K, α, and F_1, F_2 are given in Table 2.1 and 2.2, respectively.

2.2.3 Reese and O'Neill's method

Based on the observation of 41 loading tests, Reese and O'Neill (1989) proposed the following SPT-based relationship for the base resistance of drilled shafts embedded in sand:

$$q_b = 0.6N \cdot P_a \leq 45P_a \tag{2.10}$$

where q_b = base resistance; P_a = reference stress = 100 kPa = 0.1 MPa ≈ 1 tsf. The limit value given in (2.10) was selected because no ultimate bearing pressure was observed beyond that value for any of the loading test results. In (2.10), the SPT N value should be mean uncorrected value within a distance of two times the base diameter (B_b) below the base of the drilled shaft.

In order to restrict the settlement of large-diameter shafts, they also suggested to use a reduced value of the base resistance ($q_{b,r}$) as follows:

Table 2.1 Values of K and α for different soil types.

Type of Soil	K	α (%)
Sand	10.0	1.4
Silty sand	8.0	2.0
Clayey silty sand	7.0	2.4
Clayey sand	6.0	3.0
Silty clayey sand	5.0	2.8
Silt	4.0	3.0
Sandy silt	5.5	2.2
Clayey sandy silt	4.5	2.8
Clayey silt	2.3	3.4
Sandy clayey silt	2.5	3.0
Clay	2.0	6.0
Sandy clay	3.5	2.4
Sandy silty clay	3.0	2.8
Silty clay	2.2	4.0
Silty sandy clay	3.3	3.0

Table 2.2 Values of F_1 and F_2 for different pile types.

Type of Pile	F_1	F_2
Franki Piles	2.50	5.0
Steel Piles	1.75	3.5
Precast Concrete Piles	1.75	3.5
Bored Piles	3.0 – 3.50	6.0 – 7.0

$$q_{b,r} = 1.25 \cdot \left(\frac{B_R}{B_b} \right) \cdot q_b \qquad \text{for } B_b \geq 1.25\ B_R \tag{2.11}$$

where $q_{b,r}$ = reduced base resistance; B_R = reference length = 1 m ≈ 40 in. ≈ 3.28 ft. According to Reese and O'Neill (1989), it is not recommended to use the above expressions for drilled shafts with a depth less than 15 ft (4.6 m) or a diameter less than 24 in (610 mm). For the shaft resistance of drilled shaft in sands, they recommend the use of the β method.

2.2.4 Briaud and Tucker's method

Based on the review and parametric study of 33 instrumented pile load tests, Briaud and Tucker (1984) developed a method for determining base (q_b) and shaft (q_s) resistance as a function of pile settlement (s). In this method, both q_b versus s and q_s versus s are modeled as hyperbolic curves. Residual stress resulting from rebounding after pile driving was also considered in that hyperbolic formula. The hyperbolic equations for both base and shaft resistance are given by:

$$q_b = \frac{s}{\frac{1}{K_p} + \frac{s}{q_{\max} - q_{res}}} + q_{res} \tag{2.12}$$

$$q_s = \frac{s}{\frac{1}{K_\tau} + \frac{s}{q_{s,\max} - q_{s,res}}} - q_{s,res} \tag{2.13}$$

where $$K_p = 18684 (N_{pt})^{0.0065} \left(\frac{P_a}{B_R} \right) \tag{2.14}$$

$$q_{\max} = 19.75(N_{pt})^{0.36} P_a \tag{2.15}$$

$$q_{res} = 5.57 L \Omega P_a \tag{2.16}$$

$$\Omega = \sqrt{\frac{K_\tau P}{A E_p}} \tag{2.17}$$

$$K_\tau = 200(N_{side})^{0.27}\left(\frac{P_a}{B_R}\right) \tag{2.18}$$

$$q_{s,\max} = 0.224(N_{side})^{0.29} P_a \tag{2.19}$$

$$q_{s,res} = q_{res} A_p / A_s \; < \; q_{s,\max} \tag{2.20}$$

In (2.12) – (2.20), P_a = reference stress = 100 kPa = 0.1 MPa ≈ 1tsf; B_R = reference length = 1 m ≈ 40 in.; L, P, E_p, and A are the pile length, perimeter, modulus and cross section area, respectively; A_p and A_s are the pile base and shaft areas; N_{pt} is the uncorrected average SPT blow count within the zone from 4 diameters above to 4 diameters below the pile base; and N_{side} is the uncorrected average SPT blow count within the layer where shaft resistance is considered.

2.2.5 Neely's method

Neely (1990, 1991) suggested new empirical relationships between SPT N value and base resistance for expanded-base and auger-cast piles in sands. For expanded-base piles such as a Franki pile, he pointed out that the ultimate base resistance of twice the value for conventional driven piles, as suggested by Meyerhof (1956), would result in overestimated value of base resistance, based on the observation of load tests on 93 expanded-base piles. It was explained that the overestimated base resistance for expanded-base piles by Meyerhof's (1956) suggestion is due to the ignorance of casing effect. The piles having uncased and compacted concrete shaft create very large

pressures between the shaft and surrounding soil and show greater load capacity than comparable piles having cased shaft.

According to Neely (1990), the ultimate base resistance of expanded-base piles in sands can be given as:

$$q_b = 0.28 \cdot N \frac{D}{D_b} P_a \leq 2.8 \cdot N \cdot P_a \tag{2.21}$$

where q_b = base resistance

D = embedment depth of the maximum cross section of the base resistance as the sum of the driven length and on-half the base diameter.

D_b = diameter of expanded base

N = SPT N value

P_a = reference stress = 100 kPa = 0.1 MPa ≈ 1 tsf.

The limit value of 2.8N applies whenever the ratio of D/D_b is greater than 10. For augered, cast-in-place (auger-cast) piles, the base resistance was suggested as follows (Neely 1991):

$$q_b = 1.9N \cdot P_a \tag{2.22}$$

The auger-cast piles are different from the conventional drilled shafts in terms of the installation process. The auger-cast piles are installed supporting the side of augered hole by the soil-filled auger without use of temporary casing or bentonite slurry.

From the comparison with the results of loading test on auger-cast piles, it was shown that (2.22) results reasonable agreement with the measured value of base resistance of auger-cast piles. It was also observed that the ratio q_b/N increases as mean grain size (D_{50}) increases, and decreases as fines content increases (Neely 1989).

2.3 Estimation of Pile Load Capacity Based on CPT Results

Similarly to what is done in the case of the SPT, the determination of pile load capacity based on CPT results can be expressed as:

$$q_b = c_b q_c \tag{2.23}$$

$$q_s = \sum c_{si} q_{ci} \tag{2.24}$$

where q_b = base resistance

c_b = empirical parameter to convert q_c to base resistance

q_c = cone resistance at the pile base level

q_s = shaft resistance

c_{si} = empirical parameter to convert q_c to shaft resistance

q_{ci} = representative cone resistance for layer i

Values of c_b and c_{si} have been proposed mostly based on empirical correlations developed between pile load test results and CPT results. Because different authors proposed different values of c_b and c_{si}, the use of such parameters should be applied under conditions similar to those under which they were determined (Bandini and Salgado 1998). Although most expressions were based on cone resistance q_c, some authors (Price and Wardle 1982, Schmertmann 1978) suggested the use of cone sleeve friction f_s for the estimation of shaft resistance with the following general expression:

$$q_s = c_{sfi} f_{si} \tag{2.25}$$

where c_{sfi} is a empirical parameter to convert cone sleeve friction to shaft resistance and f_{si} is a representative cone sleeve friction for layer i. In this section, some of the methods for the determination of pile load capacity using CPT results are described.

2.3.1 The Dutch method

In the Dutch method (DeRuiter and Beringen 1979), pile base resistance in cohesionless soil is computed from the average cone resistance q_c between the depth of 8B above and 4B below a pile base, where B is the pile diameter. As can be seen in Figure 2.2, the average cone resistance q_{c1} for the layer below the pile base is determined along the path 'abcd', in which 'x' is selected so as to minimize q_{c1}. Similarly, the average cone resistance q_{c2} for the layer above the pile base is calculated along the path 'efgh'. The base resistance q_b is then obtained from the average of q_{c1} and q_{c2} as follows:

$$q_b = \frac{w(q_{c1} + q_{c2})}{2} \leq 150\ P_a \tag{2.26}$$

where q_b = base resistance

w = correlation factor

q_{c1} = average cone resistance for the layer below pile base

q_{c2} = average cone resistance for the layer above pile base

P_a = reference stress = 100 kPa = 0.1 MPa ≈ 1 tsf

The values of correlation factor w for several soil conditions are given in Table 2.3.

Table 2.3 Values of correlation factor w for the Dutch method.

Soil Condition	Values of w
Sand with OCR = 1	1.0
Very gravelly coarse sand; sand with OCR = 2 to 4	0.67
Fine gravel; sand with OCR = 6 to 10	0.50

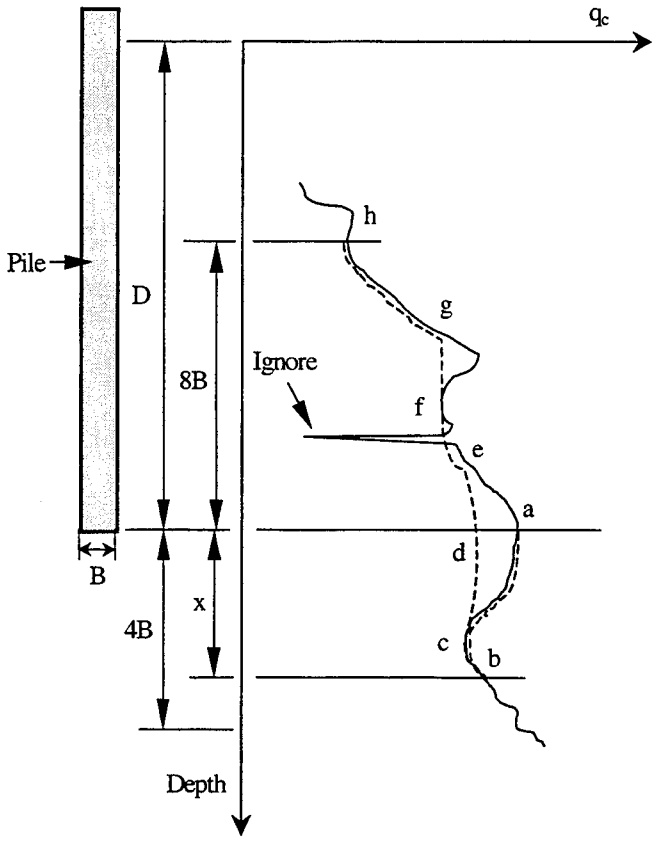

Figure 2.2 Dutch method for determination of base resistance.

2.3.2 Schmertmann's method

For the estimation of pile base resistance in stiff cohesive soil, Schmertmann (1978) proposed the use of an average cone resistance with multiplying the reducing factor shown in Figure 2.3. The average cone resistance is calculated within a depth between 8B above and 0.7B to 4B below a pile base in the same way as in the Dutch method described previously. He also recommended reducing the base resistance that is obtained from the Dutch method by 60% in case of using mechanical cone for a cohesive soil.

For shaft resistance in sand, the following values of the shaft resistance factor c_s of (2.24) were proposed for different pile types:

$c_s = 0.008$ for open-end steel tube piles

$c_s = 0.012$ for precast concrete and steel displacement piles

$c_s = 0.018$ for vibro and cast-in-place displacement piles with steel driving tube removed, and timber piles

According to Schmertmann (1978), the cone sleeve friction f_s can also be used to estimate shaft resistance in cohesive soil. The values of c_{sf} of (2.25) that relates cone sleeve friction to shaft resistance are given by Table 2.4 for displacement piles.

Table 2.4 Values of the factor c_{sf} by Schmertmann (1978).

f_s/P_a	Values of c_{sf}	
	Steel Piles	Concrete and Timber piles
0.25	0.97	0.97
0.50	0.70	0.76
0.75	0.48	0.58
0.88	0.40	0.52
1.00	0.36	0.47
1.50	0.27	0.43
2.00	0.20	0.40

* P_a = reference stress = 100 kPa = 0.1 MPa ≈ 1 tsf .

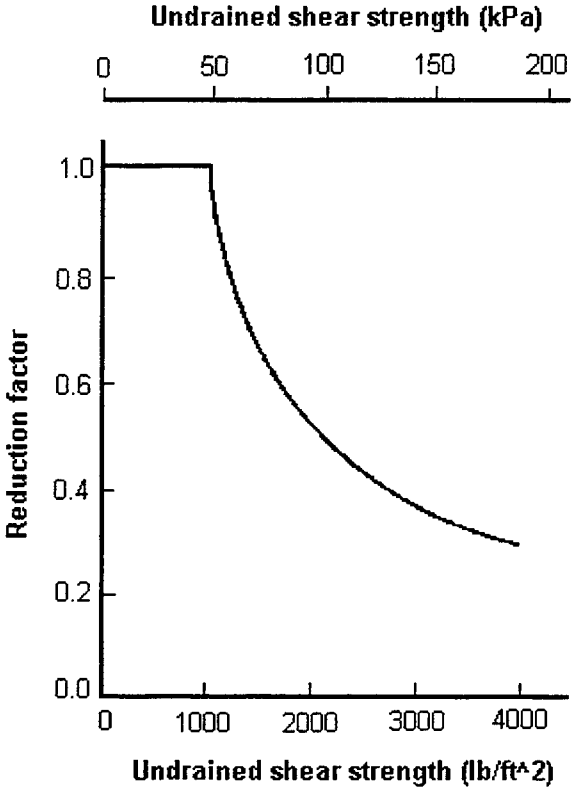

Figure 2.3 Reduction factor in Schmertmann's method (1978).

2.3.3 Aoki and Velloso's method

Based on the load tests and CPT results, Aoki and Velloso (1975) proposed the following relationship for both shaft and base resistance in terms of cone resistance q_c:

$$q_b = \frac{1}{F_1} q_c \tag{2.27}$$

$$q_s = \frac{\alpha}{F_2} q_c \tag{2.28}$$

where α, F_1 and F_2 are the same empirical parameters as shown in Table 2.1 and 2.2.

2.3.4 LCPC method

From a number of load tests and CPT results for several pile and soil types, Bustamante and Gianeselli (1982) presented a pile design method using factors related to both pile and soil types. The method presented by them is often referred to as the LCPC method. The basic formula for the LCPC method can be written as:

$$q_b = k_c q_{ca} \tag{2.29}$$

$$q_s = \frac{1}{k_s} q_c \tag{2.30}$$

where k_c = base resistance factor;

q_{ca} = equivalent cone resistance at pile base level;

k_s = shaft resistance factor;

q_c = representative cone resistance for the corresponding layer

The values of k_c and k_s depend on the nature of soil and its degree of compaction as well as the pile installation method. Tables 2.5 and 2.6 show the values of k_s and k_c with different soil and pile types, respectively. According to Bustamante and Gianeselli (1982), the values of k_c for driven piles cannot be directly applied to H-piles and tubular piles with an open base without proper investigation of full-scale load tests.

The equivalent cone resistance q_{ca} used in (2.29) represents an arithmetical mean of the cone resistance measured along the distance equal to 1.5B above and below the pile base, where B = pile diameter. The procedure for determining q_{ca} consists of the following steps (see also Figure 2.4):

(1) The curve of the cone resistance q_c is smoothened in order to eliminate local irregularities of the raw curve.
(2) Beginning with the smoothened curve, the mean cone resistance q_{cm} of smoothened resistance between the distance equal to 1.5B above and below pile base is obtained.
(3) The equivalent cone resistance q_{ca} is calculated as the average after clipping the smoothened curve at $0.7q_{cm}$ to $1.3q_{cm}$. This clipping is carried out for the values higher than 1.3 q_{cm} below the pile base, and the values higher than 1.3 q_{cm} and lower than $0.7q_{cm}$ above the pile base.

In the LCPC method, separate factors of safety are applied to the shaft and base resistance. A factor of safety equal to 2 for shaft resistance and 3 for base resistance were considered, so that the carrying load is given by:

$$Q_w = \frac{Q_L^s}{2} + \frac{Q_L^b}{3} \tag{2.31}$$

where Q_w = allowable load
Q_L^s = limit shaft load
Q_L^b = limit base load

Table 2.5 Values of k_s for different soil and pile types.

Nature of Soil	q_c / P_a	Value of k_s				Maximum q_s / P_a					
		Type				Type					
		IA	IB	IIA	IIB	IA	IB	IIA	IIB	IIIA	IIIB
Soft clay and mud	<10	30	30	30	30	0.15	0.15	0.15	0.15	0.35	-
Moderately compact clay	10 to 50	40	80	40	80	0.35 (0.8)	0.35 (0.8)	0.35 (0.8)	0.35	0.8	≤ 1.2
Silt and loose sand	≤ 50	60	150	60	120	0.35	0.35	0.35	0.35	0.8	-
Compact to stiff clay and compact chalk	> 50	60	120	60	120	0.35 (0.8)	0.35 (0.8)	0.35 (0.8)	0.35	0.8	≤ 2.0
Soft chalk	≤ 50	100	120	100	120	0.35	0.35	0.35	0.35	0.8	-
Moderately compact sand and gravel	50 to 120	100	200	100	200	0.8 (1.2)	0.35 (0.8)	0.8 (1.2)	0.8	1.2	≤ 2.0
Weathered to fragmented chalk	> 50	60	80	60	80	1.2 (1.5)	0.8 (1.2)	1.2 (1.5)	1.2	1.5	≤ 2.0
Compact to very compact sand and gravel	>120	150	300	150	200	1.2 (1.5)	0.8 (1.2)	1.2 (1.5)	1.2	1.5	≤ 2.0

- P_a = reference stress = 100 kPa = 0.1 MPa ≈ 1 tsf
- Type IA: Plain bored piles, mud bored piles, hollow auger bored piles, cast screwed piles, piers, barrettes, and micropiles installed with low injection pressure.
- Type IB: Bored piles with steel casing and driven cast piles.
- Type IIA: Driven or jacked precast piles and prestressed concrete piles.
- Type IIB: Driven or jacked steel piles.
- Type IIIA: Driven grouted piles and driven rammed piles.
- Type IIIB: High pressure grouted piles with diameter greater than 250 mm and micropiles installed with high injection pressure.

Table 2.6 Values of k_c for different soil and pile types.

Nature of Soil	q_c / P_a	Value of k_c	
		Group I	Group II
Soft clay and mud	< 10	0.40	0.50
Moderately compact clay	10 to 50	0.35	0.45
Silt and loose sand	≤ 50	0.40	0.50
Compact to stiff clay and compact silt	> 50	0.45	0.55
Soft chalk	≤ 50	0.20	0.30
Moderately compact sand and gravel	50 to 120	0.40	0.50
Weathered to fragmented chalk	> 50	0.20	0.40
Compact to very compact sand and gravel	120	0.30	0.40

- P_a = reference stress = 100 kPa = 0.1 MPa ≈ 1 tsf.
- Group I: Plain bored piles, cased bored piles, mud bored piles, hollow auger bored piles, piers, barrettes, micropiles installed with low injectionpressure.
- Group II: Driven cast-in-place piles and piles in Type IIA, IIB, IIIA, and IIIB of Table 2.5.

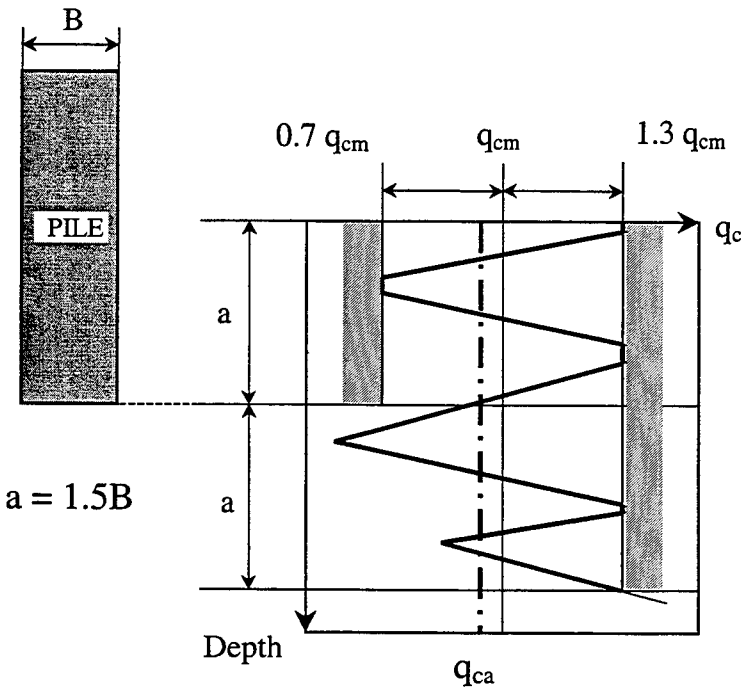

Figure 2.4 Equivalent cone resistance q_{ca} for LCPC method.

2.4 Summary

Pile design methods using in-situ test results can be classified in two categories, indirect and direct methods. Indirect methods require the evaluation of the soil characteristic parameters in the estimation of pile bearing capacity. On the other hand, the direct methods utilize the in-situ test results directly in the estimation of pile bearing capacity.

Direct methods have been based mainly on the standard penetration test (SPT) and the cone penetration test (CPT). In SPT methods, most proposed expressions relate the pile bearing capacity to the SPT blow count N and correlation parameters. These methods include Meyerhof (1976, 1983), Aoki-Velloso (1975), Reese and O'Neil (1989), and Neely (1990, 1991), while Briaud and Tucker (1984) presented a hyperbolic formula for the base and shaft resistance as a function of pile settlement with SPT N value in the evaluation of equation parameters. It should be noticed that, since every method has been developed under different conditions, including soil and pile type, the consideration of such factors must be taken into account for the selection of pile design methods.

The cone penetration test is regarded as a better alternative to the SPT because it reflects well the vertical pile loading mechanism. The widely used CPT methods include the Dutch method (DeRuiter and Beringen 1979), Schmertmann (1978), Aoki-Velloso (1975), and the LCPC method (Bustamante and Gianeselli 1982). Most CPT methods relate the base and shaft resistance to the cone penetration resistance q_c using empirical parameters. The empirical parameters relating pile resistance to q_c are given as a function of soil and pile type. The LCPC method (Bustamante and Gianeselli 1982) provides relatively detailed information regarding soil and pile types. Some authors propose the use of cone sleeve friction f_s for the estimation of shaft resistance, while others propose that it be done on the cone penetration resistance q_c.

CHAPTER 3 METHODS OF INTERPRETATION OF LOAD-SETTLEMENT CURVES

3.1 Introduction

The pile load-settlement curve obtained from a load test provides an important indication of pile load-carrying capacity. In general, however, there is no unique criterion that can clearly define a "failure load" or "bearing capacity" of a pile based on a load-settlement curve. Although several methods for evaluating the "failure" load of a pile have been proposed, they produce a very wide range of results (Horvitz et al. 1981). The approach selected for interpreting a load-settlement curve should account for the characteristics of the load-settlement curve and the soil condition.

For geotechnical structures to perform "properly", it is necessary that the structure satisfy certain fundamental requirements. Whenever a geotechnical structure or a part thereof fails to satisfy a performance criterion, it is said to have reached a "limit state". Potentially, the number of limit state events is infinite. It is therefore necessary that the consideration of limit state events be reduced to a relatively small number of critical events in order to achieve a balance between the needs for safety and economy in design (Bolton 1989).

In this chapter, some of the methods proposed for interpretation of pile load-settlement curves will be reviewed. Additionally two important types of limit states in geotechnical engineering and tolerable settlement for different types of structures are discussed.

3.2 Interpretation Methods

3.2.1 90% and 80% methods

The 90% method was proposed by Brinch Hansen (1963). In the 90 % method, the failure point in the load-settlement curve is defined as the load that causes a settlement twice as large as that caused by 90% of that same load (see Figure 3.1). The main goal of this method is to define the failure load as the point from which significant change in the rate of displacement to load increment occurs.

For the application to both the quick and slow maintained pile load tests, Brinch Hansen also suggested 80% method. In this method, the failure load is defined as the load that produces four times the strain caused by 80% of the same load. The failure load (Q_f) and corresponding settlement (s_f) in the 80% method are defined based on the hyperbolic relationship of a transformed load-settlement curve. As shown in Figure 3.2, the load-settlement curve is plotted in terms of $\sqrt{s}/Q$ versus s, where s = settlement and Q = load. From the relationships between $0.8Q_f$ versus $0.25s_f$ and Q_f versus s_f through a hyperbolic equation in Figure 3.2, the failure load (Q_f) and corresponding settlement (s_f) can be obtained as:

$$Q_f = \frac{1}{2\sqrt{C_1 C_2}} \tag{3.1}$$

$$s_f = \frac{C_2}{C_1} \tag{3.2}$$

in which C_1 and C_2 are the slope and the intersection point of the curve in Figure 3.2, respectively.

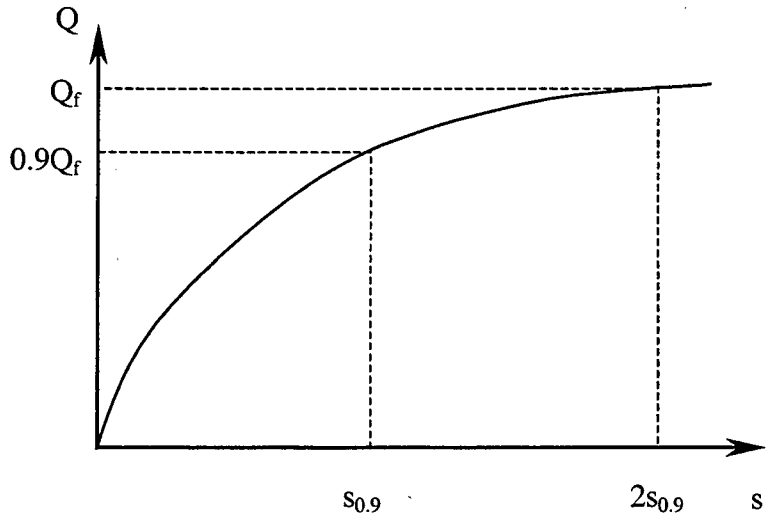

Figure 3.1 Definition of failure load in 90% method.

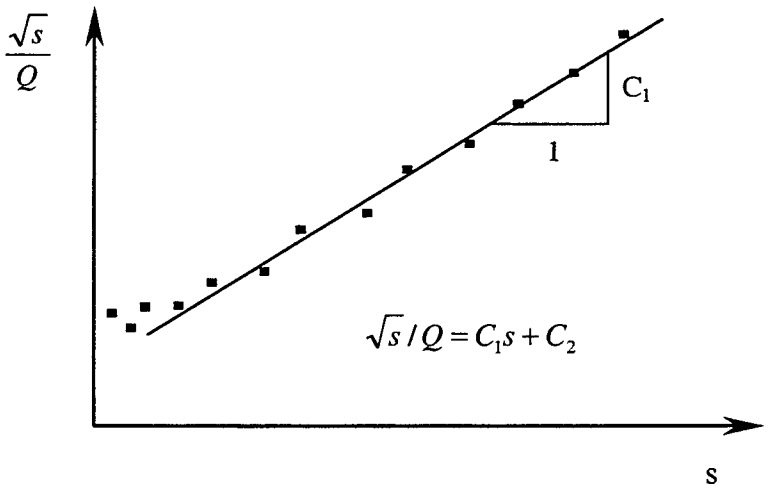

Figure 3.2 Brinch Hansen's 80% method.

3.2.2 Butler and Hoy's method

Butler and Hoy (1977) considered the failure load as the load that is the intersection point of two lines tangent to the load-settlement curve at different points. One tangent line is the initial straight line that can be thought of as an elastic compression line. The other line is tangent to a point having a slope of $0.00125B_R/Q_r$ in the load-settlement curve, where B_R = reference length = 1 m ≈ 40 in. ≈ 3.28 ft and Q_r = reference load = 1 ton ≈ 9.8 kN.

Usually, the rebound portion of the load-settlement curve is more or less parallel to the true elastic line. Based on this observation, Fellenius (1980) suggested the use of a rebound line as an elastic compression line instead of an initial straight line in Figure 3.3 for determining a "failure" load.

3.2.3 Chin's method

Based on the assumption that the pile load-settlement curve is approximately hyperbolic, Chin (1970) proposed the following (Figure 3.4):

(1) The load-settlement curve is drawn in terms of s/Q versus s;
(2) The failure load (Q_f) or ultimate load (Q_{ult}) is defined as $Q_f = 1/C_1$.

Chin's failure method is applicable to both the quick and slow maintained load tests. It may, however, provide an unrealistic "failure load" if a constant time increment is not used in the pile load test. Extrapolation for hyperbolic load-settlement curve also requires that the load test be extended sufficiently far.

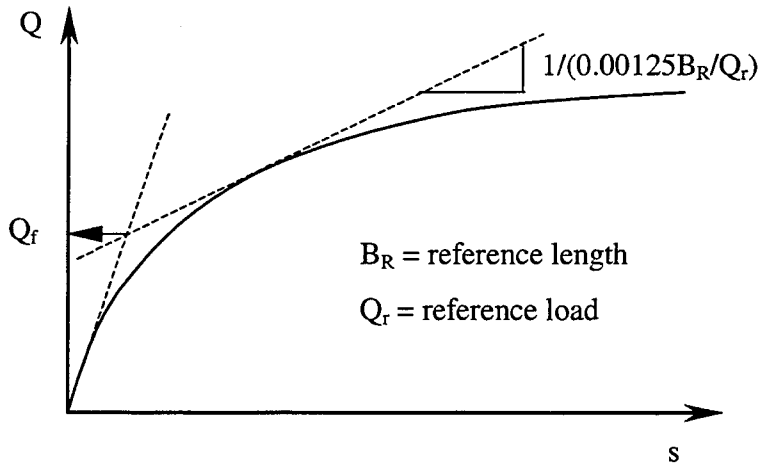

Figure 3.3 Definition of failure load in Butler and Hoy's method.

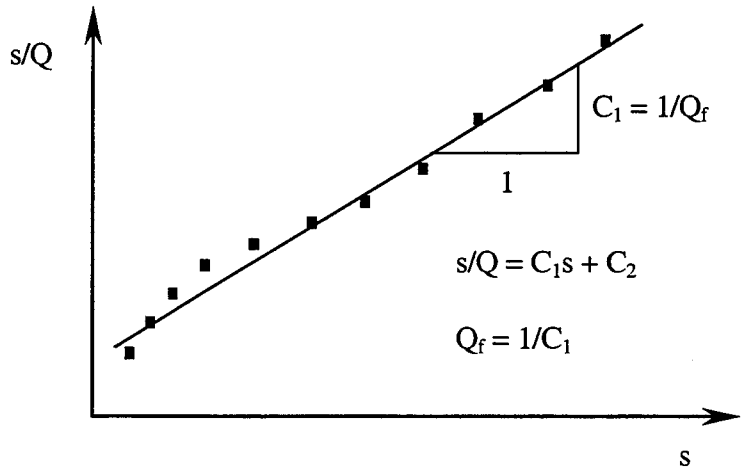

Figure 3.4 Chin's method for definition of failure load.

3.2.4 Davisson's method

In Davisson's method (Davisson 1972), the "failure" load is defined as the load leading to a deformation equal to the summation of the pile elastic compression and a deformation equal to a percentage of the pile diameter. This relationship is given by:

$$s_f = \frac{QL}{AE} + 0.00381B_R + \frac{1}{3.05} \cdot \frac{B}{B_R} \tag{3.3}$$

where s_f = settlement at failure condition

Q = applied load

L = pile length

E = Young's modulus of pile

A = cross sectional area of pile

B_R = reference length = 1 m ≈ 40 in. ≈ 3.28 ft

B = pile diameter.

As can be seen in Figure 3.5, the elastic compression line of the pile can be obtained from the elastic deformation equation of a column which is given by a equation of $s_{elastic}$ = QL/AE.

Since this method is, in general, regarded conservative, it appears to work best with data from quick maintained load tests. Due to the dynamic effect, loads obtained from the quick maintained load tests tend to be higher than loads obtained from the slow maintained load tests, sometimes significantly so in clayey material (Fellenius 1975). It may, therefore, lead to overly conservative results when applied to data from the slow maintained load tests resulting in considerable underestimation of a pile failure load (Coduto 1994).

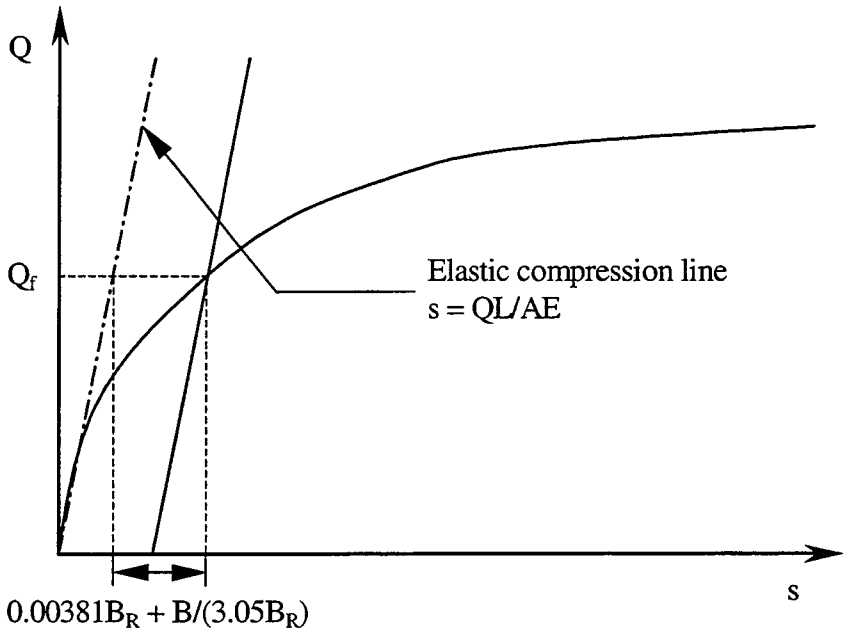

Figure 3.5 Definition of failure load in Davisson's method.

3.2.5 De Beer's method

De Beer (1967) defined the "failure load" as the load corresponding to the point of maximum curvature on the load-settlement curve. In this method, the load-settlement curve is plotted using log-log scale as shown in Figure 3.6. The failure load is then determined as the load corresponding to the point at which two straight lines intersect. This method was, however, originally proposed for the slow maintained pile load test.

3.2.6 Permanent set method

In the permanent set method (Horvitz et al. 1981), failure is defined by a certain specified amount of permanent deformation that occurs after full load removal. To determine the failure load with this method, the value of the permanent settlement should be predefined prior to performing a load test.

As shown in Figure 3.7, the failure load corresponding to a specified permanent settlement can be determined by conducting the load-rebound for each applied load. The permanent settlement appearing as a result of unloading is generally associated with plastic soil deformation. This method does not provide one "failure" load, as "failure" in this case depends on what level of permanent settlement the user associates with "failure".

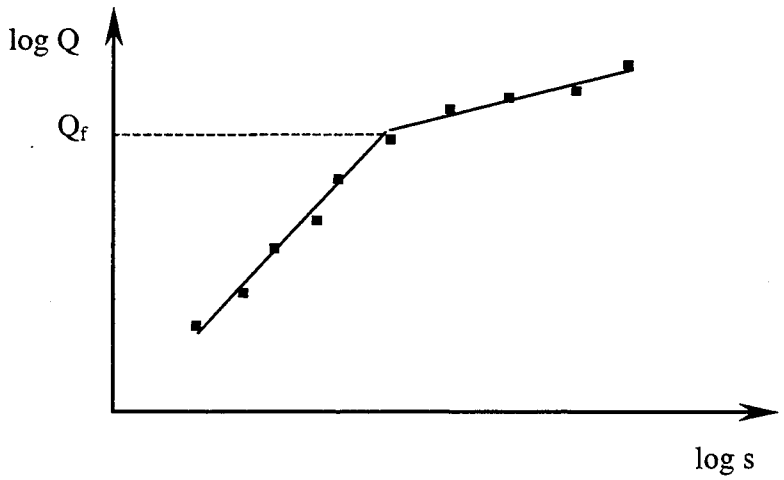

Figure 3.6 Definition of failure load in De Beer's method.

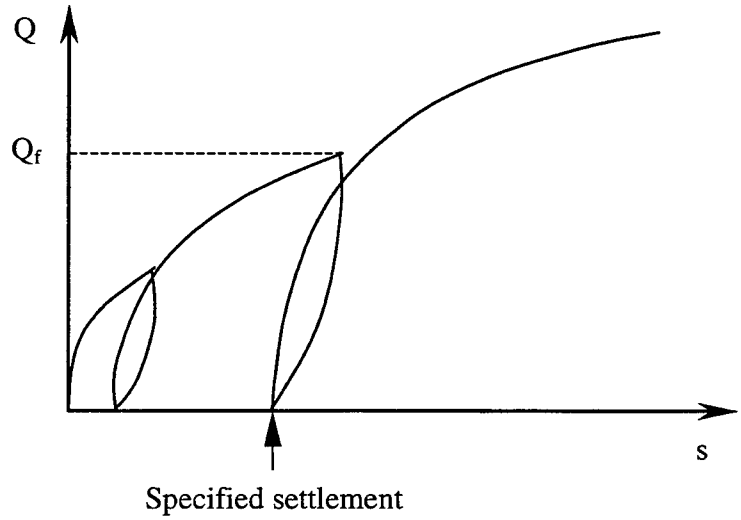

Figure 3.7 Definition of failure load in permanent set method.

3.3 Limit States Design

In general, there are two types of limit states in civil engineering design: ultimate and serviceability limit states (Ovesen and Orr 1991). An ultimate limit state is reached when loss of static equilibrium, severe structural damage, or rupture of critical components of the structure occurs. On the other hand, a serviceability limit state is associated with loss of functionality of the structure, typically related to settlement, deformation, utility, appearance, and comfort. Figure 3.8 illustrates the characteristic difference of the load levels between ultimate and serviceability limit states on the load-deformation curve.

In practice, it is usually difficult to determine which type of limit states governs design. It is, therefore, required that both the ultimate and serviceability limit states be investigated.

3.3.1 Limit states design in Eurocode 7

The Eurocodes were established for common use of design codes in European communities. Design criteria in the Eurocodes are based on the limit states concept. Geotechnical design is addressed in Eurocode 7 (1993). Three categories of design problems are defined in order to establish minimum requirements for the extent and quality of geotechnical investigation and calculations as well as construction control-checks (Franke 1990, Ovesen and Orr 1991).

The factors taken into consideration for determination of the geotechnical categories in each particular design situation are as follows:

(1) Nature and size of the structure;
(2) Conditions related to the location of the structures (neighboring structures, utilities, vegetation, etc.);

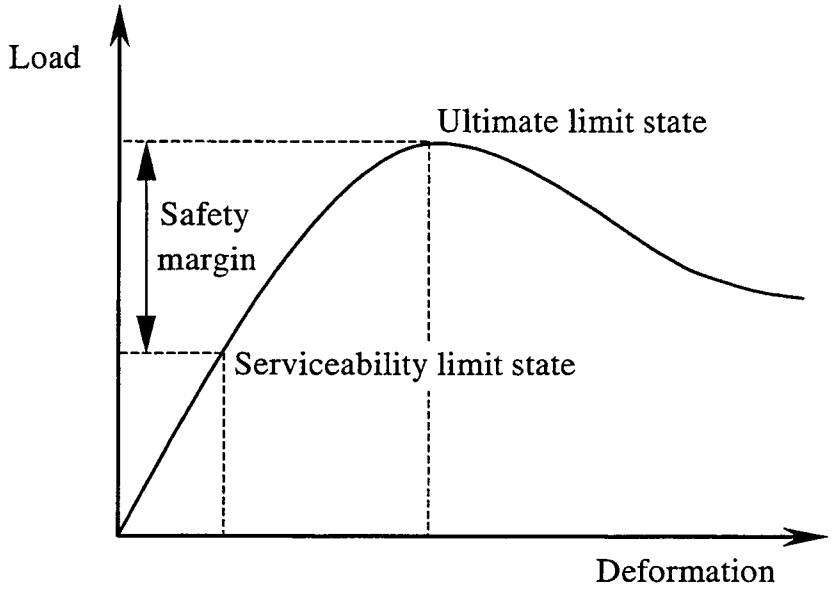

Figure 3.8 Load levels at ultimate and serviceability limit states.

(3) Ground conditions;
(4) Groundwater conditions;
(5) Regional seismicity;
(6) Influence of the environment (hydrology, surface water, subsidence, seasonal changes of moisture, etc.)

Geotechnical Category 1

This includes small and relative simple structures for which it is possible to ensure that the performance criteria will be satisfied on the basis of experience and qualitative geotechnical investigations with no risk for property and life.

Geotechnical Category 2

This category includes structures for which quantitative geotechnical data and analysis are necessary to ensure that the performance criteria will be satisfied, but for which conventional procedures of design and construction may be used. These necessitate the involvement of qualified engineers with relevant experience.

Geotechnical Category 3

This category includes very large or unusual structures, structures involving abnormal risks or unusual or exceptionally difficult ground or loading conditions, or structures in highly seismic areas.

3.3.2 Limit states design for pile foundations

The limit states for a pile foundation under axial loading condition, according to Eurocode 7, are defined as follows (Salgado 1995):

(IA) Bearing capacity failure of single pile, which may correspond to either
  (IA-1) a condition of large settlement for unchanged load on the pile;
  (IA-2) the crushing or other damage to the pile element itself;

(IB) Collapse or severe damage to the superstructure due to foundation movement;

(II) Loss of functionality or serviceability of the superstructure due to displacement of the foundations;

(III) Overall stability failure, consisting of the development of a failure mechanism involving the pile foundation or a part thereof.

Limit state (III) is a possibility for the case where the structure is located close to a topographic discontinuity area such as a slope, river and retaining wall. In most pile design situations under axial loading condition, either limit state (II) or limit state (IB) governs design. This is so because either the serviceability or the stability of the supported structure would be jeopardized before a given pile developed a classical bearing capacity failure. The settlement required for the limit state (IB) is usually greater than that for limit state (II).

It is necessary to establish tolerable settlements s_{IB} and s_{II} according to limit state IB and II (Franke 1991, 1993). The tolerable settlements s_{IB} and s_{II} can be related to the corresponding differential settlements Δs_{IB} and Δs_{II}. The angular distortion (β), defined as the ratio of differential settlement between two adjacent columns to the distance between them, is often used to determine tolerable differential settlements.

Figure 3.9 shows the settlements at the foundation level with smaller- and larger-diameter piles, caused by the superstructure. As can be seen in Figure 3.9, a_s and a_l represent the distances between two adjacent piles, and $\Delta s_{s,max}$ and $\Delta s_{l,max}$ are the maximum differential settlements for the smaller- and larger-diameter piles, respectively.

It must be realized that the distance a_l is generally greater than a_s because larger-diameter piles are used to carry heavier axial loads with larger spans. The maximum angular distortion β_{max} for each case can be defined as:

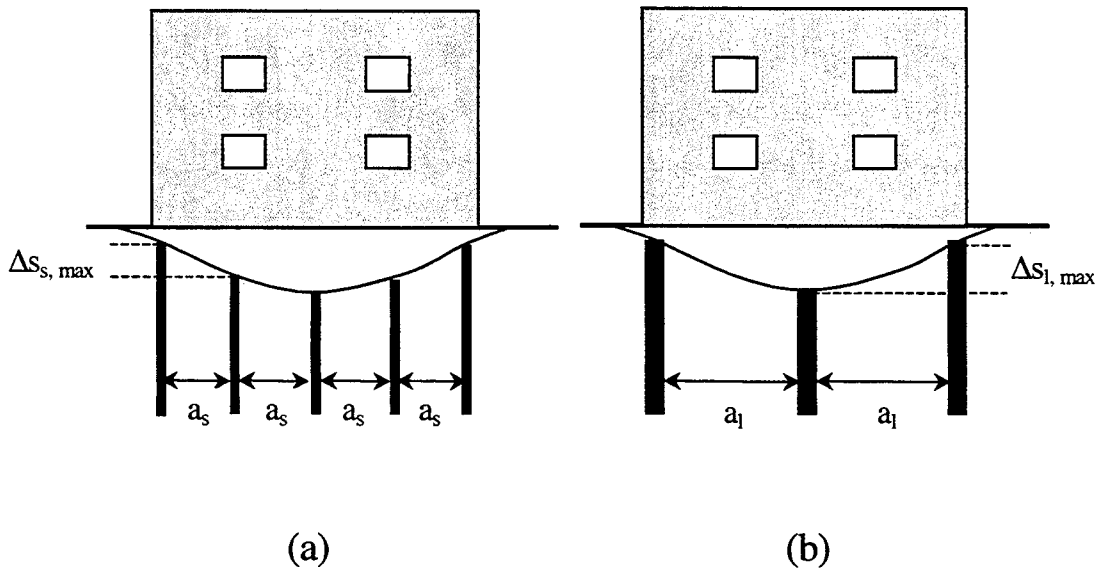

Figure 3.9 Differential settlements for (a) smaller-diameter and (b) larger-diameter piles.

for smaller-diameter piles $$\beta_{max} = \frac{\Delta s_{s,max}}{a_s} \quad (3.4)$$

for larger-diameter piles $$\beta_{max} = \frac{\Delta s_{l,max}}{a_l} \quad (3.5)$$

Irrespective of pile size, the maximum angular distortion β_{max} given in (3.4) and (3.5) cannot be larger than the value of the tolerable angular distortion. This implies that the tolerable differential settlement Δs usually increases with the span. The total tolerable settlement accordingly, also increases with span. Given that the pile diameters also increase with span, a common way to define limit states for piles is to establish a value of tolerable relative settlement s_R as a ratio of the pile settlement s to the pile diameter B. According to Franke (1991), the relative settlement required to cause either loss of functionality or collapse of the superstructure is larger than $s_R = 0.1$. As shown in Figure 3.10, by the time s_R reaches 0.1, the shaft resistance has already been fully mobilized. This implies that the evaluation of the base resistance is a key element in the limit states design of piles.

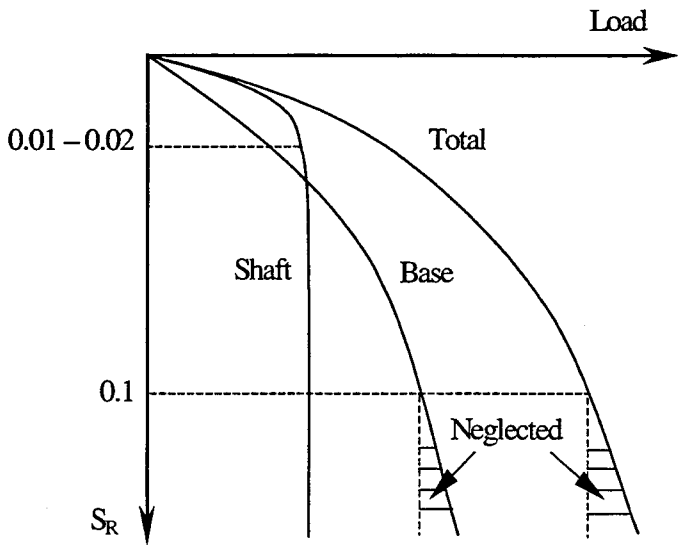

Figure 3.10 Load-settlement curves with load versus s_R (after Franke 1991).

3.4 Tolerable Settlements for Buildings and Bridge Foundations

3.4.1 Buildings

Tolerable settlements for buildings have been extensively studied by several authors (Skempton and MacDonald 1956, Polshin and Tokar 1957, Burland and Wroth 1974, Wahls 1981). Skempton and MacDonald (1956) presented the values of tolerable movement for building structures based on the observed settlements and damages of 98 buildings. These values of tolerable movement for building structures are still widely accepted as a satisfactory criterion. Because most of the observed damage appeared to be related to distortional deformation, the angular distortion (β) was selected as the critical index of settlement. From the field data, a limit value of angular distortion equal to β = 1/300 was suggested for the condition of cracking in panel walls. The corresponding differential settlement for a typical span equal to 20 ft is about 3/4 in. The limit value of angular distortion that caused structural damage in frames was observed to be β = 1/150.

Based on the examination of the case histories, Skempton and MacDonald (1956) also suggested the correlation between the maximum angular distortion and total settlement. As would be expected, the angular distortion for a given maximum settlement was smaller for a raft than for isolated foundations. It was observed as well that the angular distortion for a given maximum settlement was smaller for a clay than for a sand. These relationships can be given by (3.6) – (3.9) with the numerical factors suggested by Skempton and MacDonald (1956):

$$\rho_{max} = 25 B_R \cdot \beta_{max} \qquad \text{for clay with isolated foundations} \qquad (3.6)$$

$$\rho_{max} = 15 B_R \cdot \beta_{max} \qquad \text{for sand with isolated foundations} \qquad (3.7)$$

$$\rho_{max} = 31.25 B_R \cdot \beta_{max} \qquad \text{for clay with raft foundations} \qquad (3.8)$$

$$\rho_{max} = 18.75 B_R \cdot \beta_{max} \qquad \text{for sand with isolated foundations} \qquad (3.9)$$

in which ρ_{max} = the maximum settlement; β_{max} = the maximum angular distortion; and B_R = reference length = 1 m ≈ 40 in. Table 3.1 summarizes the limit values of total settlement, and the correlation factor R representing the ratio of angular distortion to the total settlement suggested by Skempton and MacDonald (1956). The values of Table 3.1 were based on the tolerable angular distortion of β = 1/300 for the different types of foundations and soils.

Polshin and Tokar (1957) proposed separate tolerable settlement criteria for framed structures and load bearing walls. For framed structures, the limit values of angular distortion are similar to those by Skempton and MacDonald (1956), ranging from 1/500 to 1/200. For load bearing walls, the limit values of angular distortion were suggested in terms of deflection ratio Δ/L, where Δ = maximum relative settlement from two reference points and L = distance between them, depending on the length to height ratio. Figure 3.11 shows the common settlement criteria including the deflection ratio.

More recently, guidelines for tolerable settlement can be found in Eurocodes. The tolerable movement criteria in the Eurocodes are very similar to those by Skempton and MacDonald (1956) and Polshin and Tokar (1957). Table 3.2 shows the values of tolerable settlements in Eurocode 1 (1993). It can be seen that the values of tolerable angular distortion in the Eurocode 1 appear to be more restrictive than those by Skempton and Macdonald (1956) and Polshin and Tokar (1957).

Table 3.1 Relationship between angular distortion and total settlement (after Skempton and MacDonald 1956).

		Isolated foundation	Raft foundation
Clay	R	1/25	1/31.25
	ρ_{max}	$0.075 \cdot B_R$[a]	$0.075 \cdot B_R$ to $0.125 \cdot B_R$[a]
Sand	R	1/15	1/18.75
	ρ_{max}	$0.05 \cdot B_R$[a]	$0.05 \cdot B_R$ to $0.075 \cdot B_R$[a]

[a] B_R = reference length = 1 m ≈ 40 in. ≈ 3.28 ft.

Table 3.2 Tolerable movement for buildings (after Eurocode 1).

Total settlement	
• Isolated foundations	25 mm
• Raft foundations	50mm
Differential settlement between adjacent columns	
• Open frame	20 mm
• Frames with flexible cladding or finishing	10 mm
• Frames with rigid cladding or finishing	5 mm
Angular distortion	1/500

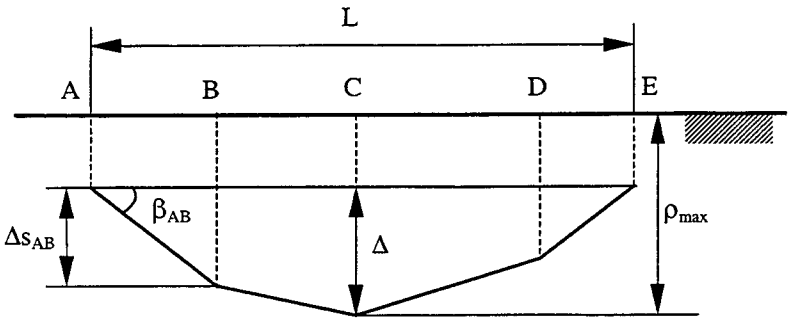

(a) settlement without tilt

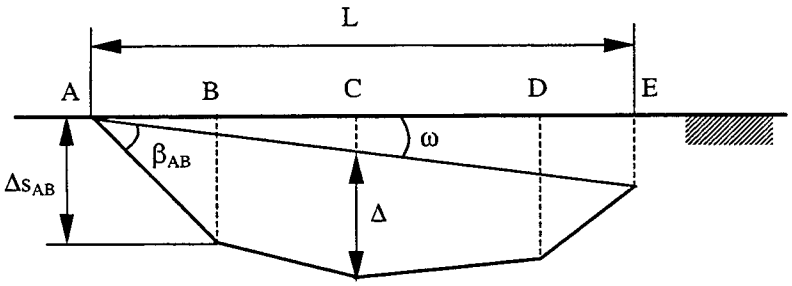

(b) settlement with tilt

Δs_{AB} = differential settlement between A and B
β_{AB} = angular distortion between A and B
ρ_{max} = total settlement
L = distance between two reference points (A and E)
ω = tilt = rigid body rotation
Δ = relative deflection
= maximum displacement from a straight line connecting two reference points (A and E)
Δ/L = deflection ratio

Figure 3.11 Settlement criteria (after Wahls 1994).

3.4.2 Bridges

According to Walkinshaw (1978), the tolerability of the movement should be assessed qualitatively by the agency responsible for each bridge using the following definition: "Movement is not tolerable if damage requires costly maintenance and/or repairs and a more expensive construction to avoid this would have been preferable". Although said of bridges, this is a concept of general applicability.

As shown in Figure 3.12, the settlement of a bridge can be divided into three components: uniform settlement, tilt (or rotation), and nonuniform settlement. Uniform settlement represents a condition where all foundation elements settle by the same amount. Although it may cause such problems as drainage and clearance at the end of the bridge, it does not cause significant distortion of the bridge superstructure (Stermac 1978, Yokel 1990, Wahls 1990). Uniform tilt or rotation corresponds to a uniform angular distortion. This pattern of settlement is possible only for single-span bridges or bridges with very stiff superstructures. This can also cause some problems with the approach slab, with drainage, and with clearance, while distortion effects are largely absent in the superstructure.

Nonuniform settlement can be categorized by two representative types: regular nonuniform [see Figure 3.12 (c)] and irregular [see Figure 3.12 (d)] nonuniform settlement. If the same amount of total settlement is considered, irregular settlement will cause more significant distortion of the superstructure than regular settlement, mainly due to the greater differential settlement (Xanthakos 1995). Foundation design must control the differential settlement and angular distortion not to exceed the limit state.

Limit values of tolerable settlements for bridge have been proposed by several investigators (Walkinshaw 1978, Bozozuk 1978, Grover 1978, Wahls 1990). No single measure of settlement or distortion, however, can be regarded as a sole indicator of bridge damage, due to the complexity of settlement patterns. Table 3.3 shows criteria of tolerable bridge settlements in terms of the magnitude of the settlement. Although the

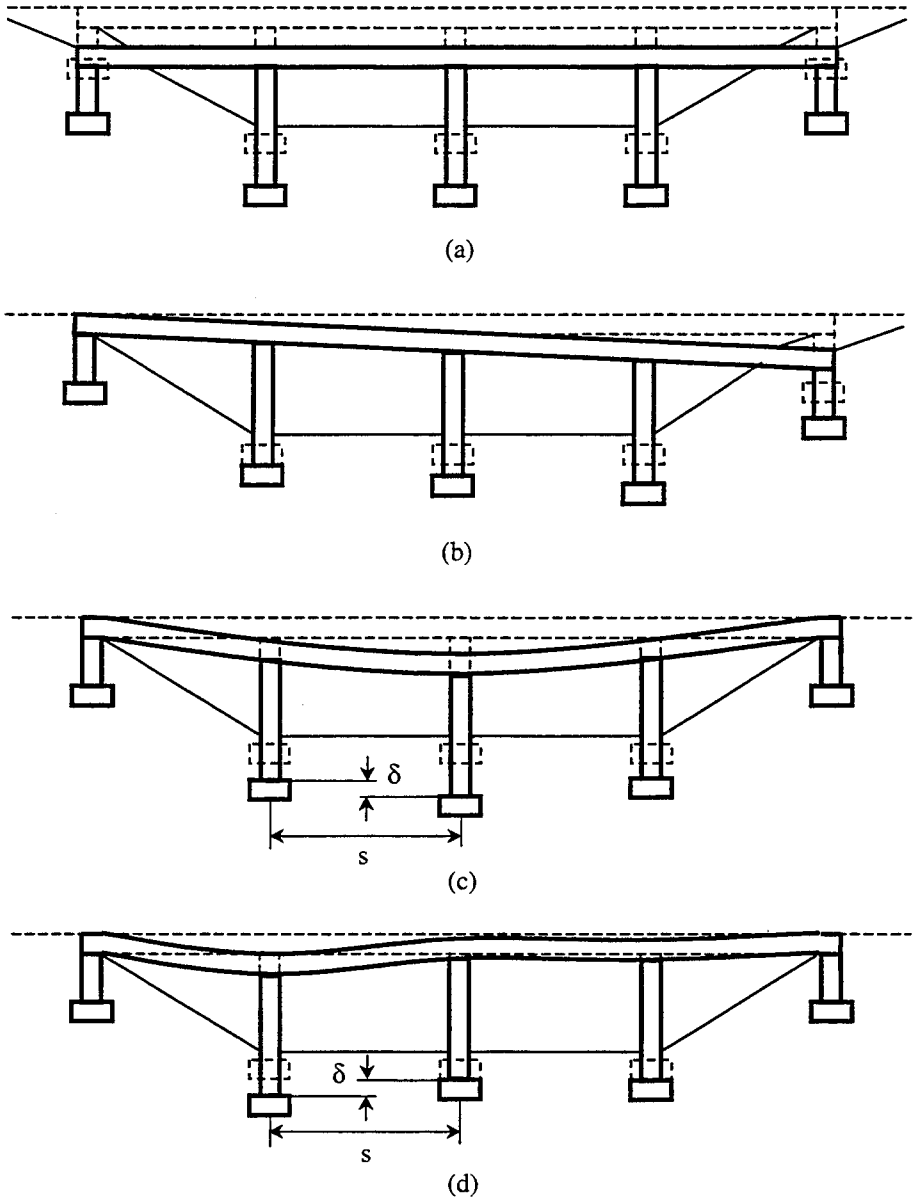

$$\text{Angular distortion} = \frac{\delta}{s}$$

Figure 3.12 Components of settlement and angular distortion in bridge for (a) uniform settlement, (b) uniform tilt or rotation, (c) nonuniform regular settlement, and (d) nonuniform irregular settlement (after Duncan and Tan 1991).

values and degree of damage were suggested by different authors, it appears that they are reasonably consistent.

As shown in Table 3.3, the smallest value of approximately 50 mm was suggested by Bozozuk (1978) as not harmful. The upper limit value of approximately 100 mm was suggested as the settlement that may cause some damage, yet remaining tolerable. Later findings by the Federal Highway Administration (FHWA) (Moulton et al. 1985, Moulton 1986) turned out to be reasonably consistent with the tolerable values given in Table 3.3. They found that the movement could be regarded as tolerable for 90% of the cases for which the vertical movement was less than 100 mm and the horizontal movement was less than 50 mm, based on the measurements of bridge movement for 439 abutment and 269 piers.

According to Moulton et al. (1985), the angular distortion gives a rational basis for establishing tolerable movement magnitude for bridges. The values of tolerable angular distortion for bridges, suggested by Moulton et al. (1985), are shown in Table 3.4. The criteria given in Table 3.4 were based on the observation for 56 simple span and 119 continuous span bridges.

Table 3.3 Settlement criteria for bridges expressed in terms of settlement magnitude.

Settlement Magnitude (mm)	Basis for recommendation	Recommended by
51	Not harmful	Bozozuk (1978)
63	Ride quality	Walkinshaw (1978)
> 63	Structural distress	Walkinshaw (1978)
102	Ride quality and structural distress	Grover (1978)
102	Harmful but tolerable	Bozozuk (1978)
> 102	Usually intolerable	Wahls (1990)

The details considered in Table 3.4 are summarized in Table 3.5. Although most bridges are less complex than buildings, the values shown in Table 3.4 are just slightly higher than those for buildings. The criteria for the tolerable angular distortion in AASHTO (1994) were also established based on the recommendations of Moulton et al. (1985).

Duncan and Tan (1991), however, indicated that the tolerable angular distortion for single-span bridges, equal to $\beta = 1/200$, may be overly conservative based on the review of data used by Moulton et al. (1985). They recommended the use of the tolerable angular distortion for single-span bridge as $\beta = 1/125$.

Table 3.4 Tolerable angular distortion for bridges (Moulton et al. 1985).

Angular distortion	Basis for recommendation
1/250	Tolerable for multi-span bridge
1/200	Tolerable for single-span bridge

Table 3.5 Data used by Moulton et al. (1985) to establish criteria for angular distortion.

Angular distortion	% of 199 continuous bridges for which this amount of angular distortion was considered to be tolerable	% of 56 single-span bridges for which this amount of angular distortion was considered to be tolerable
0.000 – 0.001	100%	98% (100%)
0.001 – 0.002	97%	98% (100%)
0.002 – 0.003	97%	98%(100%)
0.003 – 0.004	96%	98% (100%)
0.004 – 0.005	92%	98% (100%)
0.005 – 0.006	88%	96% (98%)
0.006 – 0.008	85%	93% (95%)

3.5 Summary

The concept of a "failure load" of an axially loaded pile is potentially controversial. Most criteria proposed to define a failure load based on pile load-settlement curves associate failure with relatively dramatic changes in settlement increment for a given load increment. These methods include the 90% criteria method (Brinch Hansen 1963), the Butler and Hoy method (1977), the Davisson method (1972) and the permanent set method (Horvitz et al. 1981). The 80% method (Brinch Hansen 1963), Chin's method (1970), and DeBeer's method (1967), on the other hand, define the failure conditions from the transformed load-settlement curve using either hyperbolic relationship or log-log scale. Because different methods may produce widely different values of failure load, the selection of the method for defining the failure condition should account for the characteristic shape of load-settlement curve and soil condition.

The limit state concept has been proposed as a modern design approach, in which the adequate technical quality of foundations and superstructures is considered. Whenever a geotechnical structure or part of a geotechnical structure fails to satisfy one of its performance criteria, it is said to have reached a "limit state". In general, there are two limit states in civil engineering design: ultimate and serviceability limit states. A serviceability limit state is reached when a structure loses functionality, while an ultimate limit state is reached when there is a loss of static equilibrium or severe structural damage. Franke (1991) suggested that if relative settlement s_R is kept below a limit value of 10% neither loss of functionality nor collapse of the superstructure will take place.

The value of tolerable settlement associated with serviceability and ultimate limit states may differ depending on the type, functionality and importance of a given structure. For building structures, values of tolerable settlement have been proposed mainly based on the results proposed by Skempton and MacDonald (1956) and Polshin and Tokar (1957). The results suggested by these two authors are relatively consistent, showing that the angular distortion varies from 1/150 to 1/500.

For bridge structures, several authors proposed limit values for tolerable settlement. No single measure of settlement or angular distortion, however, can be regarded as a sole indicator of bridge damage due to the complex settlement patterns. Bozozuk (1978) suggested the limit value of settlement equal to approximately 100 mm as a tolerable settlement for bridges. This value is similar to that proposed by Federal Highway Administration (Moulton 1986).

CHAPTER 4 MECHANICAL BEHAVIOR OF SAND

4.1 Introduction

The simplest way to describe mechanical behavior of a soil may be linear elasticity. In linear elasticity, the stress-strain relationship is represented by linearity in the absence of the definition of a failure condition. Although linear elasticity is simple, hence convenient to use, it is usually not suitable for typical stress-strain ranges in geotechnical problems. Linear elastic behavior can be observed in soil from the initially unstrained condition up to strains of the order of 10^{-5}. After this strain range, the soil usually shows highly non-linear behavior.

In order to represent the non-linear stress-strain behavior of a soil before the failure condition takes place, several soil models have been proposed (Kondner 1963, Duncan and Chang 1970, Hardin and Drnevich 1972, Fahey and Carter 1993, Tatsuoka et al. 1993). The hyperbolic types of soil models are among the most popular soil models for representing the non-linear behavior of a soil. These types of soil models are relatively simple to use, and are reasonably accurate. Fundamentally, the hyperbolic types of soil models are based on the quasi-linear elastic model assuming piece wise linear behavior for each increment of stress and strain.

Stability problems are concerned mostly with the portion of the stress-strain curve where large strains result from modest stress increases. These large deformations are usually associated with plastic response. Description of the plastic condition requires two basic concepts, i.e. definition of a failure criterion and flow rule. A failure criterion defines a stress state in a soil that leads to a failure condition. After the stress state

satisfies a failure criterion, the stress-strain relationship can no longer be defined by either linear elasticity or non-linear elasticity. The flow rule defines the relationship between stress and strain in the plastic state through the plastic potential function. If the plastic potential function is the same as the failure criterion, the flow rule is referred to as associated. Otherwise, it is referred to as a non-associated flow rule. After satisfying the failure criterion, the soil may harden, soften, or remain without any change in stress.

This chapter will start by describing the basic concept of the stress tensor. The fundamental ways to describe the stress-strain relationship of soil, including linear elastic, non-linear elastic and plastic responses are then discussed. Indicial notation, originally adopted by Einstein, will be used in the mathematical treatment of these concepts.

4.2 Stress Tensor and Invariants

As shown in Figure 4.1, there are nine components of stress in a soil element in a Cartesian coordinate system. The stress tensor is a set of these nine components of stress and is denoted by σ_{ij}. The stress tensor σ_{ij} can be expressed in matrix notation as follows:

$$\sigma_{ij} = \begin{bmatrix} \sigma_{11} & \sigma_{12} & \sigma_{13} \\ \sigma_{21} & \sigma_{22} & \sigma_{23} \\ \sigma_{31} & \sigma_{32} & \sigma_{33} \end{bmatrix} \tag{4.1}$$

Imposing moment equilibrium on the stress tensor σ_{ij} shown in (4.1), it follows that it is symmetric:

$$\sigma_{ij} = \sigma_{ji} \tag{4.2}$$

or

$$\sigma_{12} = \sigma_{21}$$

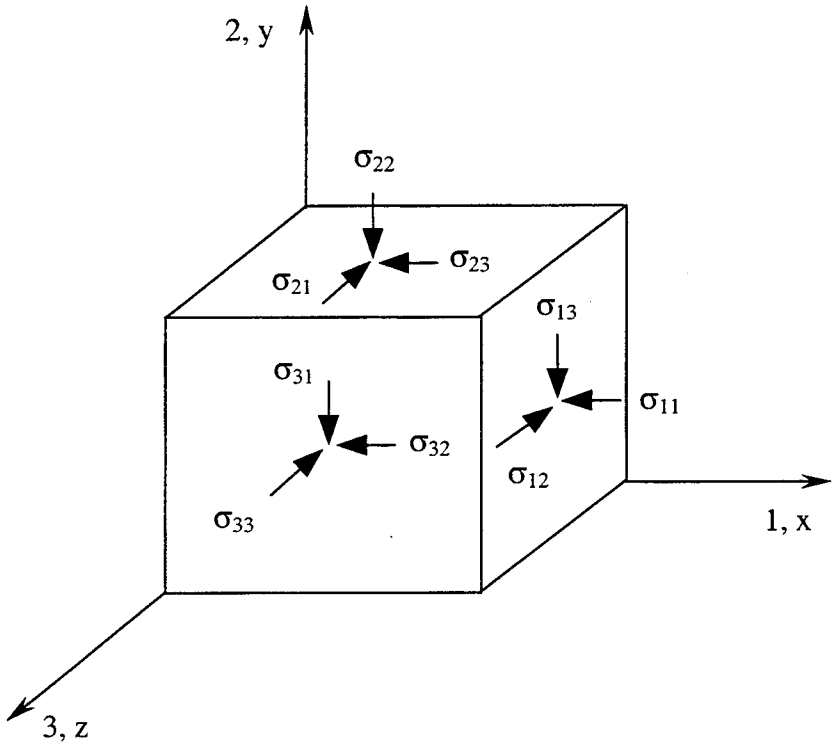

Figure 4.1 Nine components of stress tensor in a soil element.

$$\sigma_{13} = \sigma_{31}$$
$$\sigma_{23} = \sigma_{32} \tag{4.3}$$

The stress tensor σ_{ij} of (4.1) can also be written, using other symbols, as:

$$\sigma_{ij} = \begin{bmatrix} \sigma_{11} & \sigma_{12} & \sigma_{13} \\ \sigma_{21} & \sigma_{22} & \sigma_{23} \\ \sigma_{31} & \sigma_{32} & \sigma_{33} \end{bmatrix} \equiv \begin{bmatrix} \sigma_{xx} & \sigma_{xy} & \sigma_{xz} \\ \sigma_{yx} & \sigma_{yy} & \sigma_{yz} \\ \sigma_{zx} & \sigma_{zy} & \sigma_{zz} \end{bmatrix} \equiv \begin{bmatrix} \sigma_x & \tau_{xy} & \tau_{xz} \\ \tau_{yx} & \sigma_y & \tau_{yz} \\ \tau_{zx} & \tau_{zy} & \sigma_z \end{bmatrix} \tag{4.4}$$

The diagonal stress components of (4.4) are normal to the planes xz, xy, yz while the other stress terms are tangential to these planes and are referred to as shear stresses. The stress tensor given by (4.4) is a second-order symmetric tensor. According to the characteristics of a tensor, stresses have the invariant property. The invariants of a tensor represent the quantities that are constant irrespective of the rotation of the coordinate axes. The invariants of a tensor can be obtained from the characteristic equation of the square matrix given by:

$$\sigma^3 - I_1\sigma^2 + I_2\sigma - I_3 = 0 \tag{4.5}$$

From the characteristic equation of (4.5) and the stress tensor matrix of (4.4), the quantities of I_1, I_2, and I_3 are obtained as follows:

$$I_1 = \sigma_{ii} = \sigma_{11} + \sigma_{22} + \sigma_{33} = \sigma_x + \sigma_y + \sigma_z \tag{4.6}$$

$$\begin{aligned} I_2 &= \begin{vmatrix} \sigma_{11} & \sigma_{12} \\ \sigma_{12} & \sigma_{22} \end{vmatrix} + \begin{vmatrix} \sigma_{22} & \sigma_{23} \\ \sigma_{23} & \sigma_{33} \end{vmatrix} + \begin{vmatrix} \sigma_{11} & \sigma_{13} \\ \sigma_{13} & \sigma_{33} \end{vmatrix} \\ &= \begin{vmatrix} \sigma_y & \tau_{yz} \\ \tau_{zy} & \sigma_z \end{vmatrix} + \begin{vmatrix} \sigma_x & \tau_{xz} \\ \tau_{zx} & \sigma_z \end{vmatrix} + \begin{vmatrix} \sigma_x & \tau_{xy} \\ \tau_{yx} & \sigma_y \end{vmatrix} \end{aligned} \tag{4.7}$$

$$I_3 = \text{determinant of } \sigma_{ij} = \left|\sigma_{ij}\right| \tag{4.8}$$

The invariants of the stress tensor shown in (4.6) – (4.8) are often expressed using different formulation:

$$\bar{I}_1 = I_1 = \sigma_{ii} = \sigma_{11} + \sigma_{22} + \sigma_{33} \tag{4.9}$$

$$\bar{I}_2 = \frac{1}{2}\sigma_{ij}\sigma_{ij} = \frac{1}{2}(I_1^{\,2} - 2I_2) \tag{4.10}$$

$$\bar{I}_3 = \frac{1}{3}\sigma_{ik}\sigma_{km}\sigma_{mi} = \frac{1}{3}(I_1^{\,3} - 3I_1I_2 + 3I_3) \tag{4.11}$$

where $\bar{I}_1$, $\bar{I}_2$, and $\bar{I}_3$ are the first, second, and third invariants of the stress tensor, respectively while some authors refer I_1, I_2, and I_3 to as the first, second, and third invariants of the stress tensor. Another important property of the second-order symmetric tensor is the existence of principal directions related to invariants. For a given stress tensor, this implies that a set of planes, for which only the normal stresses are non-zero, can be found. The directions of these normal stresses acting on such planes are referred to as the principal directions, and the corresponding normal stresses are the principal stresses. In principal planes, the shear stresses are always equal to zero. Using the principal stresses, the stress tensor of (4.1) can be rewritten as:

$$\sigma_{ij} = \begin{bmatrix} \sigma_1 & 0 & 0 \\ 0 & \sigma_2 & 0 \\ 0 & 0 & \sigma_3 \end{bmatrix} \tag{4.12}$$

where σ_1, σ_2, and σ_3 are the principal stresses. In general, the largest principal stress is referred to as the major principal stress while the smallest is called the minor principal stress. The third principal stress is referred to as the intermediate principal stress. The

principal stresses can be determined from the characteristic equation of the stress tensor given in (4.5). Three real roots of the equation correspond to the major, minor, and intermediate principal stresses.

It is possible to decompose the stress tensor of (4.4) into two parts; one called the spherical or the hydrostatic stress tensor, and the other one called the deviatoric stress tensor. In matrix form, the hydrostatic tensor is given by:

$$p\delta_{ij} = \begin{bmatrix} p & 0 & 0 \\ 0 & p & 0 \\ 0 & 0 & p \end{bmatrix} \tag{4.13}$$

where

$$p = \frac{1}{3}\sigma_{kk} = \frac{1}{3}(\sigma_{11} + \sigma_{22} + \sigma_{33}) = \frac{1}{3}I_1 \tag{4.14}$$

and

$$\delta_{ij} = \begin{bmatrix} 1 & 0 & 0 \\ 0 & 1 & 0 \\ 0 & 0 & 1 \end{bmatrix} \tag{4.15}$$

The deviatoric stress tensor S_{ij} is defined by subtracting the hydrostatic stress tensor from the original stress tensor of (4.4). Then the deviatoric stress tensor is written as:

$$S_{ij} = \sigma_{ij} - p\delta_{ij} \tag{4.16}$$

with the corresponding matrix form given as:

$$S_{ij} = \begin{bmatrix} S_{11} & S_{12} & S_{13} \\ S_{21} & S_{22} & S_{23} \\ S_{31} & S_{32} & S_{33} \end{bmatrix} = \begin{bmatrix} \sigma_{11} - p & \sigma_{12} & \sigma_{13} \\ \sigma_{21} & \sigma_{22} - p & \sigma_{23} \\ \sigma_{31} & \sigma_{32} & \sigma_{33} - p \end{bmatrix} \tag{4.17}$$

The deviatoric stress tensor represents physically the shear deviatoric state of stress excluding the hydrostatic state of stress. Because the deviatoric stress tensor is also a second-order symmetric tensor, the invariants of the deviatoric stress tensor can be obtained from the characteristic equation. It should be noticed that the first invariant of the deviatoric stress tensor is zero, as:

$$\begin{aligned} S_{ii} &= S_{11} + S_{22} + S_{33} \\ &= \sigma_{ii} - \frac{1}{3}\sigma_{kk}\delta_{ii} \\ &= \sigma_{ii} - \sigma_{mm} \\ &= 0 \end{aligned} \tag{4.18}$$

The second invariant J_2 of the deviatoric stress tensor is given by:

$$\begin{aligned} J_2 &= \frac{1}{2} S_{ij} S_{ij} \\ &= \frac{1}{2}(S_{11}{}^2 + S_{12}{}^2 + S_{13}{}^2 + S_{21}{}^2 + S_{22}{}^2 + S_{23}{}^2 + S_{31}{}^2 + S_{32}{}^2 + S_{33}{}^2) \\ &= \frac{1}{2}[(\sigma_{11} - p)^2 + (\sigma_{22} - p)^2 + (\sigma_{33} - p)^2 + 2S_{12}{}^2 + 2S_{23}{}^2 + 2S_{13}{}^2] \end{aligned} \tag{4.19}$$

Since $S_{12} = \sigma_{12}$, $S_{23} = \sigma_{23}$, and $S_{13} = \sigma_{13}$, (4.19) can be rewritten as:

$$J_2 = \frac{1}{2}(\sigma_{11}{}^2 + \sigma_{22}{}^2 + \sigma_{33}{}^2 + 2\sigma_{12}{}^2 + 2\sigma_{23}{}^2 + 2\sigma_{13}{}^2 - 3p^2) \tag{4.20}$$

or

$$J_2 = \frac{1}{6}[(\sigma_{11} - \sigma_{22})^2 + (\sigma_{22} - \sigma_{33})^2 + (\sigma_{11} - \sigma_{33})^2] + \sigma_{12}{}^2 + \sigma_{23}{}^2 + \sigma_{13}{}^2 \tag{4.21}$$

Using the principal stresses,

$$J_2 = \frac{1}{6}[(\sigma_1 - \sigma_2)^2 + (\sigma_2 - \sigma_3)^2 + (\sigma_1 - \sigma_3)^2] \tag{4.22}$$

The third invariant of the deviatoric stress tensor can be expressed as:

$$J_3 = \frac{1}{3} S_{ij} S_{jm} S_{mi}$$

$$= \frac{1}{3}(\sigma_{ij} - \frac{\bar{I}_1}{3}\delta_{ij})(\sigma_{jm} - \frac{\bar{I}_1}{3}\delta_{jm})(\sigma_{mi} - \frac{\bar{I}_1}{3}\delta_{mi})$$

$$= \bar{I}_3 - \frac{2}{3}\bar{I}_1\bar{I}_2 + \frac{2}{27}\bar{I}_1^3 \tag{4.23}$$

where $\bar{I}_1, \bar{I}_2$, and $\bar{I}_3$ are the first, second and third invariants of the stress tensor.

4.3 Elastic Stress-Strain Relationship

The complete definition of mechanical behavior of a body requires three basic relationships: equilibrium condition, compatibility condition and stress-strain relationship. Figure 4.2 illustrates how these relationships are connected with each other. The equilibrium condition defines the relationship between the internal stresses σ and the external forces including surface tractions **T** and body forces **F**. The compatibility condition defines the relationship between the displacement **u** and the strain ε. The stress-strain relationship is also called constitutive equation because it reflects the internal constitution of the material.

The linear relationship between stress σ_{ij} and strain ε_{kl} is referred to as linear elasticity and can be defined by the generalized Hooke's law as follows:

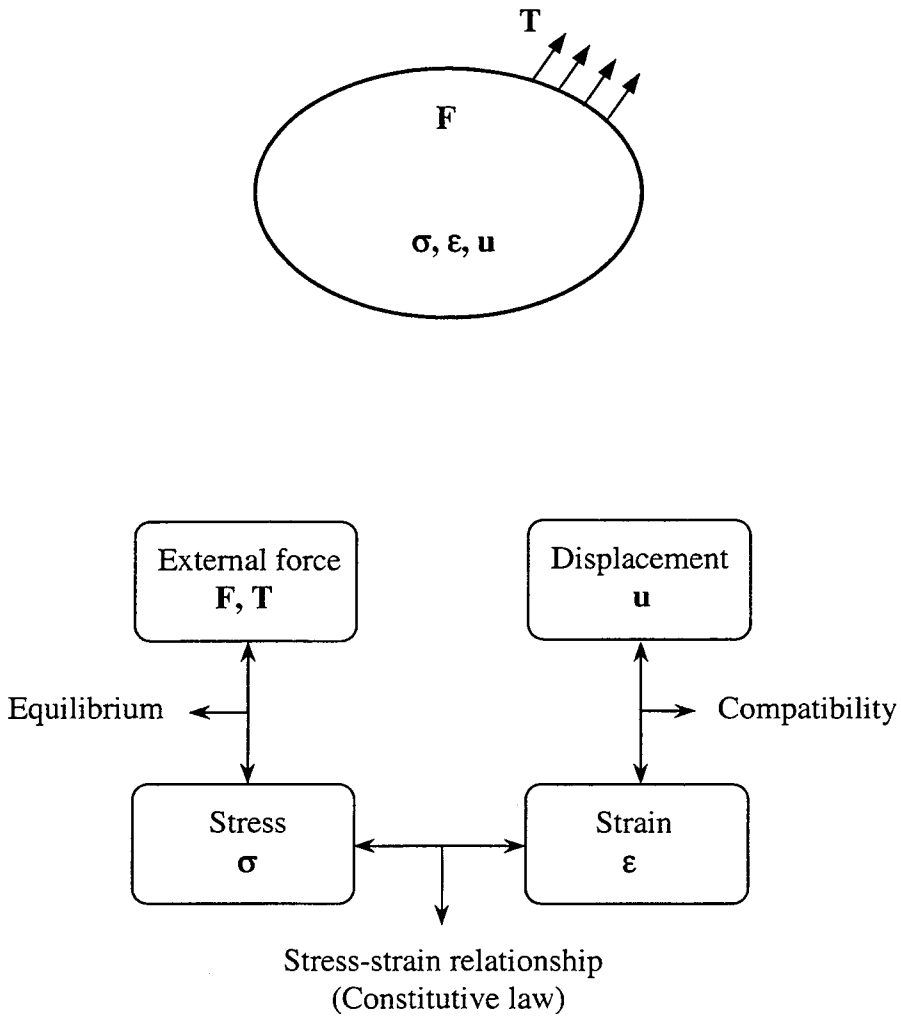

Figure 4.2 Definition of mechanical behavior of a body (after Chen and Han 1988).

$$\sigma_{ij} = C_{ijkl}\varepsilon_{kl} \tag{4.24}$$

where i, j, k, and l = 1, 2, and 3; and C_{ijkl} is the fourth-order elastic moduli tensor. Eq. (4.24) implies that the strain generated by the stress is always recoverable for the condition of eliminating or decreasing the stress. Since both σ_{ij} and ε_{kl} are the symmetric tensors, C_{ijkl} is also symmetric. Using a number of modulus symmetries the number of independent constants can be reduced to 21. The final expression for C_{ijkl} of (4.24) is then written in matrix form as:

$$\begin{Bmatrix} \sigma_{11} \\ \sigma_{22} \\ \sigma_{33} \\ \sigma_{12} \\ \sigma_{23} \\ \sigma_{13} \end{Bmatrix} = \begin{bmatrix} C_{1111} & C_{1122} & C_{1133} & C_{1112} & C_{1123} & C_{1113} \\ C_{2211} & C_{2222} & C_{2233} & C_{2212} & C_{2223} & C_{2213} \\ C_{3311} & C_{3322} & C_{3333} & C_{3312} & C_{3323} & C_{3313} \\ C_{1211} & C_{1222} & C_{1233} & C_{1212} & C_{1223} & C_{1213} \\ C_{2311} & C_{2322} & C_{2333} & C_{2312} & C_{2323} & C_{2313} \\ C_{1311} & C_{1322} & C_{1333} & C_{1312} & C_{1323} & C_{1313} \end{bmatrix} \begin{Bmatrix} \varepsilon_{11} \\ \varepsilon_{22} \\ \varepsilon_{33} \\ \gamma_{12} \\ \gamma_{23} \\ \gamma_{13} \end{Bmatrix} \tag{4.25}$$

where ε_{11}, ε_{22}, and ε_{33} = axial strains; γ_{12}, γ_{23}, and γ_{13} = shear strains. For an isotropic material, the general form of the fourth-order tensor C_{ijkl} can be given by:

$$C_{ijkl} = \lambda\delta_{ij}\delta_{kl} + \mu\delta_{ik}\delta_{jl} + \alpha\delta_{il}\delta_{jk} \tag{4.26}$$

where λ, μ, and α are scalar constants. Because C_{ijkl} is a symmetric tensor, the following relationship should be satisfied:

$$C_{ijkl} = C_{jikl} \tag{4.27}$$

This leads to

$$\lambda\delta_{ij}\delta_{kl} + \mu\delta_{ik}\delta_{jl} + \alpha\delta_{il}\delta_{jk} = \lambda\delta_{ji}\delta_{kl} + \mu\delta_{jk}\delta_{il} + \alpha\delta_{jl}\delta_{ik} \tag{4.28}$$

From (4.27) and (4.28), it can be seen that $\mu = \alpha$. Then we are left with:

$$C_{ijkl} = \lambda\delta_{ij}\delta_{kl} + \mu(\delta_{ik}\delta_{jl} + \delta_{il}\delta_{jk}) \tag{4.29}$$

Taking (4.29) into (4.24), we get:

$$\sigma_{ij} = \lambda\delta_{ij}\delta_{kl}\varepsilon_{kl} + \mu(\delta_{ik}\delta_{jl} + \delta_{il}\delta_{jk})\varepsilon_{kl} \tag{4.30}$$

or

$$\sigma_{ij} = \lambda\delta_{ij}\varepsilon_{kk} + 2\mu\varepsilon_{ij} \tag{4.31}$$

The two independent material constants μ and λ in (4.31) are referred to as Lame's constants. Following Hooke's law for the three dimensional and isotropic element, the stress-strain relationships can be expressed as follows:

$$\varepsilon_{11} = \frac{1}{E}[\sigma_{11} - \nu(\sigma_{22} + \sigma_{33})] \tag{4.32}$$

$$\varepsilon_{22} = \frac{1}{E}[\sigma_{22} - \nu(\sigma_{11} + \sigma_{33})] \tag{4.33}$$

$$\varepsilon_{33} = \frac{1}{E}[\sigma_{33} - \nu(\sigma_{11} + \sigma_{22})] \tag{4.34}$$

$$\gamma_{12} = \frac{1}{G}\sigma_{12} \tag{4.35}$$

$$\gamma_{23} = \frac{1}{G}\sigma_{23} \tag{4.36}$$

$$\gamma_{13} = \frac{1}{G}\sigma_{13} \tag{4.37}$$

where E and ν = Young's modulus and Poisson's ratio; G = elastic shear modulus. In (4.35) – (4.37), σ_{12}, σ_{23} and σ_{13} represent the shear stresses. Using indicial notation, (4.32) - (4.37) can be rewritten as:

$$\varepsilon_{ij} = \frac{1+\nu}{E}\sigma_{ij} - \frac{\nu}{E}\sigma_{kk}\delta_{ij} \tag{4.38}$$

or

$$\sigma_{ij} = \frac{E}{1+\nu}\varepsilon_{ij} - \frac{\nu E}{(1+\nu)(1-2\nu)}\varepsilon_{kk}\delta_{ij} \tag{4.39}$$

Comparing (4.39) and (4.31), Lame's constants μ and λ can be obtained as:

$$\mu = G = \frac{E}{2(1+\nu)} \tag{4.40}$$

$$\lambda = \frac{\nu E}{(1+\nu)(1-2\nu)} \tag{4.41}$$

There is another elastic parameter, called the bulk modulus K, which defines the relationship between the hydrostatic stress and the volumetric strain. For the condition of hydrostatic compression, (4.31) is expressed as:

$$\sigma_{kk} = 3\lambda\varepsilon_{kk} + 2\mu\varepsilon_{kk} \tag{4.42}$$

From the relationship of $p = \sigma_{11} = \sigma_{22} = \sigma_{33} = \frac{\sigma_{kk}}{3}$,

$$p = (\lambda + \frac{2}{3}\mu)\varepsilon_{kk} \tag{4.43}$$

where $\varepsilon_{kk} = \varepsilon_{11} + \varepsilon_{22} + \varepsilon_{33}$ = volumetric strain. Then the bulk modulus K is defined as:

$$K = \frac{p}{\varepsilon_{kk}} = \lambda + \frac{2}{3}\mu \tag{4.44}$$

Using (4.40) and (4.41), the bulk modulus K is rewritten as:

$$K = \frac{E}{3(1-2\nu)} \tag{4.45}$$

Table 4.1 summarizes the relationships between the different elastic parameters described so far. Using these elastic parameters, the elastic moduli tensor C_{ijkl} shown in (4.25) can be written in a matrix form as:

$$[C] = \frac{E}{(1+\nu)(1-2\nu)} \begin{bmatrix} (1-\nu) & \nu & \nu & 0 & 0 & 0 \\ \nu & (1-\nu) & \nu & 0 & 0 & 0 \\ \nu & \nu & (1-\nu) & 0 & 0 & 0 \\ 0 & 0 & 0 & \frac{(1-2\nu)}{2} & 0 & 0 \\ 0 & 0 & 0 & 0 & \frac{(1-2\nu)}{2} & 0 \\ 0 & 0 & 0 & 0 & 0 & \frac{(1-2\nu)}{2} \end{bmatrix} \tag{4.46}$$

or

$$[C] = \begin{bmatrix} K+\frac{4}{3}G & K-\frac{2}{3}G & K-\frac{2}{3}G & 0 & 0 & 0 \\ K-\frac{2}{3}G & K+\frac{4}{3}G & K-\frac{2}{3}G & 0 & 0 & 0 \\ K-\frac{2}{3}G & K-\frac{2}{3}G & K+\frac{4}{3}G & 0 & 0 & 0 \\ 0 & 0 & 0 & G & 0 & 0 \\ 0 & 0 & 0 & 0 & G & 0 \\ 0 & 0 & 0 & 0 & 0 & G \end{bmatrix} \tag{4.47}$$

Table 4.1 Relationship between different elastic modulus.

Constant	Basic Pair		
	$\lambda, \mu = G$	E, ν	K, μ
λ	λ	$\frac{\nu E}{(1+\nu)(1-2\nu)}$	$\frac{3K-2\mu}{3}$
μ	μ, G	$\frac{E}{2(1+\nu)}$	μ
K	$\frac{3\lambda+2\mu}{3}$	$\frac{E}{3(1-2\nu)}$	K
E	$\frac{\mu(3\lambda+2\mu)}{\lambda+\mu}$	E	$\frac{9K\mu}{3K+\mu}$
ν	$\frac{\lambda}{2(\lambda+\mu)}$	ν	$\frac{3K-2\mu}{6K+2\mu}$

4.4 Elastic Behavior of Soil

4.4.1 Initial elastic modulus at small strain

It is well known that the stress-strain behavior of soil is highly non-linear. The non-linear soil response is in part associated with strains that cannot be fully recovered upon unloading. There is, however, a certain strain range within which the soil behaves as a linear elastic material and the stress-strain relationship is fully recoverable. As can be seen in Figure 4.3, this linear-elastic strain range is usually very narrow with an upper limit of 10^{-5} for sands. The elastic modulus for this strain range is referred to as the initial elastic modulus at small strains. It has been observed that the initial shear modulus G_o is a constant, for a given soil condition, regardless of the nature of the loading type, i.e., whether the loading is monotonic or cyclic (Shibuya et al. 1992).

There are a number of ways to evaluate the initial shear modulus for a given soil. Those include in-situ tests, laboratory tests, and empirical equations (Janbu 1963, Hardin and Richart 1963, Yu and Richart 1984, Baldi et al 1989, Viggiani and Atkinson 1995, Salgado et al. 1997c). In most field and laboratory tests, the initial shear modulus is determined by measuring the shear wave velocity based on the following relationship:

$$G_0 = \rho(V_s)^2 \tag{4.48}$$

where G_o = initial shear modulus; ρ = mass density of the medium through which the shear wave is transmitted; and V_s = shear wave velocity. The cross-hole test, the spectral analysis of surface wave test (SASW) and the seismic cone penetration test are the typical examples of in-situ tests for evaluating initial shear modulus. The seismic cone penetration test is regarded as one of the most economical and rapid in-situ tests for obtaining the initial shear modulus. The test is performed in a similar manner to a down-hole test using the wave generated at the surface (Robertson et al. 1985). Figure 4.4 shows the schematic illustration of the seismic cone penetration test.

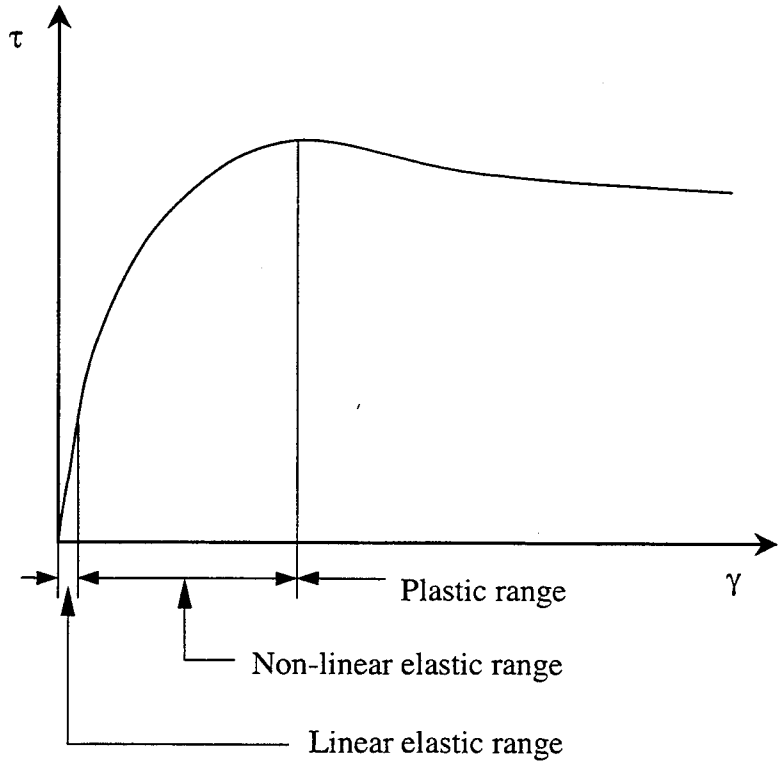

Figure 4.3 Non-linear stress-strain behavior of soil.

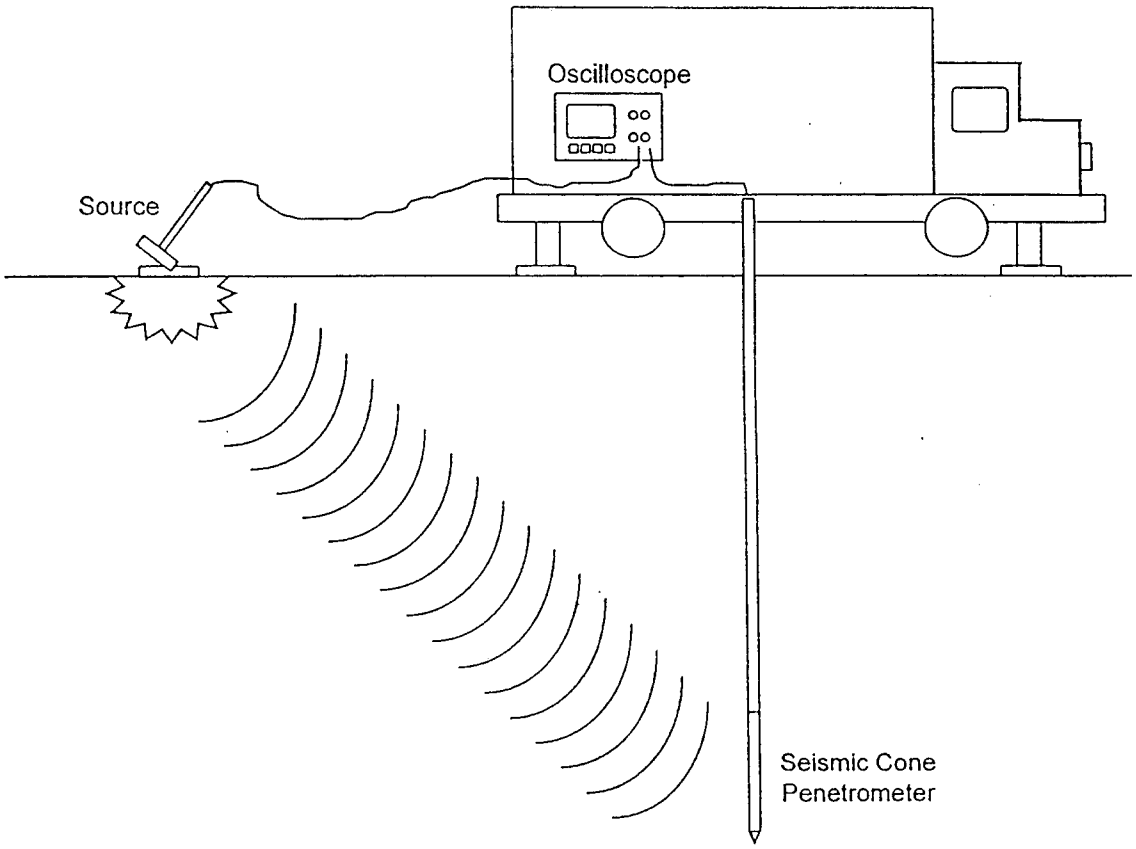

Figure 4.4 Seismic cone penetration test.

For laboratory testing, the resonant column test and the bender element test are often used. The bender element test has been developed relatively recently, but has been used increasingly since. The test can be easily performed using the same soil sample as in a conventional triaxial test, with the wave generator and receiver (called bender elements) attached at the end caps of a triaxial sample. Because the strains generated by the shear wave do not disturb the initial soil condition, the conventional triaxial test can be performed immediately after the bender element test for the initially assumed soil condition.

The empirical equations for the initial shear modulus are generally expressed as a form of:

$$\frac{G_o}{P_a} = CF(e)\left(\frac{p'}{P_a}\right)^n \tag{4.49}$$

where G_o = initial shear modulus; P_a = reference pressure used for normalization; C = non-dimensional material constant; F(e) = function of the void ratio; n = material constant; p' = mean effective stress in the same units as P_a. Eq (4.49) indicates the dependence of the initial shear modulus on the degree of compactness of the soil and the magnitude of the confinement. One of the commonly used empirical equations for the initial shear modulus of sand is the one suggested by Hardin and Black (1966) and written as follows:

$$G_o = C_g \frac{(e_g - e_o)^2}{1+e_o}(p_a)^{(1-n_g)}(\sigma'_m)^{n_g} \tag{4.50}$$

where C_g, e_g and n_g = material constants that depend only on the nature of the soil; e_o = initial void ratio; P_a = reference pressure = 100 kPa $\approx$ 1 kgf/cm^2; and σ'_m = initial mean effective stress in the same unit as P_a. In the original work by Hardin and Black (1966), the values of C_g, e_g, and n_g were suggested for round grains (Ottawa sand) and angular

grains (crushed Quartz). After Hardin and Black (1966), several authors presented the values of C_g, e_g, and n_g for other kinds of sands. Table 4.2 shows the values of C_g, n_g, and e_g for different sands.

4.4.2 Hyperbolic stress-strain relationship

As discussed in the previous section, the stress-strain behavior of a soil shows highly non-linear relationship from the early stage of loading. The hyperbolic family of soil models has been widely used to represent such non-linear behavior of a soil over a wide range of strains. Since Kondner (1963) first proposed the original hyperbolic equation for the stress-strain relationship, several modifications have been suggested (Duncan and Chang 1970, Hardin and Drnevich 1972, Fahey and Carter 1993, Purzin and Burland 1996). The hyperbolic soil-models are based on the quasi-linear elastic stress-strain relationship assuming piece-wise linear behavior with respect to a stress and strain level.

The conventional hyperbolic equation for stress-strain curve by Kondner (1963) is written for triaxial or plane-strain condition as:

$$\sigma_1 - \sigma_3 = \frac{\varepsilon}{a + b\varepsilon} \tag{4.51}$$

where σ_1 and σ_3 are the major and minor principal stresses; ε is the axial strain; and a and b are the material constants that characterize the feature of stress-strain curve. As can be seen in Figure 4.5, the constants a and b in the conventional hyperbolic equation by Kondner (1963) correspond to the value of the reciprocals of the initial elastic modulus E_o, and of the asymptotic value $(\sigma_1 - \sigma_3)_{ult}$ of deviatoric stress in the hyperbolic stress-strain curve.

Table 4.2 Values of C_g, e_g, and n_g for different sand type (after Salgado 1993, Salgado et al. 1999)

Sand type	C_g	e_g	n_g
Ottawa	612	2.17	0.44
Ticino	647	2.27	0.43
Toyoura	900	2.17	0.40
Hokksund	942	1.96	0.46
Monterey No.0	326	2.97	0.50

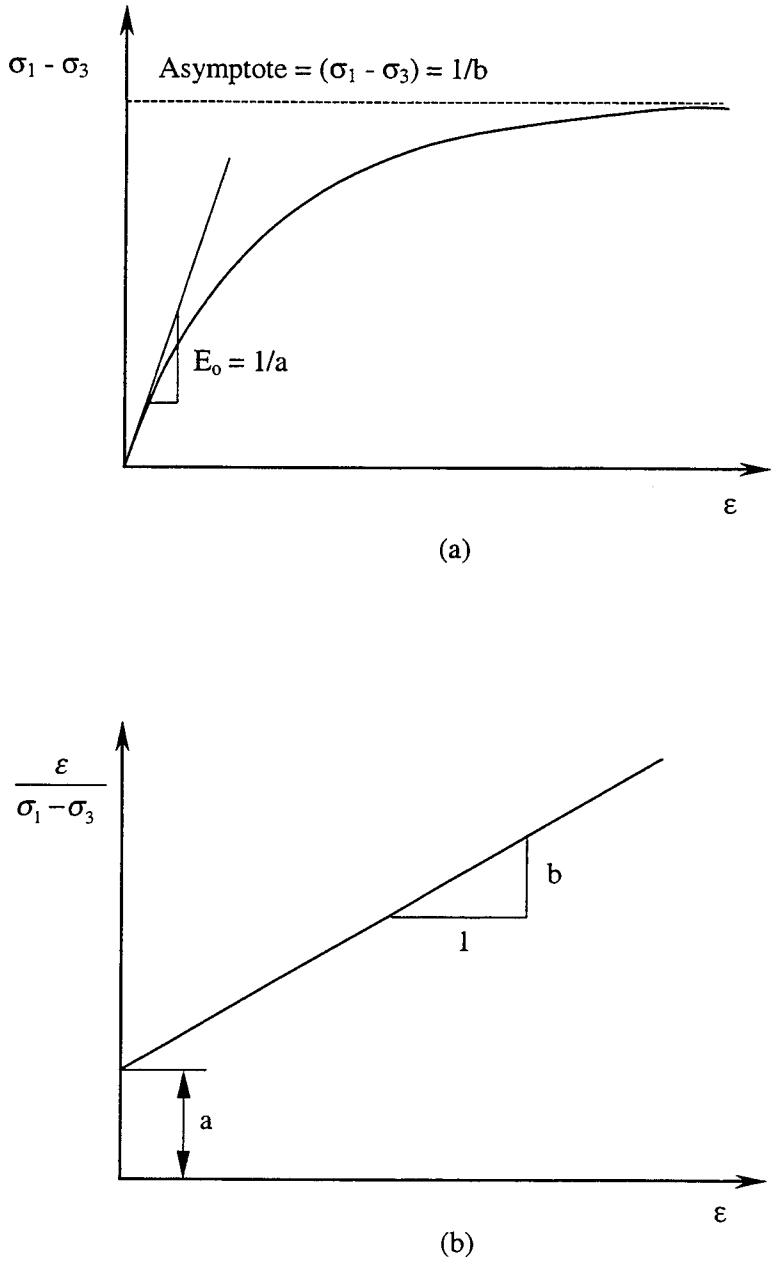

Figure 4.5 Hyperbolic model (a) stress-strain curve and (b) linear representation.

From (4.51) and Figure 4.5, it is easily seen that an infinite amount of strain is required for the stress-strain curve to reach the ultimate stress level $(\sigma_1 - \sigma_3)_{ult}$. This also implies that the ultimate stress $(\sigma_1 - \sigma_3)_{ult}$ in the conventional hyperbolic stress-strain relationship is greater than the actual soil strength, which is taken as the maximum stress at failure.

For the purpose of better fitting the hyperbolic relationship to a real soil stress-strain curve, Duncan and Chang (1970) modified the hyperbolic equation by introducing the material constant R_f into the equation. The factor R_f is referred to as the failure ratio, relating the ultimate deviatoric stress $(\sigma_1 - \sigma_3)_{ult}$ of the original hyperbolic stress-strain curve to the actual deviatoric stress of soil at failure $(\sigma_1 - \sigma_3)_f$:

$$(\sigma_1 - \sigma_3)_f = R_f (\sigma_1 - \sigma_3)_{ult} \tag{4.52}$$

The modified hyperbolic equation is then written as:

$$(\sigma_1 - \sigma_3) = \frac{\varepsilon}{\frac{1}{E_o} + \frac{\varepsilon \cdot R_f}{(\sigma_1 - \sigma_3)_f}} \tag{4.53}$$

where the deviatoric stress at failure $(\sigma_1 - \sigma_3)_f$ is determined from the Mohr-Coulomb failure criterion:

$$(\sigma_1 - \sigma_3)_f = \frac{2c \cdot \cos\phi + 2\sigma_3 \cdot \sin\phi}{1 - \sin\phi} \tag{4.54}$$

where c and ϕ are the Mohr-Coulomb shear strength parameters. If the factor R_f is less than 1, the asymptotic value $(\sigma_1 - \sigma_3)_{ult}$ is $1/R_f$ times greater than the actual deviatoric stress $(\sigma_1 - \sigma_3)_f$ at failure. The hyperbolic model describes the non-linearity of the stress-

strain relationship without recourse to plasticity concepts. As a result, it can be readily incorporated into numerical analyses using an incremental elastic implementation.

4.4.3 Degradation of Elastic Modulus

The hyperbolic equation given by (4.53) can be rewritten so as to be expressed in terms of shear stress and strain:

$$\tau = \frac{\gamma}{\frac{1}{G_o} + \frac{\gamma \cdot R_f}{\tau_{max}}} \tag{4.55}$$

where G_o = initial shear modulus in the very small strain range; and τ_{max} = maximum shear stress at failure. Using the relationship $\gamma = \tau / G$, (4.55) can be written as:

$$\tau = \frac{\frac{\tau}{G}}{\frac{1}{G_o} + \frac{\tau \cdot R_f}{\tau_{max} \cdot G}} \tag{4.56}$$

Thus,

$$\frac{G}{G_o} = 1 - R_f \frac{\tau}{\tau_{max}} \tag{4.57}$$

where G = secant shear modulus. Eq. (4.57) describes the degradation of the shear modulus from its initial maximum value G_o according to the magnitude of shear stress. Duncan and Chang (1970) implicitly described the degradation ratio G/G_o of elastic stiffness as varying linearly with the stress level τ/τ_{max} according to (4.57). The degraded

magnitude of the elastic modulus at failure is determined by the value of R_f in (4.57). According to Duncan and Chang (1970), the value of R_f typically lies between 0.75 and 1.0.

4.5 Failure Criterion and Soil Plasticity

4.5.1 Failure criterion

Although the non-linear behavior of soil starts from the very early stages of loading, there is a condition for which relatively dramatic changes of stress, for a given strain increment, can be observed. When the soil is in this condition, it is said to have "failed" and behaves as a plastic material. The failure criterion is used to define the limit stress state at which the material exhibits plastic behavior. In most classical plastic theories, the material is considered as elastic below the failure surface which is defined by a failure criterion. Once the material has reached a failure condition and started exhibiting plastic behavior, Hooke's law, given by (4.24), is no longer valid.

For a given temperature, the failure criterion F can be expressed as a function of stress components as follows:

$$F = F(\sigma_{ij}) = F(\sigma_{11}, \sigma_{22}, \sigma_{33}, \sigma_{12}, \sigma_{23}, \sigma_{13}) \tag{4.58}$$

where F = failure criterion; σ_{ij} = six stress components. If the soil is assumed to be isotropic, the soil properties are the same as all directions, thus the material constants are not affected by coordinate transformations. It follows that the failure criterion can be given in terms of principal stresses or stress invariants, for isotropic conditions, as follows:

$$F = F(\sigma_1, \sigma_2, \sigma_3) \tag{4.59}$$

or

$$F = F(I_1, J_2, J_3) \tag{4.60}$$

where σ_1, σ_2, and σ_3 = major, intermediate, and minor principal stresses; I_1 = the first invariant of stress tensor; and J_2 and J_3 = the second and third invariants of deviatoric stress tensor. For certain materials, experimental observations show that the influence of hydrostatic pressure on failure of the material is minimal. Based on the these observations, the failure criterion is expressed for these materials in a more simplified form as follows:

$$F = F(J_2, J_3) \tag{4.61}$$

In some elastic-plastic models in soil mechanics, a soil remains in the elastic range before the failure criterion is reached and deforms under a constant shear stress in the plastic range. For such materials, referred to as perfectly plastic, the following holds:

$$F < 0 \quad \text{for the elastic range} \tag{4.62}$$

and

$$F = 0 \quad \text{at failure and beyond} \tag{4.63}$$

For a perfectly plastic material, the condition $F > 0$ is physically impossible. Figure 4.6 illustrates the elastic and plastic stress states for the elastic-plastic material. In the figure σ_{ij} and $d\sigma_{ij}$ represent the current stress and the stress increment at failure, respectively. If the stress state takes place inside the failure surface given by (4.59) or (4.60), it corresponds to the elastic condition of (4.62). As shown in Figure 4.6, when the stress state remains on the failure surface, this is referred to as the loading condition. On the other hand, the case where the stress state drops below the failure surface is called unloading condition.

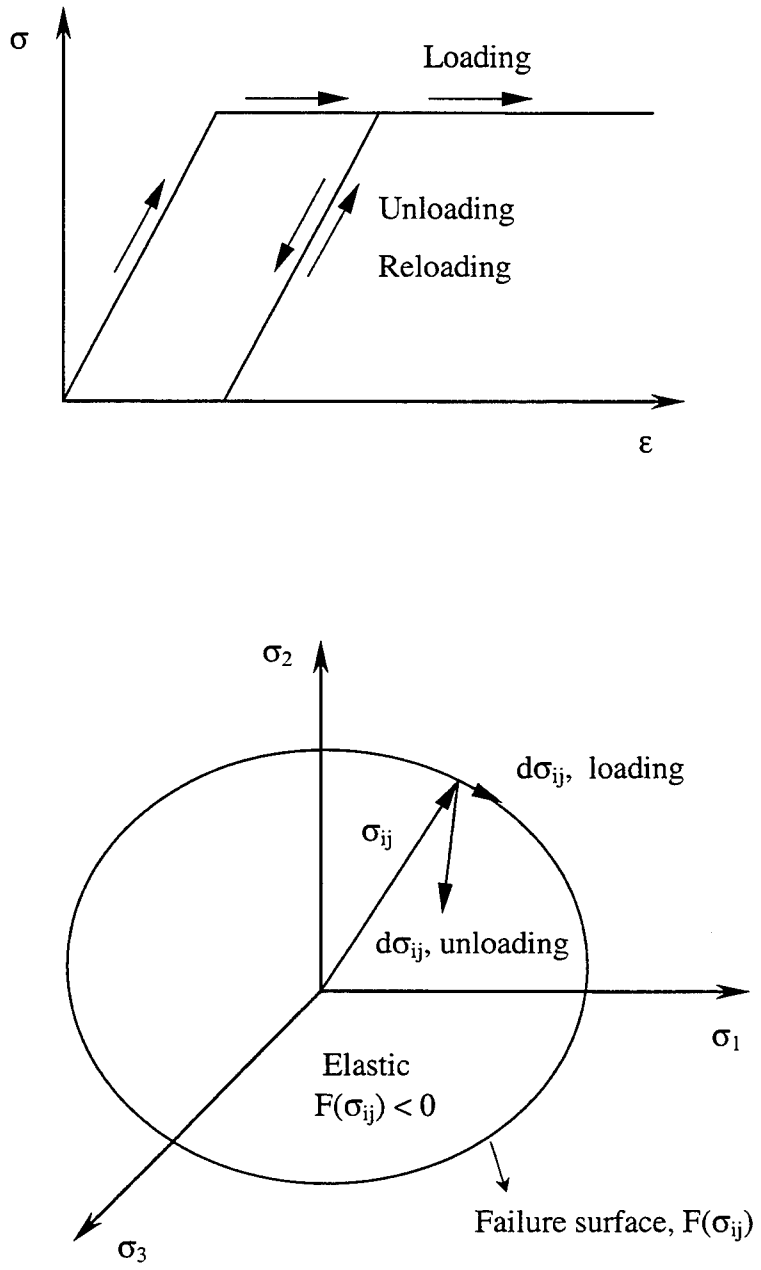

Figure 4.6 Stress states for elastic-perfectly plastic material.

Considering a small stress increment $d\sigma_{ij}$ from the current stress state σ_{ij}, the conditions for loading and unloading are given by:

$$f(\sigma_{ij}) = 0 \quad \text{and} \quad df = \frac{\partial f}{\partial \sigma_{ij}} d\sigma_{ij} = 0 \tag{4.64}$$

for loading and

$$f(\sigma_{ij}) = 0 \quad \text{and} \quad df = \frac{\partial f}{\partial \sigma_{ij}} d\sigma_{ij} < 0 \tag{4.65}$$

for unloading.

4.5.2 Flow rule and stress hardening

When the stress state of a elastic-plastic material reaches a failure surface, the material starts exhibiting plastic behavior. The total strain increment tensor at plastic state can be given by the sum of the elastic and plastic strain increment:

$$d\varepsilon_{ij} = d\varepsilon_{ij}^{\ e} + d\varepsilon_{ij}^{\ p} \tag{4.66}$$

where $d\varepsilon_{ij}$ = total strain increment; $d\varepsilon_{ij}^{e}$ and $d\varepsilon_{ij}^{p}$ = elastic and plastic strain increment. The flow rule defines the relationship between the plastic strain and the current stress state. Based on the flow rule, the magnitude and direction of the plastic strain increment can be determined. The flow rule is given by:

$$d\varepsilon_{ij}^{\ p} = \lambda \frac{\partial \Omega}{\partial \sigma_{ij}} \tag{4.67}$$

where λ is a positive scalar factor of proportionality and Ω is a plastic potential function. When the plastic potential function Ω is the same as the failure criterion F, the flow rule is called an associated flow rule. Otherwise it is referred to as a non-associated flow rule. Eq. (4.67) also indicates that the direction of the plastic strain vector $d\varepsilon_{ij}^{p}$ is normal to the plastic potential surface defined by a plastic potential function Ω in the stress space. This condition is referred to as the normality rule.

For the perfectly plastic material, the work done by the stress increment $d\sigma_{ij}$ and strain increment $d\varepsilon_{ij}$ in the plastic state should be equal to zero since no further increment of stress, after the failure condition is reached, is possible. Some materials, however, show positive amount of work done by additional stress and strain increments. This condition is referred to as work hardening or a stable material condition. According to Drucker, the following two conditions should be satisfied for the hardening material:

(1) During the application of the added set of forces, the work done by the external force on the changes in displacements it produces is positive.
(2) Over the cycle of application and removal of the added set of forces, the new work performed by the external agency on the change in displacements it produces is non-negative.

The first condition can be given by:

$$d\sigma_{ij} \cdot d\varepsilon_{ij} > 0 \tag{4.68}$$

or

$$d\sigma_{ij}(d\varepsilon_{ij}^{\ e} + d\varepsilon_{ij}^{\ p}) > 0 \tag{4.69}$$

The second condition implies that:

$$d\sigma_{ij} \cdot d\varepsilon_{ij}^{\ p} > 0 \tag{4.70}$$

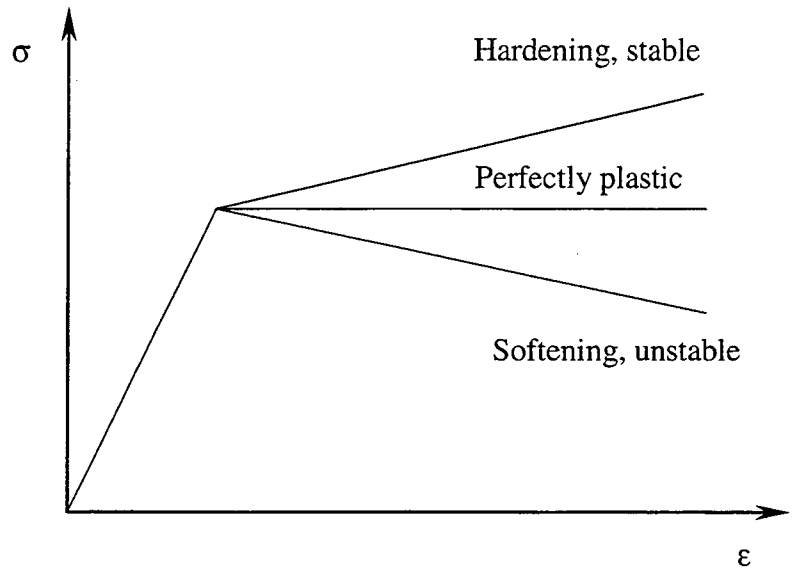

Figure 4.7 Stress-strain behavior for hardening, perfectly plastic and softening material.

If the work done by additional stress and strain increment is negative, the material is referred to as work softening or unstable. Figure 4.7 shows the conditions for the work hardening, perfectly plastic, and work softening materials.

4.5.3 Soil dilatancy and critical state of sand

An important property that characterizes the state of cohesionless granular materials is the relative density. The relative density is defined as the degree of compactness of the soil with respect to its most and least dense states. The relative density D_R is written as:

$$D_R = \frac{e_{max} - e_o}{e_{max} - e_{min}} \times 100\% = \frac{\gamma_{d,max}}{\gamma_d} \frac{\gamma_d - \gamma_{d,min}}{\gamma_{d,max} - \gamma_{d,min}} \times 100\% \qquad (4.71)$$

where D_R = relative density; e_{max} and e_{min} = maximum and minimum void ratios; e_o = initial void ratio; $\gamma_{d,max}$ and $\gamma_{d,min}$ = maximum and minimum dry unit weight; γ_d = initial dry unit weight. Relative densities equal to D_R = 100% and 0% represent the densest and loosest conditions of sand, respectively.

The stress-strain behavior and volumetric changes of sand during shearing differ significantly depending on the level of relative density. As can be seen in Figure 4.8, the looser sand shows a stress-strain curve with gradually decreasing curvature until failure, showing hardening behavior. On the other hand, the denser sand has a stress-strain curve with a clear peak.

With respect to the volumetric strain of dense sand, it is usually observed that negative volumetric strains, representing increases of volume, occur following the contractive behavior initially observed. This phenomenon observed in dense sand is referred to as dilatancy. For the same amount of confinement, consequently, the denser the sand, the greater the shear strength, and the higher the peak friction angle. The other

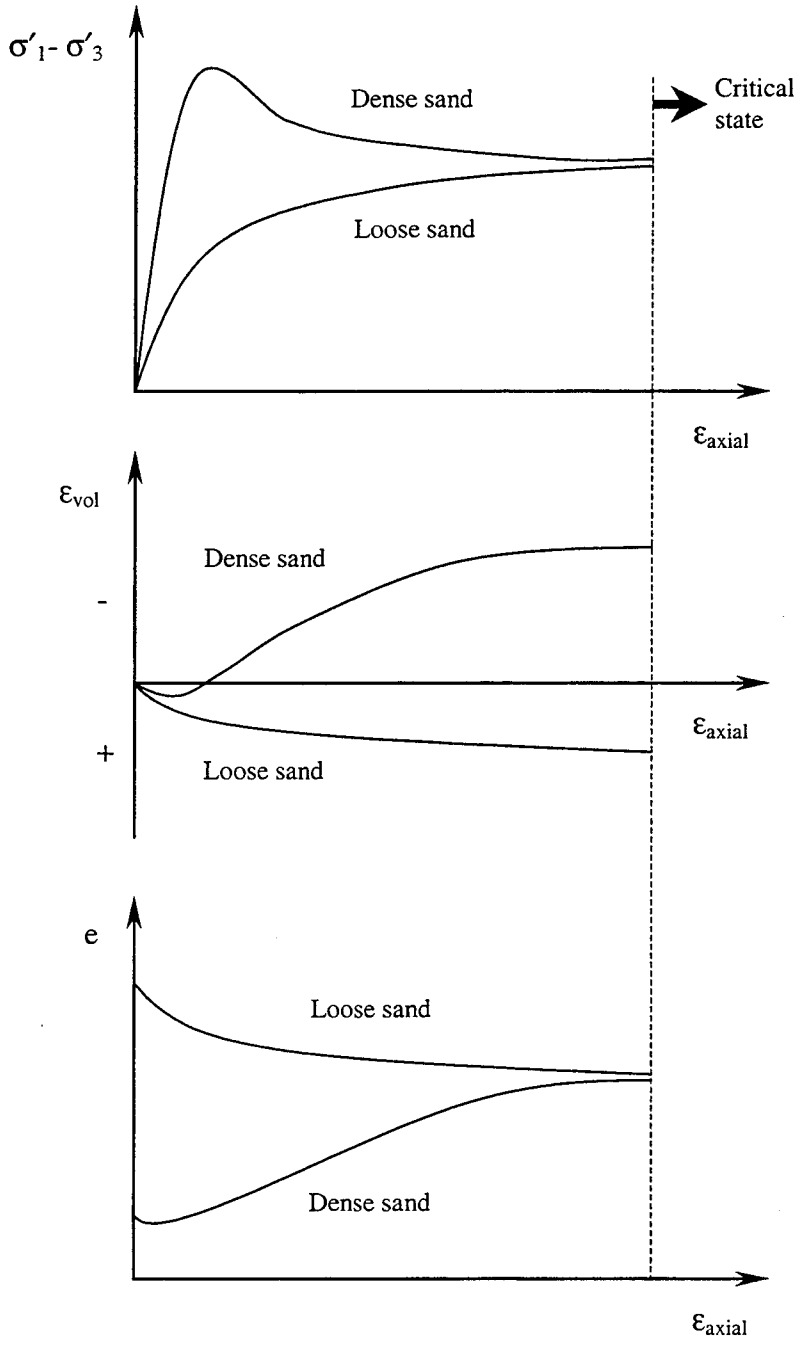

Figure 4.8 Different behavior of dense and loose sand (after Lambe and Whitman 1986).

factor that affects the dilatancy of sand is the confinement. It has been observed that lower confinement produces higher dilatancy in sand.

There is a condition far beyond the peak point of the stress-strain curve, for which no volume change is observed. This stage is referred to as the critical state. As shown in Figure 4.8, the volumetric strain ε_{vol}, deviatoric stress $\sigma'_1 - \sigma'_3$ and void ratio e at the critical state remain constant. The friction angle at this stage is regarded as a material property that depends only on the nature of the sand, and not on either the initial density or confining stress.

The friction angle at the critical state of sand is given by:

$$\sin\phi_c = \frac{\sigma'_{1c} - \sigma'_{3c}}{\sigma'_{1c} + \sigma'_{3c}} \tag{4.72}$$

where ϕ_c = friction angle at the critical state; and σ'_{1c} and σ'_{3c} = major and minor principal stresses at the critical state.

In order to quantify the dilatancy of sand, Bolton (1986) proposed the following relationship based on the experimental test results:

$$\phi_p = \phi_c + 0.8\psi_p \tag{4.73}$$

in which ϕ_p = peak friction angle; ϕ_c = friction angle at the critical state; and ψ_p = dilatancy angle. The dilatancy angle ψ_p is given by:

$$\psi_p = 6.25 I_R \quad \text{for plane-strain conditions} \tag{4.74}$$

and

$$\psi_p = 3.75 I_R \quad \text{for triaxial conditions} \tag{4.75}$$

The dilatancy index I_R in (4.74) and (4.75) is given by:

$$I_R = I_D[Q + \ln(\frac{P_a}{100P_p'})] - 1 \qquad (4.76)$$

where I_D = relative density as a number between 0 and 1; P_a = reference stress = 100kPa ≈ 1kgf/cm^2; P'_p = mean effective stress at peak strength in the same units as P_a; and Q = material constant approximately equal to 10 for clean silica sand. From (4.73) through (4.76), it is seen that the dilatancy angle ψ_p depends on both relative density and confinement. The higher the relative density, the higher the dilatancy angle, whereas the higher the confinement, the lower the dialtancy angle. For practical purposes, Bolton (1986) limits the values of the dilatancy angle at:

$$\phi_p - \phi_c < 20° \quad \text{for plane-strain conditions} \qquad (4.77)$$

and

$$\phi_p - \phi_c < 12° \quad \text{for triaxial conditions} \qquad (4.78)$$

4.6 Summary

In this chapter, the mechanical behavior of soil was discussed. The linear elastic relationship between stress σ_{ij} and strain ε_{kl} can be defined by the generalized Hooke's law as following equation:

$$\sigma_{ij} = C_{ijkl}\varepsilon_{kl}$$

where the elastic moduli tensor C_{ijkl} is expressed in terms of two elastic constants, either the bulk modulus K and shear modulus G or Young's modulus E and Poisson's ratio ν.

Hyperbolic stress-strain models have been used to represent the non-linear behavior beyond the very small strains for which soil behaves as a linear elastic material. Hyperbolic soil models are based on quasi-linear elasticity and can be expressed in terms of the degraded elastic modulus as a function of the stress or strain level. The degraded elastic modulus can be obtained from the ratio of the current stress level to the maximum stress level and the initial elastic modulus, which is given by the confinement and the relative density for sands.

At large strains, soil exhibits plastic behavior. For the description of plastic behavior of soil, two conditions are required: a failure criterion and a flow rule. The failure criterion defines the stress limit under which soil remains as an elastic material. After this stress limit, soil no longer follows the elastic stress-strain relationship. The flow rule represents the relationship between the stress and strain rate in the plastic range. The magnitude and direction of the plastic strain increment can be determined based on the flow rule.

The peak friction angle of sands can be expressed in terms of the friction angle at the critical state and the dilatancy angle. The friction angle at the critical state is a constant for a given sand, and depends only on the nature of the sands. The dilatancy angle, on the other hand, is a function of confinement and relative density. Bolton (1986) proposed the following relationship in order to quantify the dilatancy of sand:

$$\phi_p = \phi_c + 0.8\psi_p$$

where ϕ_p = peak friction angle; ϕ_c = friction angle at critical state; and ψ_p = dilatancy angle determined as a function of density and confining stress. As a result, the failure surface of sands, which is determined by the peak friction angle, is regarded as a non-linear surface.

CHAPTER 5 3-D NON-LINEAR ELASTIC-PLASTIC STRESS-STRAIN MODEL

5.1 Introduction

The non-linear elastic models mentioned in the previous chapter were developed on the basis of a plane-strain condition. Vertical loading of either a pile in the free field or a circular plate within a calibration chamber is an axi-symmetric problem, thus requiring three-dimensional modeling. In order to obtain more realistic results for such problems, therefore, the full description of the stress-strain relationship including non-linear elastic and plastic behavior in three dimensions is necessary.

In this chapter, we discuss first the characteristics of the intrinsic and state soil variables that will be used in the stress-strain model. The full non-linear elastic-plastic soil model for three dimensions is then presented.

5.2 Intrinsic and State Soil Variables

Soil variables used for the description of soil behavior can be classified as either intrinsic or state variables. Intrinsic soil variables do not change with soil state and are only a function of soil particle, mineralogy, shape, and size distribution (Been et al. 1991, Salgado et al. 1997a). This implies that the intrinsic soil variables for a given soil can be uniquely determined irrespective of the stress state, history or initial condition. These variables include the friction angle at the critical state (ϕ_c), specific gravity (G_s), and

maximum and minimum void ratios (e_{max}, e_{min}). The parameters C_g, e_g, and n_g used in (4.50) for the initial shear modulus are also regarded as intrinsic soil variables.

Soil state variables, on the other hand, are determined by the soil state. The soil state represents the physical condition under which the soil exists. The initial void ratio (e_o) or relative density (D_R), and in-situ vertical and horizontal stresses (σ'_v, σ'_h) are the most important state variables of sands, and control the behavior of the sand (Been et al. 1986). In contrast to the intrinsic variables, the determination of state variables (for example by using laboratory tests) requires undisturbed soil samples. This presents significant difficulties for the determination of soil state variables, particularly for cohesionless soils. The recent use of in-situ testing methods, such as the cone penetration test and the pressuremeter test, however, offers more effective, indirect ways to estimate soil state variables under in-situ conditions.

A useful soil model should be able to relate the stress-strain behavior to soil intrinsic and state variables. With the rapid growth of computing power, the use of more complex soil models have come to be practical for more realistic analyses of geotechnical problems. In the applications of such soil models, the most critical factor for obtaining accurate results may be the reasonably accurate determination of soil and model parameters. The procedures to determine these parameters in general require significant experimental efforts. The more complicated the soil models are, the more laborious the determination of soil and model parameters.

As a simplified approach, the secant modulus is sometimes used to represent the non-linear behavior of soil before a failure condition (Figure 5.1). However, the non-linearity that soil shows is quite complex, varying significantly with the initial density level, stress state, and displacement level of interest. Consequently, the selection of the value of the secant modulus depends on the soil condition and the characteristics of the geotechnical structure being analyzed. It also implies that there is no single value of secant modulus that will produce acceptable results for all possible initial conditions.

It is possible to back-estimate the secant modulus using experimental results as a function of displacement level. This approach, however, is not a fundamental solution,

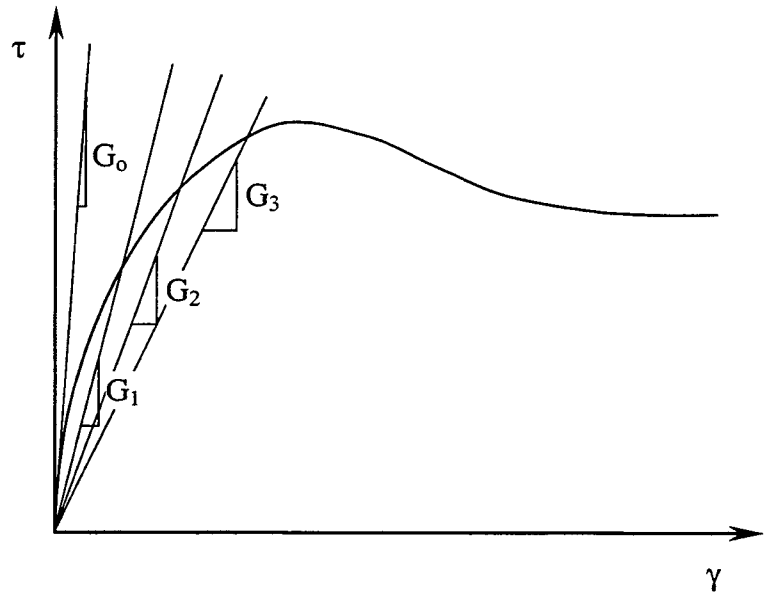

Figure 5.1 Secant modulus for non-linear stress-strain behavior.

and may result in an inaccurate relationship between modulus, density level and stress state due to the limited number of experimental results. The use of the intrinsic and state soil variables in a non-linear elastic-plastic soil model combined with suitable numerical techniques allows a more fundamental solution to geotechnical problems.

5.3 Modified Hyperbolic Model for Non-Linear Elasticity

The conventional hyperbolic equation of (4.57) implies that the degradation of the elastic modulus with respect to stress level is linear. However, the measured degradation curves of real soils under static or quasi-static loading can be quite different from linear. Figure 5.2 shows measured modulus degradation curves of normally consolidated sand and the degradation line by the conventional hyperbolic equation plotted together. The figure was plotted in terms of normalized shear modulus G/G_o and normalized shear stress τ/τ_{max} where G_o and τ_{max} represent the initial shear modulus and the maximum shear stress at failure, respectively. As can be seen, the modulus degradation curve for cyclic loading shows good agreement with the conventional hyperbolic equation. On the other hand, the modulus degradation curve for monotonic loading reveals significantly different response from that of the conventional hyperbolic equation. The measured modulus degradation for monotonic loading from the initial shear modulus G_o is initially quite rapid. The rate of the degradation then drops as the normalized shear stress increases.

In order to account for the characteristics of the modulus degradation observed in real soils, Fahey and Carter (1993) proposed a modification of the conventional hyperbolic model. The modification consists of the introduction of a parameter g into (4.57):

$$\frac{G_s}{G_o} = 1 - f\left(\frac{\tau}{\tau_{max}}\right)^g \tag{5.1}$$

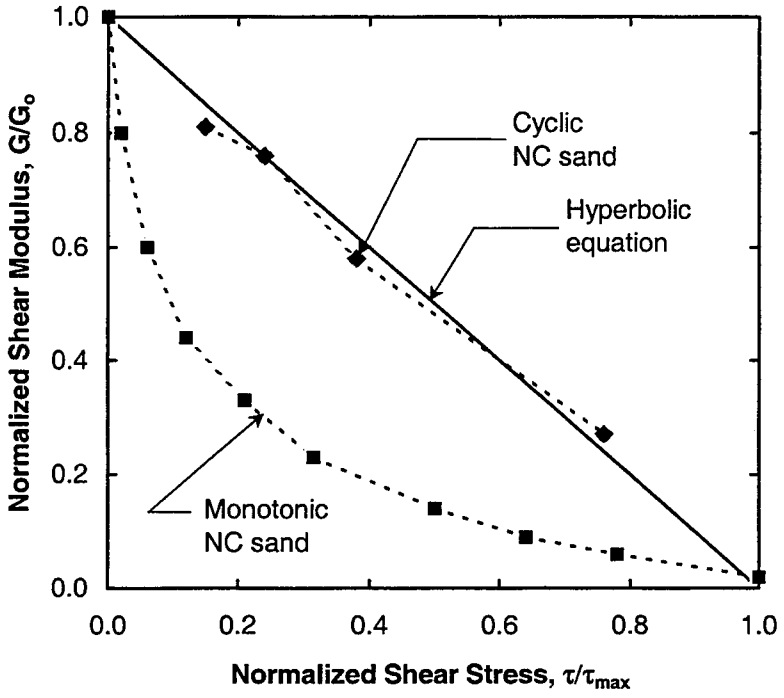

Figure 5.2 Modulus degradation relationship for normally consolidated sand (after Teachavorasinskun et al. 1991).

The parameter f in (5.1) has the same role as R_f in Duncan and Chang's hyperbolic equation of (4.53) and (4.55). The parameter g determines the shape of the degradation curve in terms of the stress level. If f and g are both set equal to 1, (5.1) becomes the original hyperbolic equation by Kondner (1963). If f is equal to 0, (5.1) represent the linear elastic relationship with a constant value of shear modulus irrespective of stress level as:

$$\frac{G}{G_o} = 1 \qquad \text{or} \qquad G = G_o \tag{5.2}$$

If g is set to be equal to 1 with a certain value of f, the Duncan and Chang hyperbolic relationship given by (4.57) results. Figure 5.3 shows typical modulus degradation curves for different values of f and g. For a typical normally consolidated sand, Fahey and Carter (1993) suggested that the value of f = 0.98 and g = 0.25 lead to reasonable agreement with observed modulus degradation curve.

In numerical analysis of soil behavior using non-linear stress-strain models, a tangent modulus with successive incremental procedure rather than a secant modulus with successive iterative procedure is often used (Duncan and Chang 1970, Desai and Christian 1977). According to Duncan and Chang (1970), the advantage of the incremental procedure is that the initial stress state can readily be taken into account, which is very important in geotechnical problems. The accuracy of the incremental procedure can significantly be improved by combining the iterative method for each increment. The tangent shear modulus G_t can be obtained from the differentiation of (5.1). Using the relationship $\tau = G \cdot \gamma$, (5.1) is rewritten as:

$$\frac{\tau}{G_o \gamma} = 1 - f\left(\frac{\tau}{\tau_{max}}\right)^g \tag{5.3}$$

or

$$\frac{1}{\gamma} = G_o \tau^{-1} - G_o f \left(\frac{1}{\tau_{max}}\right)^g (\tau)^{g-1} \tag{5.4}$$

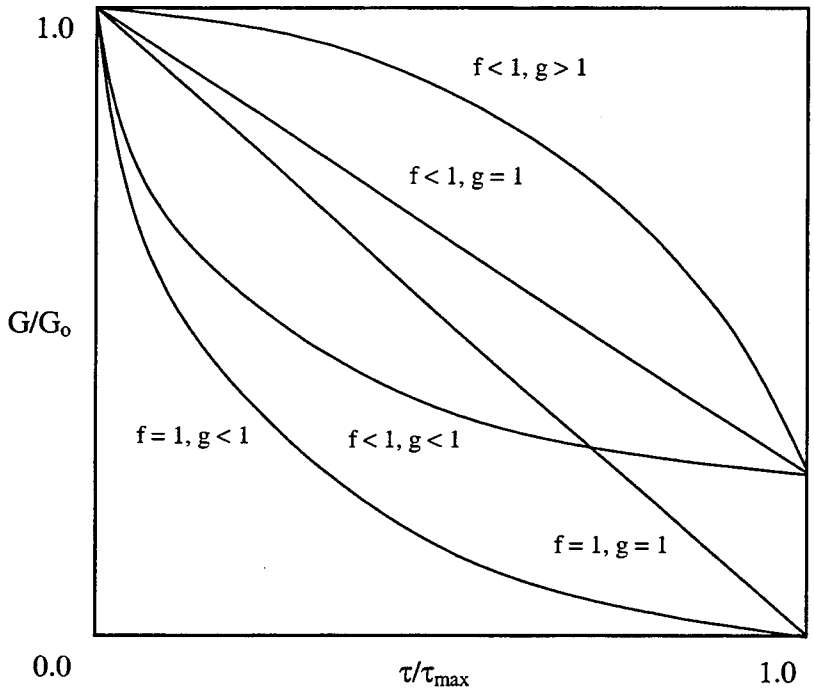

Figure 5.3 Modulus degradation curve for different values of f and g.

Replacing $1/\gamma$ by ξ:

$$\gamma = \xi^{-1} \tag{5.5}$$

Then,

$$\frac{d\gamma}{d\tau} = -\xi^{-2}\frac{d\xi}{d\tau}$$

$$= -\xi^{-2}[-G_o\tau^{-2} - G_o f(g-1)(\frac{1}{\tau_{\max}})^g(\tau)^{g-2}]$$

$$= \xi^{-2}[G_o\tau^{-2} + G_o f(g-1)(\frac{1}{\tau_{\max}})^g(\tau)^{g-2}]$$

$$= \frac{G_o\tau^{-2}[1 - f(1-g)(\frac{\tau}{\tau_{\max}})^g]}{[G_o\tau^{-1} - G_o f(\frac{1}{\tau_{\max}})^g(\tau)^{g-1}]^2} \tag{5.6}$$

Thus,

$$\frac{d\gamma}{d\tau} = \frac{1 - f(1-g)(\frac{\tau}{\tau_{\max}})^g}{G_o[1 - f(\frac{\tau}{\tau_{\max}})^g]^2} \tag{5.7}$$

Because $G_t = \frac{d\tau}{d\gamma}$, (5.7) becomes:

$$\frac{1}{G_t} = \frac{1 - f(1-g)(\frac{\tau}{\tau_{\max}})^g}{G_o(\frac{G}{G_o})^2} \tag{5.8}$$

or

$$\frac{G_t}{G_o} = \frac{(\frac{G}{G_o})^2}{1 - f(1-g)(\frac{\tau}{\tau_{\max}})^g} \tag{5.9}$$

Using (5.9), the tangent modulus G_t corresponding to the current stress level τ/τ_{max} and the current secant shear modulus G can be obtained.

5.4 Non-Linear Elastic Model for Three Dimensions

5.4.1 Modified hyperbolic stress-strain relationship for three dimensions

Application of the hyperbolic model to the analysis of the loading of a natural soil deposit requires the resolution of two issues. Firstly, there is the issue of how to define what shear stresses to use in the stress-strain model. In naturally deposited soil, the stress state is anisotropic with an existing initial shear stress which is determined by a coefficient of lateral earth pressure at-rest, $K_0 = \sigma'_h/\sigma'_v$. Most laboratory studies on stress-strain response, however, have been done on isotropically consolidated samples. In order for the analysis to be more realistic, the initial shear stress existing in a natural soil deposit should be taken into account. A second issue is related to the extension of the non-linear elastic models, which have been based on common laboratory tests and are two-dimensional, to three dimensions.

In the modified hyperbolic model by Fahey and Carter (1993), the degradation of shear modulus is expressed in terms of shear stress level τ/τ_{max} with the model parameters f and g. To take account of the initial shear stress due to initial stress anisotropy in the hyperbolic model, the following formulation should be used instead of (5.1):

$$\frac{G_s}{G_o} = 1 - f\left(\frac{\tau - \tau_o}{\tau_{max} - \tau_o}\right)^g \qquad (5.10)$$

where τ_o = initial shear stress due to the initial K_0 condition. Figure 5.4 illustrates how τ_o, τ and τ_{max} were defined in the present study. In Figure 5.4 (a), it should be noticed

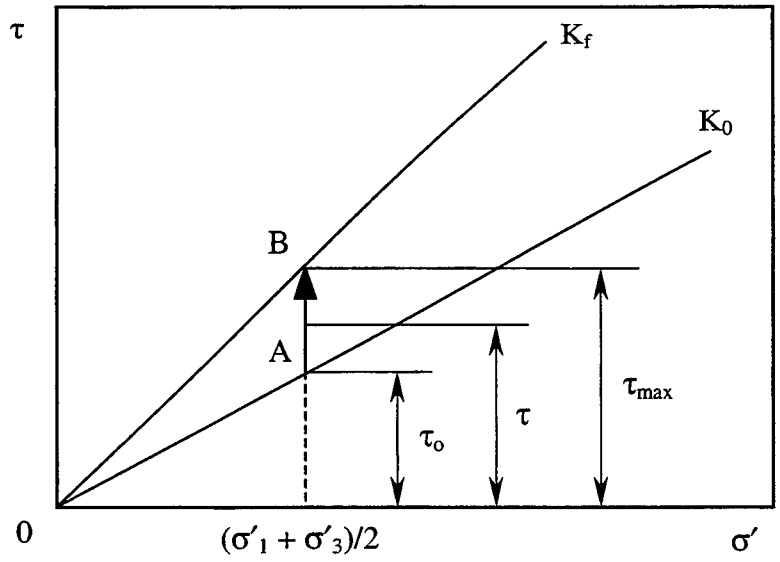

(a)

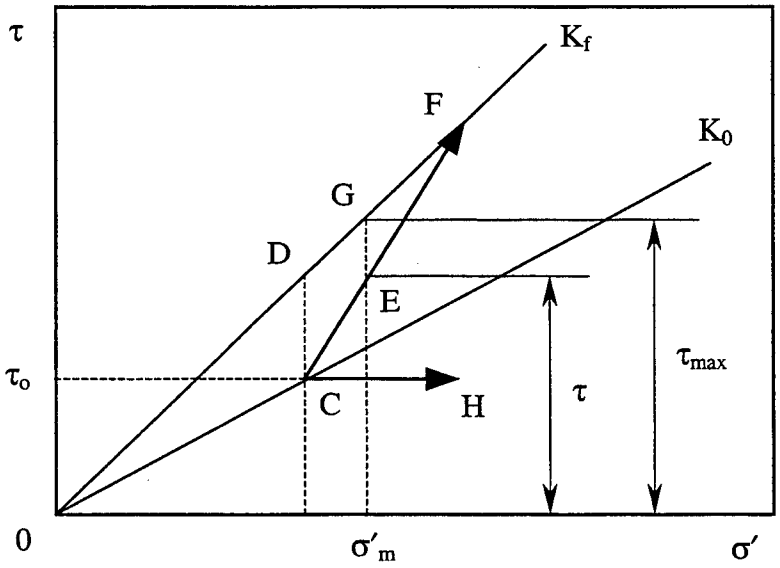

(b)

Figure 5.4 Definition of τ_o, τ and τ_{max} for (a) constant and (b) varying confinement.

that τ_o, τ and τ_{max} are all defined at the same confining stress as represented by $(\sigma'_1 + \sigma'_3)/2$. The stress path AB is only possible in a simple shear test with initially anisotropic stress condition. The stress path CF in Figure 5.4 (b), on the other hand, is more representative of the axial loading of a foundation for soils with an initial K_0 condition, where failure is reached as a result of increases in both shear and confining stresses. For the stress path CF, the maximum shear stress τ_{max} varies along the line DF, depending on the current shear stress on line CF. As an illustration, for point E in Figure 5.4 (b) representing the current shear stress τ, point G (obtained by vertically projecting point E onto the K_f line) represents the maximum shear stress corresponding to the current shear stress τ and confining stress σ'_m.

Full description of the stress state under various types of external loading requires a specification of the intermediate principal stress as well as the major and minor principal stresses. Three-dimensional stress conditions may also be represented by the use of stress invariants. The first invariant I_1 of the stress tensor given by (4.9) is a measure of confining stress, and the square root of the second invariant J_2 of the deviatoric stress tensor given by (4.22) is a measure of shear stress in three dimensions. Using the stress invariants, the hyperbolic relationship of (5.10) may now be rewritten for three dimensions as:

$$\frac{G_s}{G_o} = 1 - f\left(\frac{\sqrt{J_2} - \sqrt{J_{2o}}}{\sqrt{J_{2\max}} - \sqrt{J_{2o}}}\right)^g \tag{5.11}$$

where $\sqrt{J_2}$, $\sqrt{J_{2o}}$ and $\sqrt{J_{2\max}}$ are the 3-D equivalents of τ_o, τ and τ_{max} in (5.10). It is necessary for J_{2max} to be defined using a three-dimensional failure criterion. The Drucker-Prager failure criterion was selected in this study for that purpose. The Drucker-Prager failure criterion is given by:

$$F = \sqrt{J_2} - \alpha I_1 - \kappa = 0 \tag{5.12}$$

where α and κ are related to the Mohr-Coulomb strength parameters c and ϕ through:

$$\alpha = \frac{2\sin\phi}{\sqrt{3}(3-\sin\phi)} \tag{5.13}$$

and

$$\kappa = \frac{6c\cdot\cos\phi}{\sqrt{3}(3-\sin\phi)} \tag{5.14}$$

In (5.13) and (5.14), ϕ and c represent the friction angle and cohesion, respectively. For sands, c and hence $\kappa = 0$. From (5.12), J_{2max} for sands at a given confinement would be obtained as:

$$J_{2\max} = \alpha^2 I_1^{\,2} \tag{5.15}$$

As a result, the 3-D stress plane of I_1 versus $\sqrt{J_2}$ is used, instead of the 2-D stress plane of σ versus τ, to obtain the stress level associated with (5.11) in a manner similar to that of Figure 5.4.

Considering the stress path CH in Figure 5.4 (b), the shear modulus should increase due to the increase of confinement, while the magnitude of shear stress is kept constant. In order to account for the influence of confinement on shear modulus during loading, (5.11) is modified as follows:

$$\frac{G_s}{G_o} = [1 - f(\frac{\sqrt{J_2} - \sqrt{J_{2o}}}{\sqrt{J_{2\max}} - \sqrt{J_{2o}}})^g](\frac{I_1}{I_{1o}})^{n_g} \tag{5.16}$$

where I_1 and I_{1o} are the first invariants of the stress tensor at the current and initial states. The parameter n_g is the same as appears in (4.50). In both equations, n_g represents the dependence of shear modulus on confinement. Use of (5.16), rather than (5.11), permits that the degradation of shear modulus be properly expressed in terms of both shear stress

and confining stress levels. Eq. (5.16) reverts to (5.11) for the simple shear case in which $I_1 = I_{1o}$ at any stress level.

5.4.2 Variation of bulk modulus and Poisson's ratio

As discussed in chapter 4, the stress-strain response of an elastic material is described by two constants; the bulk modulus K and the shear modulus G are often used. The elastic stress-strain relationship using the bulk modulus K and the shear modulus G can be written in matrix form as follows:

$$\begin{Bmatrix} \sigma_{11} \\ \sigma_{22} \\ \sigma_{33} \\ \sigma_{12} \\ \sigma_{23} \\ \sigma_{13} \end{Bmatrix} = \begin{bmatrix} K+4G/3 & K-2G/3 & K-2G/3 & 0 & 0 & 0 \\ K-2G/3 & K+4G/3 & K-2G/3 & 0 & 0 & 0 \\ K-2G/3 & K-2G/3 & K+4G/3 & 0 & 0 & 0 \\ 0 & 0 & 0 & G & 0 & 0 \\ 0 & 0 & 0 & 0 & G & 0 \\ 0 & 0 & 0 & 0 & 0 & G \end{bmatrix} \begin{Bmatrix} \varepsilon_{11} \\ \varepsilon_{22} \\ \varepsilon_{33} \\ \gamma_{12} \\ \gamma_{23} \\ \gamma_{13} \end{Bmatrix} \qquad (5.17)$$

As the stress state changes in a non-linear elastic model, the elastic parameters K and G of (5.17) also change. Thus, the complete description of a non-linear elastic relationship requires proper representation of variations in both shear modulus G and bulk modulus K. As described earlier, the shear modulus is given by the non-linear stress-strain relationship as a function of current stress state. The magnitude of the bulk modulus depends mainly on the magnitude of the confining stress (Naylor et al. 1981). The K-G model is one of the ways for accounting for the nonlinear elastic characteristics before yield (Naylor et al. 1981, Salgado 1993). The basic considerations of the K-G model are:

1. The magnitude of the shear modulus increases with increasing confining stress.
2. The magnitude of the shear modulus decreases with increasing shear stress.

3. The magnitude of the bulk modulus increases with increasing confining stress.

The first two considerations have already been included in the development of the non-linear elastic relationship of (5.16).

Based on the discussion on the K-G model by Naylor et al. (1981), the tangent bulk modulus K_t can be represented by the following equation:

$$K_t = D_s \cdot (\sigma'_m)^{n_k} (P_a)^{(1-n_k)} \tag{5.18}$$

where P_a = reference stress = 100 kPa ≈ 1 kgf/cm^2; σ'_m = mean effective stress in the same units as P_a; D_s = material constant that can be calculated from the initial values of bulk modulus and confining stress; and n_k can be taken as 0.5 with reasonable accuracy. The values of the initial bulk modulus may be obtained from the initial shear modulus G_o and the initial Poisson's ratio ν_o, which can, in most cases, be taken in the 0.1 - 0.15 range.

The expression of Poisson's ratio ν in terms of the current loading state can be obtained from the relationships of Table 4.1. Based on these relationships, the ratio of the tangent Young's modulus E_t to the initial Young's modulus E_o can be written as either:

$$\frac{E_t}{E_o} = \frac{G_t(1+\nu)}{G_o(1+\nu_o)} \tag{5.19}$$

or

$$\frac{E_t}{E_o} = \frac{K_t(1-2\nu)}{K_i(1-2\nu_o)} \tag{5.20}$$

in which ν_o = initial Poisson's ratio; K_i, K_t, G_o, and G_t = initial and current bulk and shear moduli, respectively. From (5.19) and (5.20), the Poisson's ratio ν at the current stress state can be given by:

$$\nu_t = \frac{\frac{K_t}{K_i}(1+\nu_o) - \frac{G_t}{G_o}(1-2\nu_o)}{2\frac{K_t}{K_i}(1+\nu_o) + \frac{G_t}{G_o}(1-2\nu_o)} \tag{5.21}$$

In (5.21), it is seen that the Poisson's ratio approaches 0.5 as the shear modulus approaches zero, as expected.

5.4.3 Determination of the parameters f and g

The parameters f and g in (5.16) determine the characteristics of degradation of the elastic modulus. In order to evaluate the values of f and g, a set of triaxial test results performed by Giuseppe (1991) and Vecchia (1991) for Ticino sand was analyzed. Ticino sand has been studied extensively (Salgado 1993, Bellotti et al. 1996) and involved in a number of laboratory plate load and cone penetration tests (Ghionna et al. 1994, Salgado et al. 1997a). The properties of Ticino sand are shown in Table 5.1.

When the modulus degradation relationship is to be determined from triaxial test results, it should be pointed out that the soil specimen under triaxial loading is subjected to continuously increasing confinement. The conventional triaxial test is performed by applying first an isotropic cell pressure σ'_3, then a deviatoric axial stress, which is increased (or decreased) until failure. If confinement is defined through the mean effective stress $\sigma'_m = (\sigma'_1+2\sigma'_3)/3$ rather than σ'_3, a triaxial soil specimen can be considered to undergo changes in both confinement and shear stress. As a result, it is not possible to define a single value of maximum shear stress for a triaxial loading condition, due to continuously varying confinement, as discussed in the previous section. Instead, it is possible to identify a different value of maximum shear stress corresponding to each value of current confinement σ'_m, as illustrated in Figure 5.4(b).

The use of Young's modulus is more suitable for obtaining the modulus degradation relationship from triaxial tests. Young's modulus in a triaxial test is calculated from the

Table 5.1 Basic properties of Ticino sand (after Ghionna et al. 1994).

D_{10} (mm)	0.36
D_{50} (mm)	0.54
Specific gravity (G_s)	2.623
Coefficient of uniformity (U)	1.5
Friction angle at critical state (ϕ_c)	34.8°
e_{max}	0.922
e_{min}	0.573
γ_{max} (kN/m^3)	16.68
γ_{min} (kN/m^3)	13.65
C_g	647
n_g	0.44
e_g	2.27

applied axial stress $(\sigma'_1 - \sigma'_3)$ and the axial strain ε_{axial} with the lateral stress σ'_3 remaining constant. The stress level can be determined from the applied axial stress $(\sigma'_1 - \sigma'_3)$ normalized with respect to the unique value of maximum axial stress at failure, $(\sigma'_1 - \sigma'_3)_f$.

Figures 5.5 through 5.17 show the measured and calculated modulus degradation curves obtained from triaxial tests on samples with two different relative density levels (i.e. medium dense sand with relative density equal to approximately 50%, and dense sand with relative density equal to or higher than 90%). As can be seen in the figures, the degradation curves were plotted in terms of normalized Young's modulus E_s/E_o versus deviatoric axial stress level $(\sigma'_1 - \sigma'_3)/(\sigma'_1 - \sigma'_3)_f$, where E_s and E_o represent the secant and initial Young's modulus respectively. The initial Young's modulus E_o was calculated from the initial shear modulus given by (4.50) and the initial Poisson's ratio at small strain taken as 0.15.

The values of f and g for the medium dense sand shown in Figures 5.5 – 5.8 were found to be in the 0.96 - 0.97 and 0.15 - 0.20 range, respectively. Those for the medium dense sand were in the 0.93 – 0.95 and 0.2 - 0.32 range, respectively. Table 5.2 summarizes the initial elastic modulus and the values of f and g for the triaxial soil samples used in Figures 5.5 - 5.17. From Figures 5.5 - 5.17 and Table 5.2, it is observed that the values of f and g vary according to the relative density level. As the relative density increases, the value of f decreases while the value of g increases. This result indicates that the ratio of the elastic modulus at failure to its initial value is higher for denser than for looser sand, and the rate of degradation of elastic modulus is higher for looser than for denser sand. The results for both cases are in agreement with intuition.

Because the triaxial tests by Giuseppe (1991) and Vecchia (1991) were performed for only two relative density levels, the values of f and g shown in Table 5.2 cannot be directly applied to other relative density levels. In order to determine the parameters f and g for other relative density levels, the values of f and g for D_R = 30% and 70% were extrapolated and interpolated, respectively, from those corresponding to D_R = 50% and 90% which were obtained based on the measured modulus degradation relationship.

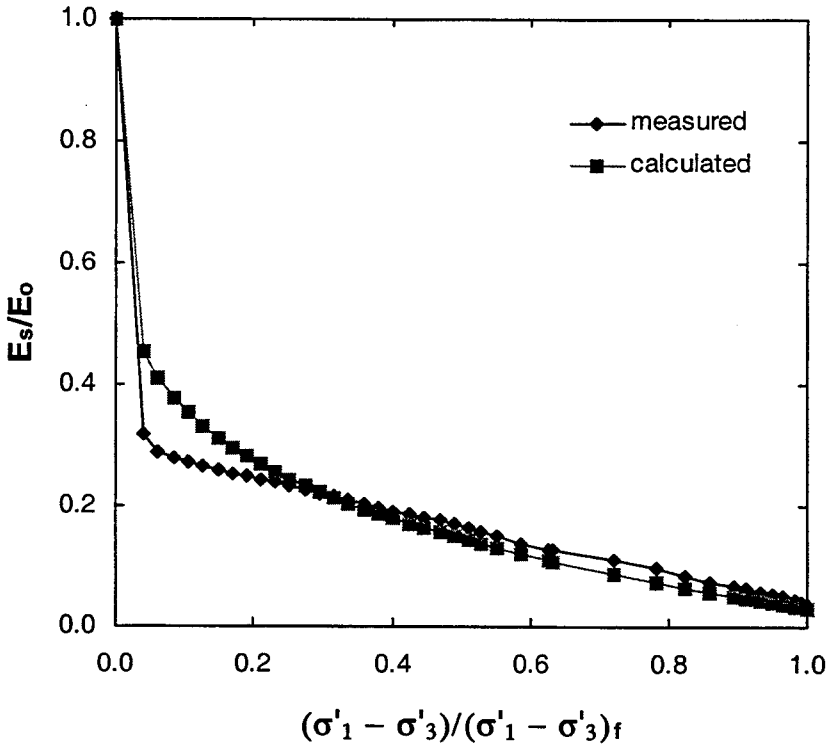

Figure 5.5 Modulus degradation curves for $D_R = 51.5\%$ and $\sigma_3 = 400$ kPa with $f = 0.97$ and $g = 0.18$.

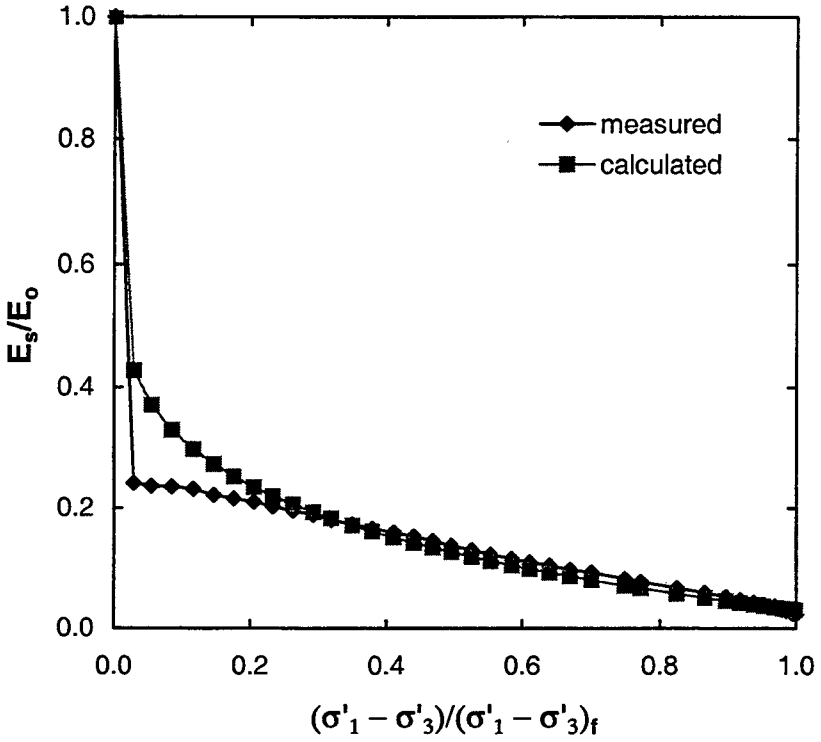

Figure 5.6 Modulus degradation curves for $D_R = 48.8\%$ and $\sigma_3 = 200$ kPa with $f = 0.97$ and $g = 0.15$.

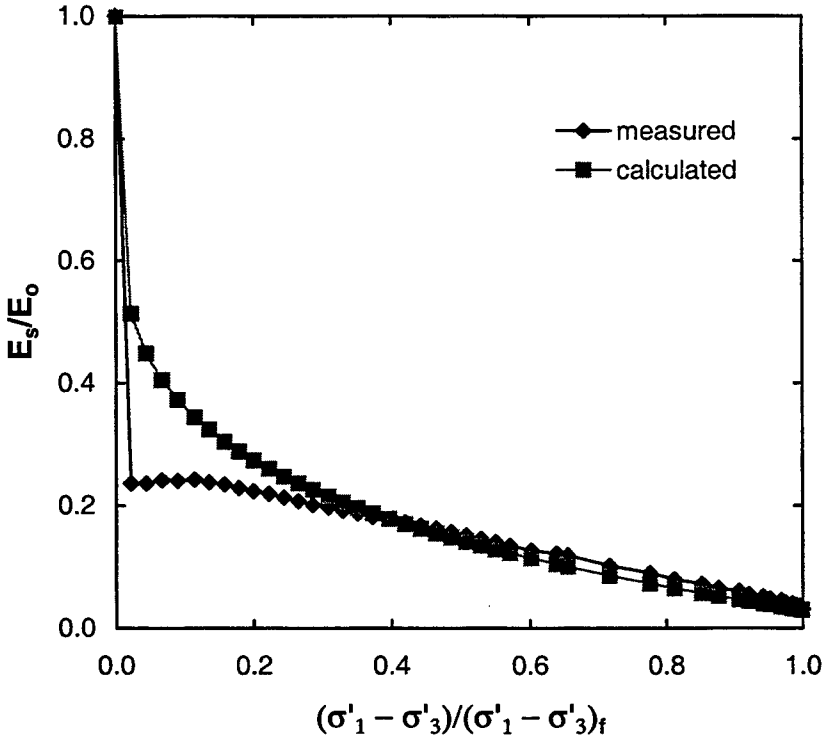

Figure 5.7 Modulus degradation curves for $D_R = 48.2\%$ and $\sigma_3 = 500$ kPa with $f = 0.97$ and $g = 0.18$.

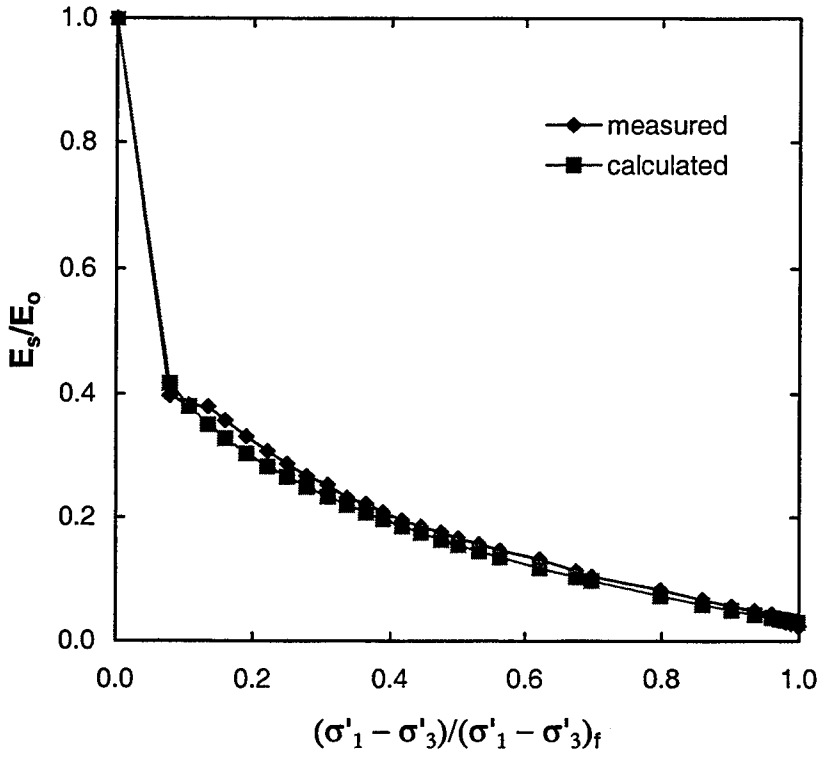

Figure 5.8 Modulus degradation curves for $D_R = 50.8\%$ and $\sigma_3 = 110$ kPa with $f = 0.97$ and $g = 0.20$.

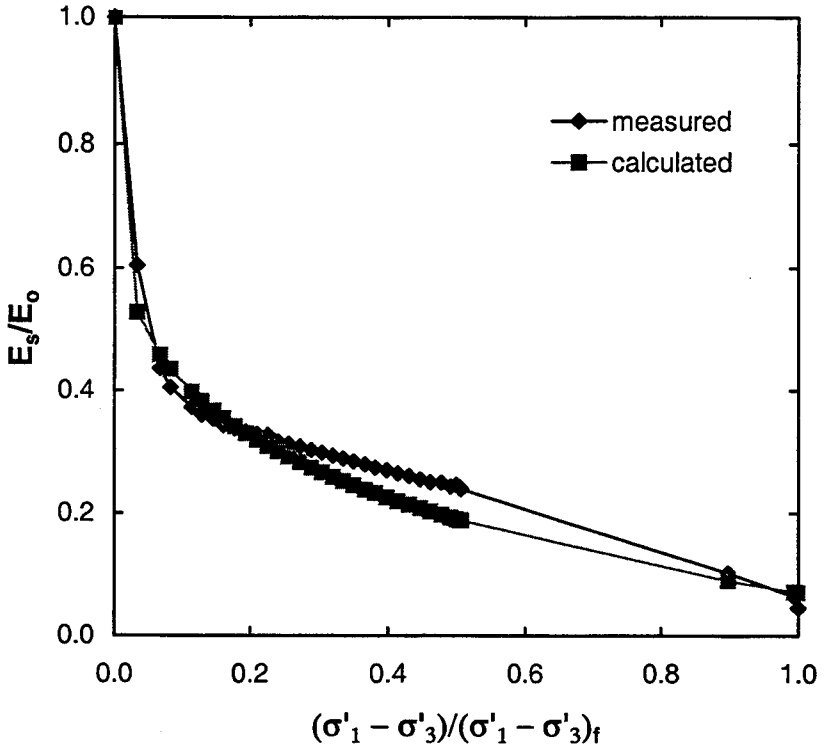

Figure 5.9 Modulus degradation curves for $D_R = 84.6\%$ and $\sigma_3 = 650$ kPa with $f = 0.93$ and $g = 0.20$.

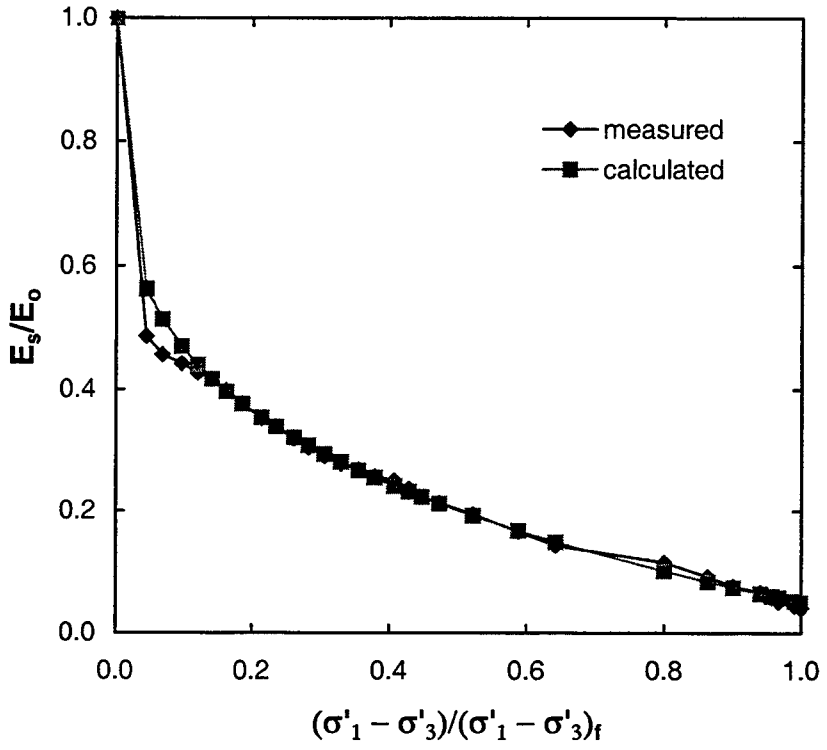

Figure 5.10 Modulus degradation curves for $D_R = 82.3\%$ and $\sigma_3 = 100$ kPa with $f = 0.95$ and $g = 0.25$.

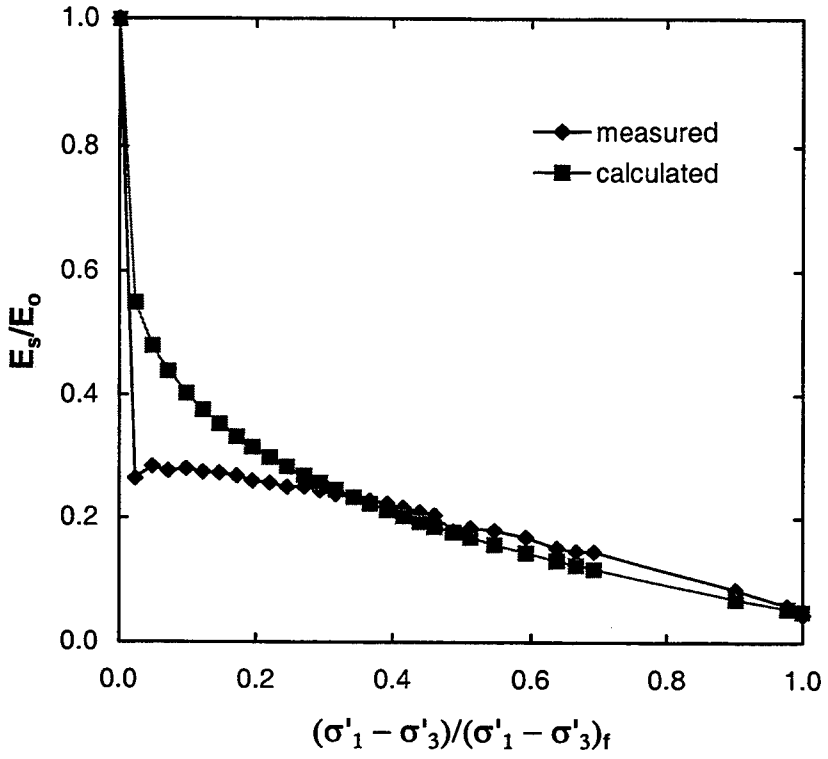

Figure 5.11 Modulus degradation curves for $D_R = 88.9\%$ and $\sigma_3 = 200$ kPa with $f = 0.95$ and $g = 0.20$.

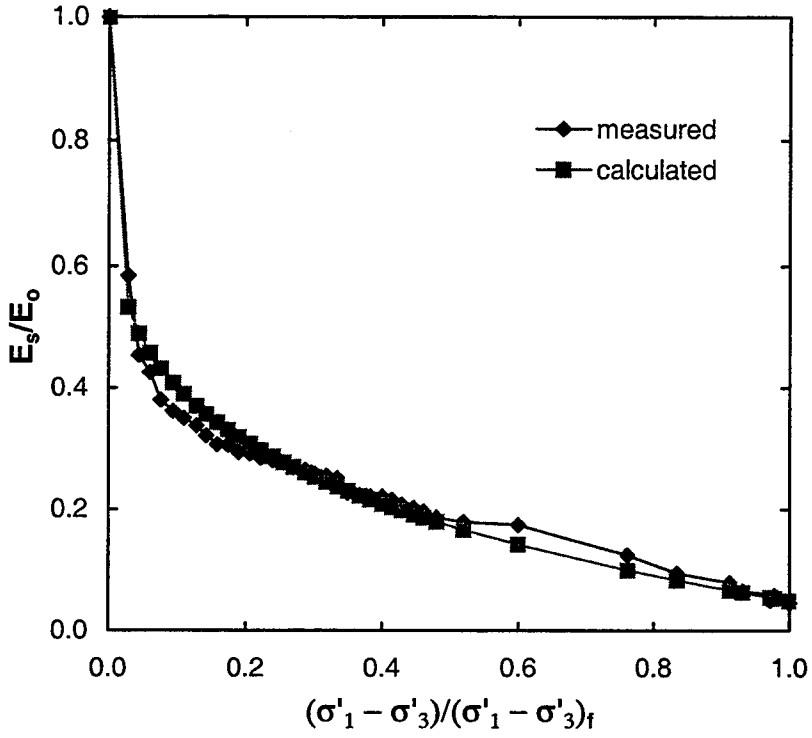

Figure 5.12 Modulus degradation curves for $D_R = 91.1\%$ and $\sigma_3 = 150$ kPa with $f = 0.95$ and $g = 0.20$.

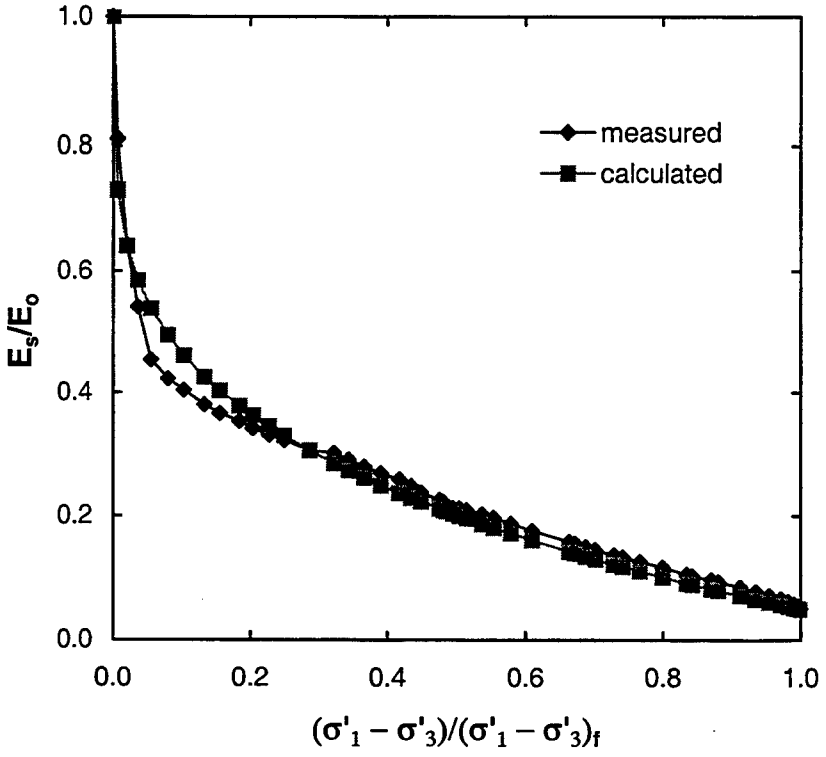

Figure 5.13 Modulus degradation curves for $D_R = 100\%$ and $\sigma_3 = 200$ kPa with $f = 0.95$ and $g = 0.25$.

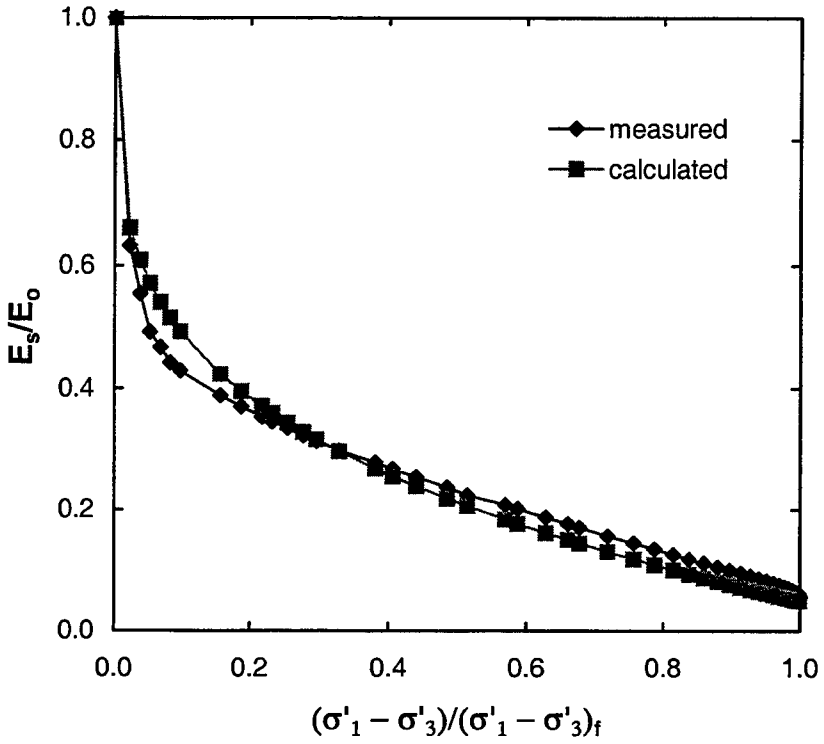

Figure 5.14 Modulus degradation curves for $D_R = 100\%$ and $\sigma_3 = 400$ kPa with $f = 0.95$ and $g = 0.27$.

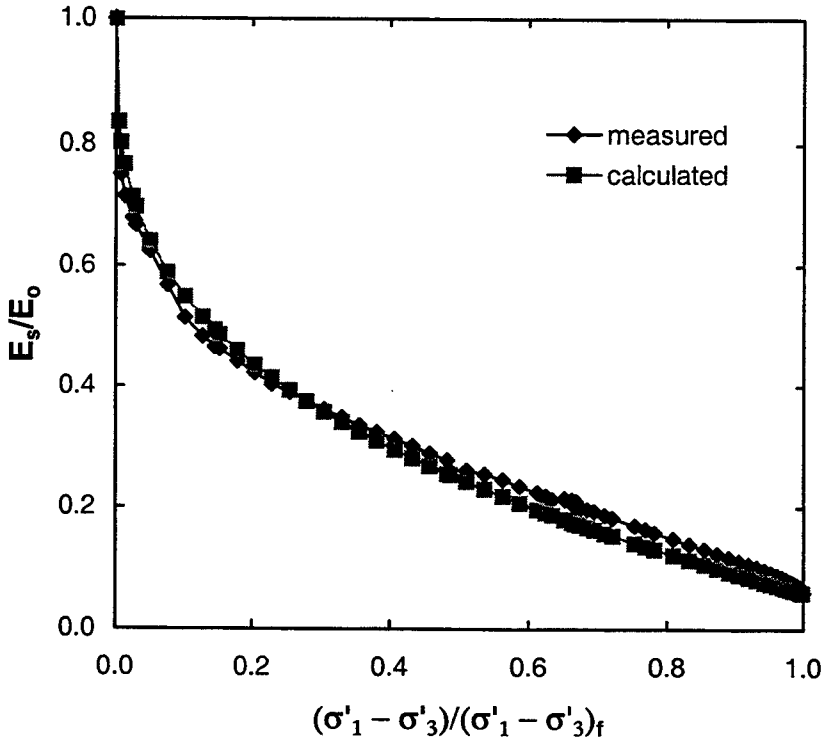

Figure 5.15 Modulus degradation curves for $D_R = 100\%$ and $\sigma_3 = 600$ kPa with $f = 0.94$ and $g = 0.32$.

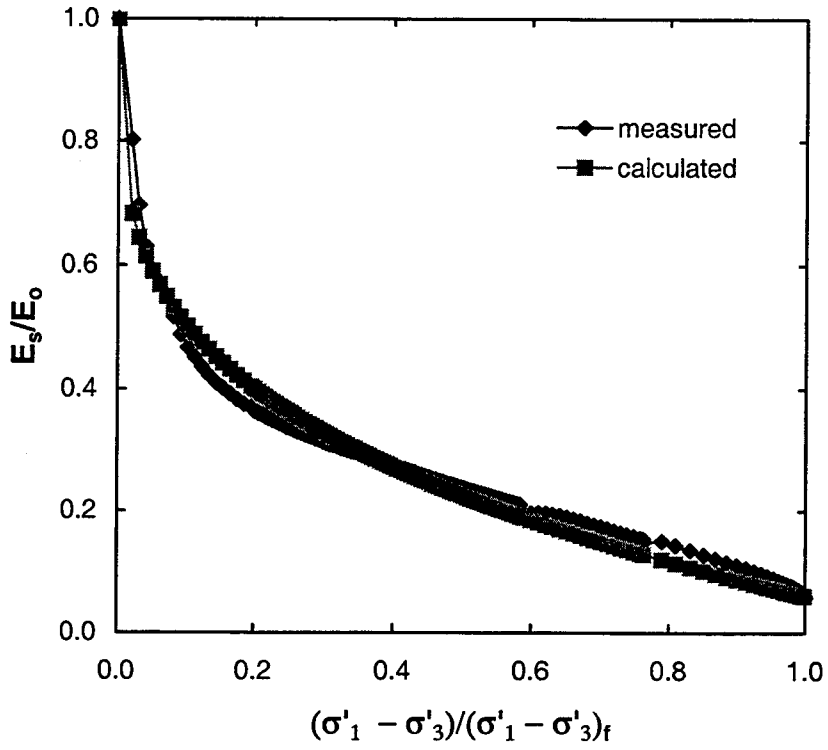

Figure 5.16 Modulus degradation curves for $D_R = 100\%$ and $\sigma_3 = 800$ kPa with $f = 0.94$ and $g = 0.28$.

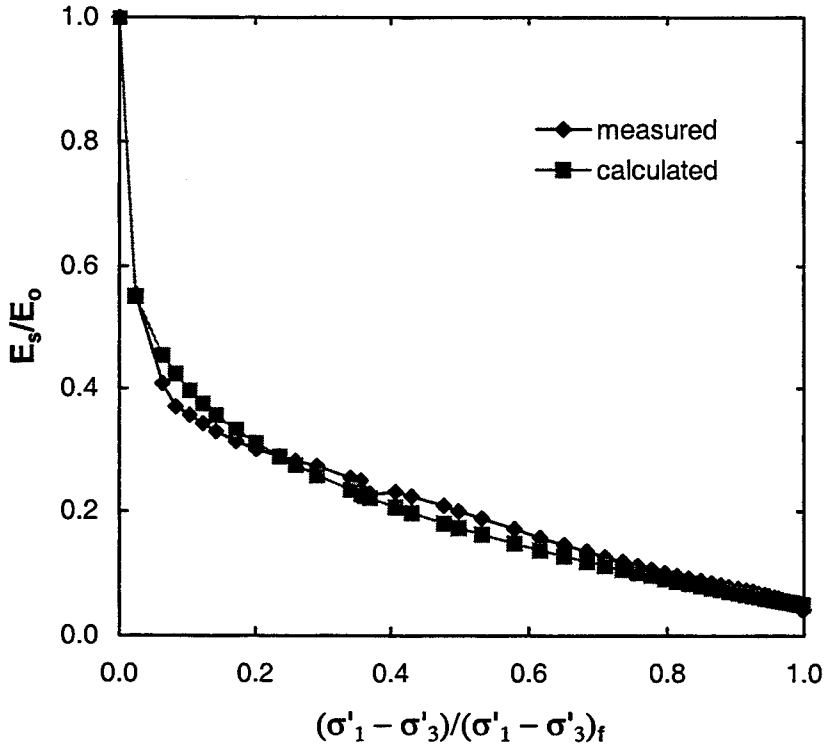

Figure 5.17 Modulus degradation curves for $D_R = 98.6\%$ and $\sigma_3 = 100$ kPa with $f = 0.94$ and $g = 0.20$.

Table 5.3 shows the values of f and g for D_R = 30%, 50%, 70% and 90%. These values will be used for the analysis of calibration chamber plate load tests and pile load tests in the next chapters.

Table 5.2 Values of f and g from triaxial test results.

D_R (%)	σ'_3 (kPa)	E_o (MPa)	f	g
51.5	400	367.1	0.97	0.18
48.8	200	266.0	0.97	0.15
48.2	500	396.6	0.97	0.18
50.8	110	207.2	0.97	0.20
84.6	650	563.6	0.93	0.20
82.3	100	243.7	0.95	0.25
88.9	200	344.2	0.95	0.20
91.1	150	307.8	0.95	0.20
100	200	369.6	0.95	0.25
100	400	501.4	0.95	0.27
100	600	599.3	0.94	0.32
100	800	680.2	0.94	0.28
98.6	100	270.5	0.94	0.20

Table 5.3 Values of f and g for different relative densities.

D_R (%)	f	g
30	0.98	0.17
50	0.97	0.20
70	0.96	0.23
90	0.95	0.26

5.5 Plastic Stress-Strain Relationship for Three Dimensions

5.5.1 Drucker-Prager failure criterion

In geotechnical engineering, the Mohr-Coulomb failure criterion has been often used to describe plastic soil behavior. The basic assumption in the Mohr-Coulomb failure criterion is the plane-strain condition assuming two-dimensional stress state in which only the major and minor principal stresses are considered. It cannot, therefore, be directly applied to the analysis of three-dimensional problems in which the major and minor principal stresses as well as the intermediate principal stress should be taken into account. In order to describe failure and post-failure soil response for the three-dimensional stress state, the Drucker-Prager plastic model was adopted in this study.

As can be seen in (5.12), the Drucker-Prager failure criterion is expressed in terms of the stress invariants J_2 and I_1 given by (4.22) and (4.9). When the stress state reaches the failure surface in the Drucker-Prager plastic model, it should satisfy the condition of:

$$F = \sqrt{J_2} - (\alpha I_1 + \kappa) = 0 \tag{5.22}$$

where the parameters α and κ are given by (5.13) and (5.14) in terms of the Mohr-Coulomb strength parameter c and ϕ obtained from the triaxial conditions. For plane-strain conditions, the parameters α and κ are expressed as follows:

$$\alpha = \frac{\tan\phi}{(9 + 12\tan^2\phi)^{1/2}} \tag{5.23}$$

$$\kappa = \frac{3c}{(9 + 12\tan^2\phi)^{1/2}} \tag{5.24}$$

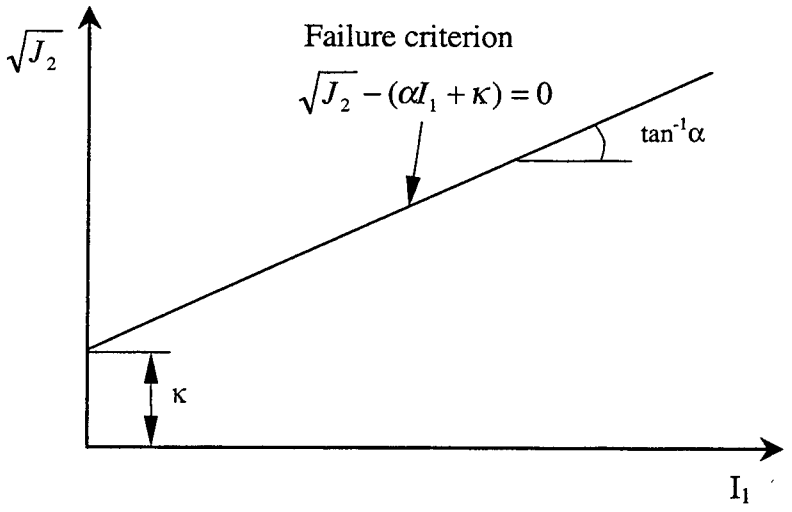

(a)

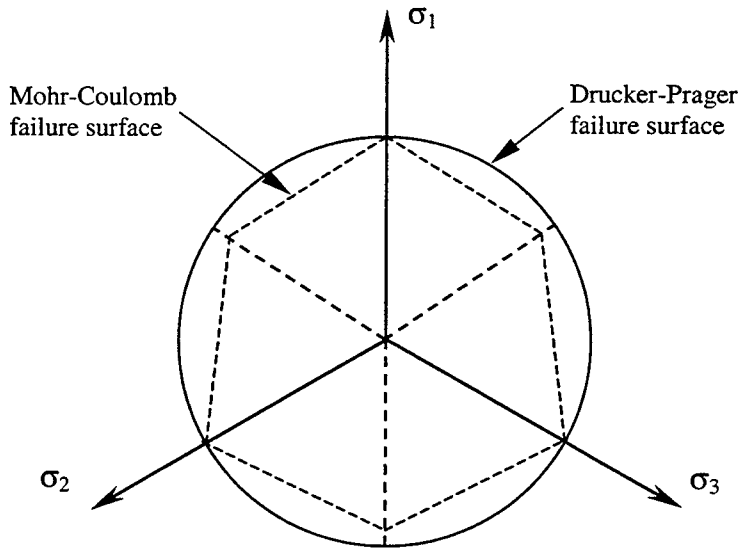

(b)

Figure 5.18 Drucker-Prager failure surface (a) in I_1-$\sqrt{J_2}$ plane and (b) in principal stress plane.

Since the stress invariants shown in (5.22) include all components of the three principal stresses, (5.22) can be used for the description of a failure condition under the three-dimensional stress states.

Figure 5.18 shows the failure surface defined by the Drucker-Prager failure criterion in both I_1-$\sqrt{J_2}$ plane and principal stress plane. As shown in Figure 5.18, the Drucker-Prager failure surface appears as a straight line in I_1-$\sqrt{J_2}$ plane, and a smooth circle in π-plane. As a result, the Drucker-Prager failure criterion is readily incorporated into a numerical procedure while the Mohr-Coulomb cannot readily be used in numerical computation due to the corners of the hexagon in Figure 5.18 (b)

5.5.2 Non-linear failure surface and flow rule

The failure surface given by the original Drucker-Prager failure criterion is defined as a straight line as shown in Figure 5.18 (a) with the Drucker-Prager friction parameter α. As discussed in chapter 4, the peak friction angle ϕ_p for sand is not constant, varying with relative density and confining stress. This relationship was expressed in (4.73) – (4.76). Because the α parameter in the Drucker-Prager failure criterion is obtained from the peak friction angle using (5.13), the envelope of the Drucker-Prager failure surface is also non-linear. As a result, the failure surface becomes steeper as the level of confining stress decreases.

It has been widely recognized that the original Drucker-Prager plastic model with an associated flow rule always causes a large negative volumetric increment, i.e., excessive dilational behavior (Desai and Siriwarden 1984, Chen and Baladi 1985). This is illustrated in Figure 5.19. The associated flow rule requires that the plastic strain increment vector $d\varepsilon_{ij}^{p}$ be perpendicular to the failure surface, such as at point A in Figure 5.19. The plastic strain increment vector $d\varepsilon_{ij}^{p}$ can be decomposed into the vertical ($d\varepsilon_{ij}^{ps}$) and horizontal ($d\varepsilon_{ij}^{pv}$) components as:

$$d\varepsilon_{ij}^{\ p} = d\varepsilon_{ij}^{\ ps} + d\varepsilon_{ij}^{\ pv} \tag{5.25}$$

The vertical component $d\varepsilon_{ij}^{ps}$ represents the plastic shear-strain. The horizontal component $d\varepsilon_{ij}^{pv}$ represents the plastic volumetric-strain that has a negative direction for an associated flow rule. This indicates that the plastic flow in the original Drucker-Prager plastic model is always accompanied by an increase in volume.

In order to suppress unrealistic dilation in the plastic state, a non-associated flow rule with the von Mises plastic potential function was adopted (Borja et al. 1989). The von Mises plastic potential function can be given by:

$$\Omega = \sqrt{J_2} - \kappa \tag{5.26}$$

where Ω is the von Mises plastic potential function and J_2 is the second invariant of the deviatoric stress tensor. Figure 5.20 shows the non-linear failure surface used in this study and plastic strain increment with the non-associated flow rule.

5.5.3 Incremental stress-strain relationship

The most common approach for applying plasticity theory to numerical analysis is the incremental method calculating the tangent stiffness for a plastic condition. According to the concept of perfect plasticity theory, the increment of plastic strain cannot be uniquely determined from the current stress state σ_{ij} and stress increment $d\sigma_{ij}$. The stress increment $d\sigma_{ij}$, however, can be obtained from a current stress σ_{ij} and a given plastic strain increment $d\varepsilon_{ij}^{p}$. This relationship is refereed to as the consistency condition, which forces the stress state to remain on the failure surface, and given by:

$$dF = \frac{\partial F}{\partial \sigma_{ij}} d\sigma_{ij} = 0 \tag{5.27}$$

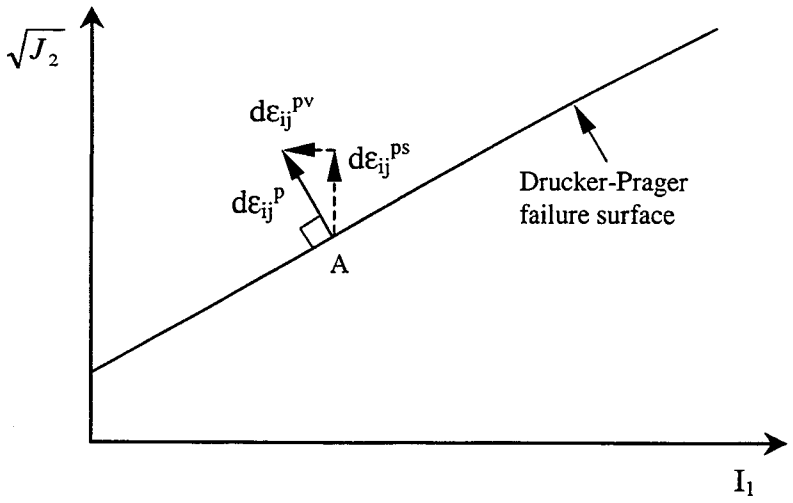

Figure 5.19 Plastic strain in Drucker-Prager failure criterion with associated flow rule.

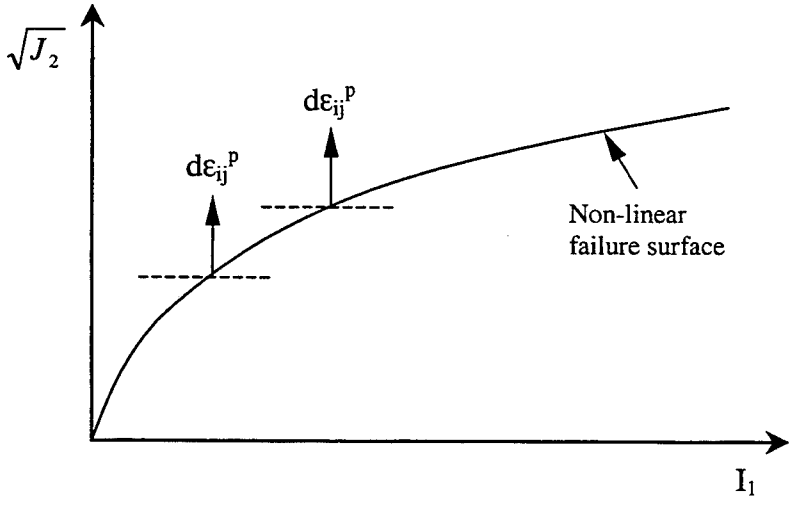

Figure 5.20 Non-linear failure surface with non-associated flow rule.

The consistency condition of (5.27) has already been discussed in Chapter 4 and is one of the conditions required for perfectly plastic behavior. From the flow rule given by (4.66) and (4.67), the stress increment $d\sigma_{ij}$ with Hooke's law can be written as:

$$d\sigma_{ij} = C_{ijkl}(d\varepsilon_{kl} - d\varepsilon_{kl}^{\ p}) \tag{5.28}$$

Thus,

$$d\sigma_{ij} = C_{ijkl}d\varepsilon_{kl} - \lambda C_{ijkl}\frac{\partial \Omega}{\partial \sigma_{kl}} \tag{5.29}$$

in which C_{ijkl} = elastic moduli matrix; $d\varepsilon_{kl}$ and $d\varepsilon_{kl}^{p}$ = total and plastic strain increment; and Ω = Von-Mises plastic potential function. Plugging (5.29) into (5.27), λ is obtained as:

$$\lambda = \frac{\dfrac{\partial F}{\partial \sigma_{ij}} C_{ijkl} d\varepsilon_{kl}}{\dfrac{\partial F}{\partial \sigma_{rs}} C_{rstu} \dfrac{\partial \Omega}{\partial \sigma_{tu}}} \tag{5.30}$$

Equation (5.30) indicates that, for a given material with a failure surface F and strain increment $d\varepsilon_{ij}$, the factor λ can be uniquely determined through (5.30). Substituting (5.30) into (5.29), the incremental stress-strain relationship is expressed as a form of:

$$d\sigma_{ij} = [C_{ijkl} - \frac{C_{ijmn}\dfrac{\partial \Omega}{\partial \sigma_{mn}}\dfrac{\partial F}{\partial \sigma_{pq}} C_{pqkl}}{\dfrac{\partial F}{\partial \sigma_{rs}} C_{rstu} \dfrac{\partial \Omega}{\partial \sigma_{tu}}}]d\varepsilon_{kl} \tag{5.31}$$

All indicies in (5.31) are based on index notation as used in Chapter 4. The stress-strain relationship in a plastic state can then be defined using (5.31). The coefficient tensor of (5.31) represents the elastic-plastic tensor of tangent modulus:

$$C_{ijkl}^{ep} = C_{ijkl} - \frac{C_{ijmn}\frac{\partial \Omega}{\partial \sigma_{mn}}\frac{\partial F}{\partial \sigma_{pq}}C_{pqkl}}{\frac{\partial F}{\partial \sigma_{rs}}C_{rstu}\frac{\partial \Omega}{\partial \sigma_{tu}}} \tag{5.32}$$

Since the function Ω and F are expressed in terms of the stress invariants, the following relationships can be obtained:

$$\frac{\partial \Omega}{\partial \sigma_{mn}} = \frac{\partial \Omega}{\partial I_1}\frac{\partial I_1}{\partial \sigma_{mn}} + \frac{\partial \Omega}{\partial J_2}\frac{\partial J_2}{\partial \sigma_{mn}} + \frac{\partial \Omega}{\partial J_3}\frac{\partial J_3}{\partial \sigma_{mn}} \tag{5.33}$$

and

$$\frac{\partial F}{\partial \sigma_{pq}} = \frac{\partial F}{\partial I_1}\frac{\partial I_1}{\partial \sigma_{pq}} + \frac{\partial F}{\partial J_2}\frac{\partial J_2}{\partial \sigma_{pq}} + \frac{\partial F}{\partial J_3}\frac{\partial J_3}{\partial \sigma_{pq}} \tag{5.34}$$

in which I_1 = the first invariant of stress tensor; and J_2 and J_3 = the second and third invariants of the deviatoric stress tensor. In (5.33) and (5.34), the derivatives of the stress invariants are written as:

$$\frac{\partial I_1}{\partial \sigma_{ij}} = \delta_{ij} \tag{5.35}$$

$$\frac{\partial J_2}{\partial \sigma_{ij}} = S_{ij} \tag{5.36}$$

$$\frac{\partial J_3}{\partial \sigma_{ij}} = S_{ik}S_{kj} - \frac{2}{3}J_2\delta_{ij} \tag{5.37}$$

where δ_{ij} = Kronecker delta; and S_{ij} = deviatoric stress tensor. From (5.22) and (5.26), the derivatives of the functions Ω and F with the stress invariants, which appear in (5.33) and (5.34), can be obtained as follows:

$$\frac{\partial \Omega}{\partial I_1} = 0 \tag{5.38}$$

$$\frac{\partial \Omega}{\partial J_2} = \frac{1}{2\sqrt{J_2}} \tag{5.39}$$

$$\frac{\partial \Omega}{\partial J_3} = 0 \tag{5.40}$$

and

$$\frac{\partial F}{\partial I_1} = -\alpha \tag{5.41}$$

$$\frac{\partial F}{\partial J_2} = \frac{1}{2\sqrt{J_2}} \tag{5.42}$$

$$\frac{\partial F}{\partial J_3} = 0 \tag{5.43}$$

Then, (5.33) and (5.34) are rewritten as:

$$\frac{\partial \Omega}{\partial \sigma_{mn}} = \frac{1}{2\sqrt{J_2}} S_{mn} \tag{5.44}$$

and

$$\frac{\partial F}{\partial \sigma_{pq}} = \frac{1}{2\sqrt{J_2}} S_{pq} - \alpha \delta_{pq} \tag{5.45}$$

Now the elastic-plastic tangent modulus matrix of (5.32) can be given more explicitly by:

$$C_{ijkl}^{ep} = C_{ijkl} - \frac{C_{ijmn}(\frac{1}{2\sqrt{J_2}}S_{mn})(\frac{1}{2\sqrt{J_2}}S_{pq} - \alpha\delta_{pq})C_{pqkl}}{(\frac{1}{2\sqrt{J_2}}S_{rs} - \alpha\delta_{rs})C_{rstu}(\frac{1}{2\sqrt{J_2}}S_{tu})} \tag{5.46}$$

As a result, the incremental stress-strain relationship for the plastic state is obtained as:

$$d\sigma_{ij} = C_{ijkl}^{ep} d\varepsilon_{kl} \tag{5.47}$$

And the plastic strain component can be expressed as:

$$d\varepsilon_{ij}^{p} = \lambda(\frac{S_{ij}}{2\sqrt{J_2}} - \alpha\delta_{ij}) \tag{5.48}$$

in which λ is given by (5.30).

5.6 Summary

The conventional hyperbolic stress-strain relationship is based on plane-strain analyses which may be used for two-dimensional stress states. Vertical loading of either a pile in the free field or a circular plate within a calibration chamber is an axi-symmetric problem. Although the analysis of such problem is much simpler than that of ordinary three-dimensional problems, it still requires the definition of stress states in three dimensions, including vertical, radial, and tangential stresses. In that sense, an axi-symmetric problem is certainly different from the plane-strain condition, which is suitable to treatment using two-dimensional stress-strain relationships and failure criteria.

In this chapter, the non-linear elastic-plastic soil model for three dimensions was presented. This soil model takes advantage of the intrinsic and state soil variables that

can be uniquely determined for a given soil type and condition. For the description of soil behavior before a failure condition is reached, the three-dimensional non-linear elastic model was developed based on the modified hyperbolic stress-strain relationship by Fahey and Carter (1993). This non-linear elastic model represents changes of elastic parameters (the shear modulus G and the bulk modulus K) according to the stress level. The stress invariants were used to represent the three-dimensional stress state. The expressions for the variation of shear modulus and bulk modulus according to the stress level are given by:

$$\frac{G_s}{G_o} = [1 - f(\frac{\sqrt{J_2} - \sqrt{J_{2o}}}{\sqrt{J_{2\max}} - \sqrt{J_{2o}}})^g](\frac{I_1}{I_{1o}})^{n_g}$$

and

$$K_t = D_s \cdot (\sigma'_m)^{n_k} (P_a)^{(1-n_k)}$$

The parameters f and g in (5.49) were determined from triaxial test results. From the measured modulus degradation curves, it is observed that the values of f and g vary according to the relative density level. As the relative density increases, the value of f decreases while the value of g increases.

In order to describe failure and post-failure soil response for the three-dimensional stress state, the Drucker-Prager plastic model with non-associate flow rule was adopted in this study. The Drucker-Prager failure criterion is given by:

$$F = \sqrt{J_2} - (\alpha I_1 + \kappa) = 0$$

where the parameters α and κ are related to the Mohr-Coulomb strength parameter c (which is zero for cohesionless soils) and ϕ obtained from the triaxial conditions. Because the peak friction angle for sand is not constant due to the dilatancy, the friction

parameter α was defined in terms of the dilatancy friction angle and the friction angle at critical state.

CHAPTER 6 NUMERICAL ANALYSIS AND EXPERIMENTAL INVESTIGATION OF CALIBRATION CHAMBER TESTS

6.1 Introduction

Calibration chamber tests have been used to investigate both the load-settlement response of the base of non-displacement piles and cone penetration resistance under a variety of conditions (Parkin 1991, Ghionna et al. 1994). Calibration chamber tests can be performed at any desired values of relative density and vertical and horizontal stresses under controlled conditions.

Based on the 3-D non-linear elastic-plastic stress-strain model presented in the previous chapter, calibration chamber tests are modeled and analyzed using the finite element approach. The analytical results will be compared with the measured values of plate resistance in calibration chamber plate load tests. The objective of this chapter is to verify the accuracy of the model predictions for plate resistance and assess calibration chamber size effects on plate resistance values.

6.2 Calibration Chamber Plate Load Tests

6.2.1 Description of test and experimental procedures

A calibration chamber plate load test can be used to simulate the axial loading of a non-displacement pile. In such a test, a cylindrical sand specimen is carefully prepared,

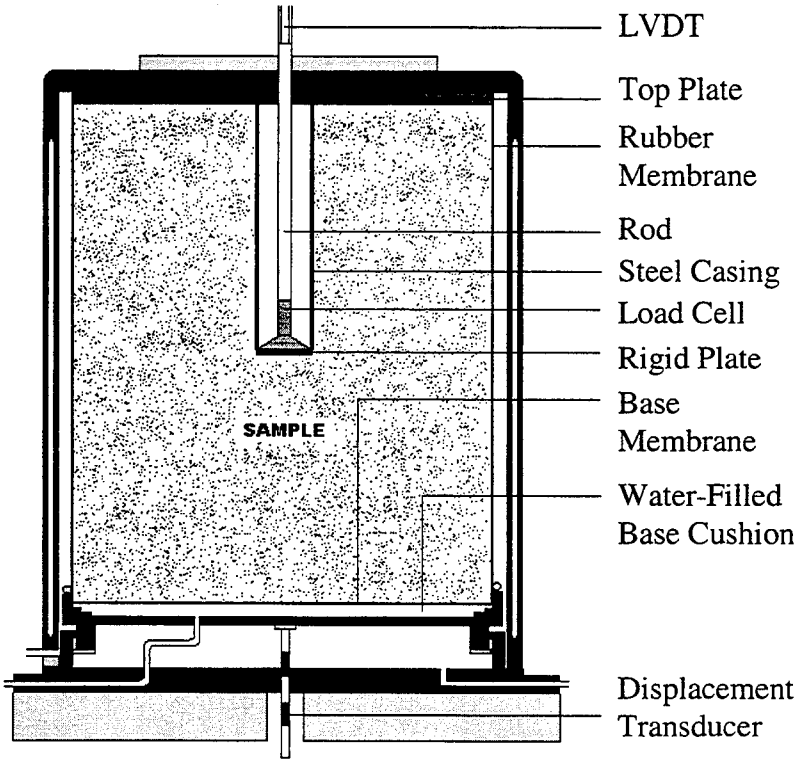

Figure 6.1 Plate load test in calibration chamber.

consolidated to a desired stress state, and tested (Salgado et al. 1998a,b, Lee and Salgado 1999a). In order to simulate the load-settlement response of the base of a non-displacement pile under a variety of conditions, plate load tests were performed within a flexible calibration chamber (Figure 6.1) with a diameter equal to 1.2 m and height equal to 1.5 m. The series of 30 tests was previously described by Ghionna et al. (1994), where details regarding the experimental procedures are discussed at length.

The test samples were formed by pluviation, which was interrupted when the surface of the sample reached mid-height, so that a rigid circular plate having a diameter of 104 mm could be positioned on top of the sample. After the plate connected to an inner rod was positioned, an outer casing with the same diameter as the plate was positioned above the plate and fixed to the calibration chamber. Sample pluviation was then continued outside the outer casing. A sample prepared in this manner simulates the conditions near the base of a non-displacement pile. Since the loading rod is separated from the soil by the outer casing, there is no side resistance along the push rod and the vertical load-displacement response of the plate simulates the load-displacement response of the base of a non-displacement pile.

After preparation is completed, the sample is consolidated under K_o-conditions. The relative density of each sample was controlled by the intensity of the sand flow during pluviation, and was accurately determined at the end of each test when the sample was disassembled. Both dense and medium-dense samples were tested. The test results are presented later.

6.2.2 Test material and boundary conditions for calibration chamber plate load tests

The sand used in the calibration chamber plate load tests was Ticino sand, a silica sand, whose properties are shown in Table 5.1. The relative densities used in the tests are divided typically into two different levels, medium dense and dense. The medium dense and dense samples represent the relative-density levels equal to around D_R = 50%

and $D_R = 90\%$, respectively. Both normally- and over-consolidated conditions were used in the tests. For over-consolidated soil samples, the over-consolidation ratio (OCR) were within the 2.73 – 7.61 range. The desired confining stress levels were established by applying separately the vertical and lateral boundary stresses on the sample surfaces. This allows different K_0 values. The vertical boundary stresses were in the 62 – 513 kPa range while the lateral boundary stresses were in the 25 – 235 kPa range. Accordingly, the value of K_0 used in the tests were in the 0.34 – 0.97 range. Table 6.1 shows the soil and stress conditions of the test samples used in calibration chamber plate load tests.

In calibration chamber tests, four different types of boundary conditions can be used. These boundary conditions include BC1, BC2, BC3, and BC4 conditions according to the types of boundary conditions imposed on the lateral, top and bottom chamber surfaces. Table 6.2 and Figure 6.2 illustrate the types of boundary conditions used in the calibration chamber plate load tests and how these boundary conditions differ from each other. Based on the lateral boundary conditions that has indeed significant influence on the plate resistance or cone penetration resistance, the boundary conditions can be classified into two categories, constant-stress and fixed boundary conditions. The constant-stress boundary conditions include BC1 and BC4 conditions while BC2 and BC3 conditions are categorized as the fixed boundary conditions.

It should be noticed that none of these boundary conditions perfectly reproduces the boundary conditions corresponding to real field situations. This is so because the calibration chamber used in a test has a limited size. The difference of results between calibration chamber tests and free-field tests would not exist if calibration chambers with infinite sizes were used. The other limitation is that BC2 and BC3 conditions are not as useful as BC1 and BC4 conditions (Salgado et al. 1998b). This is because achieving a true no-displacement condition for the lateral sample boundary is very difficult due to the characteristics of flexible chambers. The 30 calibration chamber plate load test by Ghionna et al. (1994) include 26 tests under BC1 condition, 1 test under BC2 conditions, 2 tests under BC3 conditions, and 1 test under BC4 conditions. The boundary conditions used in each calibration chamber test are shown in Table 6.1.

Table 6.1 Soil and stress conditions in calibration chamber tests.

Test No.	Boundary Condition	D_R (%)	σ'_v (kPa)	σ'_h (kPa)	K_0	OCR
300	BC1	51.0	115.0	51.0	0.443	1.00
301	BC1	92.0	115.0	40.0	0.347	1.00
302	BC1	50.4	113.0	51.0	0.451	2.73
303	BC1	55.2	313.0	140.0	0.447	1.00
304	BC1	55.2	214.0	92.0	0.429	1.00
305	BC1	58.4	512.0	223.0	0.435	1.00
306	BC1	49.4	116.0	76.0	0.655	2.70
307	BC1	92.8	314.0	123.0	0.391	1.00
308	BC1	92.5	216.0	85.0	0.393	1.00
309	BC1	92.5	115.0	77.0	0.669	2.73
310	BC1	90.9	66.0	25.0	0.378	1.00
311	BC1	91.7	63.0	25.0	0.396	1.00
312	BC1	55.5	513.0	235.0	0.458	1.00
313	BC1	51.7	62.0	26.0	0.419	1.00
314	BC1	49.1	54.0	52.0	0.962	7.61
315	BC1	43.5	410.0	189.0	0.460	1.00
316	BC1	56.8	512.0	184.0	0.359	1.00
317	BC1	55.2	62.0	24.4	0.393	1.00
318	BC1	59.0	216.0	92.0	0.425	1.00
319	BC1	58.0	65.0	53.0	0.815	6.34
320	BC1	59.3	63.0	50.0	0.793	6.54
321	BC1	60.2	412.0	177.0	0.429	1.00
322	BC1	92.2	314.0	129.0	0.410	1.00
323	BC1	92.0	66.0	64.0	0.969	6.27
324	BC1	91.2	66.0	27.0	0.409	1.00
325	BC3	91.4	116.0	47.0	0.405	1.00
326	BC3	91.2	65.0	25.0	0.384	1.00
327	BC2	90.9	65.0	26.0	0.400	1.00
328	BC4	90.9	65.0	26.0	0.400	1.00
329	BC1	90.6	65.0	26.0	0.400	1.00

Table 6.2 Boundary conditions in calibration chamber tests.

Boundary Condition	Lateral Boundary Condition	Top/Bottom Boundary Condition
BC1	Constant stress (σ_h = constant)	Constant stress (σ_v = constant)
BC2	No displacement ($u_h = 0^a$)	No displacement ($u_v = 0^b$)
BC3	No displacement ($u_h = 0$)	Constant stress (σ_v = constant)
BC4	Constant stress (σ_h = constant)	No displacment ($u_v = 0$)

[a] u_h represents horizontal displacement

[b] u_v represents vertical displacement

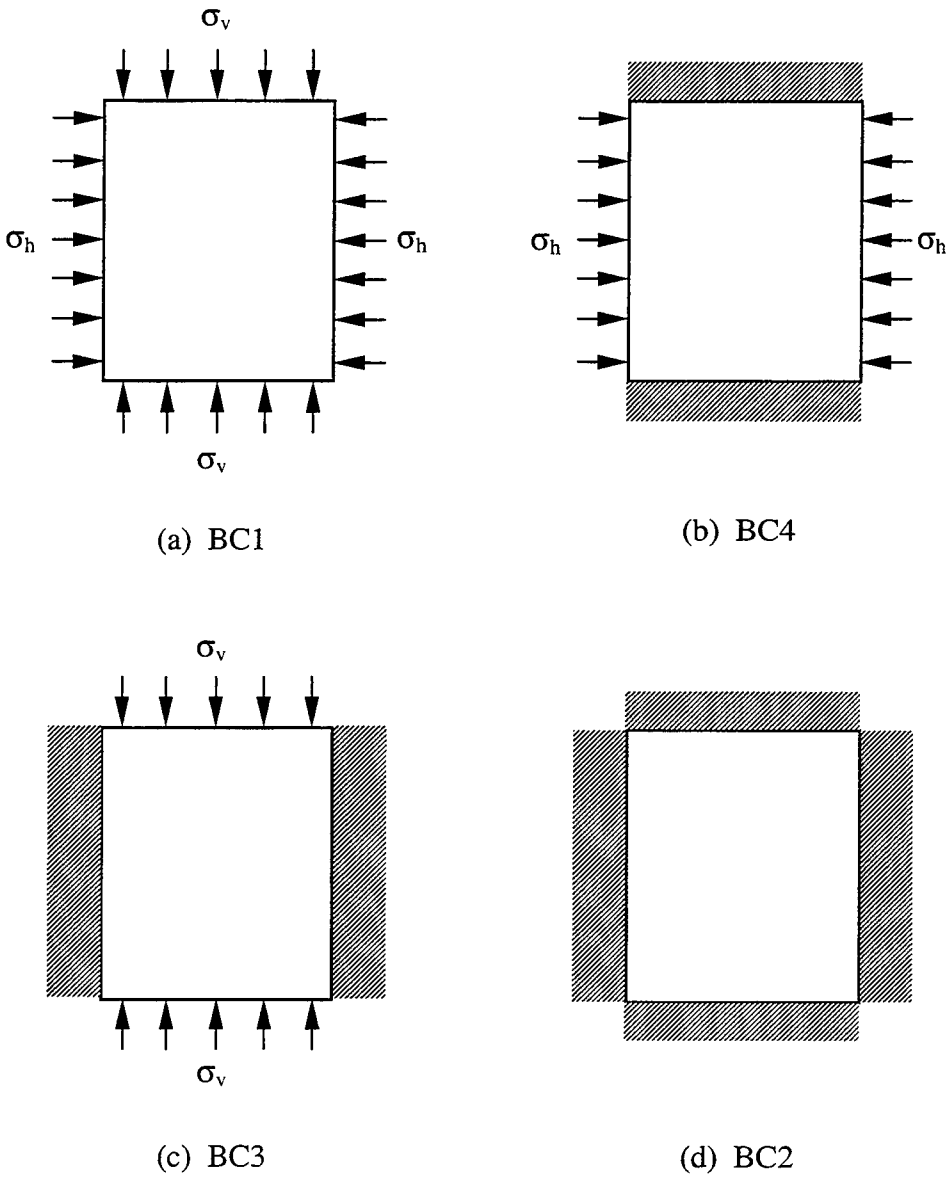

Figure 6.2 Types of boundary conditions in calibration chamber test.

6.3 Numerical Modeling of Plate Load Tests in Calibration Chambers

6.3.1 Program ABAQUS

Finite-element analysis of calibration chamber plate load tests or pile load tests in the free field requires an accurate model of the stress-strain relationship that can represent the complicated behavior of the soil around the rigid plate or pile base. The description of a stress-strain relationship for soils, therefore, must take into account the non-linear, stress-dependent stress-strain response before failure as well as the post-failure soil behavior with non-linear strength envelope.

The commercial finite-element program ABAQUS (Hibbitt, Karlsson & Sorensen, Inc., Pawtucket, R.I.) was used to model both the calibration chamber plate load tests and the axial loading of non-displacement piles. The program ABAQUS has been used to analyze many engineering problems. It provides a set of material models available for geotechnical problems and several types of elements. The analysis procedure is divided in two parts (Lee et al. 1999):

(1) interpretation of model information;
(2) implementation of history data.

Model information includes element types, material definitions, and boundary conditions, which are required in the analysis. The history data consist of analysis type and any control parameter necessary for a non-linear solution procedure. In most geotechnical problems, the initial condition is defined as a geostatic equilibrium state.

Instead of using the optional material model provided by the original program, a subroutine was written for the 3-D non-linear stress-strain relationship described in the previous chapter.

6.3.2 Finite element modeling of plate load test

The load-displacement curve for each calibration chamber plate load test was predicted numerically using the finite element method with the non-linear elastic plastic model discussed earlier. Figure 6.3 shows a typical finite element mesh used to model the plate load tests in calibration chamber. This finite element mesh was constructed using the same dimensions as those of the real calibration chamber having a diameter equal to 1.2 m and height equal to 1.5 m. The elements were eight-noded axisymmetric elements, necessary for modeling the three-dimensional loading conditions, with four internal integration points. In ABAQUS, the finite element model with axi-symmetric elements can be plotted using any visual angle desired. The finite element mesh shown in Figure 6.3 was plotted with a visual angle equal to 180° for better visualization.

The finite element model for the calibration chamber plate load test shown in Figure 6.3 consists of two different element groups, i.e. soil and casing elements. The soil elements were modeled using the 3-D non-linear stress-strain relationship written in a specific subroutine. Because the steel casing is relatively rigid compared to the soil, the casing elements were modeled as a linear elastic material with very high stiffness. The steel casing in the finite element model was set to be fixed allowing no displacement throughout the analysis, as that was how the actual tests were performed.

Since the axial load is applied only on the circular rigid-plate located at the middle of the calibration chamber, no significant friction between the soil and casing is expected to occur. However, in order to simulate the calibration chamber plate load test more realistically, thin-layer interface elements were used between the soil and casing elements. The thin-layer interface elements have zero initial thickness, and allow the relative movement of the soil and casing, i.e. slippage. The interface elements follow a Coulomb friction mechanism, where slippage takes place when the tangential stress exceeds a critical shear stress defined by a friction angle and normal stress acting on the surface between the casing and soil.

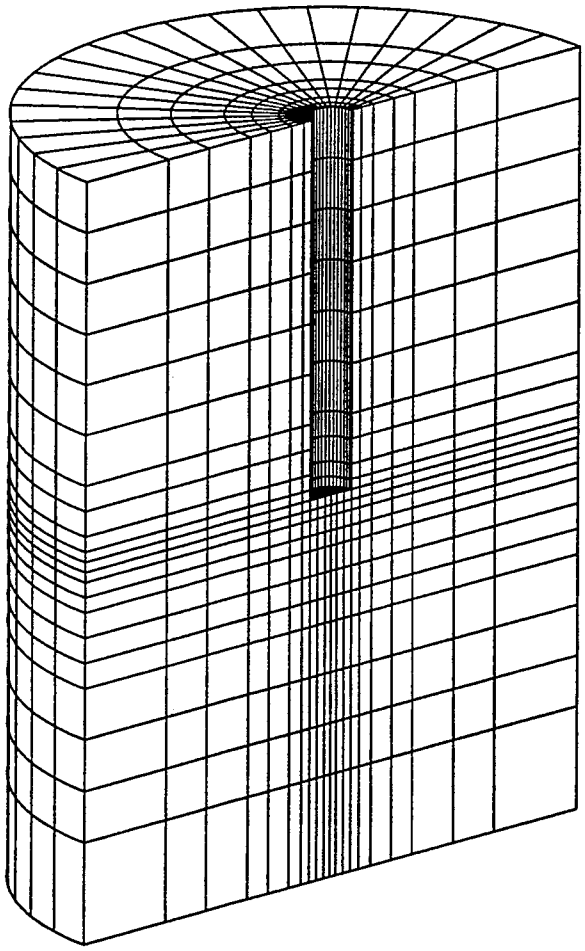

Figure 6.3 Finite element model for calibration chamber plate load test.

As discussed in the previous section, four different types of boundary conditions were used in the calibration chamber plate load tests. In the numerical modeling, the boundary conditions imposed on the finite element mesh were those actually imposed on the samples in the actual tests.

The values of the parameters f and g, which define the degradation of the elastic modulus, were $f \approx 0.97$ and $g \approx 0.20$ for $D_R = 50\%$ level, and $f \approx 0.95$ and $g \approx 0.26$ for $D_R = 90\%$ level, selected with basis on the values given in Table 5.3. The only other soil parameters required in the analyses were the intrinsic and state variables, which are given in Tables 5.1 and 6.1 (C_g, n_g, e_g, ϕ_c, e_{max}, e_{min}, e_o, σ'_v, σ'_h).

After defining all the required geometry information and material properties, the analysis is performed first by checking the initial geostatic equilibrium condition for a given boundary condition and stress state.

6.3.3 Predicted and measured plate resistance

Figures 6.4 - 6.7 show the graphical results of the numerical analyses for the calibration chamber plate load tests. All these results were obtained at the relative settlement (defined as the ratio of the vertical settlement to the plate or pile base diameter) equal to s/B = 10%. The displacement of the deformed finite element mesh shown in Figure 6.4 was exaggerated by a magnification factor equal to 5 for better visualization.

Figures 6.5 – 6.7 represent the vertical stress, vertical displacement, and lateral displacement distribution, respectively. From the distribution of stress and displacement, it can be seen that significant stress concentration and shear stress increases are observed near the plate edge. Consequently, it is also expected that the most significant reduction of shear modulus would occur near the plate edge.

Figure 6.8 shows the variation of secant shear modulus with horizontal and vertical distances from the plate for three different settlement levels. As can be seen in Figure

6.8 (a), the reduction of secant shear modulus at the level of the plate base is most severe near the plate edge due to high shear stresses there. The shear modulus of the soil immediately below the center of the plate undergoes rather slow degradation, as the stress state is dominated by the increase of confinement rather than the increase of shear stress. Such a slow reduction of shear modulus underneath the plate is in agreement with the observation of the formation of an "elastic core" beneath the base of axially loaded piles (BCP 1971; Salgado et al. 1997*a*). Figure 6.8 (b) shows the degradation of the secant shear modulus with depth along the plate axis. At the early stages of loading (e.g. curve 1), the shear modulus initially decreases with depth down to a depth of around 10 cm (equal to the plate diameter), and then increases again. For higher loads, similar reductions can be seen down to the depth of 10 cm below the plate, but this time no increase of shear modulus is observed below that depth, due to the expansion of the shear zones (curve 2, 3). Similar observations of modulus reduction with depth from the analyses of footings were noted by Fahey et al. (1994).

Figures 6.9 – 6.16 show the measured and predicted load-settlement curves of the calibration chamber plate load tests. The curves extend up to a settlement of approximately 10 mm, corresponding to a relative settlement level equal to s/B = 10%. The predicted load-settlement curves obtained by the finite element analyses compare favorably with the measured responses in most of the cases.

Figure 6.17 shows measured versus predicted plate unit load at the relative settlement levels equal to s/B = 5 and 10% for all calibration chamber tests. Overall agreement is very satisfactory, showing a maximum error of about 20%. There is a slight underestimation of plate resistance for dense sand. This may be due to differences between the dilational response of sand under triaxial loading conditions (from which f and g were obtained) and plate load test loading conditions.

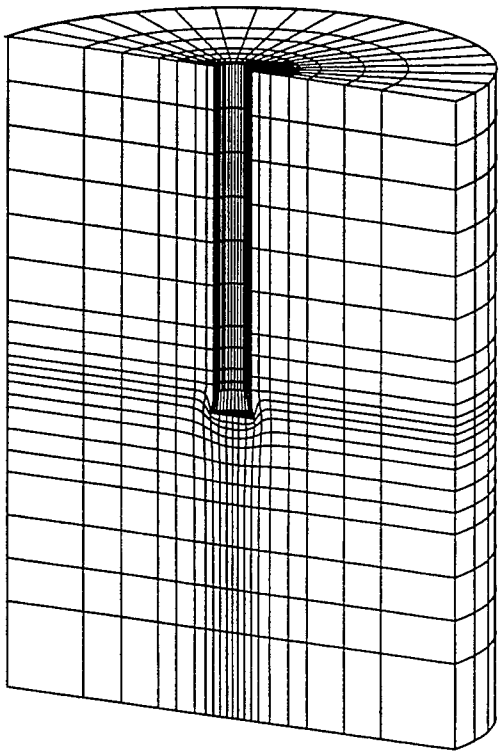

Figure 6.4 Deformed finite element mesh of calibration chamber plate load test with D_R = 55.2% , σ'_v = 62.0 kPa, and σ'_h = 24.4 kPa at s/B = 10%.

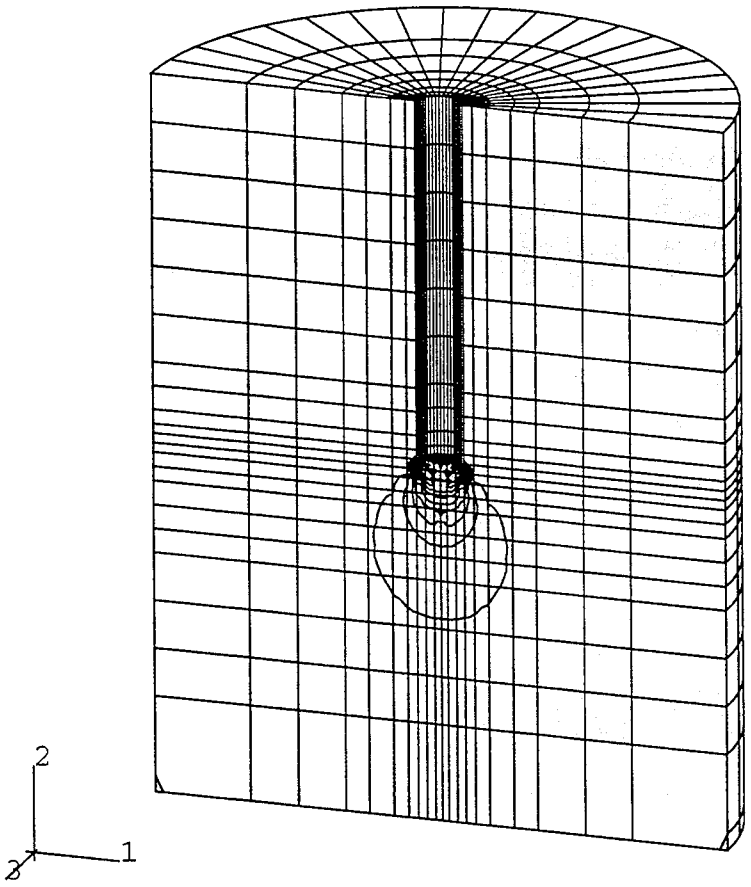

Figure 6.5 Vertical stress distribution in calibration chamber plate load test with D_R = 55.2% , σ'_v = 62.0 kPa, and σ'_h = 24.4 kPa at s/B = 10%.

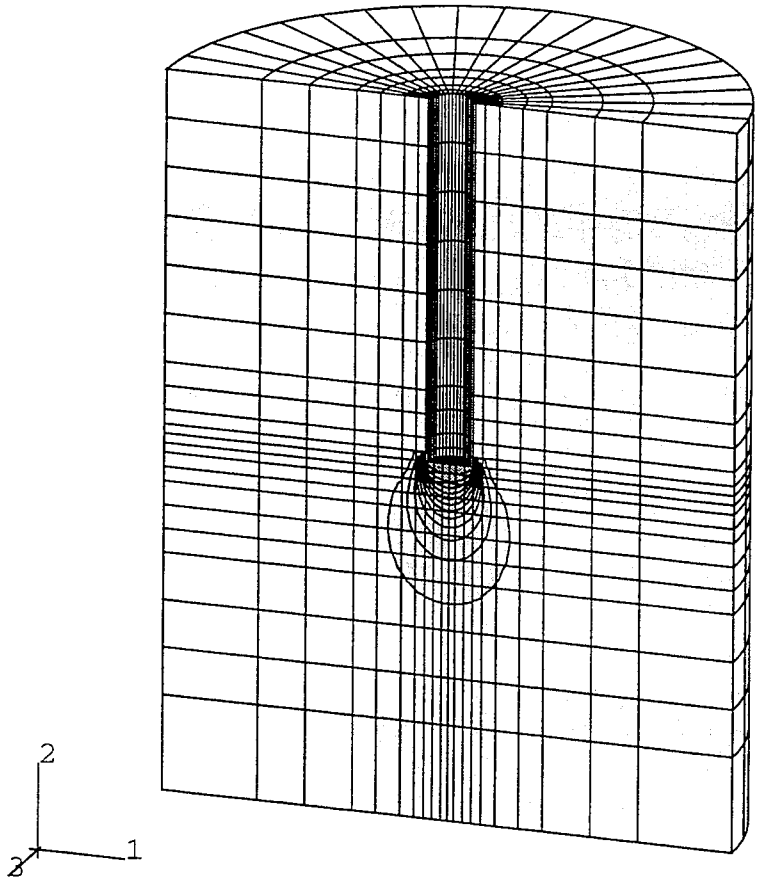

Figure 6.6 Vertical displacement distribution in calibration chamber plate load test with D_R = 55.2% , σ'_v = 62.0 kPa, and σ'_h = 24.4 kPa at s/B = 10%.

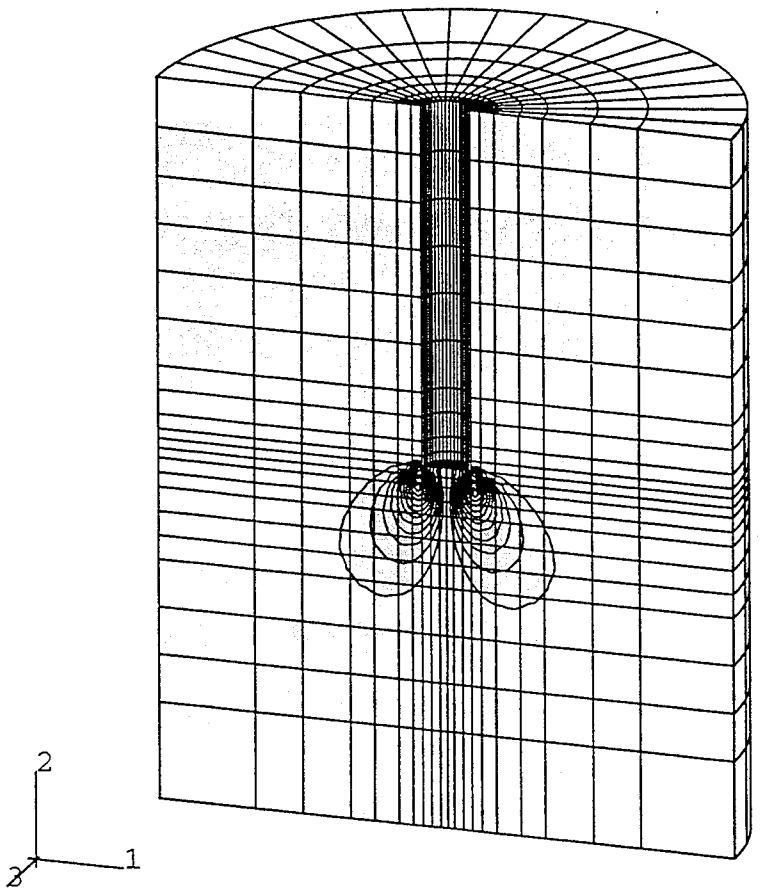

Figure 6.7 Horizontal displacement distribution in calibration chamber plate load test with D_R = 55.2% , σ'_v = 62.0 kPa, and σ'_h = 24.4 kPa at s/B = 10%.

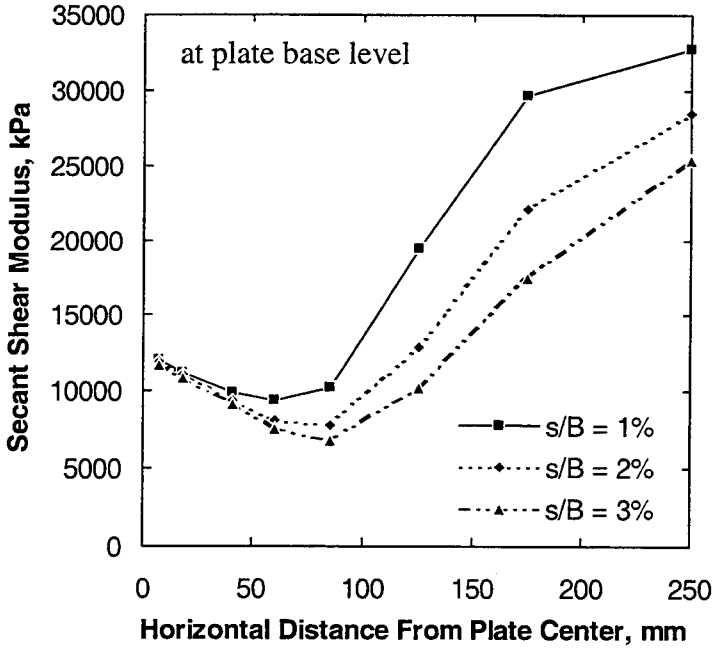

(a) at the pile base level

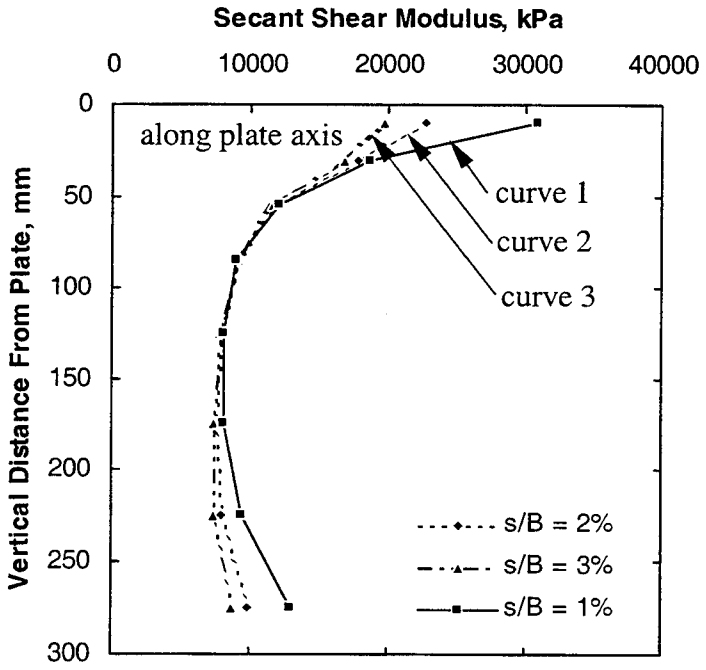

(b) along the plate axis

Figure 6.8 Variation of shear modulus.

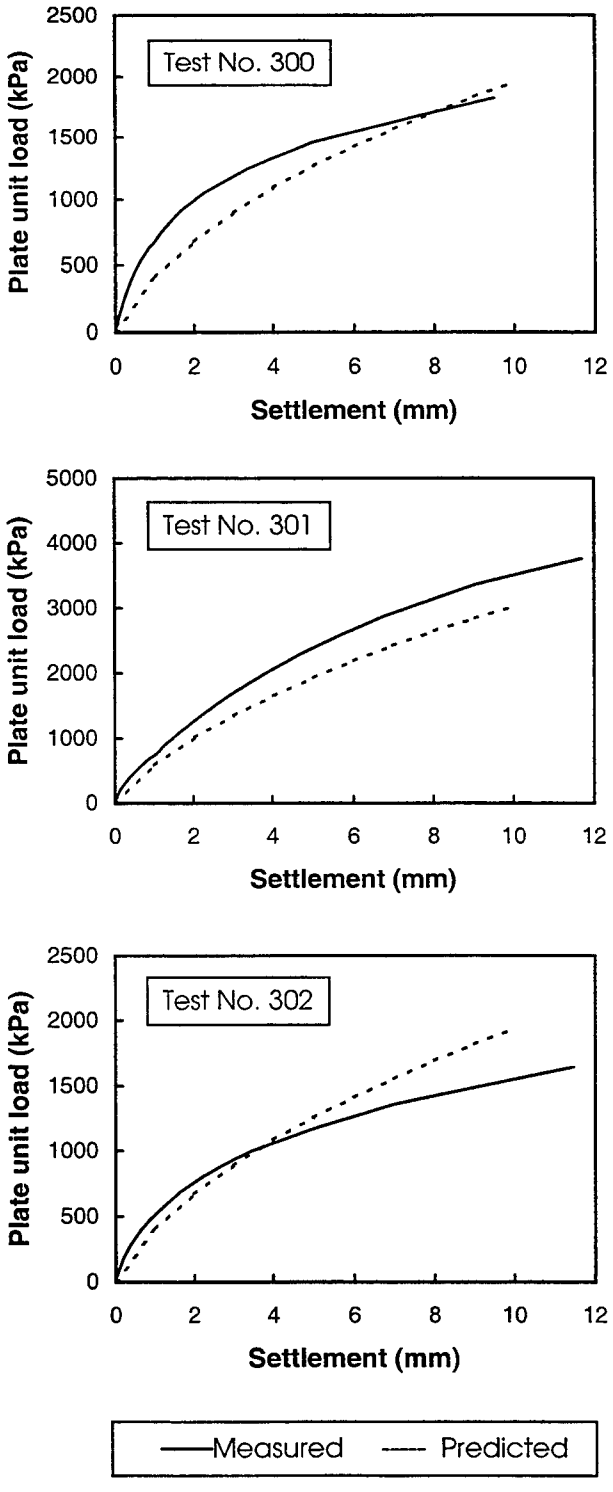

Figure 6.9 Load-settlement curves for calibration chamber plate load tests (Test No. 300, 301 and 302).

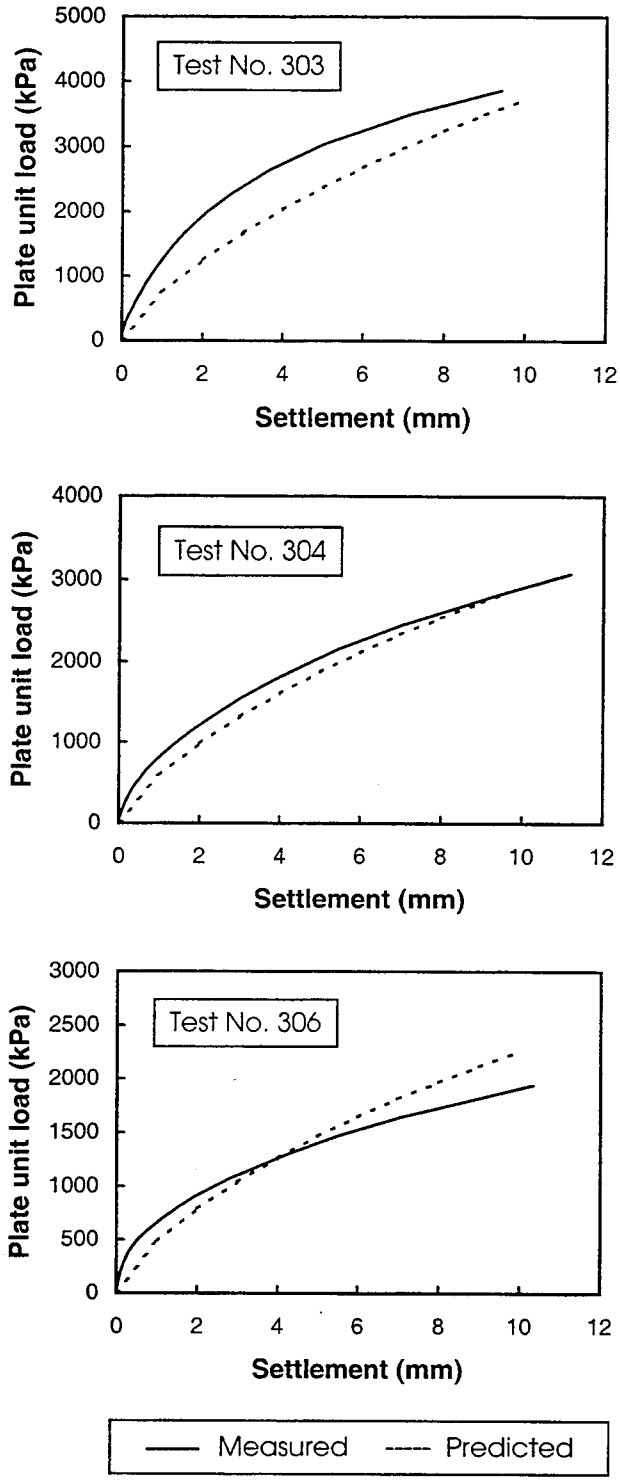

Figure 6.10 Load-settlement curves for calibration chamber plate load tests (Test No. 303, 304, and 306).

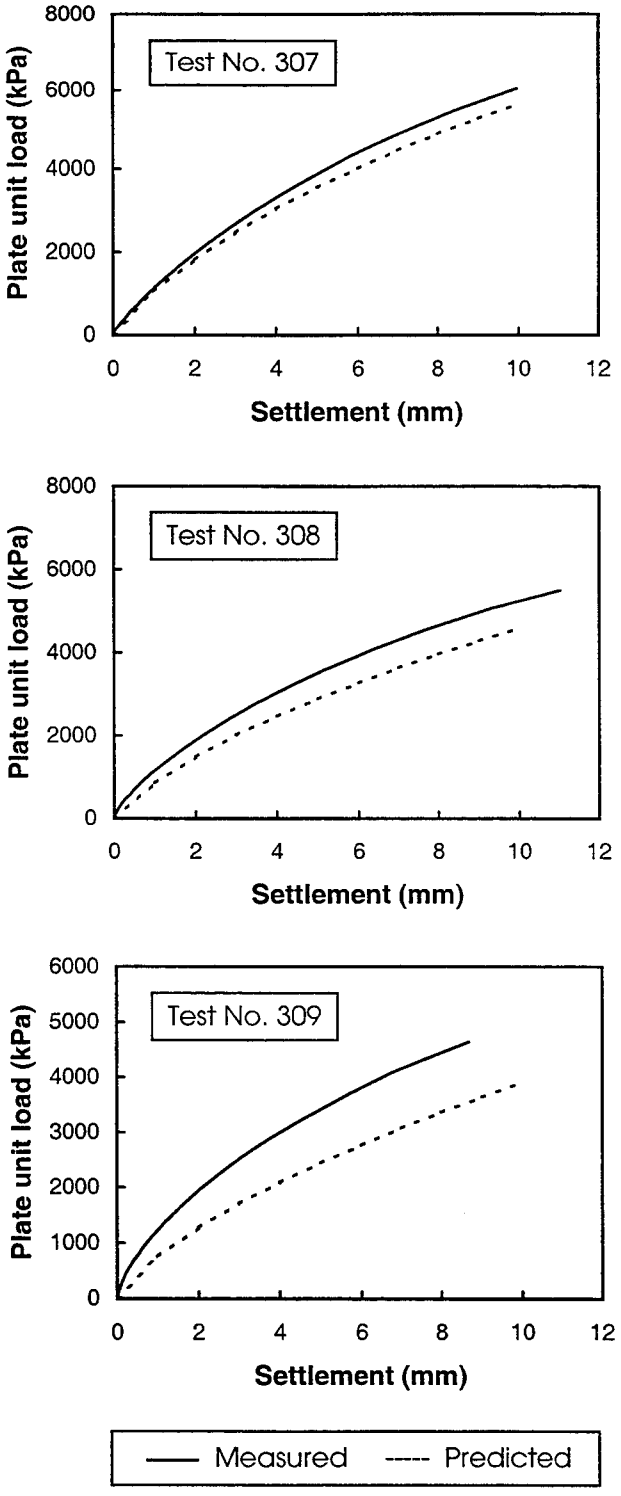

Figure 6.11 Load-settlement curves for calibration chamber plate load tests (Test No. 307, 308 and 309).

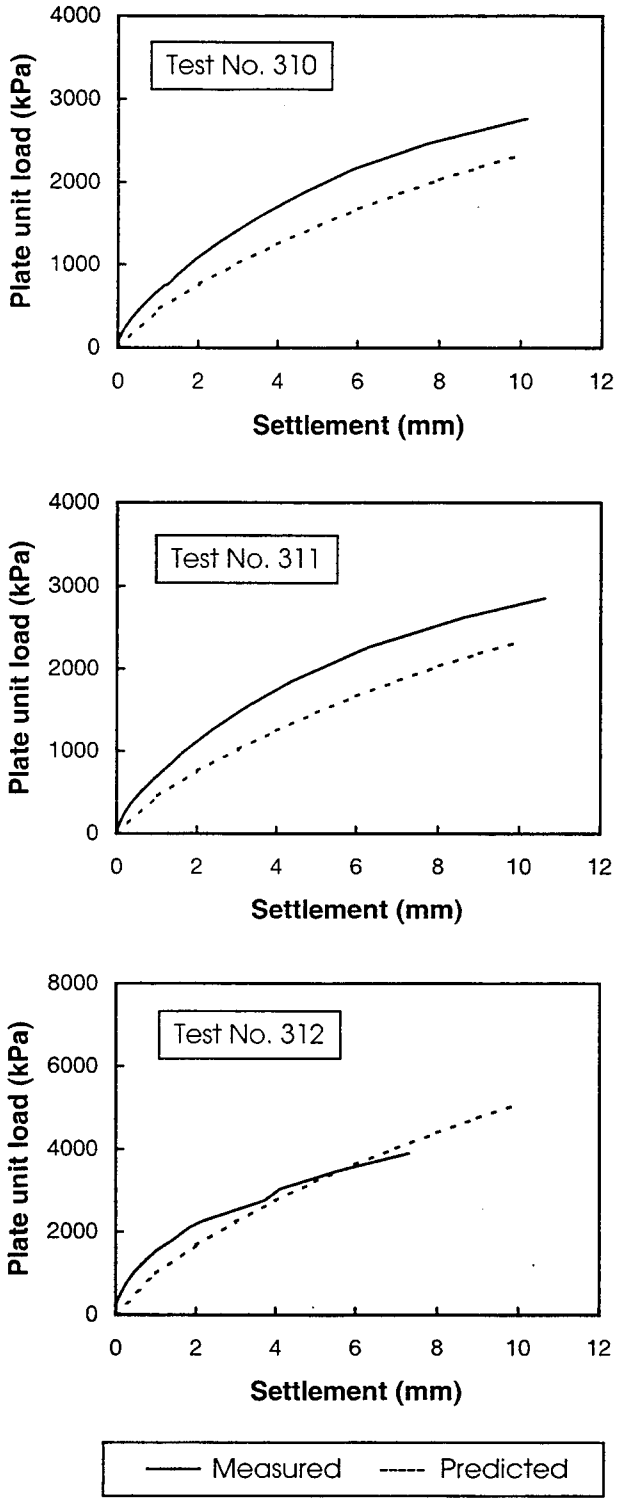

Figure 6.12 Load-settlement curves for calibration chamber plate load tests (Test No. 310, 311 and 312).

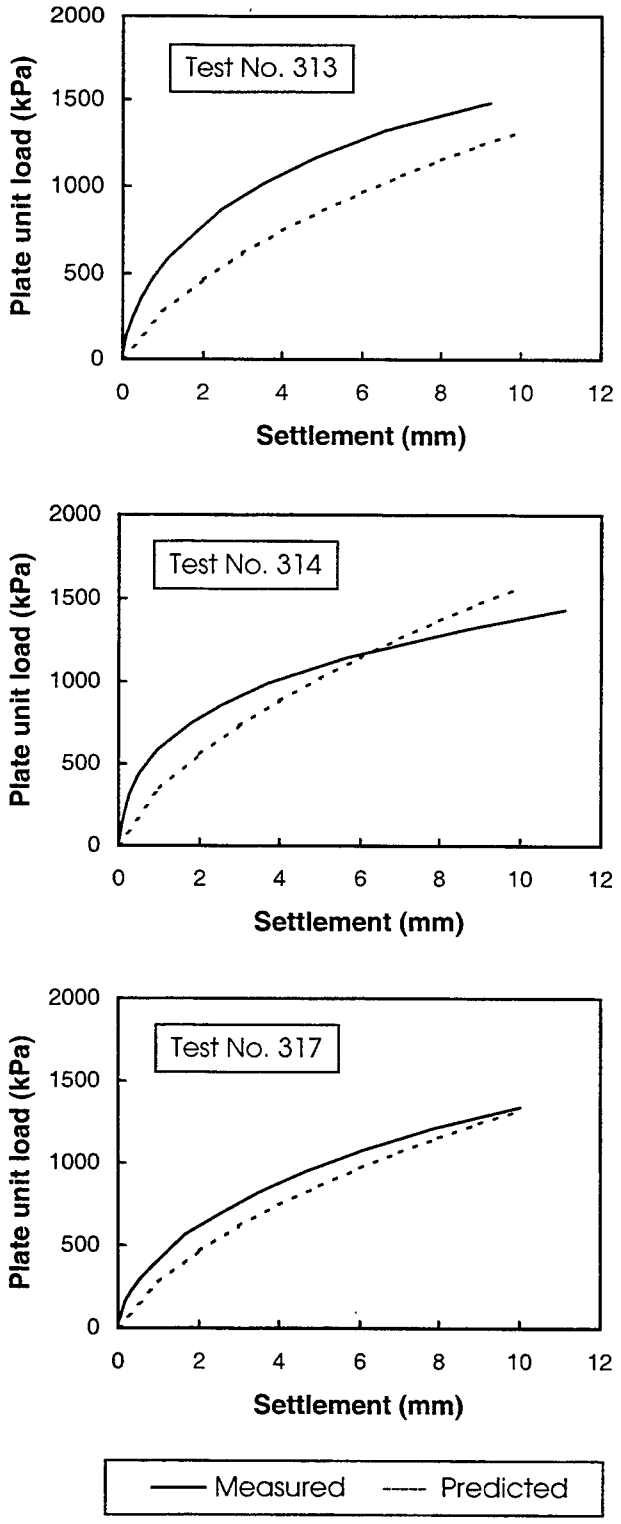

Figure 6.13 Load-settlement curves for calibration chamber plate load tests (Test No. 313, 314 and 317).

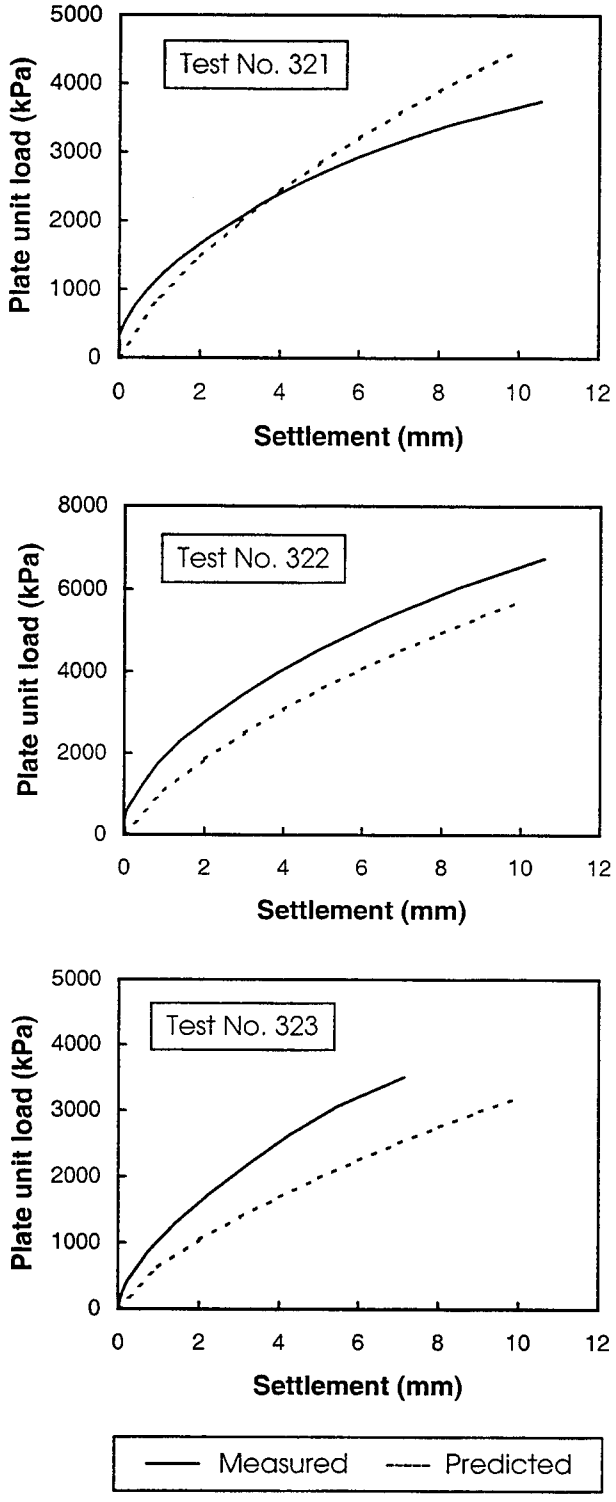

Figure 6.14 Load-settlement curves for calibration chamber plate load tests (Test No. 321, 322 and 323).

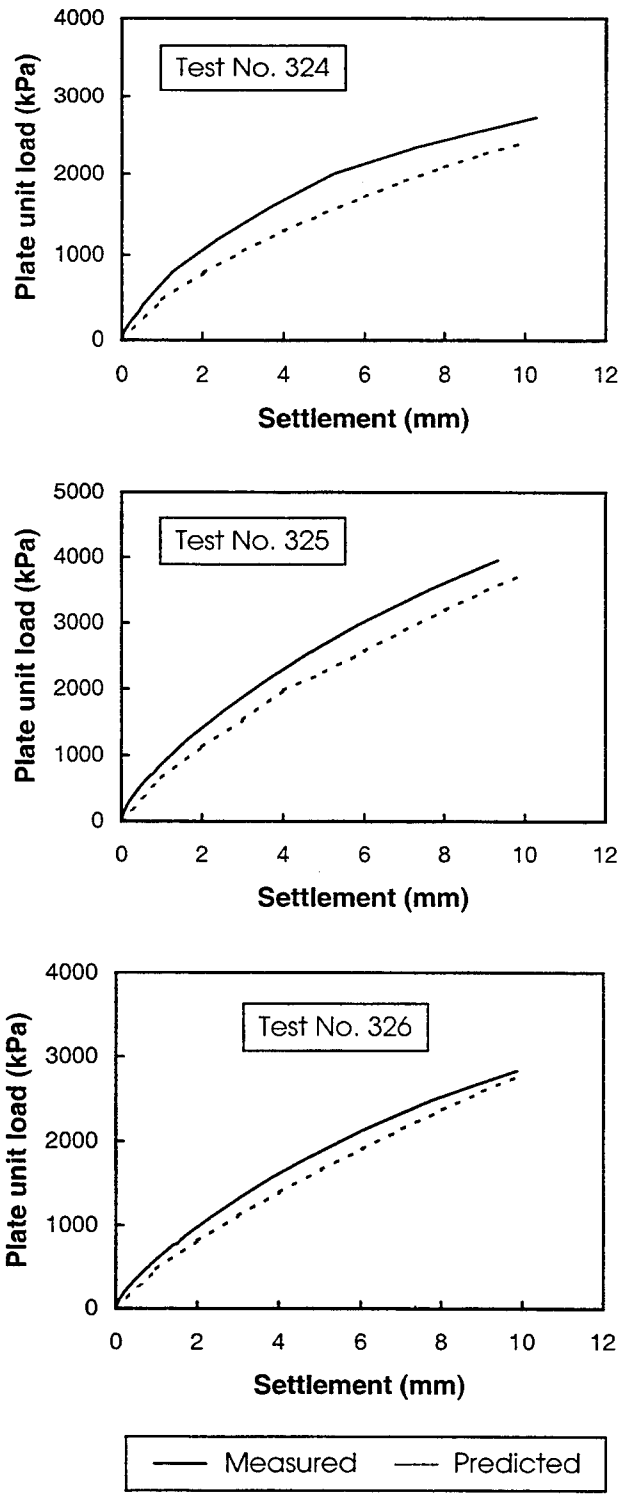

Figure 6.15 Load-settlement curves for calibration chamber plate load tests (Test No. 324, 325 and 326).

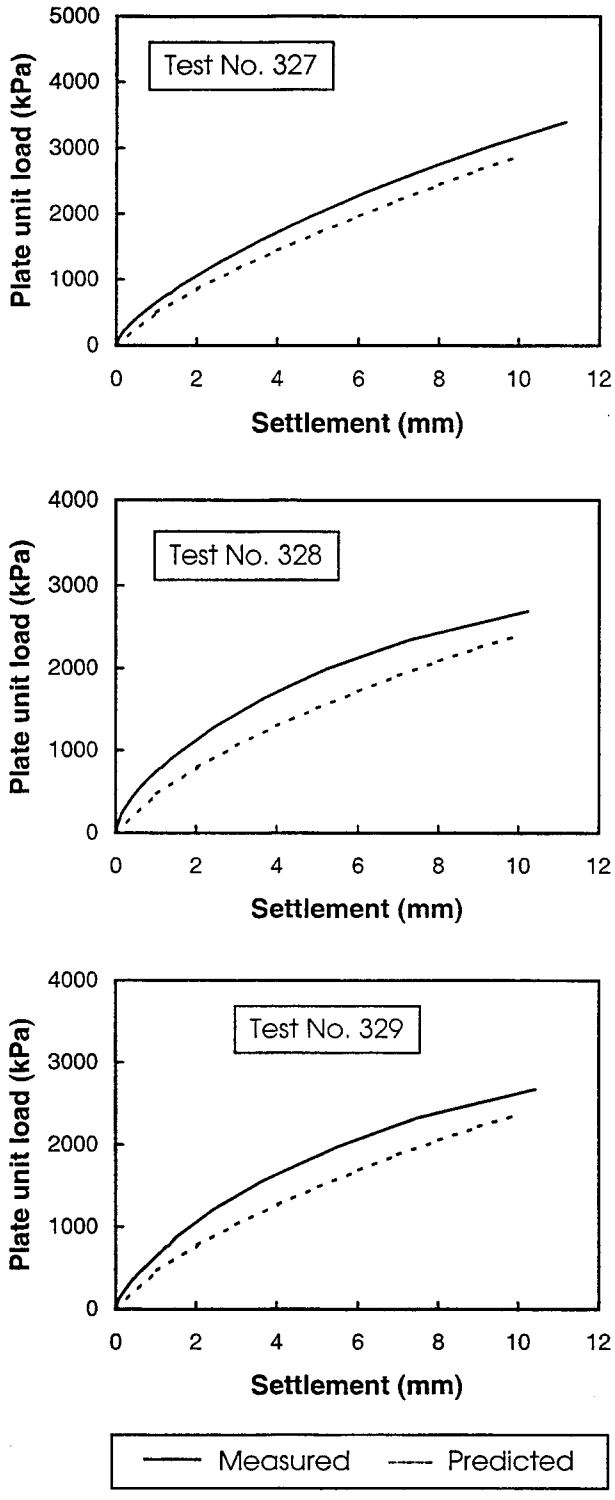

Figure 6.16 Load-settlement curves for calibration chamber plate load tests (Test No. 327, 328 and 329).

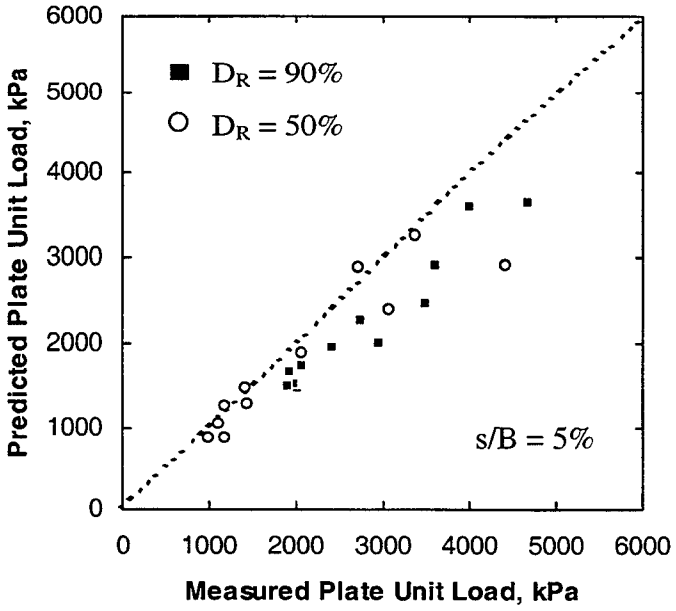

(a) s/B = 5%

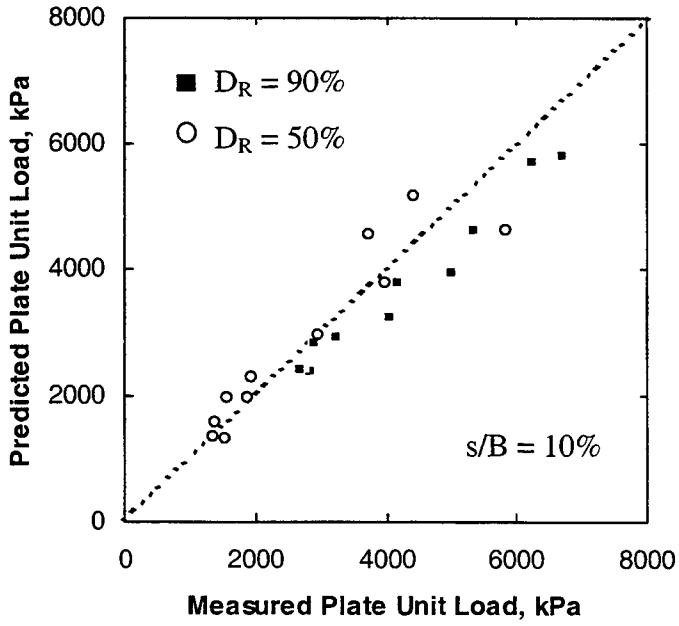

(b) s/B = 10%

Figure 6.17 Measured and predicted plate unit loads in calibration chamber tests.

6.4 Calibration Chamber Size Effects on Plate Load Test Results

6.4.1 Definition of size effect

Because of their finite size, calibration chambers do not perfectly reproduce free-field conditions. As a result, measurements made in a calibration chamber sand specimen are different from what would be observed in the field for the same relative density and stress state. These difficulties tend to be more pronounced, the smaller the chamber; hence the term *size effect.*

Calibration chamber size effects have been extensively studied in connection with cone penetration testing, where large deformations take place (e.g., Schnaid and Houlsby 1991; Mayne and Kulhawy 1991; Salgado et al. 1998a), but not with respect to plate load testing. It has been determined that size effects in calibration chambers are more significant in dense sands than in loose sands. In plate load testing, the displacements induced in the sand specimen are much less than those caused by cone penetration. On the other hand, the plate diameter used in the study (100 mm) is much larger than typical cone diameters (most commonly 35.7 mm).

For the results of calibration chamber tests to be effectively applied to pile design, the possible size effect should be properly addressed. If size effects are well understood, calibration chambers can be used to experimentally assess pile base resistance under controlled conditions.

6.4.2 Investigation of size effects for different boundary conditions

In order to investigate size effects in calibration chamber plate load tests, numerical analyses of both full-scale non-displacement piles and calibration chamber plate tests were performed. For studying the loading of non-displacement piles, three 60-cm diameter piles with lengths L = 5 m, 10 m and 20 m were analyzed. The corresponding

ratios L/B of the length L to the diameter B were equal to approximately 8, 16 and 33, respectively. The piles were positioned within a granular soil deposit with assumed values of D_R = 30, 50, 70 and 90%. The initial vertical and lateral effective stresses at the pile base level for each pile length are as follows:

(1) $\sigma'_v = 100$ kPa and $\sigma'_h = 43$ kPa for the 5-m pile

(2) $\sigma'_v = 200$ kPa and $\sigma'_h = 86$ kPa for the 10-m pile

(3) $\sigma'_v = 400$ kPa and $\sigma'_h = 172$ kPa for the 20-m pile.

All of these states correspond to a normally consolidated condition. Plate load tests in a calibration chamber were also simulated numerically for these same values of densities and stresses. Comparison of the base unit load in the full-scale pile load tests with plate unit load in the calibration chamber tests for the same relative settlement level provides the basis for conclusions regarding size effects. The sand adopted was Ticino sand, whose properties were discussed previously.

The comparison of pile load tests and chamber tests were made for all boundary conditions that were defined in Table 6.2 and Figure 6.2. Tables 6.3 - 6.6 and Fig. 6.18 show pile base unit loads versus plate unit loads in calibration chamber tests with BC1, BC2, BC3, and BC4 conditions for the relative settlement s/B equal to 10%. The size effect in Tables 6.3 - 6.6 was defined as a ratio of the calibration chamber plate resistance to the free-field pile base resistance.

In Figure 6.18, the different points for the same pile length represent the results for relative densities D_R = 30%, 50%, 70%, and 90%. As can be seen in Figure 6.18, the results for BC4 conditions were similar to those for BC1 conditions, and the results for BC3 conditions were similar to those for BC2. This illustrates that the lateral boundary condition has an overwhelming influence on plate unit load measured in a calibration chamber.

Table 6.3 Size effect in calibration chamber test for BC1 condition.

Pile Load Test			Calibration Chamber Test			Size Effect (%)
Pile length (m)	D_R (%)	q_b (kPa) (s/B = 10%)	σ'_v (kPa)	D_R (%)	q_b (kPa) (s/B = 10%)	
5	30	1516	100	30	1286	84.8
	50	2066		50	1762	85.3
	70	2794		70	2361	84.5
	90	3631		90	3087	85.0
10	30	2152	200	30	2018	93.8
	50	2933		50	2699	92.0
	70	3869		70	3528	91.2
	90	4959		90	4497	90.7
20	30	3112	400	30	3152	100.1
	50	4162		50	4120	98.9
	70	5404		70	5262	97.4
	90	6836		90	6623	96.7

Table 6.4 Size effect in calibration chamber test for BC2 condition.

Pile Load Test			Calibration Chamber Test			Size Effect (%)
Pile length (m)	D_R (%)	q_b (kPa) (s/B = 10%)	σ'_v (kPa)	D_R (%)	q_b (kPa) (s/B = 10%)	
5	30	1516	100	30	1555	102.6
	50	2066		50	2085	100.9
	70	2794		70	2772	99.2
	90	3631		90	3600	99.1
10	30	2152	200	30	2364	109.8
	50	2933		50	3108	105.9
	70	3869		70	4017	103.8
	90	4959		90	5119	103.2
20	30	3112	400	30	3591	115.3
	50	4162		50	4625	111.1
	70	5404		70	5854	108.3
	90	6836		90	7338	107.3

Table 6.5 Size effect in calibration chamber test for BC3 condition.

Pile Load Test			Calibration Chamber Test			Size Effect (%)
Pile length (m)	D_R (%)	q_b (kPa) (s/B = 10%)	σ'_v (kPa)	D_R (%)	q_b (kPa) (s/B = 10%)	
5	30	1516	100	30	1534	101.1
	50	2066		50	2053	99.3
	70	2794		70	2717	97.2
	90	3631		90	3521	96.9
10	30	2152	200	30	2333	108.4
	50	2933		50	3063	104.4
	70	3869		70	3945	101.9
	90	4959		90	5017	101.1
20	30	3112	400	30	3549	114.0
	50	4162		50	4564	109.7
	70	5404		70	5774	106.8
	90	6836		90	7213	105.5

Table 6.6 Size effect in calibration chamber test for BC4 condition.

Pile Load Test			Calibration Chamber Test			Size Effect (%)
Pile length (m)	D_R (%)	q_b (kPa) (s/B = 10%)	σ'_v (kPa)	D_R (%)	q_b (kPa) (s/B = 10%)	
5	30	1516	100	30	1348	88.9
	50	2066		50	1828	88.4
	70	2794		70	2422	86.7
	90	3631		90	3156	86.9
10	30	2152	200	30	2106	97.8
	50	2933		50	2789	95.1
	70	3869		70	3630	93.8
	90	4959		90	4602	92.8
20	30	3112	400	30	3272	105.1
	50	4162		50	4249	102.1
	70	5404		70	5402	99.9
	90	6836		90	6778	99.1

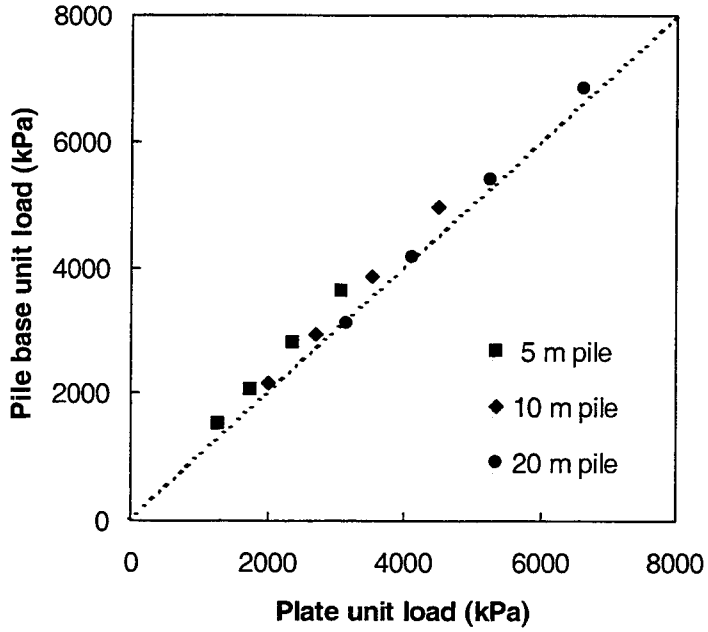

(a) BC1 conditions

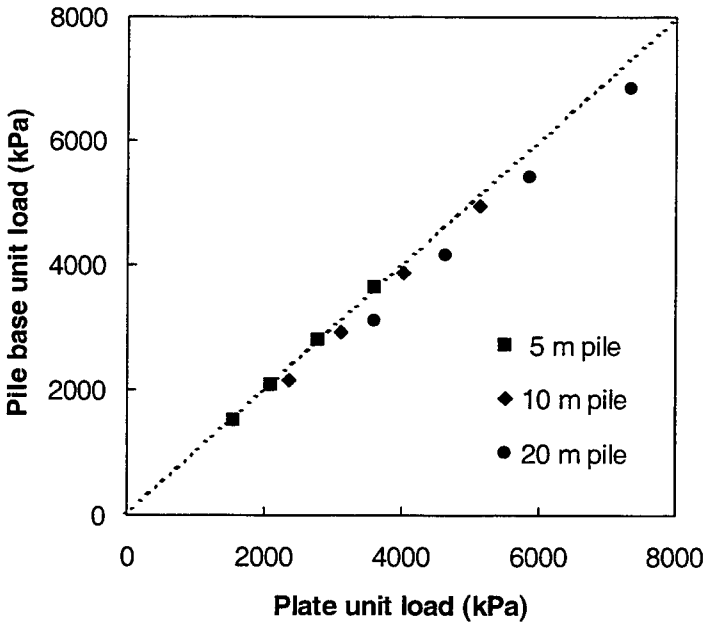

(b) BC2 conditions

Figure 6.18 Comparison of pile base unit load with plate unit load in calibration chamber plate load tests.

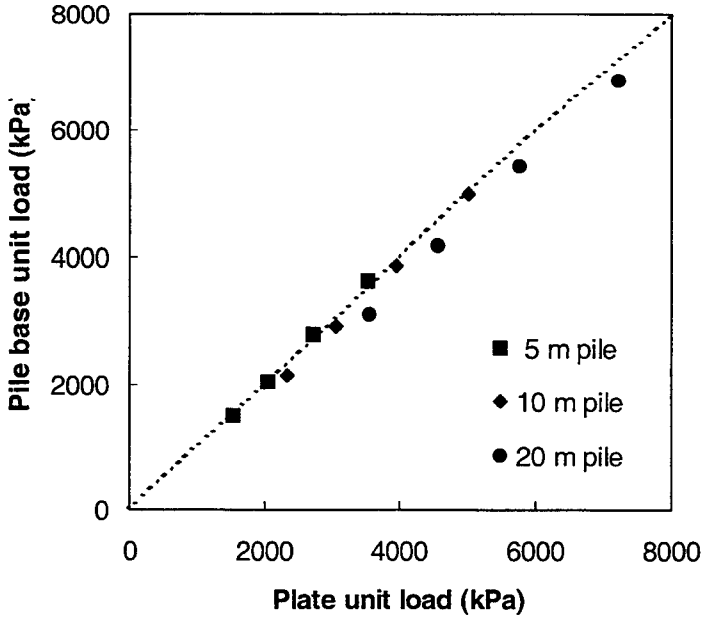

(c) BC3 conditions

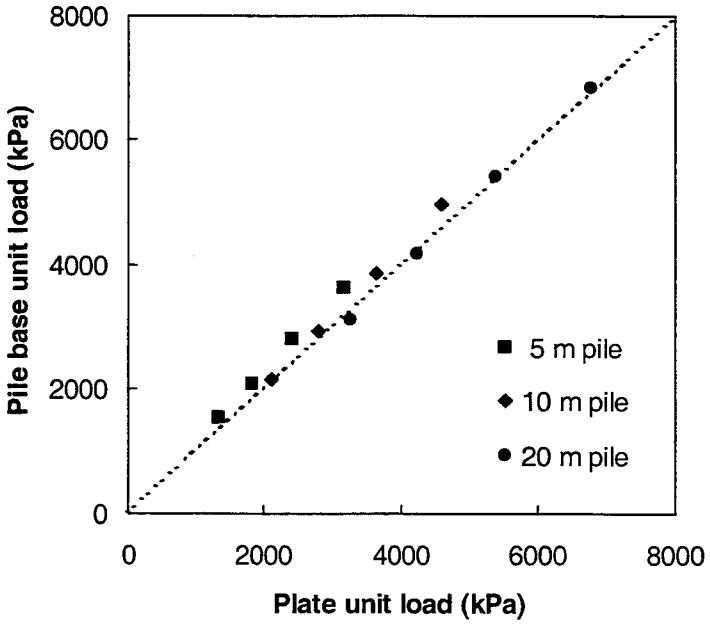

(d) BC4 conditions

Figure 6.18 Comparison of pile base unit load with plate unit load in calibration chamber plate load tests (continued).

Differences between pile base unit load and plate unit load were small for all relative density levels. It is observed, however, that the plate unit loads under BC1 conditions were smaller than the pile base unit loads, and more substantially so in the case of short piles, for which confinement is low at the level of the pile base. The differences between pile base unit load and plate unit load were around 14 to 15% for L = 5 m, 6 to 9% for L = 10 m, and 1 to 3% for L = 20 m.

The results for BC2 conditions, as shown in Figure 6.18 (b), differ from those for BC1 conditions in that the plate unit loads from the calibration chamber plate load tests were found to be greater than pile base unit load values under corresponding conditions. The differences were around 1 to 3% for L = 5 m, 3 to 9% for L = 10 m, and 7 to 15% for L = 20 m. This indicates that the differences are more significant for long piles, for which confinement is high at the pile base level.

6.5 Summary

Calibration chamber plate load tests have been used to investigate the base load-settlement relationship of non-displacement piles. In this chapter, the calibration chamber plate load tests were analyzed through the finite element method using the three-dimensional non-linear elastic-plastic model presented in the previous chapter. A series of calibration chamber tests performed by Ghionna et al. (1994) were modeled and compared with the results of finite element analyses. The predicted load-settlement curves showed good agreement with measured load-settlement curves. The comparison between computed and measured plate unit loads for the relative settlement of s/B = 5 and 10% was also made for both dense ($D_R \approx 90\%$) and medium dense ($D_R \approx 50\%$) sand. Predicted plate unit loads were in good agreement with measured results, showing relative errors not larger than about 20% at s/B = 10%.

Calibration chamber size effects, resulting from the finite size of the chamber, were also investigated for different relative densities and boundary conditions using finite

element analysis. The comparison was made between pile base unit load for piles loaded under field conditions and plate unit loads from the calibration chamber tests. The piles were modeled with three different pile lengths and four different relative densities. Plate unit loads in calibration chamber tests tend to be lower (for BC1, BC4) and higher (for BC2, BC3) than pile base unit loads. The confining stress level at the pile base level also influences size effect. The calibration chamber size effects under BC1 were more pronounced at low confinement, corresponding to shorter piles, while size effects under BC2 were more pronounced at high confinement, corresponding to longer piles. The magnitude of size effect is small, validating the use of chamber tests to simulate pile base loading. In keeping with the recommendation of Salgado et al. (1998b) regarding CPT testing in calibration chambers, it is recommended here that BC1 or BC4 be used in calibration chamber plate load testing. If this is done, our numerical results show that, for practical purposes, no correction is needed to the measured plate unit load in estimating pile base unit load, unless very short piles are being simulated.

CHAPTER 7 DETERMINATION OF PILE BASE RESISTANCE

7.1 Introduction

The standard penetration test (SPT) and the cone penetration test (CPT) are the two most popular methods for pile design using in-situ test results (Bandini and Salgado 1998). While the process followed to obtain SPT blow counts is not well related to the quasi-static pile loading process, that of the static cone penetration is better related to the pile loading process. The test is performed quasi-statically and resembles a scaled-down pile load test. According to many authors (e.g. De Beer 1984; Franke 1989,1993; Ghionna et al. 1993, 1994; Jamiolkowski and Lancellotta 1988; Fioravante et al. 1995), cone penetration resistance may be used as a proxy for limit base resistance in piles.

In this chapter, the base load-settlement curves of axially loaded piles bearing in sand are obtained for different stresses and densities using the finite element analysis with a non-linear elastic-plastic stress-strain model. Cone resistance q_c is determined for the same soil conditions from the penetration resistance analysis of Salgado et al. (1997a) using the program CONPOINT (Salgado 1993; Salgado et al. 1997a, b; Salgado et al. 1998a); q_c values determined in this manner are used to normalize the pile base load-settlement curves. The fully developed load-settlement curves in terms of q_b/q_c versus relative settlement s/B can be used to determine the normalized pile base resistance q_b/q_c for any settlement-based design criterion.

7.2 Methods for Investigating Load-Settlement Response

If a pile were continuously pushed down into a homogenous granular soil mass, it would eventually reach a condition of penetration at a constant load in the same way as a cone penetrometer does in a cone penetration test (CPT). This is a condition of limited interest in pile design, and nearly always impossible to establish with conventional load test procedures and equipment, unless the pile is relatively small in diameter and length, it is not bearing in a very strong soil layer, and the engineer specifically requires a plunging load test. Typical load-settlement curves for piles embedded in sand show gradually increasing curvature rather than a clear peak load.

Three approaches are possible to obtain the vertical load-settlement relationship for a pile. Those include full-scale pile load tests, calibration chamber tests and numerical modeling. Full-scale pile load tests are the best option to investigate the load-settlement relationship for a specific site and pile, but cannot typically be used to obtain an accurate correlation between base resistance and the soil state. Only fully instrumented load tests with significant efforts to characterize the soil around the pile could potentially be used for that purpose. Difficulties that would still need to be addressed include the fact that relative density and lateral stress are not known in the field, and that typical natural granular deposits tend to be variable (Lee and Salgado 1999b).

Calibration chamber testing and numerical analysis are more flexible than pile load testing. A variety of stress states, densities and boundary conditions can be considered. Calibration chamber plate load tests, as discussed in the previous chapter, have been used to investigate the load-settlement response of non-displacement piles (Ghionna et al. 1994, Lee and Salgado 1999a). A number of numerical techniques have been identified for the same purpose (Desai and Christian 1977, Lee et al. 1989, Poulos 1989). The finite element method is among the most popular, as it allows modeling of complicated non-linear soil behavior and various interface conditions, with different geometries and soil conditions (Lee and Salgado 1999c). A key element in a finite element analysis is the use of a relevant constitutive model, which should model the strongly non-linear soil behavior. In the present study, the non-linear elastic-plastic stress-strain presented in

chapter 5 is used in a finite element analysis to determine the load-settlement response of vertically loaded piles.

7.3 Finite Element Modeling of Pile Load Test

The commercial finite element program ABAQUS was used to model vertically loaded piles. The finite element modeling of pile load tests for obtaining load-settlement curves was done in the same way as used in the investigation of size effects in calibration chamber tests. Instead of using one of the material models available in the program, a subroutine was written for the non-linear elastic-plastic model described previously. Because the pile stiffness is very large compared to soil stiffness, the pile was assumed made of linear elastic material throughout the analysis. Eight-noded axisymmetric elements with four internal integration points were used to model both the soil and the pile. Thin layer interface elements with zero initial thickness, allowing slippage, were used between the pile and the soil. The necessity of interface elements in the analysis of axially loaded piles is discussed in Trochanis et al. (1991).

The analyses of the calibration chamber plate load tests in the previous chapter showed the validity of the proposed finite element analysis of the pile base load-settlement response in sand. In order to further assess the performance of the proposed finite element analysis, a pile load test performed by the Georgia Institute of Technology (Mayne and Harris 1993) was modeled, and the numerical and experimental results were compared. The test site has a layer of residual, silty silica sand extending down to 15.8 – 19.5 m underlain by partially-weathered rock down to 20 – 24.8 m and then sound bedrock. Grain size distribution analysis showed the soil to be composed of about 70% sand, with the clay fraction under 10%. A series of laboratory tests on the soil samples collected at several depths were performed to obtain basic soil properties. Table 7.1 shows the soil property profile with depth and layers used in the analysis.

Table 7.1 Basic soil properties used in finite element analysis.

Layer No.	Depth (m)	ϕ'	K_0	σ'_{vo} (kPa)	e_o	G_o (kPa)
1	0 – 1.82	34°	0.44	18.2	0.70	23642
2	1.82 – 3.93	34°	0.44	53.8	0.70	43838
3	3.93 – 5.93	37°	0.40	87.6	0.73	54056
4	5.93 – 7.93	33°	0.46	119.9	0.73	67081
5	7.93 – 9.93	32°	0.47	151.8	0.74	76051
6	9.93 – 11.93	32°	0.47	185.6	0.72	87849
7	11.93 – 13.93	36°	0.41	219.9	0.70	96102
8	13.93 – 14.93	38°	0.38	244.8	0.67	100472
9	14.93 – 16.76	36°	0.41	268.6	0.67	112540
10	16.76 – 18.28	36°	0.41	296.8	0.67	119145

The bottom boundary of the finite element mesh was located at a depth of 21.93 m from the surface, at which the bedrock was encountered. The last layer of the mesh from 18.28 m to 21.93 m was the partially weathered rock layer, which was assumed to behave as an elastic material. Values of initial shear modulus G_o for each soil layer were calculated based on Hardin and Black's equation for angular sand. According to the Hardin and Black equation and the observation made by Salgado et al. (1999) regarding changes in stiffness as a function of fines content, the values adopted for C_g, e_g and n_g were $C_g = 214$, $e_g = 2.97$ and $n_g = 0.5$.

The values of the model parameters f and g of the non-linear elastic plastic model were taken as 0.98 and 0.05 respectively, based on the observed non-linear elastic properties of silty sand (Salgado et al. 1999). The test drilled shaft had a diameter equal to 76 cm and a length equal to 16.8 m. Measured and predicted base load-settlement curves were plotted together in Figure 7.1. Overall, agreement is observed to be satisfactory.

7.4 Cone Penetration Resistance from Cavity Expansion Analysis

A number of methods have been proposed analytically and experimentally to correlate the cone penetration resistance q_c to stress state and soil conditions (Terzaghi 1943, Vesic 1972, Durgunoglu and Mitchell 1975, Baligh 1985, Yu and Houlby 1991, Salgado 1993, Salgado et al. 1997a). For undrained clay and fully drained sand, those are generally classified into (Yu and Mitchell 1998):

(1) Bearing capacity theory
(2) Cavity expansion theory
(3) Steady state deformation
(4) Incremental finite-element analysis
(5) Calibration chamber testing.

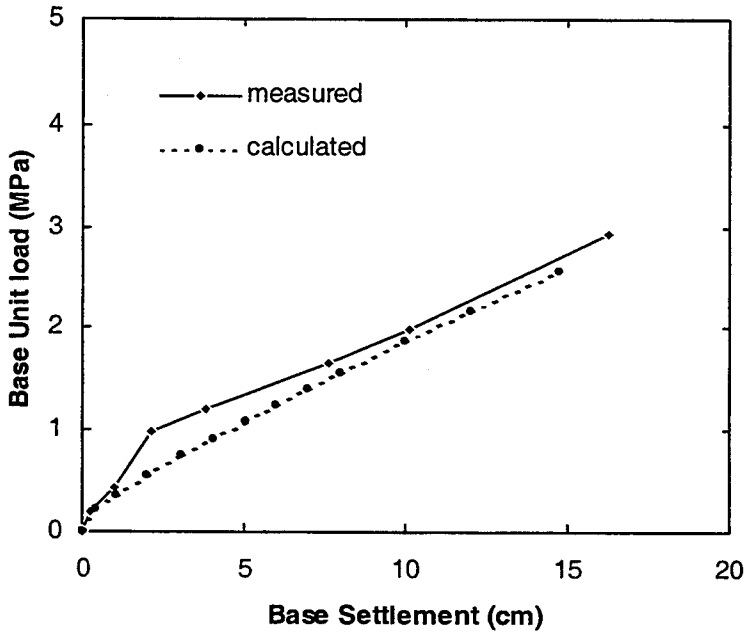

Figure 7.1 Load-settlement curves for pile load test at Georgia Tech.

A useful penetration resistance theory should be able to relate values of cone penetration resistance q_c to the intrinsic and state soil variables (Salgado et al. 1997a). The cavity expansion solution by Salgado (1993) is one of the well-validated theories for obtaining the cone penetration resistance q_c, and takes advantage of utilizing the intrinsic and state soil variables. According to Salgado et al. (1997a), for clean, uncemented soils, the cone penetration resistance q_c can be expressed as follows:

$$q_c = \mathbf{q}_c(D_R, \sigma'_v, \sigma'_h) \tag{7.1}$$

in which $\mathbf{q}_c$ = function containing intrinsic variables; D_R = relative density of sand; and σ'_v and σ'_h = in-situ vertical and horizontal effective stress. When a penetrometer is pushed into soil, it creates and expands a cylindrical cavity that has an initial radius equal to zero. The cavity expansion analysis by Salgado (1993) allows the calculation of cone penetration resistance q_c based on the cavity expansion resistance required to form such a cylindrical cavity.

Figure 7.2 shows different types of assumed failure mechanisms proposed for deep penetration. It should be noticed that the mechanism shown in Figure 7.2 (a), (b) and (d) are theoretically impossible for soils with the usual value of the coefficient of lateral earth pressure ratio K_0 that lies in the 0.3 – 1.0 range. This is so because those mechanisms violate the path of least work. In other words, the slip lines should be directed towards the side since the values of lateral stresses are smaller for these values of K_0 than that of vertical stresses. The mechanism of Figure 7.2 (c) is kinematically possible.

Based on the observation of the displacement field under the pile base (BCP 1971), Salgado (1993) proposed the slip pattern shown in Figure 7.3 considering the axisymmetirc condition of cone penetration. In Figure 7.3, σ_1^P represents horizontal principal stress on the slip line under cone penetrometer and is related to the cavity expansion pressure p_L.

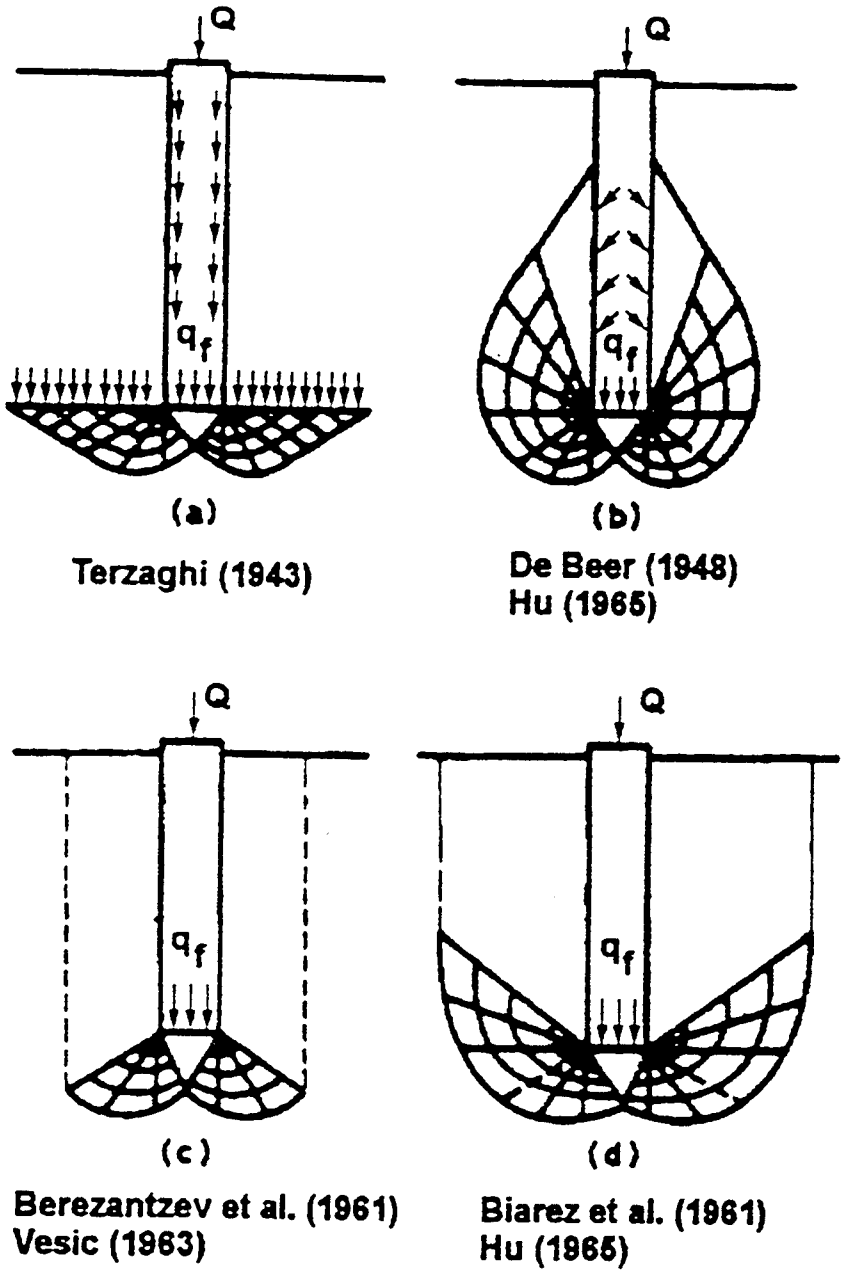

Figure 7.2 Different failure mechanisms for deep penetration.

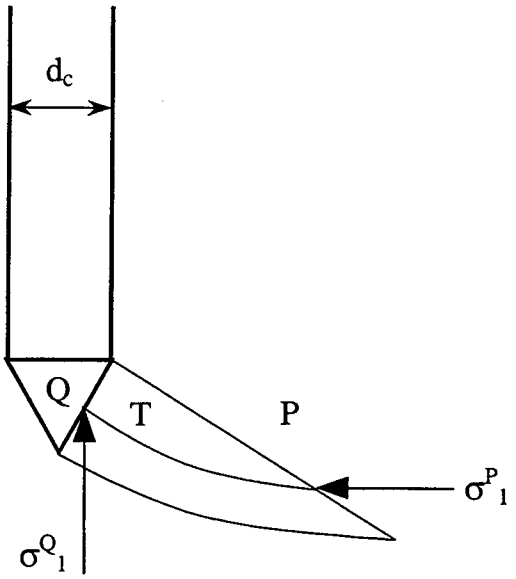

Figure 7.3 Slip pattern under cone penetrometer (after Salgado 1993).

The calculation of cavity expansion pressure p_L requires the numerical sequence considering plastic, non-linear elastic and elastic stress region around the cavity. The relationship between cavity expansion pressure p_L and cone penetration resistance q_c was established based on stress rotation analysis. Following Bolton (1979), the major principal stresses in two different zones shown in Figure 7.4 are related for the rotation angle $\Delta\psi$ as:

$$\sigma_1^A = \sigma_1^B e^{2\Delta\psi \tan\phi} \tag{7.2}$$

in which $\sigma_1{}^A$ and $\sigma_1{}^B$ = major principal stresses in zones A and B in Figure 7.4; $\Delta\psi$ = rotation angle between different principal stresses in zones A and B; and ϕ = friction angle. For the stresses in Figure 7.3, (7.2) can be written with $\Delta\psi = \pi/2$ as:

$$\sigma_1^Q = \sigma_1^P e^{\pi \tan\phi_T} \tag{7.3}$$

where $\sigma_1{}^P$ is related to the cavity expansion pressure p_L; $\sigma_1{}^Q$ is related to q_c; and ϕ_T is a representative friction angle in the transition zone T in Figure 7.3. Integrating $\sigma_1{}^Q$ with respect to the projected area of cone tip, the cone penetration resistance q_c can be determined numerically for a given stress state and soil conditions. More details regarding the procedure to compute q_c using cavity expansion analysis can be found in Salgado et al. (1997a).

The cone penetration resistance q_c obtained from this procedure will be used to normalize the pile base resistance using the program CONPOINT containing the procedure for cavity expansion solution (Salgado et al. 1997a, b, Salgado et al. 1998a, b).

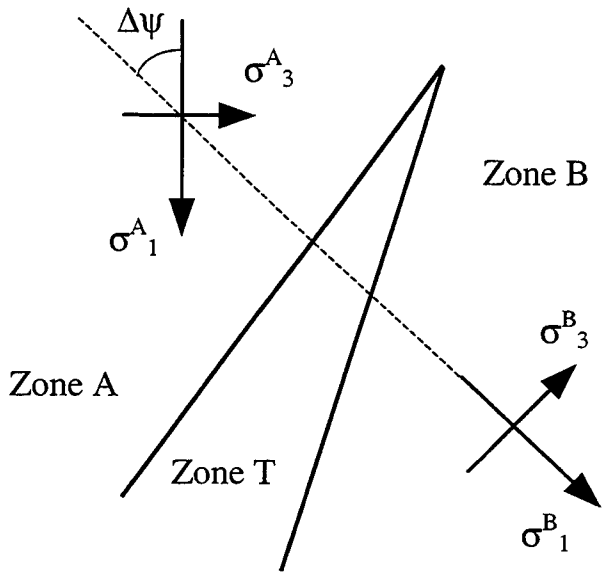

Figure 7.4 Stress rotation between different zones (after Salgado 1993).

7.5 Determination of Base Resistance for Non-Displacement Piles

7.5.1 Load-settlement response for various soil conditions

The pile base load-settlement response for various soil and stress conditions can be obtained by analyzing axially loaded piles with different pile lengths and relative densities. The pile dimensions and soil conditions used for obtaining load-settlement curves in this section are the same as used in the investigation of size effect in calibration chamber test in Chapter 6. Three pile lengths of 5 m, 10 m, and 20 m with a diameter equal to 60 cm were used. Different pile lengths imply different confining stress levels at the pile base. For an assumed unit weight = 20 kN/m^3, initial vertical stresses at the pile base level (corresponding to 5 m, 10 m and 20 m) are σ'_{vo} = 100 kPa, 200 kPa and 400 kPa, respectively.

All the piles were positioned within a granular soil deposit assumed as normally consolidated Ticino sand with K_0 = 0.43. A K_0 value of 0.43 was selected because it is near the center of the typical range of 0.39 to 0.47 observed for K_0 in sands. Ticino sand was selected because it has been studied extensively (Salgado 1993, Bellotti et al. 1996) and has been used in hundreds of calibration chamber plate load and cone penetration tests (Ghionna et al. 1994, Salgado et al. 1997a). Values of relative density D_R used in calculations were 30%, 50%, 70% and 90% for each of the pile lengths assumed. The basic pile geometry and soil conditions are illustrated in Table 7.2. In Table 7.2, σ'_v and σ'_h represent the in-situ vertical and horizontal effective stresses at the pile base level, respectively.

The finite element meshes for each pile length are shown in Figures 7.5 - 7.7. The bottom boundaries of the meshes were located at a depth larger than two times the corresponding pile length measured from the ground surface. The widths of the meshes were equal to or larger than the pile lengths. Finite element analyses performed separately with infinite elements at the lateral boundary showed that the mesh dimensions used in this study are sufficiently large to eliminate geometric boundary effects.

Figure 7.8 shows a set of pile base load-settlement curves obtained from finite element analyses done for the different pile lengths and relative densities. The curves in Figure 7.8 extend up to a base settlement equal to 12 cm, corresponding to a relative settlement s/B of 20%. It is observed that the load-settlement curves for higher relative densities show stiffer responses than those for lower relative densities under the same confinement level or pile length. The initial shear modulus of soil with higher relative density is also higher, and the rate of modulus degradation is lower.

The differences of pile base unit load between D_R = 30% and 90% appear more pronounced as the confinement level or pile length increases. For a 5-m pile, the difference was about 2.2 MPa at a settlement equal to 6 cm, which corresponds to s/B = 10%. The difference for a 20-m pile was about 3.0 MPa at the same relative settlement.

Table 7.2. Pile geometry and soil conditions used in FEM analyses.

Pile Length (m)	Relative density (%)	Type of Sand	σ'_v (kPa)	σ'_h (kPa)
5	30	Ticino	100	43
	50	Ticino	100	43
	70	Ticino	100	43
	90	Ticino	100	43
10	30	Ticino	200	86
	50	Ticino	200	86
	70	Ticino	200	86
	90	Ticino	200	86
20	30	Ticino	400	172
	50	Ticino	400	172
	70	Ticino	400	172
	90	Ticino	400	172

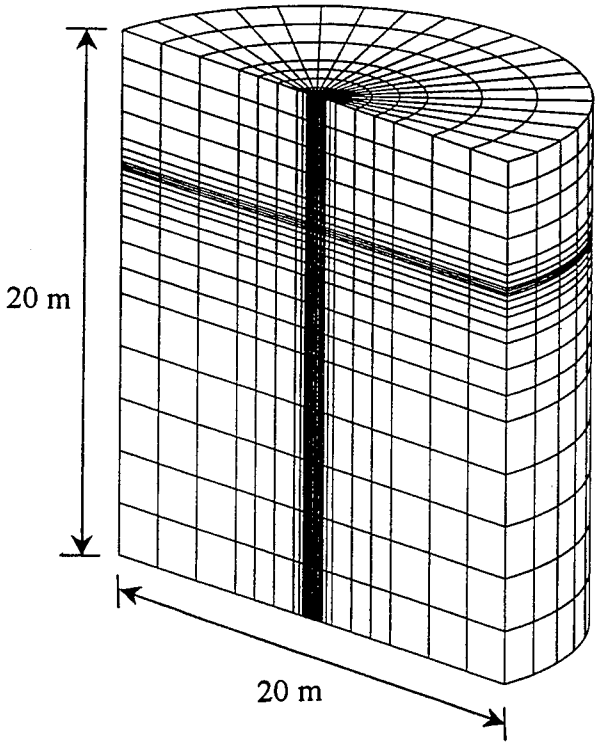

Figure 7.5 Finite element model for 5-m pile.

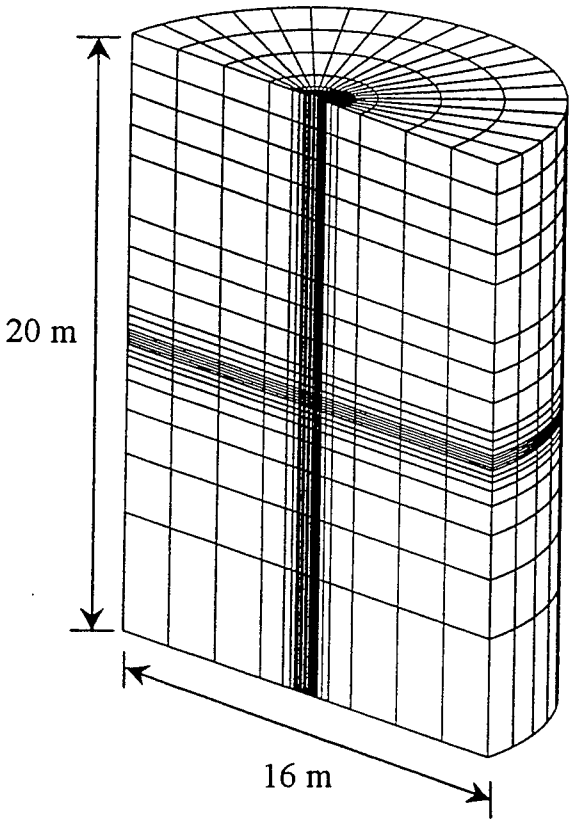

Figure 7.6 Finite element model for 10-m pile.

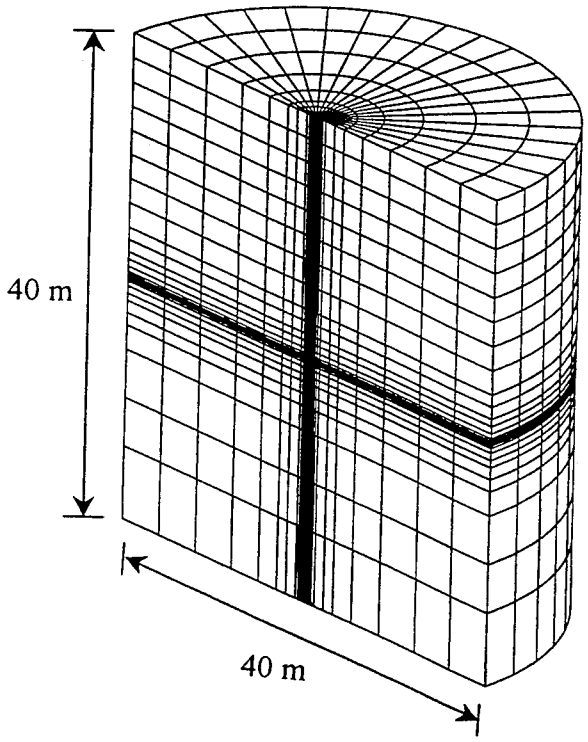

Figure 7.7 Finite element model for 20-m pile.

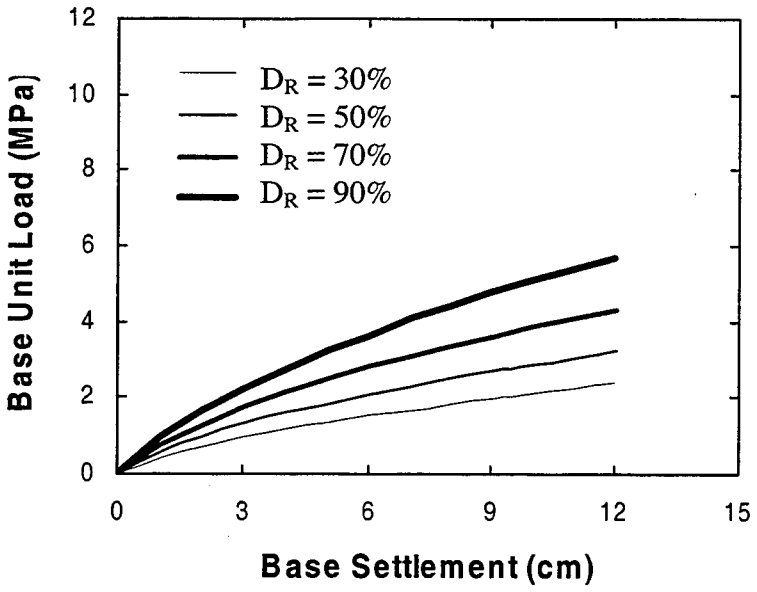

(a)

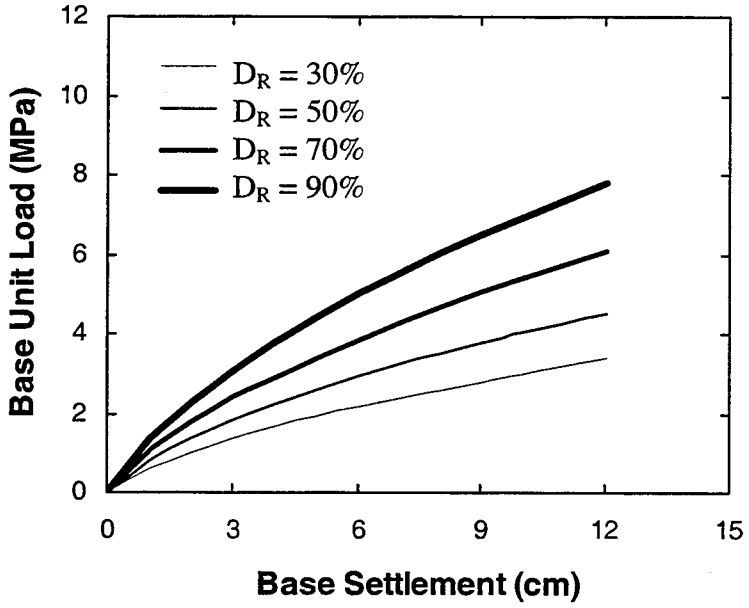

(b)

Figure 7.8 Base load-settlement curves for (a) 5-m, (b) 10-m, and (c) 20-m piles.

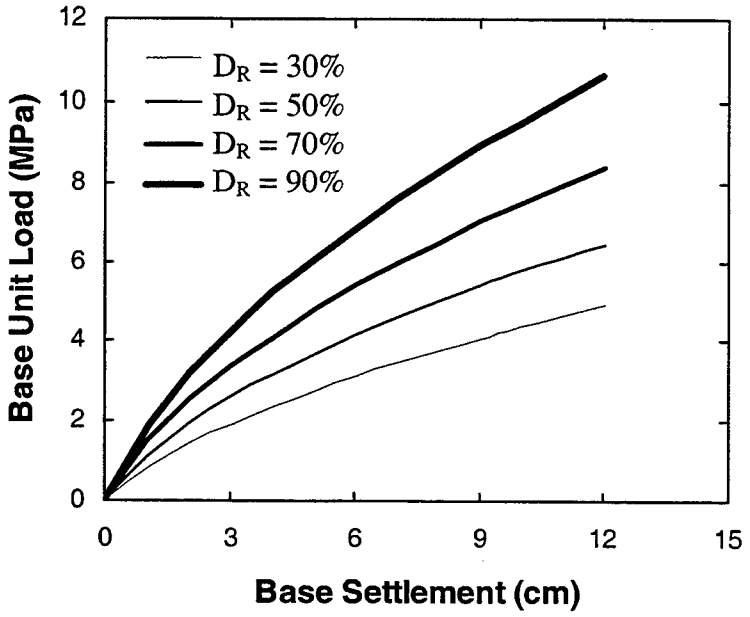

(c)

Figure 7.8 Base load-settlement curves for (a) 5-m, (b) 10-m, and (c) 20-m piles (continued).

7.5.2 Normalized base resistance for non-displacement piles

In order to relate pile base resistance to cone penetration resistance, the load-settlement curves obtained previously were normalized as follows:

(1) the base resistance q_b at a given D_R and stress state was divided by the cone resistance q_c for the same soil conditions;
(2) the settlement was divided by the pile diameter B.

The cone resistance q_c was determined using the penetration resistance analysis of Salgado et al. (1997a), contained in the program CONPOINT (Salgado 1993; Salgado et al. 1997a, b; Salgado et al. 1998a, b). Figure 7.9 shows the fully developed load-settlement curves in terms of q_b/q_c and s/B for each of the pile lengths and relative densities.

A common design approach for non-displacement piles is to stipulate that so long as the load is less than the load required for the pile settlement to reach a certain percentage of the shaft diameter B, serviceability and ultimate limit states are not reached. A modest safety factor can also be used. Franke (1993), for example, proposed that the critical load corresponds to s/B = 0.1, while Reese and O'Neill (1988) define a critical load corresponding to s/B = 0.05. The British code for pile design is based on the s/B = 0.1 criterion. It may be stipulated in a given project, based on structural or architectural requirements, that some other values of s/B not be exceeded. Table 7.3 shows different values of q_b/q_c recommended by several authors.

Table 7.4 shows the values of q_b/q_c at s/B = 5% and 10% for different relative densities and pile lengths obtained using the finite element and penetration resistance analyses. It can be seen that values of q_b/q_c fall within the 0.07 – 0.13 range for s/B = 5% and the 0.12 – 0.21 range for s/B = 10%.

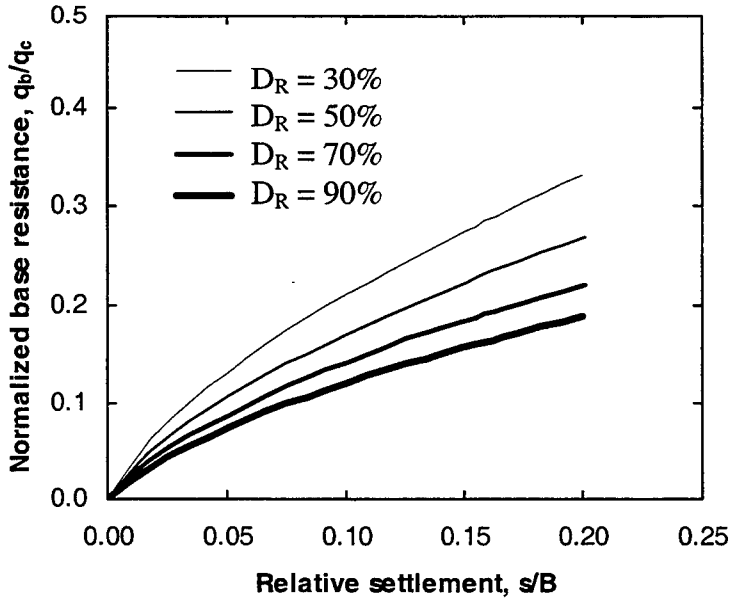

(a)

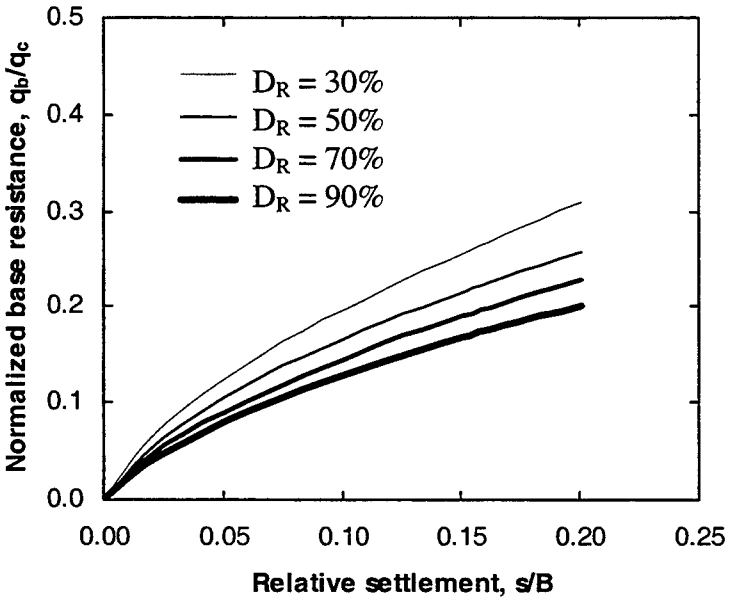

(b)

Figure 7.9 Normalized load-settlement curves for (a) 5-m, (b) 10-m, and (c) 20-m piles in terms of q_b/q_c and s/B.

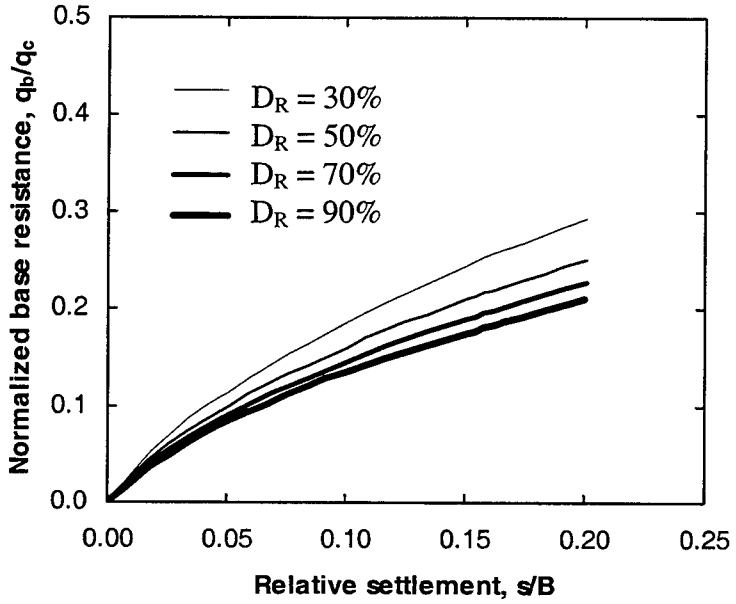

(c)

Figure 7.9 Normalized load-settlement curves for (a) 5-m, (b) 10-m, and (c) 20-m piles in terms of q_b/q_c and s/B (continued).

Table 7.3 Values of q_b/q_c according to several authors.

	q_b/q_c (s/B = 5%)	q_b/q_c (s/B = 10%)
German Specification (DIN 4014, Franke 1993)	N/A	0.2
Franke (1989)	N/A	0.2
Jamiolkowski and Lancellotta (1988)	0.2 (for B < 60 cm)	N/A
Ghionna et al. (1994)	0.09 ± 0.02	0.13 ± 0.02
Salgado (1995)	N/A	0.15

Table 7.4 Values of q_b/q_c at s/B = 5% and 10%.

Pile Length (m)	D_R (%)	q_b (s/B = 5%) (kPa)	q_b (s/B = 10%) (kPa)	q_c (kPa)	q_b/q_c (s/B = 5%)	q_b/q_c (s/B = 10%)
5	30	939	1517	7157	0.13	0.21
	50	1303	2062	12052	0.10	0.17
	70	1726	2789	19562	0.09	0.14
	90	2238	3630	30121	0.07	0.12
10	30	1343	2158	10922	0.12	0.20
	50	1817	2915	17544	0.10	0.16
	70	2409	3871	26644	0.09	0.14
	90	3054	4970	38816	0.08	0.13
20	30	1933	3106	16716	0.11	0.19
	50	2590	4158	25694	0.10	0.16
	70	3357	5401	36718	0.09	0.15
	90	4289	6845	50524	0.08	0.13

Figure 7.10 illustrates the influence of pile length (i.e., confinement at pile base level) and relative density on the normalized base resistance q_b/q_c. The values of q_b/q_c in Figure 7.10 correspond to the relative settlement level of s/B = 10%. From Figure 7.10 (a), it is observed that the effect of pile length on q_b/q_c is not significant. This is because the pile-base resistance q_b and the cone penetration resistance q_c depend on initial confining stress in a similar way. Only a slight decrease of q_b/q_c can be observed for loose sand as the pile length increases. For dense sand, pile length has essentially no influence on q_b/q_c for the range of lengths investigated.

As can be seen in Figure 7.10(b), the influence of relative density on the normalized base resistance is substantial. The normalized base resistance q_b/q_c decreases as the relative density increases. The value of q_b/q_c at s/B = 10% is 0.19 to 0.2 for D_R = 30%, whereas it is 0.12 to 0.13 for D_R = 90%. These results indicate that larger settlements are required for soils with higher relative densities to reach a base resistance equal to a set percentage of cone penetration resistance q_c.

The results also offer some insight into why most pile design methods that calculate q_b by multiplying q_c by a certain constant (e.g., 0.2 for 10% relative settlement, according to Franke 1989) also place an upper limit, which is usually taken as a value in the 4.5 – 5 MPa range, on possible values of q_b. When piles are embedded in very dense sand layers, the results of the present analysis indicate that, as an example, $q_b = 0.2\ q_c$ [the value proposed by Franke (1989) irrespective of relative density] would be too high. Following the results given in Table 7.4, the value of $q_b/q_c = 0.12$ would be more appropriate. Placing a limit on q_b (of say 5 MPa) serves a purpose in that case. However, if the q_b/q_c values of Table 7.4 and Figure 7.9 are used, there may not be a need for setting an upper limit on q_b.

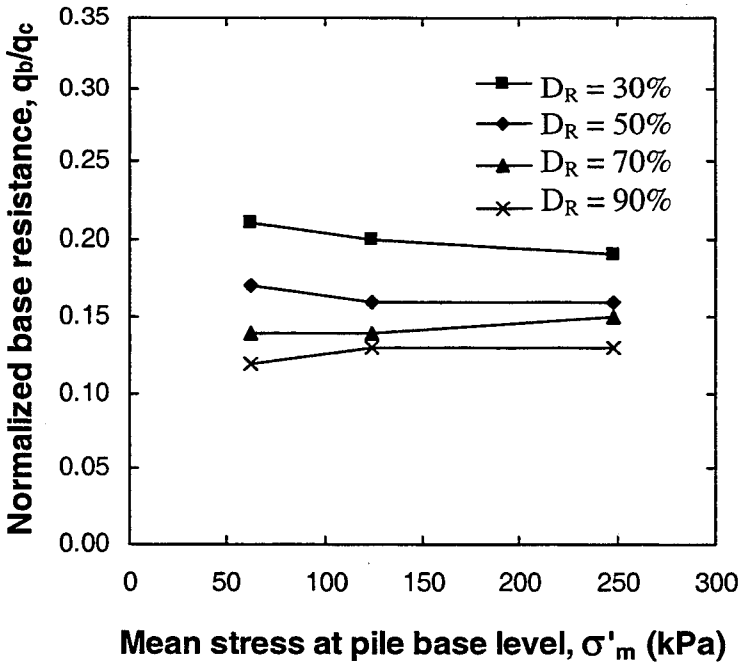

(a)

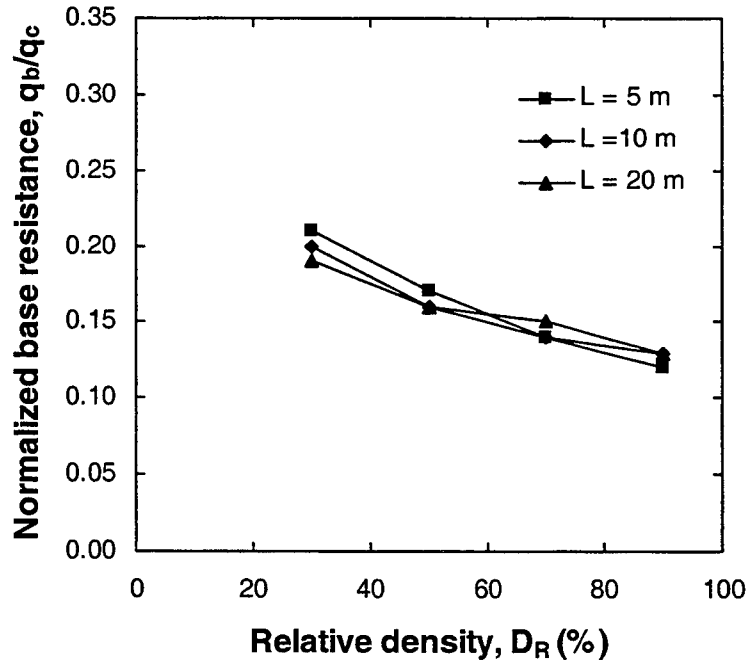

(b)

Figure 7.10 Normalized base resistance q_b/q_c with (a) mean effective stress (σ'_m) at the pile base level and (b) relative density (D_R).

7.5.3 The effect of initial stress ratio K_0

Normally consolidated sand deposits have initial values of the coefficient of lateral earth pressure at rest (K_0) in the 0.39 – 0.5 range. Overconsolidated sand deposits have K_0 values typically higher than that of normally consolidated deposits. In order to investigate the effects of K_0 on normalized base resistance q_b/q_c, three K_0 values (0.4, 0.7 and 1.0) were assumed in a series of finite element analyses. The value of K_0 = 1.0, corresponding to an isotropic stress condition, may be regarded, for practical purposes, as the upper limit on K_0, observed for highly overconsolidated sand deposits.

Figure 7.11 represents the effects of K_0 on the normalized base resistance q_b/q_c. The value of normalized base resistance q_b/q_c in Figure 7.11 were determined for the relative settlement equal to s/B = 10%. The curves shown in Figure 7.11 were plotted for different relative densities (D_R = 30%, 50%, 70% and 90%) and three pile lengths (L = 5 m, 10m and 20 m).

It is observed that q_b/q_c tends to decrease as the initial K_0 increases, although deviation from this trend can be seen in the case for the highest relative density of D_R = 90%. This trend was most obvious for the lowest relative density. For D_R = 30% and L = 5 m, the difference between the normalized base resistance q_b/q_c at K_0 = 0.4 and at K_0 = 1.0 was equal to approximately 0.05. No difference in the normalized base resistance q_b/q_c was found at D_R = 90% for K_0 = 0.4 to 1.0. Comparing the three cases (L = 5, 10 and 20 m) in Figure 7.11, it can also be observed that the confinement at the pile base level, which is determined by the pile length, does not have as much influence as the relative density on the relationship between q_b/q_c and K_0.

These results suggest that, when the soil is loose and has a high K_0 value, the values of normalized base resistance q_b/q_c given in Table 7.4 and Figure 7.9 need to be modified considering the variations in the values of q_b/q_c shown in Figure 7.11. For very dense soil, no such modification of the value of q_b/q_c is necessary.

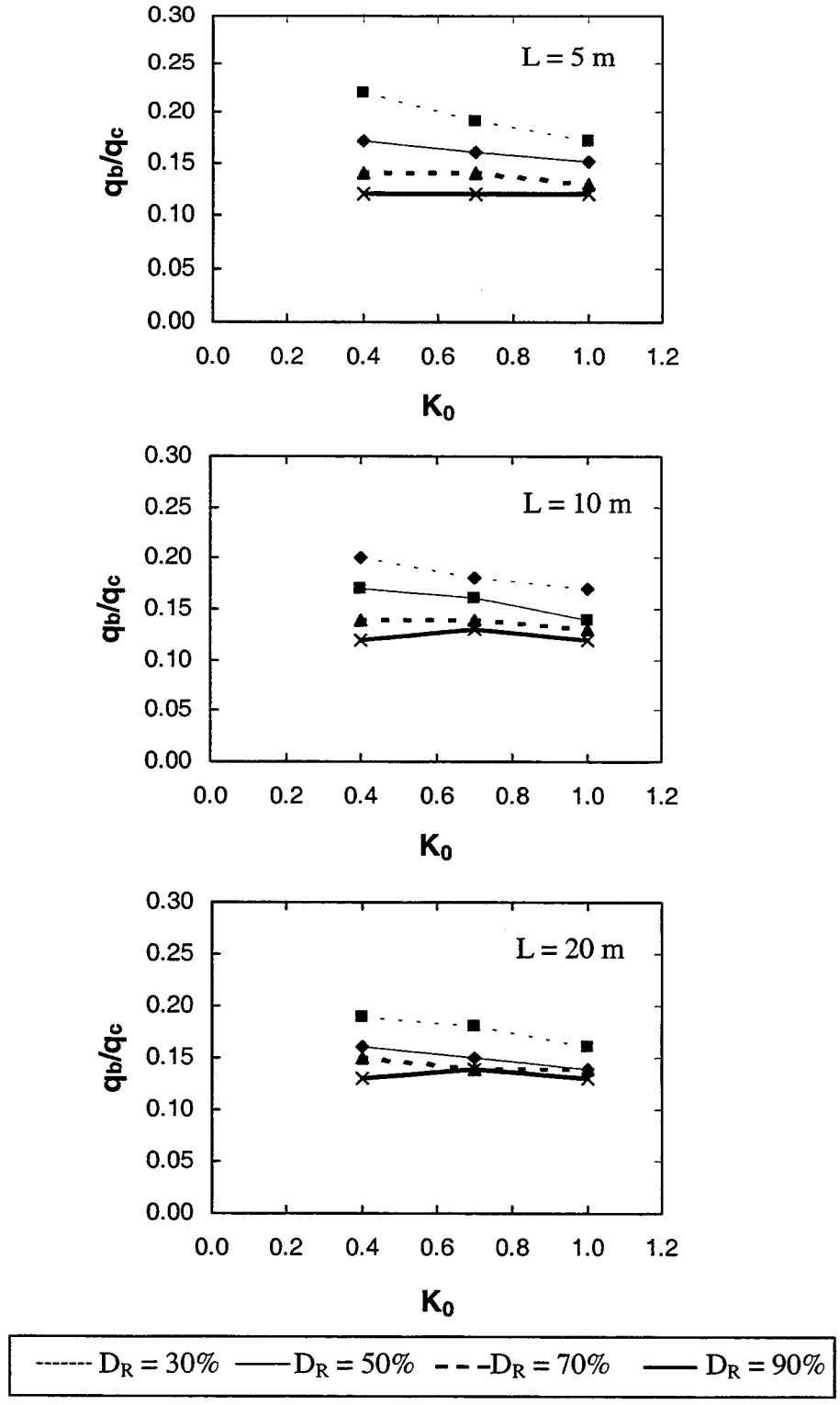

Figure 7.11 Effect of K_0 on normalized base resistance q_b/q_c.

7.6 Determination of Base Resistance for Displacement Piles

Values and analyses presented previously were developed for non-displacement piles. The limit base resistance q_{bL}, as mentioned earlier, is mobilized at very large settlement levels and is conceptually identical for both non-displacement and displacement piles (De Beer 1984, 1988, Ghionna et al. 1993, Salgado et al. 1997a). The normalized base resistance values of Figure 7.9 for non-displacement piles, however, cannot be directly applied to displacement piles, because of the very different load-settlement response of displacement and non-displacement piles for low to moderate settlement levels.

De Beer (1984, 1988) has shown that, under the same conditions, the loads carried by a displacement pile and a geometrically identical non-displacement pile differ significantly for values of relative settlement s/B of interest in pile design. Non-displacement piles settle more than displacement piles for the same applied load. This is mainly due to the different installation processes for these two types of piles. The installation of displacement piles usually causes considerable densification of the soil around the pile. In terms of base resistance, this process could be seen as a preloading of the soil in the immediate neighborhood of the pile base, hence the stiffer response when compared with non-displacement piles. The difference between the loads carried by the two types of pile for the same settlement level becomes less pronounced as settlement increases. De Beer's observations were later confirmed by other authors (e.g., Jamiolkowski and Lancellotta 1988, Ghionna et al. 1993).

Table 7.5 shows the typical ratio of base resistance of displacement piles to base resistance of non-displacement piles for different values of relative settlement but same initial soil conditions. As can be seen, the ratio of q_b of a non-displacement pile to q_b of a geometrically identical displacement pile is much smaller than 1 at small relative settlements, but approaches 1 as the settlement approaches infinity. A simple approach that may be used to determine q_b/q_c values as a function of s/B for displacement piles is the application of the ratios of Table 7.5 to the results of Table 7.4 for non-displacement

piles. Such an approach can provide useful design criteria, but is naturally subject to more uncertainties than the values proposed for non-displacement piles in Table 7.4. Table 7.6 provides the normalized base resistance q_b/q_c for displacement piles obtained using this approach.

Table 7.5 Base resistance ratio for displacement and non-displacement piles.

Relative Settlement (s/B)	$q_{b,ND}$[a] / $q_{b,D}$[b]	
	De Beer (1988)	Ghionna et al. (1993)
2.5%	0.482	
5%	0.517	0.15 – 0.21
10%	0.587	0.3 – 0.5
25%	0.715	0.3 – 0.7
$\rightarrow \infty$	$\rightarrow$ 1.0	$\rightarrow$ 1.0

[a] $q_{b,ND}$ = base resistance for non-displacement pile
[b] $q_{b,D}$ = base resistance for displacement pile

Table 7.6 Values of q_b/q_c for displacement piles.

Pile Length (m)	D_R (%)	q_b/q_c (s/B = 5%)	q_b/q_c (s/B = 10%)
5	30	0.25	0.35
	50	0.19	0.29
	70	0.17	0.24
	90	0.14	0.20
10	30	0.23	0.34
	50	0.19	0.27
	70	0.17	0.24
	90	0.15	0.22
20	30	0.21	0.32
	50	0.19	0.27
	70	0.17	0.26
	90	0.15	0.22

7.7 Normalized Base Resistance for Silty Sands

Natural sand deposits often contain a certain amount of fines. These sand deposits are also bearing layers for piles, if the fines contents of soils are not high and soils are sufficiently strong to support axial loads. In order to investigate the normalized base resistance q_b/q_c for soils containing fines, the load-settlement response of piles in silty sands was analyzed.

The mechanical properties of silty sands were extensively studied by Salgado et al. (1999) and Bandini (1999). They investigated the behavior of silty sands focusing on stiffness and strength characteristics. The material used was Ottawa sand with silt contents equal to 5%, 10%, 15%, and 20% in weight. Tables 7.7 and 7.8 show the soil intrinsic parameters of silty sands with different fines contents. The parameters shown in the tables are the same as used in (4.50) and (4.76) for the initial shear modulus and dilatancy angle of sand, respectively. As can be seen in Table 7.7, the parameter C_g decreases as the silt content increases, while the exponent parameter n_g for the confining stress increases. On the other hand, as shown in Table 7.8, the higher the silt content, the higher the friction angle ϕ_c at critical state. This also resulted in higher peak friction angles with increasing silt content. The dilatancy parameters Q and R for silty sands in Table 7.8 were obtained from the best-fit regression of test results, while the original Bolton (1986) correlation was based on fixing R = 1.

The finite element analysis of pile load tests in silty sands was done using the parameters given in Tables 7.7 and 7.8. Since it is usually desirable for piles to be placed into granular soil deposit with low fines content, silt contents equal to 5% and 10% were considered in the finite element analyses. The values of the parameters f and g for the non-linear elastic-plastic stress-strain model were determined based on the stress-strain relationship of silty sands by Bandini (1999). Table 7.9 shows the values of the parameters f and g for different relative densities and silt contents.

Table 7.7 Values of soil intrinsic parameters with different silt contents (after Salgado et al. 1999, Bandini 1999).

Silt content (%)	C_g	e_g	n_g	e_{min}	e_{max}
0	612	2.17	0.439	0.48	0.78
5	454	2.17	0.459	0.42	0.70
10	357	2.17	0.592	0.36	0.65

Table 7.8 Values of friction angle ϕ_c at critical state and dilatancy parameters Q and R with different silt contents (after Salgado et al. 1999, Bandini 1999).

Silt content (%)	ϕ_c	Q	R
0	29.0	9.0	0.49
5	30.5	9.0	-0.50
10	32.0	8.3	-0.69

Table 7.9 Values of f and g used in finite element analyses for silty sands.

D_R (%)	5% silt		10% silt	
	f	g	f	g
30	0.98	0.15	0.98	0.13
50	0.97	0.18	0.97	0.16
70	0.96	0.21	0.96	0.19
90	0.95	0.24	0.95	0.22

Finite element meshes and stress states used in the analyses were the same as those for clean sands previously presented. The cone resistance q_c at the pile base level was obtained using the program CONPOINT (Salgado et al. 1997a, b, 1998a, b) with soil intrinsic parameters given in Tables 7.7 and 7.8.

Table 7.10 and Figure 7.12 show the normalized base resistance q_b/q_c for silty sands with different relative densities and pile lengths. For both 5% and 10% silt contents, most values of q_b/q_c were in the 0.12 – 0.17 range. As discussed earlier, the influence of the confining stress on the value of q_b/q_c for clean sands was small irrespective of the relative density. For silty sands, however, the influence of the confining stress was more significant. As can be seen in Table 7.10, q_b/q_c for lower relative density ($D_R \approx 30\%$) decreases with increase in pile length. On the other hand, the value of q_b/q_c for higher relative density ($D_R \approx 70\%$, 90%) increases as the pile length increases. This observation was more pronounced at the 10% silt content. The value of q_b/q_c of the 20-m pile for D_R = 90% with the 10% silt content was even greater than that for D_R = 30%. These results may be due to the increasing influence of the confining stress with increasing silt content. As shown in (4.50) and (4.76), the parameter n_g in Table 7.7 represents the effect of the confining stress on the elastic modulus. The higher the value of n_g, the greater the influence of the confining stress on the value of q_b/q_c. As a result, the differences of q_b/q_c for the silty sand between different pile lengths were more pronounced than those for the clean sand.

Table 7.10 Values of q_b/q_c for silty sands with different relative densities and pile lengths.

Silt content	Pile length	D_R (%)	q_b (kPa) (s/B = 5%)	q_b (kPa) (s/B = 10%)	q_c (kPa)	q_b/q_c (s/B = 5%)	q_b/q_c (s/B = 10%)
5%	5 m	30	828	1336	8012	0.103	0.167
		50	1103	1760	11911	0.093	0.148
		70	1405	2239	16960	0.083	0.132
		90	1749	2839	22488	0.078	0.126
	10 m	30	1194	1909	12509	0.095	0.153
		50	1551	2486	17391	0.089	0.143
		70	1961	3144	23321	0.084	0.135
		90	2425	3902	29800	0.081	0.131
	20 m	30	1668	2736	19705	0.085	0.139
		50	2191	3556	25596	0.086	0.139
		70	2763	4460	32390	0.085	0.138
		90	3411	5469	39808	0.086	0.137
10%	5 m	30	755	1253	8789	0.086	0.143
		50	1001	1641	12186	0.082	0.135
		70	1283	2100	16231	0.079	0.129
		90	1630	2662	20716	0.079	0.128
	10 m	30	1129	1865	14186	0.080	0.131
		50	1505	2440	18329	0.082	0.133
		70	1903	3076	22976	0.083	0.134
		90	2341	3815	27963	0.084	0.136
	20 m	30	1682	2809	22953	0.073	0.122
		50	2224	3674	27783	0.080	0.132
		70	2813	4629	32863	0.086	0.141
		90	3456	5596	38029	0.091	0.147

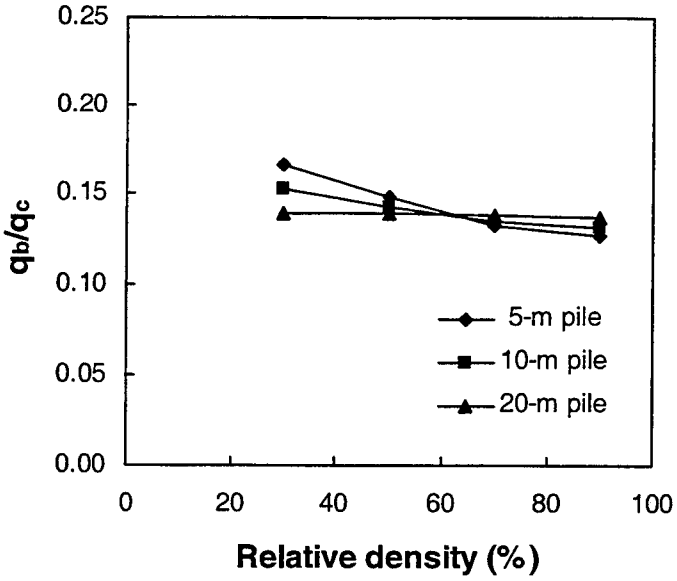

(a) 5% silt content

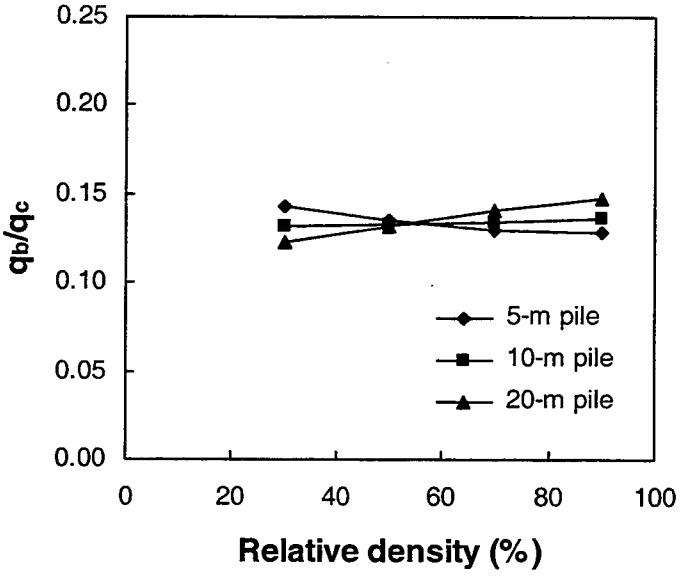

(b) 10% silt content

Figure 7.12 Values of q_b/q_c for silty sand.

7.8 Summary

The cone penetration test (CPT) resembles the vertical loading process on a pile. In this chapter, in order to take advantage of the CPT for pile design, load-settlement curves in terms of normalized base resistance (q_b/q_c) versus relative settlement (s/B) were developed. Although the limit state design concept for pile design has been used mostly with respect to either s/B = 5% or s/B = 10%, the normalized load-settlement curves obtained in this study allow determination of pile base resistance at any relative settlement level within the 0 – 20% range. This is important, as it permits consideration of specific project features, related to the superstructure or other components of the facility.

In order to obtain the pile base load-settlement relationship, finite element analyses were performed with a 3-D non-linear elastic-plastic constitutive model. Three 60-cm diameter piles with lengths of 5 m, 10 m and 20 m were used in the analyses. The piles were positioned within a granular soil deposit with D_R = 30, 50, 70 and 90%. Because the soil conditions around the piles were assumed to be the same as those existing before pile installation, the results obtained represent those corresponding to non-displacement piles. The cone resistance q_c was calculated from the penetration resistance analysis of Salgado et al. (1997a) and used to normalize the load-settlement curves in order to express them in terms of q_b/q_c and s/B.

Most q_b/q_c values obtained from the finite element and penetration resistance analyses fall within the 0.07 - 0.13 range for s/B = 5% and the 0.10 - 0.20 range for s/B = 10%. The effect of relative density on the normalized base resistance was significant, while that of the confining stress at the pile base level was small. At higher relative densities, the value of q_b/q_c was smaller (q_b/q_c = 0.12 -0.13 for D_R = 90%) than at lower relative densities (q_b/q_c = 0.19 - 0.2 for D_R = 30%). The effect of the coefficient of lateral earth pressure at rest K_0 was also investigated. The value of q_b/q_c tends to decrease as the value of K_0 increases. This trend was more pronounced at lower relative densities, and negligible for very dense sand.

Based on the results by De Beer (1984, 1988), the values of q_b/q_c for displacement piles were obtained as well. The values of q_b/q_c were typically in the 0.15 - 0.25 range for s/B = 5% and in the 0.22 - 0.35 range for s/B = 10%.

The normalized base resistance q_b/q_c for silty sands was also investigated. For both 5% and 10% silt contents, most values of q_b/q_c were in the 0.12 – 0.17 range. These values are typically smaller than those for clean sands, which ranged from 0.12 to 0.21. The confining stress was another important factor for the value of q_b/q_c of silty sand. For lower relative density ($D_R \approx 30\%$), the value of q_b/q_c decreases as the pile length increases while that for higher relative density increases.

CHAPTER 8 ASSESSMENT OF PROPOSED NORMALIZED BASE RESISTANCE VALUES BASED ON CASE HISTORIES

8.1 Introduction

In this chapter, we reexamine the values of normalized base resistance q_b/q_c presented previously. We do so in the context of a few case histories involving actual pile load tests, calibration chamber data, and other numerical analyses. Both non-displacement and displacement piles are addressed.

The case histories for non-displacement piles include two instrumented pile load tests on drilled shafts, a series of calibration chamber tests (Ghionna et al. 1994), and the numerical results of Simonini (1996). A load test on a drilled shaft performed at a site on the Georgia Tech campus in Atlanta, Georgia (Mayne and Harris 1993, Harris and Mayne 1994) and another performed at the University of São Paulo (USP), São Carlos, experimental field (Albiero et al. 1995) are analyzed.

For displacement piles, the load test on a steel H-pile performed at the Purdue University campus (Goble et al. 1972) and the load tests on the precast concrete piles carried out by NGI (Gregersen et al. 1973) were used. All the load tests used in this section were instrumented, so base load-settlement responses were recorded separately. The observed values of q_b/q_c for each case are summarized in Table 8.1.

Table 8.1 Values of q_b/q_c from load tests on non-displacement and displacement piles.

Pile Type	Test Name	q_b/q_c (s/B = 5%)	q_b/q_c (s/B = 10%)
Non-Displacement Pile (Drilled shaft)	Georgia Tech Test	0.18	0.26
	USP Test	0.09	0.20
	Simonini's Analysis	N/A	0.17
Displacement Pile (Driven pile)	Purdue Test	0.27	0.37
	NGI Test A	0.32	0.36
	NGI Test B	0.32	0.36
	NGI Test C	0.30	0.39
	NGI Test D	0.43	0.47

8.2 Non-Displacement Piles

8.2.1 Georgia Tech load test

The Georgia Tech load test was described in the previous section. The representative value of q_c for base resistance calculation, an average value between the level of the pile base and a level about one-and-a half to two pile diameters below the pile base, is 6.5 MPa. The measured base loads for the shaft at 5 and 10% relative settlement are 580 and 810 kN, corresponding to q_b/q_c values of 0.18 and 0.26 respectively. Since the relative density of the soil around the pile base was not determined, the relationship between q_c and the relative density D_R suggested by Salgado et al. (1997b) was used. The estimated relative density of the soil around the pile base with a K_0 value of 0.41 was about 20 – 30%, representing a loose state. Using Table 7.4, the corresponding values of q_b/q_c at s/B = 5 and 10% can be found as 0.12 – 0.13 and 0.20 – 0.21, respectively. The difference between measured and predicted values of q_b in this example appears to be small (20 – 30% underprediction).

8.2.2 São Paulo load test

The USP, São Paulo, test site is located near downtown São Carlos, in the state of São Paulo, Brazil (Teixeria and Albiero 1994). The site geology consists of two clayey sand layers separated by a thin layer of pebbles. The upper layer is a reddish material of Cenozoic age, collapsible upon inundation (Vilar 1979), with void ratios close to 1. The lower layer is a brownish residual soil from a sandstone of the Bauru formation. The water table oscillates, but is typically around 10 meters deep. The base of the test shaft was placed at a depth of 10 m and the shaft diameter was 50 cm. The measured base loads corresponding to s/B = 5 and 10% are 50 and 114 kN, respectively. The load for 10% relative settlement was obtained from a quick maintained load test (QMLT)

performed after a slow maintained load test (SMLT) up to 5% relative settlement. The value of q_c was obtained from the CPT sounding provided in Albiero et al. (1995) as 2.8 MPa. This yields q_b/q_c values of 0.09 and 0.20 for s/B = 5 and 10%, respectively. The measured q_b/q_c values for this case were also favorably compared with the results in Table 7.4, namely $q_b/q_c = 0.09 - 0.10$ for s/B = 5% and $q_b/q_c = 0.14 - 0.17$ for s/B = 10% for medium dense sand.

8.2.3 Simonini's results

Simonini (1996) carried out finite element analyses to obtain the base resistance of non-displacement piles in sands. The pile was modeled as having a diameter equal to 1 m and a length equal to 30 m. The soils were a dry sand deposit with $\phi_c = 33°$, $D_R = 90\%$ and soil unit weight $\gamma_m = 16.5$ kN/m^3. The value of the base resistance q_b corresponding to s/B = 10% was found to be 8.6 MPa.

In order to obtain the cone resistance q_c at the pile base level, the penetration resistance analysis of Salgado et al. (1997a, b), available in the program CONPOINT (Salgado et al. 1997a, b), was used. The soil properties used to obtain the cone resistance were the same as those used in the finite element analyses. Combining the base resistance value with q_c, the value of q_b/q_c is obtained as 0.17. This q_b/q_c value is slightly higher than that of Table 7.4, equal to approximately 0.13 for a relative density of $D_R = 90\%$.

8.2.4 Calibration chamber plate load tests

A series of 30 calibration chamber load tests were carried out by Ghionna et al. (1994) in sand samples with two different relative densities, dense ($D_R \approx 90\%$) and

medium dense ($D_R \approx 50\%$). These tests simulate the loading of the base of drilled shafts. Calibration chamber size effects on the values of q_b were shown earlier to be small. Figure 8.1 shows the values of q_b/q_c for the calibration chamber tests corresponding to s/B = 5 and 10%. The cone resistance q_c used to prepare Figure 8.1 was obtained from the penetration resistance analysis of Salgado et al. (1997a, b).

As can be seen in Figure 8.1, the values of q_b/q_c are in the 0.09 – 0.14 range for $D_R \approx 50\%$ and 0.07 – 0.10 range for $D_R \approx 90\%$ at s/B = 5%, and in the 0.11 – 0.19 range for $D_R \approx 50\%$ and 0.10 – 0.14 range for $D_R \approx 90\%$ at s/B = 10%. Although the results for $D_R \approx 50\%$ show more scatter than those for $D_R \approx 90\%$, the average values of q_b/q_c for both relative densities are in reasonable agreement with the proposed results given in Table 7.4.

8.3 Displacement Piles

8.3.1 Purdue University load test

The Purdue University load test was performed on the western side of the Purdue University campus in West Lafayette, Indiana (Goble et al. 1972). This site is located on the edge of a large terrace along the Wabash river with a variable depth of weathered loess covering stratified sand and gravel layers. A 15-m long steel H-pile (10HBP57) was driven using a DELMAG D-12 diesel hammer and load tested. H-piles are sometimes referred to as small displacement piles because their relatively small cross-section does not cause as much disturbance and densification of the surrounding soil during the installation process as concrete or pipe piles would.

The base resistance q_b and relative settlement s/B were calculated based on the equivalent circular base area transformed from the half perimeter area of the H-pile. The obtained q_b values for s/B = 5 and 10% were 2.43 MPa and 3.37 MPa, respectively. Because the standard penetration test was used instead of cone penetration test, the cone

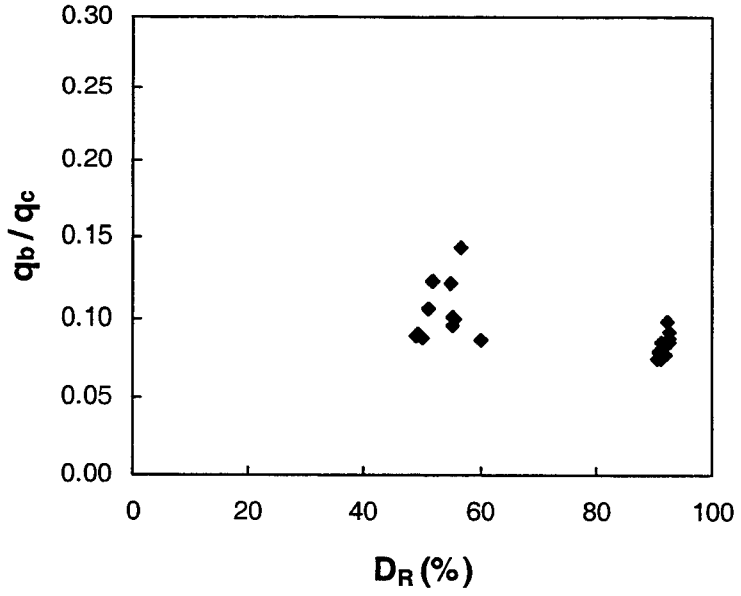

(a)

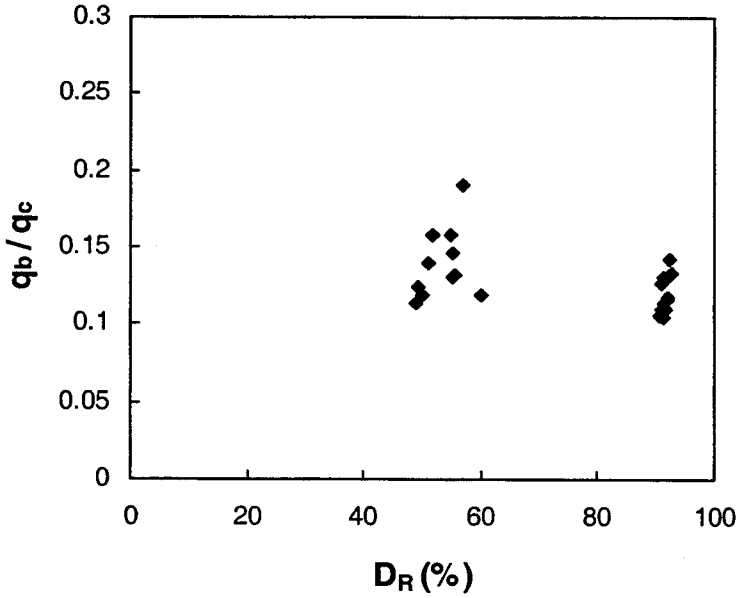

(b)

Figure 8.1 Values of q_b/q_c in calibration chamber plate tests for (a) s/B = 5% and (b) s/B = 10%.

resistance q_c was estimated from the SPT blow count at the pile base level based on the SPT-CPT correlation of Robertson and Campanella (1983). The estimated q_c value at the pile base level was about 9.0 MPa. The values of q_b/q_c corresponding to s/B = 5 and 10% were 0.27 and 0.37 respectively. These results appear to be near the upper range of the values of q_b/q_c for displacement piles shown in Table 7.6.

8.3.2 NGI load tests

The NGI load tests were performed on precast-concrete piles driven into a very loose deposit of quite homogeneous sandy soil. The site is located in a small island, Holmen, in the middle of the Drammen river near the city of Drammen, Norway. The soil layer consists of uniform, loose upper sand layer down to 30 m, underlain by a clay layer and finally bedrock. From the geological history of this area, the subsoil condition is believed to be normally consolidated (Gregersen et al. 1973). Four instrumented piles with two lengths, 8 and 16 m, were tested. The four piles are referred to by the letters A, B, C and D in Table 8.1. Piles A and C had the same length (8 m); pile A had a diameter of 28 cm, while pile C was a tapered pile with diameter varying from 28 cm at the pile top to 20 cm at the pile base. Piles B and D had the same length (16 m); pile B had a diameter of 28 cm, while pile D was made by connecting piles A and C, resulting in a pile with a diameter of 28 cm from the top to half the pile length, and then tapered with a diameter of 20 cm at the pile base. The cone resistances at depths 8 m and 16 m were 3.1 MPa and 5.0 MPa. The values of q_b/q_c for each pile are given in Table 8.1. Although pile D shows an exceptionally high value of q_b/q_c, most of the q_b/q_c values fall within the 0.29 – 0.32 range for s/B = 5% and the 0.36 – 0.39 range for s/B = 10%. Considering that the soil is in a loose state, these measured values agree well with the values proposed for displacement piles in Table 7.6.

8.4 Summary

In order to verify the normalized base resistance value q_b/q_c, several case histories for both non-displacement and displacement piles were examined. For non-displacement piles, the observed results of field pile load tests, finite element analysis, and calibration chamber plate load tests were compared with the q_b/q_c values presented in Chapter 7. Overall, the observed values of q_b/q_c were in good agreement with the proposed values given in Chapter 7.

For displacement piles, 5 pile load tests were investigated. Although the values of q_b/q_c for displacement piles were established based on the results of non-displacement piles, the comparison between the measured and the proposed q_b/q_c values showed reasonably good matches.

CHAPTER 9 PILE DESIGN USING CPT RESULTS

9.1 Introduction

In this chapter, the design of piles using CPT results is discussed. Both base and shaft resistances are addressed. Since the standard penetration test is still widely used in practice, the correlation between the SPT blow count N and the cone resistance q_c is also discussed. A proper SPT-CPT correlation makes it possible for CPT-based methods to be used when only SPT results are available.

A computer program developed for the estimation of pile load capacity based on CPT results is introduced. In this program, base and shaft resistances can be estimated using different methods.

9.2 Determination of Base and Shaft Resistances

9.2.1 Base resistance

As discussed in Chapter 2, there are several methods available for pile design using CPT results (DeRuiter and Beringen 1979, Schmertmann 1978, Aoki and Velloso 1975, Bustamante and Gianeselli 1982). All of these methods define the base resistance in terms of the cone penetration resistance q_c and correlation parameters. Since these methods were developed under different conditions, the selection of the method should be

made with consideration of the differences and recommendations of the methods. The important differences between the methods include (Bandini and Salgado 1998):

(1) the criterion adopted to define pile load capacity;
(2) the type of equipment used to obtain q_c;
(3) the selection and relative importance of q_c values above and below the pile base;
(4) soil types and conditions under which the methods were developed.

Regarding the criterion adopted to define the pile load capacity, CPT-based pile design methods do not clearly define the pile load capacity. Although for small-diameter piles the differences in pile capacity are not large, as the diameter increases the way in which load capacity is defined becomes critical. A relative settlement-based criterion for pile load capacity definition is favored, as discussed previously.

Following Franke (1991), piles must typically undergo relative settlements s/B greater than 10% to reach a limit state, including either a loss of functionality of structures or damage to the superstructure and/or foundations. Settlements less than 10% of the pile diameter, in some design situation, may cause the foundations or the supported structures to reach a limit state. Hence, in the evaluation of the value of the relative settlement associated with the limit states design of piles, the type, functionality, location, and importance of structures should also be taken into account.

Figure 9.1 shows a simple example for estimating pile base resistance using CPT results. The pile is a drilled shaft having a length of 10 m and a diameter of 50 cm. The soil is a normally consolidated, medium dense sand. The cone resistance q_c was assumed varying linearly with depth from 1 MPa at the surface to 10 MPa at the pile base level. For these given pile and soil conditions, the base resistances q_b were calculated using different methods.

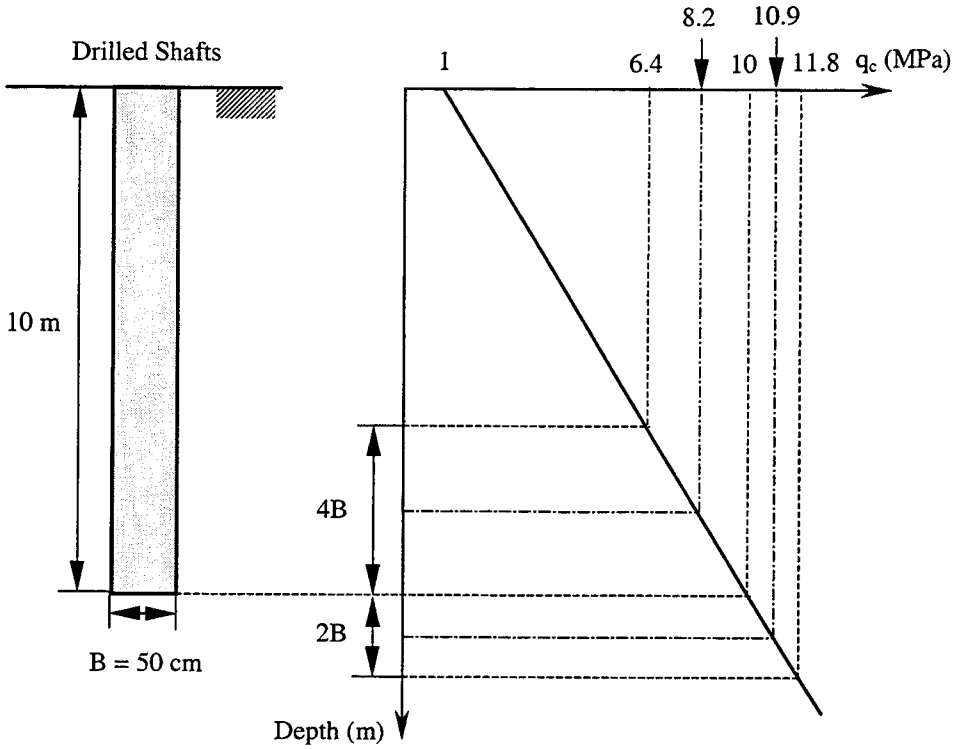

- Dutch method: $q_b = \dfrac{8.2+10.9}{2} = 9.55$ MPa
- Aoki and Velloso's method: $q_b = \dfrac{q_c}{3.25} = \dfrac{10}{3.25} = 3.07$ MPa
- LCPC method: $q_b = k_c \times q_{ca} = 0.4 \times 10 = 4.0$ MPa
- Proposed method: $q_b = 0.16 \times 10.9 = 1.74$ MPa

Figure 9.1 Estimation of pile base resistance using different methods.

For the method proposed in this study, the value of q_b/q_c was equal to 0.16 corresponding to the medium dense condition. Although the profile of cone resistance in this example is extremely simplified, the values of q_b obtained using different methods show a quite wide range. The highest value of q_b equal to 9.55 MPa was obtained from the Dutch method while the lowest one equal to 1.74 MPa was obtained from the proposed method in this study. It should be noticed that the lowest base resistance obtained from the proposed method was based on the relative settlement s/B equal to 10%.

9.2.2 Shaft resistance

The shaft resistance of piles in most cases is fully mobilized well before the maximum base resistance is reached (Franke 1993). It follows that shaft resistance can be estimated with greater simplicity, at least from a conceptual point of view, than base resistance.

Based on the review of the methods in Chapter 2, Aoki and Velloso's method (Aoki and Velloso 1975) and the LCPC method (Bustamante and Gianeselli 1982) appear to be effective approaches to estimate the shaft resistance using CPT results. Figure 9.2 shows a simple example of estimation of shaft resistance using these methods. Soils consist of two clayey layers and three sandy layers. Pile condition is the same as that for the example of base resistance estimation discussed in the previous section. The representative cone resistance q_{ci} for each sub-layer was obtained from the center of the layer. The calculated values of shaft resistance are given in Figure 9.2.

In Figure 9.2, the shaft resistances of layer 2, 4, and 5 for the LCPC method were taken as the limit values given in Table 2.5 because the calculated shaft resistances were greater than the limit values. The estimated value of the shaft resistance from Aoki and Velloso's method was significantly lower than that from the LCPC method.

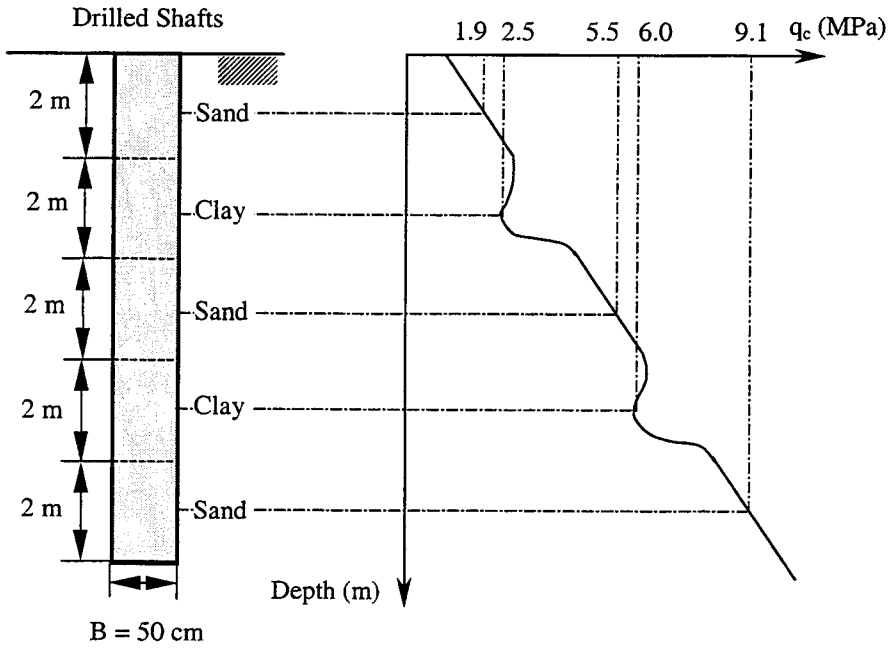

	Aoki-Velloso method				LCPC method		
Layer	q_c (kPa)	α (%)	F_2	q_{si} (kPa)	q_c (kPa)	k_s	q_{si} (kPa)
1	1900	1.4	6.5	4.1	1900	60	31.6
2	2500	6.0	6.5	23.1	2500	40	35.0
3	5500	1.4	6.5	11.8	5500	100	55.0
4	6000	6.0	6.5	55.4	6000	60	35.0
5	9100	1.4	6.5	19.6	9100	100	80.0
Σ				114.0			236.6

Figure 9.2 Estimation of pile shaft resistance using different methods.

This indicates that Aoki and Velloso's method produces very conservative results in the estimation of the shaft resistance compared to the LCPC method. The LCPC method was studied by several authors (Briaud et al. 1989, Milovic and Milovic 1993), and was found to be satisfactory.

9.2.3 Factor of safety

The selection of factors of safety in pile design is an important. In general, large factors of safety may be required in the following cases (Canadian Geotechnical society 1992):

(1) friction piles in clay;
(2) sites where only a limited number of tests are performed and where soil conditions are variable;
(3) piles in loose sands and silts for which the capacity may decrease with time.

When the pile load capacity is determined from field tests including in-situ tests and pile load tests, factors of safety in the 2 to 3 range have been proposed (Broms et al. 1988, Canadian Geotechnical society 1992). Table 9.1 shows the values of factor of safety proposed by Canadian Geotechnical society (1992) as a function of the type of field test, based on the ultimate pile load capacity corresponding to an ultimate limit state. In the table, f_p is referred to as the resistance modification factor representing the ratio of allowable pile load capacity to ultimate pile load capacity.

Some authors have proposed the use of the partial factors of safety. As mentioned earlier, the shaft resistance, in most cases, is fully mobilized before the base resistance reaches a limit state. Based on this observation, the use of separate factors of safety for the base and the shaft resistance is sometimes suggested to artificially account for the different rates of mobilization of shaft and base resistance.

Table 9.1 Resistance modification factor f_p and factor of safety for different field tests (after Canadian Geotechnical Society 1992).

Type of filed test	f_p	Factor of safety
Cone penetration test	0.5	2
Standard penetration test	0.3	3.3
Static pile load test (routine test)	0.5	2
Static pile load test (high technical level test)	0.6	1.7
Dynamic analysis using measured data of strain and acceleration	0.5	2

According to Franke (1993), the allowable design pile load capacity is given by:

$$Q_d = \frac{Q_u}{FS_g} = \frac{Q_b}{FS_b} + \frac{Q_s}{FS_s} \tag{9.1}$$

where Q_d = allowable design pile load capacity

Q_u = unfactored pile load capacity

FS_g = global factor of safety

FS_b = factor of safety for the base resistance

FS_s = factor of safety for the shaft resistance

Q_b = base resistance from a limit state

Q_s = shaft resistance.

Since

$$Q_u = Q_b + Q_s \tag{9.2}$$

the following relationship can be obtained:

$$FS_g = \frac{FS_b \cdot FS_s \cdot (1 + \frac{Q_b}{Q_s})}{FS_s + FS_b \cdot \frac{Q_s}{Q_b}} \tag{9.3}$$

If $FS_g = 2$ and $FS_s = 1$ are assumed, FS_b is obtained as in Table 9.2. From (9.3) and Table 9.2 it can be seen that for a constant global safety factor no unique value of factor of safety for the base resistance is obtained when partial safety factors are used and Q_b/Q_s is allowed to vary.

Table 9.2 Partial factor of safety for the base resistance.

Q_s/Q_b	0	0.2	0.4	0.8	0.6	1.0	>1
FS_b	2	2.5	3.33	5	10	∞	<0

Since the goal in design is to achieve a target level of safety (say $FS_g = 2$), the use of partial safety factors is yet variable, as fixed values of FS_b and FS_s would produce different levels of global safety depending on the relative contribution of base and shaft resistance to pile capacity.

9.3 Use of SPT Blow Counts in CPT-based Method

The method for estimating pile load capacity proposed in this study is based on the cone penetration resistance q_c. Although the CPT is a superior test for pile design, SPT is still widely used in many geotechnical engineering projects. If the proper correlation between the SPT blow count N and the cone penetration resistance q_c can be established, the CPT pile design methods can also make use of the SPT blow count N data. This approach may be subjected to more uncertainties, but is believed to be useful in design.

A useful CPT-SPT correlation was proposed by Robertson and Campanella (1983). According to Robertson and Campanella (1983), the ratio of the cone resistance q_c to the SPT blow count N is not a constant, varying with the mean grain size (D_{50}). Since considerable scatter was found in the values of the q_c/N ratio for silty clay, they suggested that the q_c/N ratio be used for sandy soils. Figure 9.3 shows the q_c/N ratio with respect to mean grain size.

As can be seen in the figure, the value of q_c/N increases as the mean grain size increases. For sands, the values of the q_c/N ratio were in the 4 – 6 range while those for silty sand were in the 3 – 4 range.

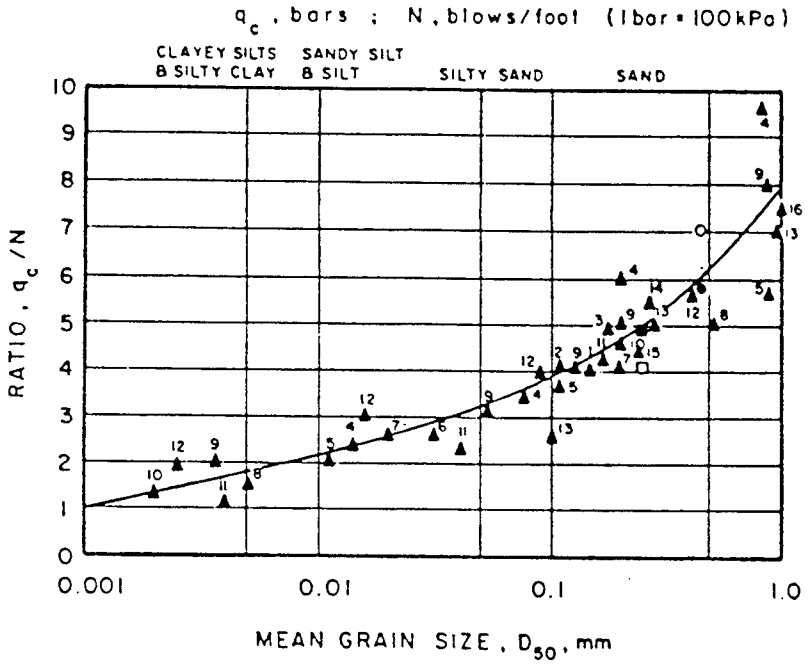

Figure 9.3 CPT-SPT correlation with the mean grain size (after Robertson and Campanella 1983).

For further investigation of the value of the q_c/N ratio, both CPT and SPT were performed at the same site. The site was located at US State route 66 over Garvin Street, Evansville, Indiana. The tests were performed under the North East end of the bridge, on the grassy area next to the bridge wall. Both CPT and SPT boring logs indicate that the test site mostly consists of sandy soil down to about 20 m. The ground was very hard to penetrate in the first few feet, making it difficult to anchor down the CPT rig. The starting test depth appeared to be at the same elevation as all the surrounding terrain. No appreciable presence of fill material was observed.

Two sand samples were obtained using the CPT soil sampler. Both samples were taken at a depth of from 14.0 m down to 14.7 m. Some of the standard laboratory tests were performed with these soil samples, including grain size distribution analysis, the maximum and minimum void ratio tests, and the specific gravity test. The mean grain size (D_{50}) was about 0.3 mm, and the maximum and minimum void ratios were 0.826 and 0.454, respectively.

Figure 9.4 shows the SPT blow counts N and the cone resistance q_c with depth. The corresponding values of q_c/N for this site are given in Table 9.3. Since the SPT N values in Figure 9.3 were based on the energy ratio of 55%, the values of N_{60}, which was corrected for the energy ratio of 60%, were used for the calculation of the q_c/N ratio in Table 9.3. As can be seen, the lowest value of q_c/N was about 1.15 at a depth of 4.33 m and the highest one was about 14.96 at a depth of 13.47 m. Most the q_c/N ratios, however, were observed in the 3 – 8 range. The averaged q_c/N ratio without including the lowest and highest values of q_c/N was approximately 5.63. This value appears to be in reasonable agreement with the value for sand given in Figure 9.3 by Robertson and Campanella (1983). This result is one more indication that the correlation of Figure 9.3 can be used for CPT pile design using the SPT blow count N for Indiana soils.

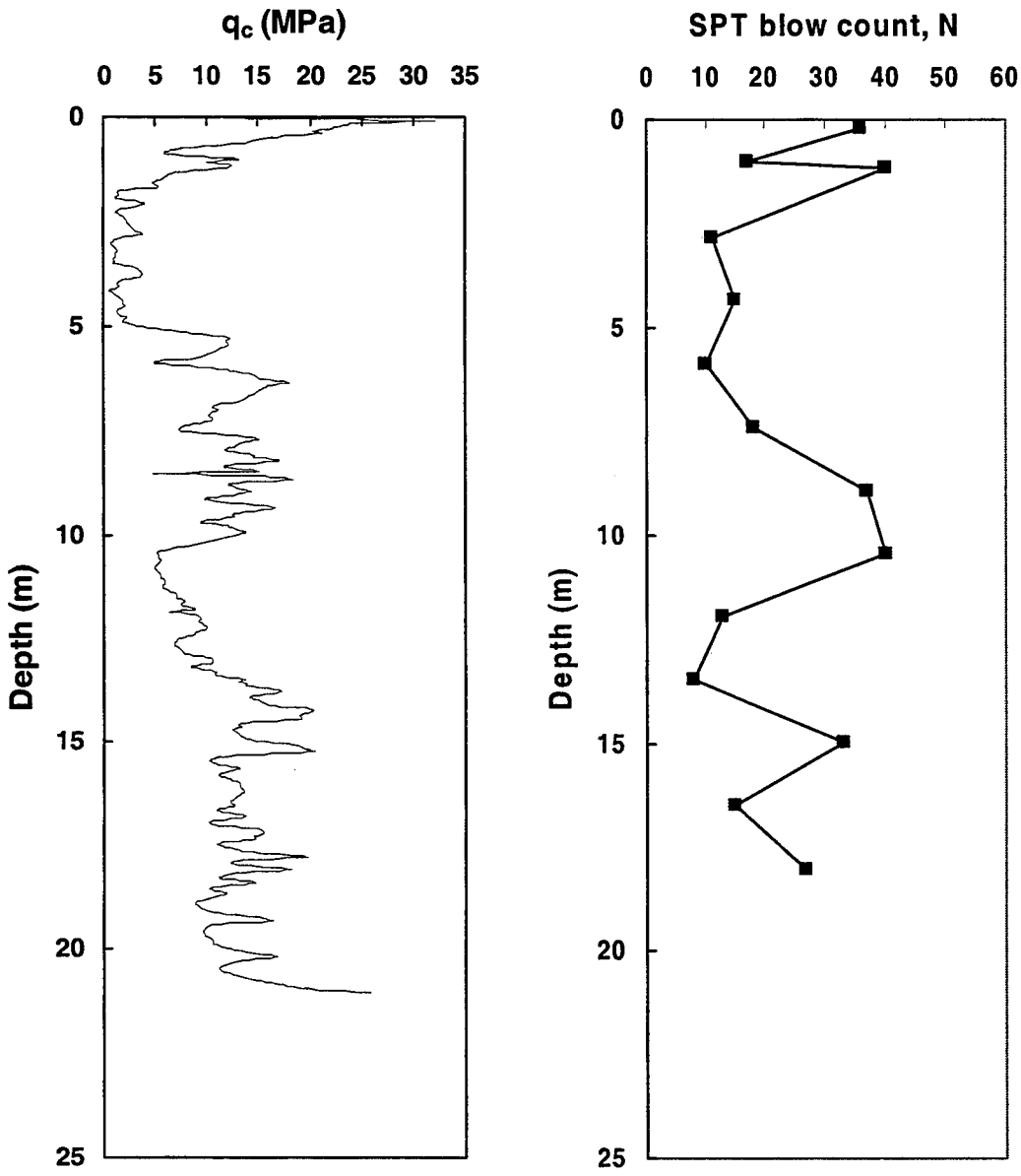

Figure 9.4 Cone resistance q_c and SPT blow count N with depth.

Table 9.3 Correlation between CPT and SPT.

Depth (m)	N	N_{60}[a]	q_c (bar)[b]	q_c/N_{60}
0.21	36	33.12	236.9	7.12
0.98	17	15.64	112.0	7.16
1.12	40	36.80	120.0	3.26
2.80	11	10.12	26.7	2.63
4.33	15	13.80	16.0	1.15
5.85	10	9.20	49.8	5.40
7.38	18	16.56	85.0	5.10
8.90	37	34.04	138.5	4.10
10.42	40	36.80	55.6	1.51
11.95	13	11.96	88.7	7.4
13.47	8	7.36	110.0	14.96
14.99	33	30.36	146.6	4.8
16.52	15	13.80	120.0	8.7
18.04	27	24.84	156.7	6.3

N_{60}[a] = SPT N value corrected for the energy ratio of 60%

bar[b] = 100 kPa

9.4 Program CONEPILE

For the effective use of the CPT-based pile design method proposed in this study in practice, it was programmed together with other methods discussed herein in program "CONEPILE". Calculation of both base and shaft resistances is addressed in the program. The methods available in the program CONEPILE are:

for the calculation of the base resistance,

(1) Aoki and Velloso's method;
(2) LCPC method;
(3) proposed method;

for calculation of the shaft resistance,

(1) Aoki and Velloso's method;
(2) LCPC method.

Program CONEPILE can be used to calculate base and shaft resistances for both non-displacement and displacement piles. Users can select a preferred method to use for a given soil condition and pile type.

The program CONEPILE consists of two different programs: a user-friendly interface program for pre- and post-processing, and the FORTRAN code used in actual calculation. The user-friendly interface program was developed using Visual-C for easy input and output data processing.

For Aoki and Velloso's method and the LCPC method, the correlation parameters given in Tables 2.1, 2.2, 2.5, and 2.6 were included in the program CONEPILE as a form of table. For the calculation of base resistance using the proposed method, regression equations matching with the normalized load-settlement curves shown in Figure 7.9 were used. The regressions were made with fourth order polynomials, and the square of the coefficient of correlation (r^2) were about 0.999. Several intermediate steps were also

used in the program. These include the estimation of the relative density, the correction for the coefficient K_0 of lateral earth pressure at rest, and the calculation of the base resistance ratio for displacement piles. Since the effect of the pile length or the confining stress at the pile base level appeared to be small (as can be seen in Figure 7.10), it was not considered for calculating the base resistance.

The estimation of relative density was made using the following relationship by Salgado et al. (unpublished paper):

$$q_c = C_1 (P_a)^{1-C_2} \sigma_h^{\ 2} \exp(C_3 D_R) \tag{9.4}$$

where q_c = cone resistance; C_1, C_2, and C_3 = correlation parameters; P_a = reference stress = 100 kPa = 0.1 MPa ≈ 1 tsf; σ_h = effective horizontal stress; and D_R = relative density. The correlation parameters C_1, C_2, and C_3 are given in Table 9.4. Using (9.4), the relative density can be obtained for a given stress state and cone resistance q_c (which need to be assigned as input data for the program CONEPILE). The estimated relative density is then used for calculating the normalized base resistance q_b/q_c.

The correction for K_0 was based on the relationship shown in Figure 7.11. Because the effect of K_0 was small for relative densities greater than 70%, it was only considered for relative densities less than 70%. Figure 9.5 shows the procedure for the estimation of the base resistance using the proposed method. More detailed information for the program CONEPILE are given in Appendix.

Table 9.4 Correlation parameters for estimation of relative density.

	Friction angle at the critical state (ϕ_c)						
	30°	31°	32°	33°	34°	35°	36°
C_1	40.0	44.7	49.7	55.3	61.6	68.6	76.4
C_2	0.524	0.519	0.514	0.508	0.501	0.496	0.490
C_3	0.0195	0.0196	0.0197	0.0197	0.0198	0.0199	0.02

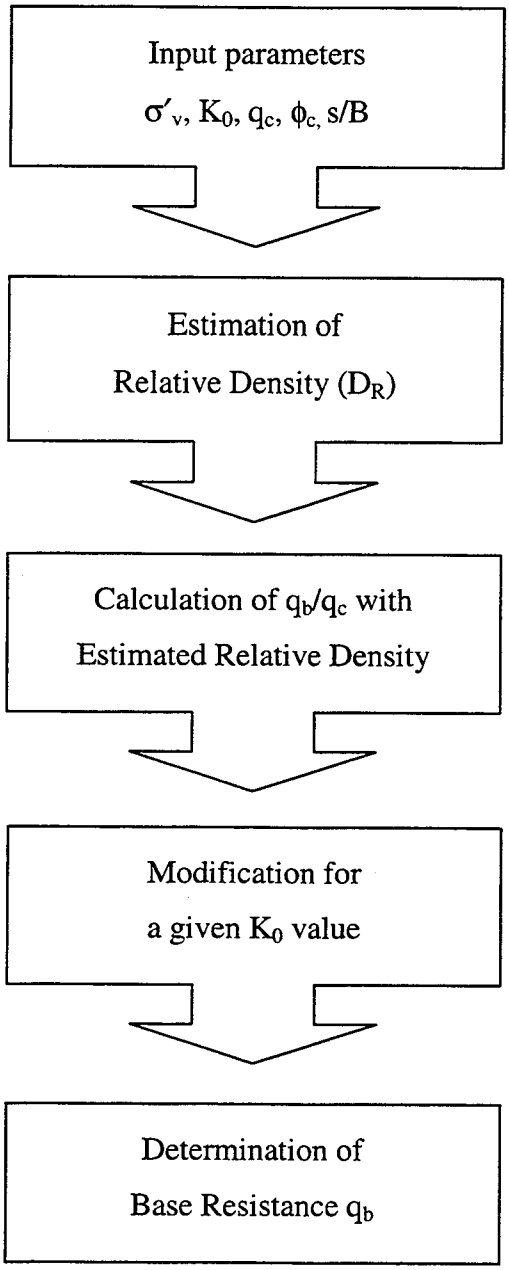

Figure 9.5 Estimation of the base resistance for a given soil condition.

9.5 Summary

In this chapter, the design of piles using CPT results was discussed. Since the CPT methods available for pile design were developed under different conditions, the selection of the method should take into account the differences and recommendations of the methods.

From the example for calculating the base resistance, it was observed that the highest value of q_b was obtained from the Dutch method while the lowest one was obtained from the method proposed in this study. The lowest base resistance obtained from the proposed method was based on a relative settlement s/B equal to 10%. For the shaft resistance, Aoki and Velloso's method produced lower values compared with the LCPC method. A global factor of safety (and not partial base and shaft factors of safety) was found to be more correct for use in pile design.

For more general use of CPT-based pile design methods, a correlation between the SPT blow count N and the cone resistance q_c can be used. Field SPT and CPT test data for an Evansville sandy soil site suggests the correlation between q_c and N proposed by Robertson and Campanella (1983) is likely applicable to Indiana sandy deposits.

The program CONEPILE developed for the estimation of the pile load capacity was introduced. This program has a user-friendly interface, which controls an underlying FORTRAN-based DLL.

CHAPTER 10 SUMMARY, CONCLUSIONS AND RECOMMENDATIONS

10.1 Summary

Pile foundations are often used for supporting large, heavy superstructures at sites where competitively priced shallow foundations would lead to excessive settlements. Based on the method of installation, piles are classified as either displacement or non-displacement. The bearing capacity of both displacement and non-displacement piles consists of both base resistance and side resistance. The side resistance of piles is in most cases fully mobilized well before the maximum base resistance is reached. As the side resistance is mobilized early in the loading process, the determination of pile base resistance is a key element of pile design.

Pile design methods using in-situ test results have been mainly based on the standard penetration test (SPT) and the cone penetration test (CPT). SPT blow counts result from dynamically driving a standard sampler one foot into the ground. Such a process is not well related to the quasi-static pile loading process. Static cone penetration, on the other hand, is better related to the pile loading process. The test is performed quasi-statically and resembles a scaled-down pile load test. In the present study, in order to take advantage of the CPT for pile design, load-settlement curves of axially loaded piles bearing in sand were developed in terms of normalized base resistance (q_b/q_c) versus relative settlement (s/B). Cone resistance q_c used to normalize the load-settlement curves was determined from the penetration resistance analysis of Salgado et al. (1997a) using the program CONPOINT. The limit state concept has been proposed as a modern design approach, in which the adequate technical quality of

foundations and superstructures is considered. Although the limit state design concept for pile design has been used mostly with respect to either s/B = 5% or s/B = 10%, the normalized load-settlement curves obtained in this study allow determination of pile base resistance at any relative settlement level within the 0 – 20% range. The normalized base resistance for both non-displacement and displacement piles were addressed.

In order to obtain the pile base load-settlement relationship, a 3-D non-linear elastic-plastic constitutive model was used in finite element analyses. The 3-D non-linear elastic-plastic constitutive model takes advantage of the intrinsic and state soil variables that can be uniquely determined for a given soil type and condition. This non-linear stress-strain model represents changes of elastic parameters (the shear modulus G and the bulk modulus K) according to the stress level before a failure condition is reached. For the description of failure and post-failure soil response for the three-dimensional stress state, the Drucker-Prager plastic model with non-associate flow rule was used.

Calibration chamber tests have been used to investigate both the load-settlement response of the base of non-displacement piles and cone penetration resistance under a variety of conditions. Because calibration chambers have finite sizes, the possibility of size and boundary effects arises. If size effects are well understood, calibration chambers can be used to experimentally assess pile base resistance under controlled conditions. A series of calibration chamber tests were modeled and analyzed using the finite element approach with the 3-D non-linear elastic-plastic stress-strain model. The analytical results were compared with the measured values of plate resistance in calibration chamber plate load tests. The predicted load-settlement curves showed good agreement with measured load-settlement curves. Calibration chamber size effects were also investigated for different relative densities and boundary conditions using the finite element analysis.

For effective use of the CPT pile design methods in practice, the method proposed in this study and some of existing methods reviewed in study were programmed with the user-friendly interface procedure. This program can be used in practice to estimate pile

load capacity for a variety of pile and soil conditions without significant difficulties for input and output procedure.

10.2 Conclusions

Based on findings of the present study, the following conclusions are drawn.

(1) The values of the parameters f and g for the 3-D non-linear elastic-plastic stress-strain model vary according to the relative density level. As the relative density increases, the value of f decreases while the value of g increases. This indicates that the ratio of the elastic modulus at failure to its initial value is higher for denser than for looser sand, and the rate of degradation of elastic modulus is higher for looser than for denser sand;

(2) Plate unit loads in calibration chamber tests tend to be lower (for BC1, BC4) and higher (for BC2, BC3) than pile base unit loads. The confining stress level at the pile base level also influences calibration chamber size effect. The calibration chamber size effects under BC1 were more pronounced at low confinement, corresponding to shorter piles, while size effects under BC2 were more pronounced at high confinement, corresponding to longer piles;

(3) The value of the normalized base resistance q_b/q_c is not a constant, varying as a function of the relative density, the confining stress, and the coefficient of lateral earth pressure at rest;

(4) The values of the normalized base resistance q_b/q_c for non-displacement piles fall within the 0.07 - 0.13 range for s/B = 5% and the 0.10 - 0.20 range for s/B = 10%;

(5) The effect of relative density on the normalized base resistance q_b/q_c was most significant, while that of the confining stress at the pile base level was small. At higher relative densities, the value of q_b/q_c was smaller (q_b/q_c = 0.12 - 0.13 for D_R = 90%) than at lower relative densities (q_b/q_c = 0.19 - 0.2 for D_R = 30%);

(6) The values of the normalized base resistance q_b/q_c for displacement piles are higher than those for non-displacement piles, showing typically the 0.15 - 0.25 range for s/B = 5% and the 0.22 - 0.35 range for s/B = 10%;

(7) The value of the normalized base resistance q_b/q_c tends to decrease as the coefficient of lateral earth pressure at rest (K_0) increases. This trend is more pronounced at lower relative densities, and negligible for very dense sand;

(8) The values of the normalized base resistance q_b/q_c for silty sands are in the 0.12 – 0.17 range, depending on the relative density and the confining stress at the pile base level. The confining stress is another important factor that influences the value of q_b/q_c for silty sands. For lower relative density, the value of q_b/q_c decreases as the pile length increases while that for higher relative density increases;

(9) Field test results of both SPT and CPT performed at the same site show reasonable agreement with the correlation proposed by Robertson and Campanella (1983). This indicates that CPT pile design method can be used with the SPT blow count N for practical purpose, if the proper value of q_c/N can be obtained for a given soil condition.

10.3 Recommendations

(1) Since pile design methods using in-situ test results were developed under different conditions, the selection of the method should be made with consideration of the differences between the methods, such as:

- the criterion adopted to define pile load capacity;
- the type of equipment used to obtain q_c;
- the selection and relative importance of q_c values above and below the pile base;
- soil types and conditions under which the methods were developed;

(2) Use of global factor of safety is more suited to pile design if a target level of safety is aimed in design irrespective of the relative contribution of base and shaft resistances to total pile capacity;

(3) The relative density is the most important factor influencing the base resistance of piles in sands. It is, therefore, recommended that the estimation of the relative density be made through a reasonable correlation with in-situ tests such as CPT, since it is very difficult to obtain undisturbed granular soil samples;

(4) Piles typically undergo relative settlements s/B greater than 10% to reach a limit state corresponding to either a loss of functionality of structures or damage to superstructures and/or foundations. However, the evaluation of the relative settlement associated with the limit states design of piles should be done with consideration of the type, functionality, location, and importance of structures.

LIST OF REFERENCES

AASHTO (1994). AASHTO LRFD Bridge Design Specification.

Albiero, J. H., Sacilotto, A. C., De Mantilla, J. N. R., Teixeira, C. Z., and Carvalho, D. (1995). "Successive Load Tests on Bored Piles", Proceedings of X Pan-American Conference of Soil Mechanics and Foundation Engineering, Guadalajara, Vol. 2, pp. 991 – 1002.

Aoki, N. and Velloso, D. A. (1975). "An Approximate Method to Estimate the Bearing Capacity of Piles", Proceedings of 5th Pan-American Conference of Soil Mechanics and Foundation Engineering, Bueno Aires, Vol. 1, 367 – 376.

Baldi, G., Bellotti, R., Ghiona, V.N., Jamiolkowski, M., and LoPresti, D.C.F. (1989). "Modulus of Sands from CPT and DMT", Proceedings of 12th International Conference on Soil Mechanics and Foundation Engineering, Balkema, Rotterdam, Vol. 1, pp 165-170.

Baligh, M.M. (1975). "Theory of Deep Static Cone Penetration Resistance", Report No. R75-56, Department of Civil and Environmental Engineering, Massachusetts Institute of Technology, Cambridge, Mass.

Bandini, P. (1999). "Static Response and Liquefaction of Silty Sands", Master Thesis, Purdue University, West Lafayette, IN.

Bandini, P. and Salgado, R. (1998). "Methods of Pile Design Based on CPT and SPT results", Proceedings of 1st International Conference on Site Characterization (P. Robertson and P. Mayne ed.), Balkema, Rotterdam, pp. 967 – 976.

BCP Committee. (1971). "Field Tests on Piles in Sand", Soils and Foundation, 11(2), 29 - 49.

Been, K., Jefferies, M.G., and Hachey, J. (1991). "The Critical State of Sands", Geotechnique, 41(3), 365-381.

Been, K., Crooks, J.H.A., Becker, D.E., and Jefferies, M.G. (1986). "The Cone Penetration Test in Sands: Part I; State Parameter Interpretation", Geotechnique, 36(2), 239 – 249.

Bellotti, R., Jamiolkowski, M., Lo Presti, D.C.F., and O'Neill, D.A. (1996). "Anisotropy of Small Strain Stiffness in Ticino Sand", Geotechnique, 46(1), 115-131.

Berezantev, K. and Golubkov (1961). "Load Bearing Capacity and Deformation of Piles Foundations", Proceedings of 5th International Conference on Soil Mechanics and Foundation Engineering, Vol. 1, pp. 11.

Biarez, J., Burel, M., and Wack, B. (1961). "Contribition A L'etude De La Force Portante Des Fondations", Proceedings of 5th International Conference on Soil Mechanics and Foundation Engineering, Vol. 1, 603 – 609.

Bolton, M. D. (1979). *A Guide to Soil Mechanics*, Macmillan Inc., Greenwich, Conn.

Bolton, M.D. (1986). "The Strength and Dilatancy of Sands", Geotechnique, 36(1), 65-78.

Bolton, M.D. (1989). "The development of codes of practice for design", Proc. of 12th International Conference on Soil Mechanics and Foundation Engineering, Vol.3, Balkema, Rotterdam, pp. 2073 – 2076.

Borja, R. I., Lee, S. R. and Seed, R. B. (1989). "Numerical Simulation of Excavation in Elastoplastic Soils", International Journal for Numerical and Analytical Methods in Geomechanics, 13(3), 231 – 249.

Bowles, J. E. (1988). *Foundation Analysis and Design*, McGraw-Hill Book Company, Singapore.

Bozozuk, M. (1978). "Bridge Foundation Move", TRR 678, Transportation Research Board, pp. 17 –21.

Briaud, J. L. and Tucker, L. (1984), "Piles in Sand: A Method Including Residual Stresses", Journal of Geotechnical Engineering, ASCE, 110(11), 1666 – 1680.

Briaud, J. L. and Gibbens, R. (1994), "Test and Prediction Results for Five Large spread Footings on Sand", Proceedings of a Prediction Symposium Sponsored by the Federal Highway Administration at the Occasion of the Settlement '94 ASCE Conference at Texas A&M University, ASCE, Geotechnical Special Publication No. 41, pp. 92 - 128.

Briaud, J. L. and Jeanjean, P. (1994). "Load Settlement Curve Method for Spread Footings on Sand", Proceedings of Settlement '94, Vertical and Horizontal Deformations of Foundations and Embankments, ASCE, Vol. 2, pp. 1774 – 1804.

Briaud, J.L, Moore, B.H, and Mitchell, G.B (1989). "Analysis of Pile Load Tests at Lock and Dam 26", Proceedings of the Congress, Foundation Engineering: Current Principles and Practices, ASCE, Vol. 1, pp. 925 – 942.

Brinch Hansen, J. (1963). "Discussion, Hyperbolic Stress-Strain response, Cohesive Soil", Journal of Soil Mechanics and Foundation Engineering Division, ASCE, 89(SM4), 241 – 242.

Broms, B.B., Chang, M.F., and Goh, A.T.C. (1988). "Bored Piles in Residual Soil and Weathered rocks in Singapore", Proceedings of the 1st International Geotechnical Seminar on Deep Foundations on Bored and Auger Piles (Van Impe, ed.), Balkema, Rotterdam, pp. 17 – 34.

Burland, J. B. (1973). "Shaft Friction of Piles in Clay – A Simple Fundamental Approach", Ground Engineering, 6(3), 30 –42.

Burland, J.B. and Wroth, O.P. (1974). "Allowable and differential settlement of structures, including damage and soil-structure interaction", Proc. of Conference on Settlement of Structures, Cambridge University, pp. 611 – 654.

Bustamante, M. and Gianeselli (1982). " Pile Bearing Capacity Prediction by Means of Static Penetration CPT", Proceedings of 2nd European Symposium on Penetration Testing, Amsterdam, Vol. 2, 493 – 500.

Butler, H.D. and Hoy, H.E. (1977). "Users Manual for the Texas Quick-Load Method for Foundation Load Testing", Federal Highway Administration, Office of Development, Washignton, pp. 59.

Campanella, R.G., Robertson, P.K., Davies, M.P., and Sy, A. (1989). "Use of In Situ Tests in Pile Design", Proceedings of International Conference on Soil Mechanics and Foundation Engineering, pp. 199 – 203.

Canadian Geotechnical Society (1992). *Canadian Foundation Engineering Manual*, The Canadian Geotechnical Society, Canada.

Chen, W. F. and Baladi, G. Y. (1985). *Soil Plasticity: Theory and Implementation*, Elsevier Science Publishing Company Inc. New York.

Chen, W. F. and Han, D. J. (1988). *Plasticity for Structural Engineers*, Springer-Verlag New York Inc. Virginia.

Chin, F.V. (1970). "Estimation of the Ultimate Load of Piles Not Carried to Failure", Proceedings of 2nd Southeast Asian conference on Soil Engineering, pp. 81 – 90.

Coduto, D.P. (1994). *Foundation Design: Principles and Practices*, Prentice Hall, Englewood Cliffs, New Jersey.

Coyle, N. M. and Castello, R. R. (1981). "New Design Correlations for Piles in Sand", Journal of the Geotechnical Engineering Division, ASCE, 107(GT7), 965 - 986.

Davisson, M.T. (1972). "High Capacity Piles", Proceedings, Lecture Series, Innovation in Foundation Construction, ASCE, Illinois Section, pp. 52.

DeBeer, E.E. (1948). "Donness Concarnat La Resistance An Oisaillement Decluities Des En Ais De Penetration En Profondeur", Geotechnique, 1, 22 – 40.

De Beer, E.E. (1967). "Proefondervindelijke Bijdrage tot de studie van zand onder funderingern op staal", Tijdshrift der Openbar Werken van het grensdraag vermogen van Beigie Nos 6-67 and 1-, 4-, 5-, 6-68.

De Beer, E.E. (1984). "Different Behavior of Bored and Driven Piles", Proceedings of VI Conference on Soil Mechanics and Foundation Engineering, Budapest (G. Petrasovits ed.), pp. 307 – 318.

De Beer, E.E. (1988). "Different Behavior of Bored and Driven Piles", Proceedings of Deep Foundation on Bored and Auger Piles (Van Impe ed.), Ghent, pp. 47 - 82.

De Mello, V.F.B. and Aoki, N. (1993). "Updating Realism on Large-Diameter Bored Piles", Proceedings of 2nd International Geotechnical Seminar on Deep Foundations on Bored and Auger Piles (Van Impe, ed.), Balkema, Rotterdam, pp. 35 – 42.

DeRuiter, J. and Beringen, F. L. (1979). " Pile Foundations for Large North Sea Structures", Marine Geotechnology, 3(3), 267 – 314.

Desai, C.S. and Christian, J. T. (1977). *Numerical Methods in Geotechnical Engineering*, Mcgraw-Hill Inc., New York.

Desai, C. S. and Siriwaden, H. J. (1984). *Constitutive Laws for Engineering Materials with Emphasis on Geologic Materials*, Pretice Hall, Englewood, Cliffs.

Duncan, J. M. and Chang, C. Y. (1970). "Nonlinear Analysis of Stress-Strain in Soils", Journal of Soil Mechanics and Foundation Enigineering Division, ASCE, 96(SM5), 1629 – 1653.

Duncan, J.M. and Tan, C.K. (1991). "Engineering manual for estimating tolerable movements of bridges", Manuals for the Design of Bridge Foundations, NCHRP Report No. 343, Transportation Research Board, National Research Council, Washington, D.C., pp. 219 – 228.

Durgunoglu, H.T. and Mitchell, J.K. (1975). "Static Penetration Resistance of Soils I: Analysis", Proceedings of ASCE Special Conference on In Situ Measurement of Soil Properties, ASCE, New York, Vol. 1, 151 – 171.

Eurocode 1 (1993). "Basis of design and actions on structures", Sixth Draft, European Committee for Standardization, TC 250.

Eurocode 7 (1993). "Geotechnical Design", Fourth and Final Draft, European Committee for Standardization, TC 250/SC7.

Fahey, M., and Carter, J.P. (1993). "A Finite Element Study of the Pressuremeter Test in Sand Using a Non-Linear Elastic Plastic Model", Canadian Geotechnical Journal, 30(2): 348-361.

Fahey, M., Robertson, P.K., and Soliman, A.A. (1994). "Towards a Rational Method of Predicting Settlements of Spread Footing on Sand", Vertical and Horizontal Deformation of Foundation and Embankments, ASCE, Geotechnical Special Publication No. 40, Vol. 1, pp. 599-611.

Fellenius, B. (1975). "Test Loading of Piles and New Proof Testing Procedure", Journal of the Geotechnical Engineering Division, ASCE, 101(GT9), 855 – 869.

Fellenius, B.H. (1980). "The Analysis of Results from Routine Pile Load Tests", Ground Engineering, Sep. pp. 19 – 31.

Fioravante, V., Ghionna, V. N., Jamiolkowski, M. and Pedroni, S. (1995). "Load Carring Capacity of Large-Diameter Bored Piles in Sand and Gravel", Proceedings of X Asian Regional Conference in Soil Mechanics and Foundation Engineering, pp. 1-13.

Franke, E. (1989). "Co-Report to Discussion, Session B, on Large Diameter Piles", 12th ICSMFE, Rio de Janeiro, Brazil.

Franke, E. (1990). "THE EUROCODE – SAFETY APPROACH AS UPRIGHT TO FOUNDATIONS", Proc. of 9th Danube-European Conference on Soil Mechanics and Foundation Engineering, AKADEMIAI KIADO, Budapest, pp. 173 – 182.

Franke, E. (1991). "EUROCODE Safety Approach as Applied to single Piles", Proc. of 4th International DFI Conference, Balkema, Rotterdam, pp. 13 – 18.

Franke, E. (1993). "Design of Bored Piles, Including Negative Skin Friction and Horizontal Loading", Proceedings of 2nd International Geotechnical Seminar on Deep Foundations on Bored and Auger Piles (Van Impe, ed.), Balkema, Rotterdam, pp. 43 – 57.

Ghionna, V. N., Jamiolkowsi, M., Lancellotta, R. and Pedroni, S. (1993). "Base Capacity of Bored Piles in Sands from In-Situ Tests", Proceedings of 2nd International Geotechnical Seminar on Deep Foundations on Bored and Auger Piles (Van Impe ed.), Balkema, Rotterdam, pp. 67 –74.

Ghionna, V. N., Jamiolkowsi, M., Pedroni, S. and Salgado, R. (1994). "The Tip Displacement of Drilled Shafts in Sands", Proceedings of Settlement '94 (Yeung and Felio ed.), Vol. 2, Geotechnical Engineering Division, ASCE, June, pp. 1039 – 1057.

Gibbens, R. and Briaud, J. (1994). "Data and Prediction Request for the Spread Footings Prediction Events", Proceedings of a Prediction Symposium Sponsored by the Federal Highway Administration at the Occasion of the Settlement '94 ASCE Conference at Texas A&M University, ASCE, Geotechnical Special Publication No. 41, pp. 11 - 85.

Giuseppe, B. (1991). "Modellazione Numerica Delle Prove Pressiometriche In Camera Di Calibrazione Per La Sabbia Del Ticino", Graduate School Thesis, Politecnico Di Torino, Italy.

Goble, G. G., Kovacs, A. M., and Rausche, F. (1972). "Field Demonstration: Response of Instrumented Piles to Driving and Load Testing", Proceedings of Specialty Conference on Performance of Earth and Earth-Supported Strfuctures, Vol. 3, ASCE, pp. 3 –38.

Gregersen, O. S., Aas, G., and Dibiagio, E. (1973). "Load Tests on Friction Piles in Loose Sand", Proceedings of the 8th International Conference on Soil Mechanics and Foundation Engineering, Vol. 2, USSR, pp. 109 - 117.

Grover, R.A. (1978). "Movements of Bridge Abutments and Settlements of Approach slabs in Ohio", Transportation Research Board 678, Tolerable Movements of Bridge Foundation, Sand Drains, K-Test, Slopes, and Culverts, Transportation Research Board, Washington, D.C., pp. 12 – 17.

Hardin, B. O. and Black, W. L. (1966). "Sand Stiffness under Various Triaxial Stresses", Journal of Soil Mechanics and Foundation Engineering Division, ASCE, 92(SM2), 27 - 42.

Hardin, B.O. and Drnevich, V. P. (1972). "Shear Modulus and Damping in Soils; Design Equations and Curves", Journal of Soil Mechanics and Foundations Division, ASCE, 98(7), 667 – 692.

Hardin, B.O., and Richart, F.E. (1963). "Elastic Wave Velocities in Granular Sands", Journal of Soil Mechanics and Foundation Engineering Division, ASCE, 89(SM1), 33-65.

Harris, D. E. and Mayne, P. W. (1994). "Axial Compression Behavior of Two Drilled Shafts in Piedmont Residual Soils", Proceedings of International Conference Design and Construction of Deep Foundations, Vol.2, Orlando, pp. 352 – 367.

Harrop-Williams, K. (1989). "Risk Correction Factors for Bearing Capacity Analysis", Proceedings of the Congress on Foundation Engineering (H. Kulhawy ed.), Vol. 2, ASCE, pp. 848-856.

Hirany, A. and Kulhawy, F.H. (1989). "Interpretation of Load Tests on Drilled Shafts Part 1: Axial Compression", Proceedings of the Congress on Foundation Engineering (H. Kulhawy ed.), Vol. 2, ASCE, pp. 1132 - 1149.

Horvitz, G.E., Stettler, D.R., and Crowser, J.C. (1981). "Comparison of Predicted and Observed Pile Capacity", Proceedings of a Session Sponsored by the Geotechnical Engineering Division at the ASCE National Convention, pp. 413 – 433.

Hu, G. (1965). "Bearing Capacity of Foundations with Overburden Shear", Sols-Soils, No. 13, 11 – 18.

Jamiolkowski, M. and Lancellotta, R. (1988). "Relevance of In-Situ Test Results for Evaluation of Allowable Base Resistance of Bored Piles in Sands", Proceedings of I International Geotechnical Seminar on Deep Foundations on Bored and Auger Piles (Van Impe ed.), Ghent, pp. 107 – 120.

Janbu, N. (1963). "Soil Compressibility as Determined by Oedometer and Triaxial Tests", Proceedings of European Conference on Soil Mechanics and Foundation Engineering, Wiesbaden, Germany, Vol.1, pp. 19-25.

Kondner, R. L. (1963). "Hyperbolic Stress-Strain Response: Cohesive Soil", Journal of Soil Mechanics and Foundation Engineering Division, ASCE, 189(SM1), 115 – 143.

Lambe, W.T. and Whitman, R.V. (1986). *Soil Mechanics, SI Version*, John Wiley and Sons, Korea.

Lee, C. Y., Allman, M. A. and Poulos, H. G. (1989). "Static Behavior of Piles in Cemented Calcareous Sands", Proceedings of the 1989 Foundation Engineering Congress, Vol. 1, ASCE, New York, pp. 485 – 499.

Lee, J. H. and Salgado, R. (1999a). "Analysis of Calibration Chamber Plate Load Tests", Canadian Geotechnical Journal, December.

Lee, J. H. and Salgado, R. (1999b). "Determination of Pile Base Resistance in Sands", Journal of Geotechnical and Geoenvironmental Engineering, ASCE, August.

Lee, J. H. and Salgado, R. (1999c). "Pre-failure Loading Response of Foundations on Sand", Proceedings of 2nd International Symposium on Pre-Failure Deformation characteristics of Geomaterials, Torino, Accepted for publication.

Lee, J. H., Salgado, R., Bernal, A., and Lovell, C.W (1999). "Shredded Tires and Rubber-Sand as Lightweight Backfill", Journal of Geotechnical and Geoenvironmental Engineering, ASCE, 125(2), 132 – 141.

Mayne, P. W. and Harris, D. E. (1993). "Axial Load-Displacement Behavior of Drilled Shaft Foundation in Piedmont Residium", Technical Report, No. 41-30-2175, FHWA.

Mayne, P.W. and Kulhawy, F.H. (1991). "Calibration Chamber Database and Boundary Effects Correction for CPT Data", Proceedings of the First International Symposium on Calibration Chamber Testing, Elsivier, New York, pp. 257 – 264.

Meyerhof, G. G. (1956). "Penetration Tests and Bearing Capacity of Cohesionless Soils", Journal of Geotechnical Engineering, ASCE, 82(1), 1- 19.

Meyerhof, G. G. (1976). "Bearing Capacity and Settlement of Pile Foundations, Journal of Geotechnical Engineering, ASCE, 102(3), 197 - 228.

Meyerhof, G. G. (1983). "Scale Effect of Ultimate Pile Capacity", Journal of Geotechnical Engineering, ASCE, 109(6), 797 - 806.

Milovic, D.M. and Milovic, S.D. (1993). "Predicted and Observed Behavior of Piles", Proceedings of the 1st International Geotechnical Seminar on Deep Foundations on Bored and Auger Piles, Balkema, Rotterdam, pp. 381 – 384.

Moulton, L.K. (1986). "Tolerable movement criteria for highway bridges", Final Report NO. FHWA-TS-85-228, Federal Highway Administration, Washington, D.C.

Moulton, L.K., GangaRao, H.V.S., and Halvorsen, G.T. (1985). "Tolerable movement criteria for highway bridges", Report No. FHWA/RD-85/107, Federal Highway Administration, Washington, D.C.

Naylor, D.J., Pande, G.N., Simpson, B., and Tabb, R. (1981). *Finite Elements in Geotechnical Engineering*, Pineridge Press, Swansea, Wales, U.K.

Neely, W. (1989). "Bearing Pressure – SPT Correlation for Expanded Base Piles in Sand", Proceedings of Congress Foundation Engineering: Current Principles and Practices, ASCE, Vol. 2, 979 – 990.

Neely, W. (1990). "Bearing Capacity of Expanded-Base Piles in Sand", Journal of Geotechnical Engineering, ASCE, 116(1), 73 - 87.

Neely, W. (1991). "Bearing Capacity of Auger-Cast Piles in Sand", Journal of Geotechnical Engineering, ASCE, 117(2), 331 - 345.

Ovesen, N.K. and Orr, T. (1991). "Limit State Design – The European Perspective", Geotechnical Engineering Congress, Geotechnical special publication No. 27, Vol. 2, ASCE, pp. 1341 – 1352.

Parkin, A.K. (1991). "Chamber Testing of Piles in Calcareous Sand and Silt", Proceedings of the First International Symposium on Calibration Chamber Testing, Elsivier, New York, pp. 289-302.

Polshin, D.E. and Tokar, R.A. (1957). "Maximum allowable non-uniform settlement of structures", Proc. of 4th International Conference on Soil Mechanics and Foundation Engineering, London, Vol. 1, pp. 402 – 406.

Poulos, H. G. (1989). " Developments in the Analysis of Static and Cyclic Lateral Response of Piles", Proceedings of IV International Conference on Numerical Methods in Geomechanics, Vol. 3, Rotterdam, Balkema, pp. 1117 – 1135.

Price, G. and Wardle I. F. (1982). "A Comparison Between Cone Penetration Test Results and the Performance of Small diameter Instrumented Piles in Stiff Clay", Proceedings of 2nd European Symposium on Penetration Testing, Amsterdam, Vol. 2, 775 – 780.

Purzin, A. M. and Burland, J. B. (1996). "A Logarithmic Stress-Strain Function for Rocks and Soils", Geotechnique, 46(1), 157 – 164.

Reese, L. C. and O'neill, M. W. (1988). *Drilled Shafts; Construction Procedures and Design Methods*, Report No. FHWA-HI-88-42, U.S. Dept. of Transportation, Washington D.C.

Reese. L. C. and O'Neill, M. W. (1989). "New Design Method for Drilled Shaft from Common Soil and Rock Test", Proceedings of Congress Foundation Engineering: Current Principles and Practices, ASCE, Vol. 2, 1026 – 1039.

Robertson, P. K. and Campanella, R. G. (1983). "SPT-CPT correlation", Journal of Geotechnical Engineering, 109(11), ASCE, 1449 – 1459.

Robertson, P. K. and Campanella, R. G. (1989). *Guidelines for Geotechnical Design Using the Cone Penetrometer Test and CPT with Pore Pressure Measurement*, 4th ed. Hogentogler & Co., Columbia, MD.

Robertson, P. K., Campanella, R. G., Gillespie, D., and Rice, A. (1985). "Seismic CPT to Measure In-Situ Shear Wave Velocity" Proceedings of Measurement and Use of Shear Wave Velocity for Evaluating Dynamic Soil Properties, ASCE, 34 – 48.

Salgado, R. (1993). "Analysis of Penetration Resistance in Sand", Ph.D. Thesis, Univ. of California, Berkeley, California.

Salgado, R. (1995). "Design of Piles in Sands Based on CPT Results", Proceedings of X Pan-American Conference of Soil Mechanics and Foundation Engineering, Vol. 3, Guadalajara, pp. 1261 – 1274.

Salgado, R., Mitchell, J.K., and Jamiolkowski, M. (1997a). "Cavity Expansion and Penetration Resistance in Sand", Journal of Geotechnical and Geoenvironmental Engineering, ASCE, 123(4), 344-354.

Salgado, R., Boulanger, R. W. and Mitchell, J. K. (1997b). "Lateral Stress Effects on CPT Liquefaction Resistance Correlations", Journal of Geotechnical and Geoenvironmental Engineering, ASCE, 123(8), 726 – 735.

Salgado, R., Drnevich, V.P., Ashmawy, A., Grant, W.P., and Vallenas, P. (1997c). "Interpretation of Large-Strain Seismic Cross-Hole Tests", Journal of Geotechnical and Geoenvironmental Engineering, ASCE, 123(4), 382-388.

Salgado, R., Mitchell, J.K., and Jamiolkowski, M. (1998a). "Chamber Size Effects on Penetration Resistance Measured in Calibration Chambers", Journal of Geotechnical and Geoenvironmental Engineering, ASCE, 124(9), 878 - 888.

Salgado, R., Jamiolkowski, M., and Mitchell, J.K. (1998b). "Penetration Resistance in Sand: Analysis and Applications to Liquefaction Potential Assessment and Estimation of Pile Base Resistance", Rivista Italiana di Geotecnica, Vol, XXXII, No.4, 5 –17.

Salgado, R., Bandini, P. and Karim, A. (1999). "Stiffness and Strength of Silty Sand", Journal of Geotechnical and Geoenvironmental Engineering, ASCE, accepted for publication.

Schmertmann, J. H. (1970). "Static Cone to Compute Static Settlement Over Sand", Journal of Soil Mechanics and Foundation Engineering Division, ASCE, 96(SM3), 1011 – 1042.

Schmertmann, J. H. (1978). "Guidelines for Cone Penetration Test, Performance and Design", U.S. Department of Transportation, FHWA-TS-78-209.

Schmertmann, J. H., Hartman, J. P., and Brown, P. R. (1978). "Improved Strain Influence Factor Diagrams", Journal of the Geotechnical Engineering Division, ASCE, 104(GT8), 1131 – 1135.

Schnaid, F., and Houlsby, G.T. (1991). "An Assessment of Chamber Size Effects in the Calibration of In Situ Tests in Sand", Geotechnique, 41(3), 437-445.

Seed, B., Tokimatsu, K., Harder, M., and Chung, R. (1985). "Influence of SPT Procedures in Soil Liquefaction Resistance Evaluations", Journal of Geotechnical Engineering, ASCE, 111(12), 1425 – 1445.

Shibuya, S., Tatsuoka, F., Teachavorasinskun, S., Kong, X.J., Abe, F., Kim, Y., and Park, C. (1992). "Elastic Deformation Properties of Geomaterials", Soils and Foundations, 32(3), 26-46.

Simonini, P. (1996). "Analysis of Behavior of Sand Surrounding Pile Tips", Journal of Geotechnical Engineering, 122(11), ASCE, 897 – 905.

Skempton, A. W. (1986). "Standard Penetration Test Procedures and the Effects in Sands of Overburden Pressure, Relative Density, Particle Size, Ageing and Overconsolidation", Geotechnique, 36(3), 425 – 447.

Skempton, A.W. and MacDonald, D.H. (1956). "Allowable settlement of buildings", Proc. of Institute of Civil Engineering, Part III, Vol. 5, pp. 727 - 768.

Stermac, A. G. (1978). "Discussion of Bridge Foundation Move", by Bozozuk, Transportation Research Board 678, Tolerable Movements of Bridge Foundation, Sand Drains, K-Test, Slopes, and Culverts, Transportation Research Board, Washington, D.C., pp. 17 –21.

Tand, K., Funegard, E., and Warden, P. (1994). "Footing Load Tests on Sand", Proceedings of Settlement '94, Vertical and Horizontal Deformations of Foundations and Embankments, ASCE, Vol. 1, pp. 164 – 178.

Tatsuoka, F., Siddiquee, M. S. A., Park, C., Sakamoto, M. and Abe, F. (1993). "Modelling Stress-Strain Relations in Sand", Soils and Foundations, 33(2), 60 – 81.

Teachavorasinskun, S., Shibuya, S., and Tatsuoka, F. (1991). "Stiffness of Sands in Monotonic and Cyclic Torsional Simple Shear", Proceedings of Geotechnical Engineering Congress, Geotechnical special publication No. 27, Vol.1, ASCE, pp. 863 – 878.

Teixeira, C.Z. and Albiero, J. H. (1994). "A Evolução da Reação de Ponta de Estacas Escavadas Submetidas a Sucessivas Provas de Carga", Proceedings of X Brazilian Conference on Soil Mechanics and Foundation Engineering, Vol.1, Foz Do Iguacu, pp. 3 – 9.

Terzaghi, K. (1943). *Theoretical Soil Mechanics*, John Wiely and Sons Inc., New York, N.Y.

Terzaghi, K. and Peck, R. B. (1948). *Soil Mechanics in Engineering Practice*, John Wiely and Sons Inc., New York, N.Y.

Terzaghi, K. and Peck, R. B. (1967). *Soil Mechanics in Engineering Practice*, 2nd Edition, John Wiely and Sons Inc., New York, N.Y.

Tomlinson, M. J. (1971). "Some Effects of Pile Driving on Skin Friction", Proceedings of Conference on Behavior of Piles, ICE, London, 107 – 114.

Trochanis, A. M., Bielak, J., and Christiano, P. (1991). "Three-Dimensional Nonlinear Study of Piles" Journal of Geotechnical Engineering, ASCE, 117(3), 429 - 447.

Vecchia, G. (1991). "Modellazione Con Il Metodo Degli Elementi Finiti Delle Prove Triassiali E Pressiometriche Utilizzando La Legge Constitutiva Di Lade", Graduate School Thesis, Politecnico di Torino, Italy.

Vesic, A.S. (1972). "Expansion of Cavities in Infinite Soil Mass",. Journal of Soil Mechanics and Foundation Engineering Division, ASCE, 98(3), 265 – 290.

Vesic, A. S. (1977). "Design of Pile Foundations", NCHRP Synthesis of Practice No. 42, Transportation Research Board, Washington, D.C., pp. 68.

Vesic, A. S. (1963). "Bearing Capacity of Deep Foundations in Sand", Hwy. Res. Board Rec. No. 39, 112 – 153.

Viggiani, G. and Atkinson, J.H. (1995). "Interpretation of Bender Element Tests", Geotechnique, 45(1), 149-154.

Vijayvergiya, V. N. and Focht, J. A. (1972). "A New Way to Predict Capacity of Piles in Clay", OTC paper 1718, 4th Offshore Technology Conference, Houston, TX.

Vilar (1979). "Estudo da Compressão Unidirecional do Sedimento Moderno (Solo Superficial) da Cidade de São Carlos", M.S. Thesis, School of Engineering of the University of São Paulo (USP), São Carlos, São Paulo.

Wahls, H.E. (1981). "Tolerable settlement of buildings", Journal of Geotechnical Engineering Division, ASCE, 107 (GT11), pp. 1489 – 1504.

Wahls, H.E. (1990). "Design and Construction of Bridge Approaches", National Cooperative Highway Research Program Synthesis of Highway Practice 159, Transportation Research Board, National Research Council, Washington, D.C. pp. 45.

Wahls, H. E. (1994). "Tolerable Deformations", Proceedings of Settlement '94, Vertical and Horizontal Deformations of Foundations and Embankments, Vol. 2, Geotechnical Special Publication No. 40, ASCE, pp. 1611 – 1628.

Walkinshaw, J.L. (1978). "Survey of bridge movements in the western United States", TRR 678, Transportation Research Board, pp. 6 – 12.

Xanthakos, P. (1995). "Bridge Substructure and Foundation Design, Prentice Hall, New Jersey.

Yokel, F.Y. (1990). "Proposed Design Criteria for Shallow Bridge Foundations", Dept. of Commerce, National Inst. of Standard and Technology, Gaithersburg, MD, pp. 50.

Yu, H.S. and Houlsby, G.T. (1991). "Finite Cavity Expansion in Dilatant Soil: Loading Analysis", Geotechnique, 41, 173 – 183.

Yu, H.S. and Mitchell, G.T. (1998). "Analysis of Cone Penetration Resistance: Review of Methods", Journal of Geotechnical and Geoenvironmental Engineering, ASCE, 124(2), 140 – 149.

Yu, P. and Richart, F.E. (1984). "Stress Ratio Effects on Shear Modulus of Dry Sands", Journal of Geotechnical Engineering, ASCE, 110(3), 331-345.

APPENDIX: THE PROGRAM CONEPILE

A.1 Introduction

The program CONEPILE is for calculating the pile load capacity including both the base and shaft resistances. The methods adopted in the program CONEPILE are:

- base resistance: Aoki and Velloso's method;
  LCPC method;
  proposed method (Lee-Salgado method);
- shaft resistance: Aoki and Velloso's method;
  LCPC method.

The details of each method can be found in Chapter 2. The program CONEPILE can calculate the base and shaft resistances for both non-displacement and displacement piles. Users can select the method desired to use for a given soil condition and pile type.

The program CONEPILE consists of two different programs: a user-friendly interface program for pre- and post-processing, and the FORTRAN code used in actual calculation. The user-friendly interface program was developed using Visual-C for easy input and output data processing.

A.2 Guidelines for Running CONEPILE

A.2.1 Starting the program

(1) Click the icon named "CONEPILE" in Windows.

(2) Click the "start" button (Figure A-1).

(3) Click the "exit" button if the program needs to be terminated (Figure A-1).

(4) Click the "continue" button after reading the introduction (Figure A-2).

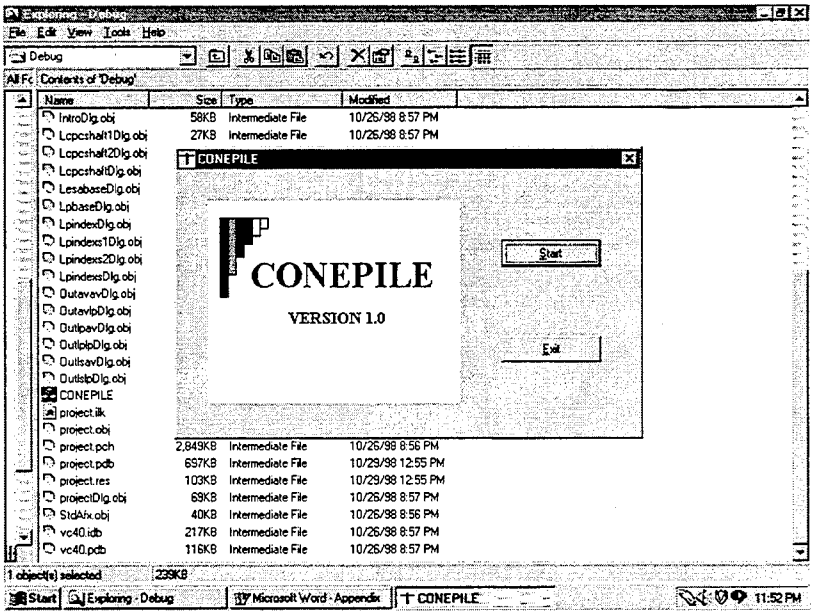

Figure A-1. Start of the program CONEPILE.

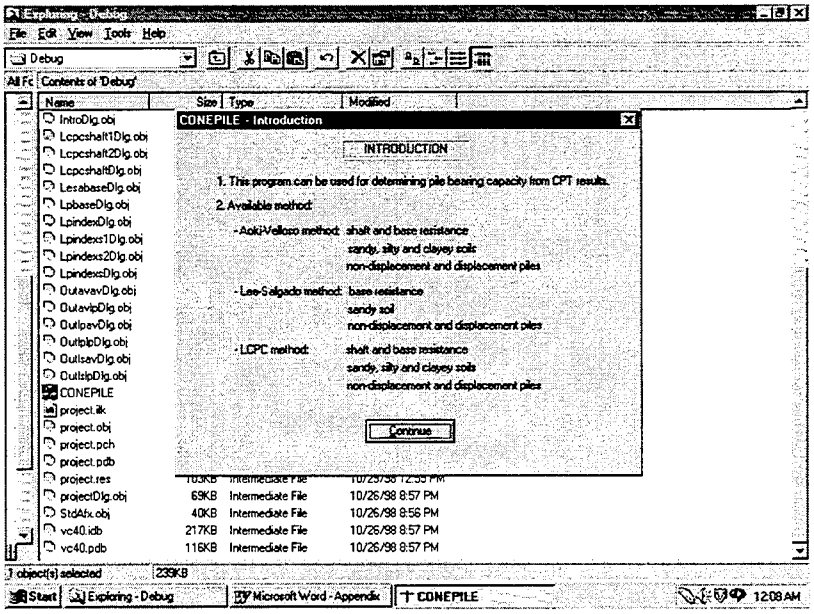

Figure A-2. Introduction of the program.

A.2.2 Selection of the method for calculating the base resistance

(1) Click a button corresponding to the method to be used (Figure A-3).

(2) Aoki-Velloso method (Figure A-4):

- Required input parameters: pile index number;
  pile diameter (B);
  cone resistance at the pile base level (q_c);
- Click "pile index" button to find a pile index number for a given pile type;
- Click "continue" after entering all required parameters.

(3) Lee-Salgado method (Figure A-5):

- Required input parameters: pile index number;
  pile diameter (B);
  representative cone resistance between 0 and 2B below pile base level (q_c);
  effective vertical stress at the pile base level (σ'_v);
  coefficient of lateral earth pressure at rest (K_0);
  relative settlement (s/B);
  critical state friction angle for the material where pile base is located (ϕ_c);
- Click "continue" after entering all required parameters.

(4) LCPC method (Figure A-6):

- Required input parameters: index numbers for pile and soil types;
  pile diameter (B);
  cone resistance at the pile base level (q_c);
- Click "index box" button to find index numbers for given pile and soil types;
- Click "continue" after entering all required parameters.

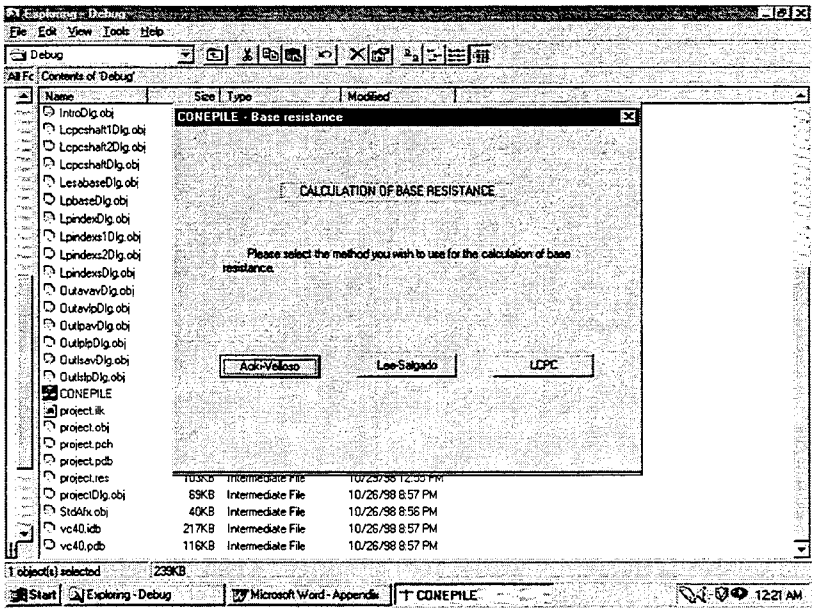

Figure A-3. Selection of the method for calculating the base resistance

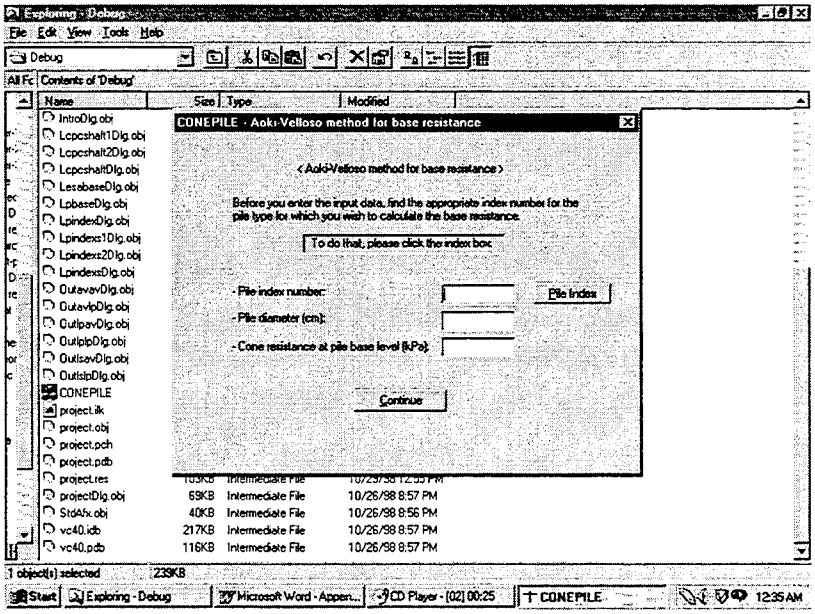

Figure A-4. Aoki-Velloso method for calculating the base resistance.

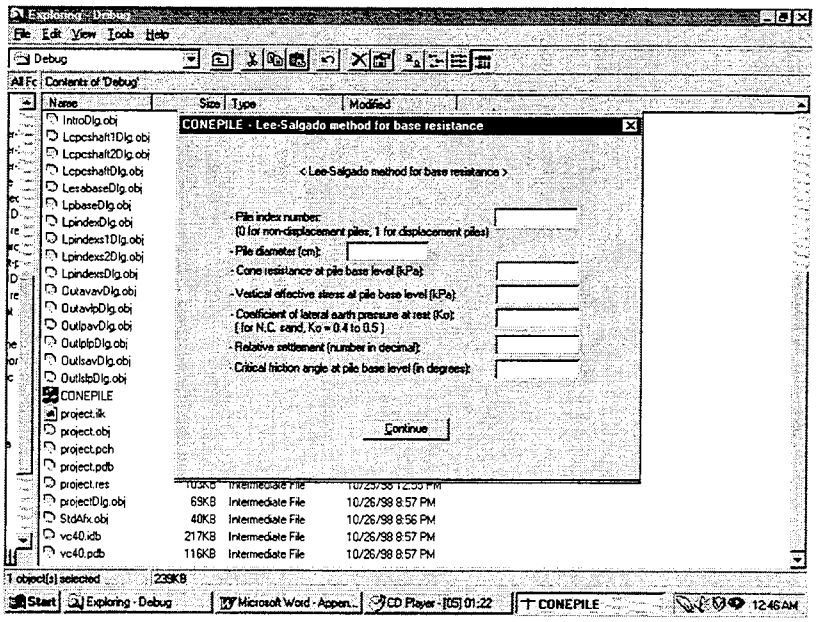

Figure A-5. Lee-Salgado method for calculating the base resistance.

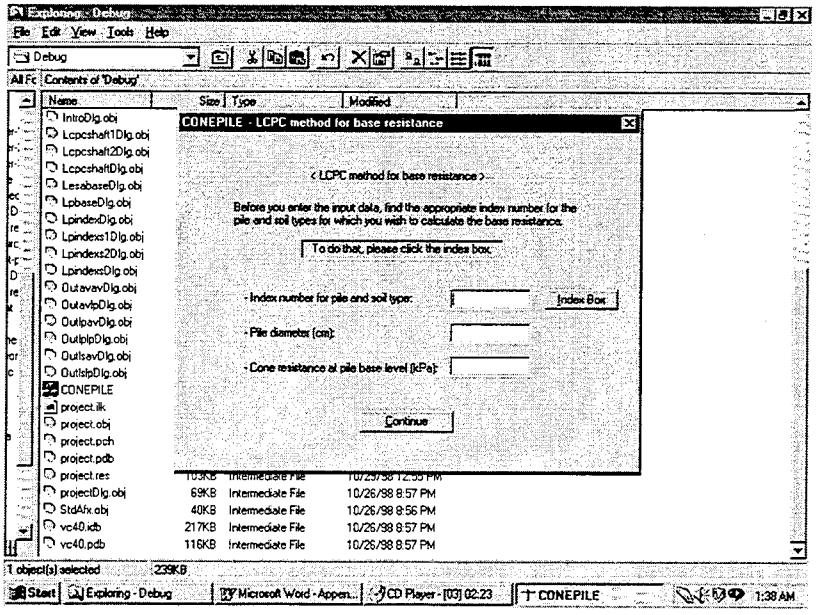

Figure A-6. LCPC method for calculating the base resistance.

A.2.3 Selection of the method for calculating the shaft resistance

(1) Click a button corresponding to the method to be used (Figure A-7).

(2) Aoki-Velloso method (Figure A-8):

- Required input parameters: pile index number;
  pile diameter (B);
  number of layers for shaft resistance calculation;
  thickeness, soil index number, and cone resistance q_c of each sub-layer;
- Click "pile index" and "soil index" buttons to find pile and soil index numbers for given pile and soil types;
- Click "continue" after entering all required parameters;

(3) LCPC method (Figure A-9):

- Required input parameters: pile diameter (B);
  number of layers for shaft resistance calculation;
  thickness, LCPC index number, and cone resistance q_c of each sub-layer;
- Click "LCPC index" button to find index numbers for given pile and soil types;
- Click "continue" after entering all required parameters;

A.2.4 Output (Figure A-10)

(1) Click "show results" button to get the calculated base and shaft resistance.

(2) Click "end" button to terminate the program.

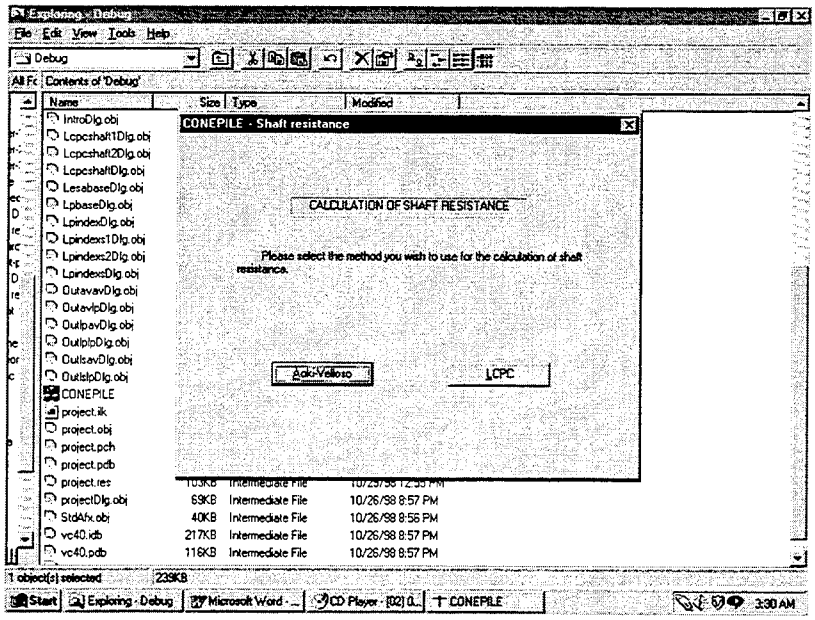

Figure A-7. Selection of the method for calculating the shaft resistance.

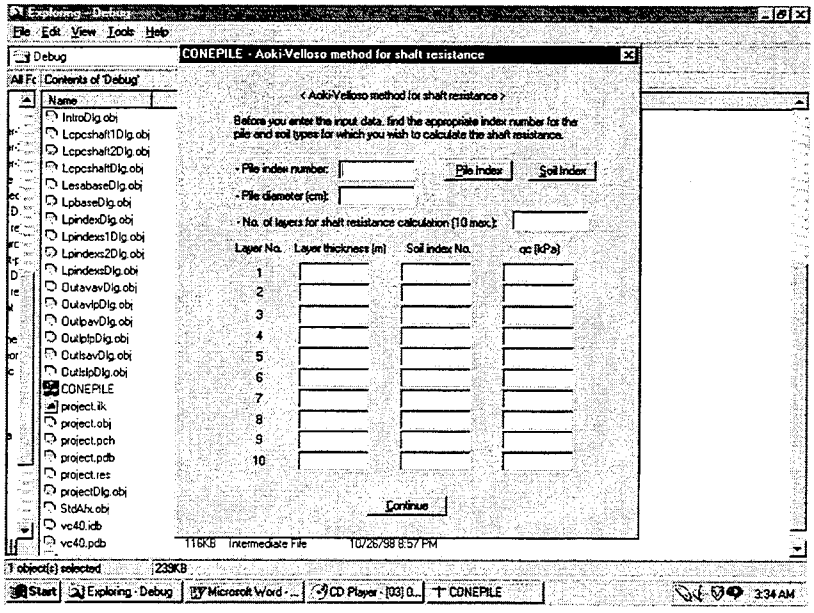

Figure A-8. Aoki-Velloso method for calculating the shaft resistance.

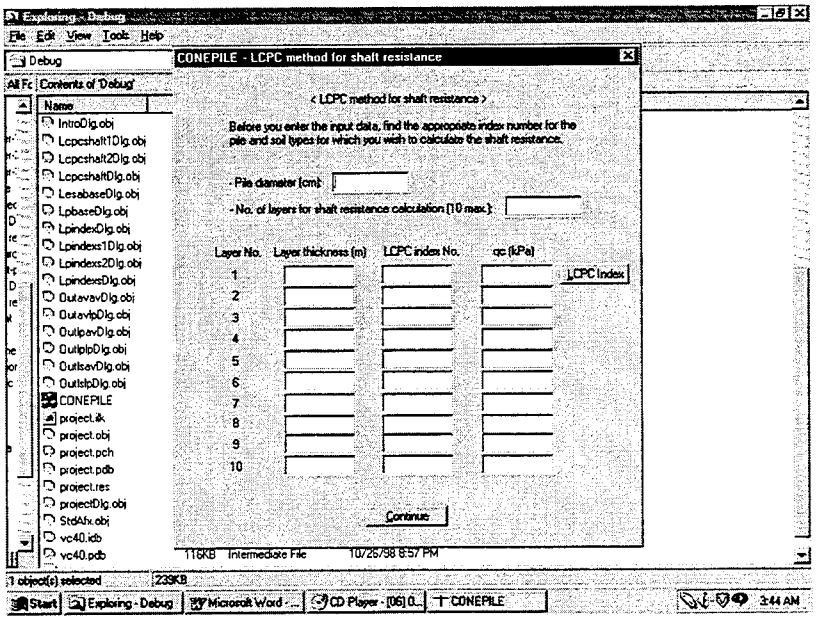

Figure A-9. LCPC method for calculating the shaft resistance.

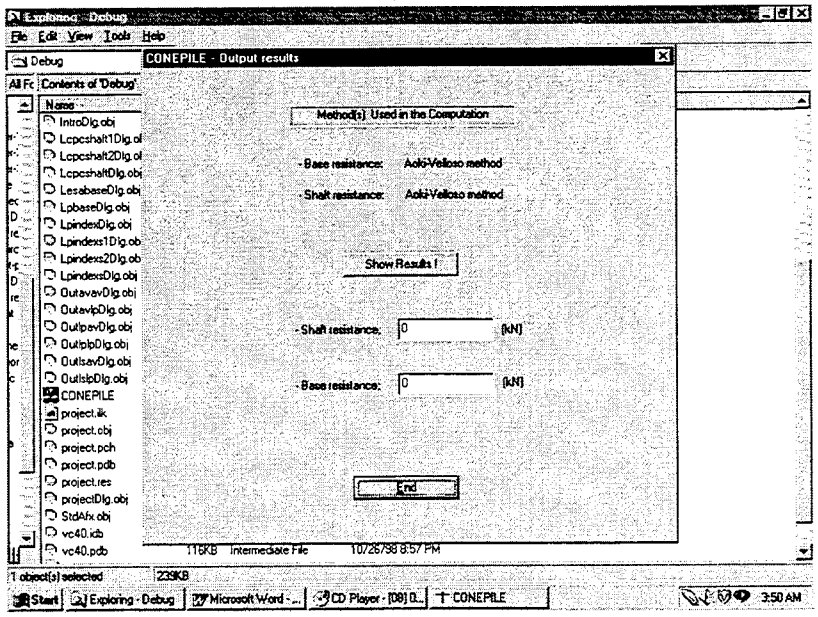

Figure A-10. Output results.